VERTICAL EDDY HEAT FLUXES

AND THE

TEMPERATURE STRUCTURE OF THE MID-LATITUDE TROPOSPHERE

by

WILLIAM JOSEPH GUTOWSKI JR.

B.S., Yale University
(1976)

Submitted to the Department of
Earth, Atmospheric, and Planetary Sciences
in Partial Fulfillment of the
Requirements for the Degree of

DOCTOR OF PHILOSOPHY

at the

MASSACHUSETTS INSTITUTE OF TECHNOLOGY

December 1983

© Massachusetts Institute of Technology, 1983

Signature of Author _____
Department of Earth, Atmospheric, and Planetary Sciences
December 1983

Certified by _____
Peter H. Stone
Thesis Supervisor

Accepted by _____
Theodore R. Madden
Chairman, Departmental Committee on Graduate Students

Lindgren
WITHDRAWN
APR 8 1984
MIT LIBRARIES

VERTICAL EDDY HEAT FLUXES AND THE TEMPERATURE STRUCTURE OF THE MID-LATITUDE TROPOSPHERE

by

WILLIAM JOSEPH GUTOWSKI JR.

Submitted to the Department of Earth, Atmospheric, and Planetary Sciences on December 5, 1983 in partial fulfillment of the requirements for the degree of Doctor of Philosophy.

ABSTRACT

A study of the interaction between vertical eddy heat fluxes and the vertical temperature structure of the mid-latitude troposphere is presented, guided by the hypothesis that a tendency of baroclinically unstable eddies to stabilize the zonal mean flow should be visible in the observed time-averaged zonal mean flow, the baroclinic adjustment hypothesis.

Vertical temperature profiles in a continuous atmosphere are derived for which the zonal mean flow is stable, using the Charney and Stern theorem. The strictly stable profiles cannot occur in the atmosphere, but an atmospheric profile similar to the strictly stable profile might be realizable. It is hypothesized that in such a case, the atmospheric profile would be effectively stable, the profile's instability being so weak that other processes would prevent the instability from manifesting itself. The observed atmosphere does display features of the vertical temperature structure adjustment.

A scaling analysis of the zonally-averaged, quasi-Boussinesq thermodynamic equation using scales for eddy fluxes suggested by studies of linear baroclinic instability and by observations shows that the heating by the vertical eddy heat flux can be as important as that produced by the meridional eddy heat flux. This result occurs because the important length scales for eddy fluxes in the zonally-averaged thermodynamic equation are the scales of the flux divergences, not the scales of the eddy oscillations. The analysis shows how averaging operators may alter the relative sizes of terms in an equation so that terms considered unimportant before averaging can become important after averaging.

A heating balance model for the vertical temperature structure is developed, motivated by the scaling analysis and by the work of others. The model computes an equilibrium among the heating rates by simplified representations of the vertical eddy heat flux, moist convection, and radiation. Model equilibrium states fall into two categories based on their temperature structures. In one, the eddy fluxes play an important role in determining the vertical temperature structure, and the temperature structure displays evidence of the eddy flux's tendency to adjust the flow to stability. In the other, the eddy flux has much less influence, and the temperature structures tend to resemble that of the model's radiative-convective equilibrium, where the eddy heating is absent. The most unstable wave tends to be the wave causing the greatest stabilization of the zonal mean flow. Model runs which neglect all physical processes contained in the full model except the eddy-mean

flow interaction illustrate the capability of the vertical eddy heat flux to adjust the flow to the effective stability hypothesized earlier. Further model runs in which neglected physical processes are selectively restored highlight the restraint on the adjustment to an effective stability imposed by processes controlling the temperature structure near the ground.

Implications of the vertical temperature structure adjustment are discussed. Suggestions are offered for the observation and accurate modeling of vertical eddy heat fluxes.

Thesis supervisor: Peter H. Stone
Title: Professor of Meteorology

DEDICATION

To

My father and my mother.

ACKNOWLEDGEMENTS

I thank my advisor, Professor Peter Stone, for his insights that motivated this thesis. I have benefited greatly from his critical guidance and from his concern for precision. I am indebted to other faculty members as well for informative discussions, most particularly Professor Ray Pierrehumbert, concerning numerical procedures, and Professor Ron Prinn, concerning radiative cooling parameterizations. I also benefited from discussions with Professors Glenn Flierl, Richard Lindzen, and Edward Lorenz, and I appreciate their taking the time to review early drafts of this thesis. I also owe thanks to Professor Barry Saltzman at Yale, who instilled in me his enthusiasm for studying problems of meteorology in general and of climate in particular.

Jeffrey Stephenson developed an early version of the model presented in Chapter III for his M.S. thesis (Stephenson, 1977); his work helped me avoid a number of modeling pitfalls along the way and inspired some avenues of inquiry.

I want to thank Virginia Mills and Jane McNab in department headquarters for keeping the red tape to a minimum in all administrative matters. I am also indebted to Diana Spiegel, who patiently answered my questions when I became frustrated by the computer system. I also thank Isabelle Cole for her speedy drafting of my many figures.

There are a number of people in and about Cambridge to whom I am eternally grateful for their advice, support, and friendship during my stay at MIT. Most particularly, I am indebted to Meg Dempsey for her love and encouragement. I also want to thank Mary Anne Carroll and Ken Finkelstein, who helped me through the complexities of being a graduate

student. There are many fellow students and other friends too numerous to list here who made the times in the classrooms and on the ballfields more enjoyable, and it was a pleasure to have shared company with them. I also owe thanks to the members of the MIT Disarmament Study Group and their friends for helping me understand my role as a scientist and as a citizen.

My first year at MIT was supported by a UCAR Graduate Fellowship. In subsequent years, I was supported through National Aeronautics and Space Administration grant NGR 22-009-727. Most numerical computations for this thesis were performed on the computer system of the Goddard Laboratory for Atmospheric Science.

TABLE OF CONTENTS

Page

Abstract.....2

Dedication.....4

Acknowledgements.....5

Table of Contents.....7

List of Figures.....9

List of Tables.....15

I. Introduction.....17

II. Vertical Eddy Heat Fluxes and Baroclinic Adjustment.....37

1. Baroclinic Adjustment and the Vertical Temperature Structure.....40

2. Baroclinic Instability and Eddy Flux Scales...73

3. Vertical Eddy Heat Flux and the Potential Vorticity Gradient.....81

III. A Vertical Balance Model.....87

1. The Thermal Balance Equation.....88

2. Eddy Heat Flux.....93

3. Radiation.....109

4. Subgrid Scale Fluxes.....111

5. Other Specified Distributions and Parameters.118

6. Numerical Integration.....121

IV. Model Results: Comparison with Observations and Other Models.....127

1. Winter Conditions Solutions.....133

2. Summer Conditions Solutions.....173

3. Sensitivity.....190

V. Model Results: Baroclinic Adjustment.....200

1. Stable Model Solutions.....201

2. Baroclinic Adjustment in the Full Model.....214

VI. Summary and Speculation.....231

Appendix A - Solutions of (2.1.4) for negative $[U]_z$...250

Appendix B - Numerical Considerations.....254

B1. Finite Differencing.....254

B2. Eigenvalue Computations.....257

B3. The Variable Time Step.....264

B4. Effects of Resolution and Grid Depth.....268

B5. Shapiro Filter.....274

B6. The Influence of $[U]_z$ in the Stratosphere...285

References.....287

Biographical Note.....294

LIST OF FIGURES

Figure — Page

1.1 $\overline{[T]}(z)$ at 45°N for winter (W) and summer (S), from Oort and Rasmusson (1971).....21

1.2 $N^2(z)$ at 45°N for winter (W) and summer (S), computed from Oort and Rasmusson's (1971) temperature and height data.....23

1.3 The heating rates (K/day) in Hantel's (1976) boxes between 30°N and 49°N. The key identifies the location in each box of the heating rate due to radiation (R), the vertical zonal mean cell flux (V_c), the vertical eddy flux (V_e), the horizontal zonal mean cell flux (H_c), and the horizontal eddy flux (H_e).....25

1.4a The transient eddy vertical heat flux in the atmosphere, as obtained by various researchers. The symbols identify the source of data: squares for a combination of observations and numerical model output, circles for observations alone. Here and in Figure 1.4b, symbols placed on curves identify the levels providing temperature data for the referenced work. C_p is the specific heat for dry air at constant pressure and g is the gravitational acceleration.....28

1.4b As in Figure 1.4a, but for the sum of transient and standing eddy fluxes.....29

2.1 Schematic representation of $[U]_A(z)$ and $\frac{\partial}{\partial y}[T]_A(z)$ for a baroclinically stable zonal mean flow, under the [U](z) adjustment. Also shown are unstable profiles for a possible unadjusted original state.....43

2.2 $\Delta T = \{\overline{[T]}(40°N) - \overline{[T]}(50°N)\}$ as a function of height for summer (S) and winter (W).....45

2.3 Idealized vertical profiles of θ and N^2 in a) the well-mixed planetary boundary layer and b) the stable planetary boundary layer.....50

2.4 Initial and adjusted vertical profiles of $[\theta]$, N^2, and $[Q]_y$ in the temperature jump model.....53

2.5 $N_A^2(z)/N_A^2(0)$ for two choices of γ. Also shown is the matching level, z_A, for each case and $r = N_0^2/N_A^2(0)$.....60

2.6 $\Delta Z/Z$ vs. γ_0.....62

Figure Page

2.7a $N^2(z)$ given by observations for winter (Oort and Rasmusson, 1971) and by the adjustment. Also shown is the N^2 given by a moist adiabat using observed temperatures and pressures.....66

2.7b As in Figure 2.7a, except for summer.....67

2.8 Matching of $\theta_A(z)$ and $\theta_0(z)$ when $N_0^2 = N_0^2(z)$.....70

2.9 The ratio in (2.3.5) as a function of height for wave number 3.....85

3.1 The annual mean heating rate due to the meridional transport of moist static energy $C_p\overline{[v\theta]} + L_v\overline{[vq]}$, using the data of Oort and Rasmusson (1971). q is the specific humidity. The contour spacing is 0.4 K/day, and positive heating is hatched.....91

3.2 $[\omega^*\alpha^*](z)$ as a function of time in Gal.'s (1976) wave-mean flow interaction experiment using wave number 7. The numbers on each curve refer to the time in days from the beginning of the experiment. Each $[\omega^*\alpha^*]$ curve is normalized by the total kinetic energy of the wave at the corresponding time.....97

3.3 Mullan's (1979) comparison of the Leovy parameterization for meridional latent heat flux with the observed eddy latent heat flux from Oort and Rasmusson (1971), for a) January and b) July. All fluxes are vertically-averaged.....105

3.4 a) Winter EAPE → EKE conversion rates calculated by Tomatsu (T) and by Chen (C), as a function of zonal wave number n_z. Also shown is the mean of the two calcuations (solid line) and the relative sizes of the peak sensible heat fluxes in the model's wave ensemble runs for winter conditions (dots). b) Summer EAPE → EKE conversion rates calculated by Tomatsu (solid line) and the relative sizes of the peak sensible heat fluxes in the model's wave ensemble runs for summer conditions (dots).....108

3.5a Specified radiative cooling rates, Q_{Do}. The figure shows the cooling profiles for winter and summer at 45°N computed by Dopplick (1979) and the adjusted profiles for each season used by the model.....112

3.5b $T_{Do}(z)$ for winter and summer.....113

3.6 Observed $\overline{[T]}(z)$ for winter (W) and summer (S) at 45°N (Oort and Rasmusson, 1971) compared with $T_m(z)$, the temperature profile for a moist adiabat intersecting the observed temperature at 1000 mb.....115

Figure | Page

3.7 Observed summer $N^2(z)$ at 45°N compared with $N^2(z)$ calculated from the summer $T_m(z)$ in Figure 3.6.....116

3.8 A flow chart of the model's integration procedure.....124

4.1a Typical $N^2(z)$ for a strong eddy solution.....134

4.1b Typical $N^2(z)$ for a weak eddy solution (solid) and $N^2(z)$ for RCE (dashed).....135

4.2 Winter $[T](z)$ from observations and from three most unstable mode solutions. The labels on the curves refer to the size of the specified EKE.....138

4.3 $[T](z)$ from 1.5 E_w single mode solutions using different wave numbers and from the RCE solution. The number identifying a curve refers to the zonal wave number used to compute the particular solution.....140

4.4 $N^2(z)$ for the temperature profiles in Figure 4.2. Again, the labels on the curves refer to the size of the specified EKE used to compute model solutions.....144

4.5 $N^2(z)$ for the winter conditions wave ensemble solution using a 1.5 E_w eddy kinetic energy.....147

4.6 $[T](z)$ for two single mode solutions, using the specified EKE indicated on the curve. Each solution uses $n_z = 4$.....149

4.7 $[Q]_y(z)$ corresponding to the $N^2(z)$ profiles in Figure 4.2. The label for each model solution curve refers to the EKE used to compute the solution. Also shown are $[\widetilde{Q}]_y$ for each profile and the steering level s.l. for each model solution.....151

4.8 Vertical eddy fluxes of sensible heat, latent heat, and their sum and the sum of the eddy and convective fluxes, all for the 1.5 E_w $n_z = 4$ solution.....156

4.9 Heating rates for the 1.5 E_w $n_z = 4$ solution.....164

4.10 The a) phases and b) amplitudes of w^*, θ^*, and ψ for the 1.5 E_w $n_z = 4$ solution. Figure 4.10a shows the phase of ψ plus $\pi/2$ so that the curve is the phase of v^*. In Figure 4.10b, the units are: w^* - 10^{-2} m/sec, θ^* - 10 K, and ψ - 100 m.....167

4.11 Spectra of a) growth rates and b) wave depths z_{cl} for baroclinically unstable waves, using the temperature profile from the 1.5 E_w $n_z = 4$ solution.....169

Figure		Page
4.12	As in Figure 4.11, only using $N^2(z) = \tilde{N}^2$ from the 1.5 E_w n_z = 4 solution	170
4.13	Comparison of $\rho C_p[w^*\theta^*]$ profiles computed by the model when $N^2 = \tilde{N}^2(z)$ and when $N^2 = \tilde{N}^2$. Both N^2 profiles are given by the 1.5 E_w n_z = 4 solution	174
4.14	Summer [T](z) from observations at 45°N and from three solutions: 1.5 E_s n_z = 4, 1.5 E_s = 6, and RCE. Numbers on the curves refer to the zonal wave number used to produce the solution	176
4.15	N^2 for the three temperature profiles in Figure 4.14	178
4.16	$[Q]_y(z)$ and $[\tilde{Q}]_y$ from observations and from the n_z = 4 and n_z = 6 solutions in Figure 4.14. Also shown is the steering level s.l. for each model solution	180
4.17	The eddy sensible heat flux, the eddy latent heat flux, the total eddy heat flux, and the total flux by all atmospheric motions in the model for a) the 1.5 E_s n_z = 4 solution and b) the 1.5 E_s n_z = 6 solution	183
4.18	Heating rates for a) the 1.5 E_s n_z = 4 solution and b) the 1.5 E_s n_z = 6 solution	187
4.19	Vertical profiles of the two terms on the left side of (2.3.4) given by the 1.5 E_s solutions using a) n_z = 4 and b) n_z = 6	188
5.1	Growth rate kc_i as a function of model time for E model runs using various wave numbers, the number on each curve identifying the wave number used	202
5.2a	[T](z) for the initial state in the E model and for the stabilized state given by the n_z = 3 E model run	203
5.2b	Like Figure 5.2a, but for $N^2(z)$. Also shown is $N^2(z)$ for a stabilize state according the adjustment theory in Chapter II	204
5.2c	Like Figure 5.2a, but for $[Q]_y(z)$	205
5.3	Gall's static stability and vertical wind shear squared as functions of pressure and time for his wave number 7 wave-mean flow interaction experiment. The data have been averaged between 35°N and 65°N. The numbers on the curves refer to the time in days from the beginning of the experiment	209

Figure | Page

5.4 $[w^*\theta^*](z)$ as a function of time in the $n_z = 3$ E model run. The numbers on the curves refer to the time in days from the beginning of the run.....211

5.5 Growth rate kc_i as a function of time for the E, E+R, and E+C model runs, all using $n_z = 3$.....215

5.6 $N^2(z)$ after 40 days in the $n_z = 3$ E+C model run.....217

5.7 $[Q]_y(z)$ and $[\tilde{Q}]_y$ for three winter conditions solutions: a) 1.5 E_w $n_z = 6$, b) 1.5 E_w $n_z = 8$, and c) 1 E_w $n_z = 4$ with $Q_{Do}(z)$ at all levels equal to one half of Dopplick's cooling rates. Also shown is the steering level s.l. for each case.....218

5.8 The variation with specified EKE of a) the maximum eddy flux, b) the growth rate kc_i, and c) the vertical mean Brunt-Vaisalla frequency squared N^2 in winter conditions solutions using $n_z = 4$.....222

5.9 S as a function of $[U]_z$ for most stabilizing mode (MSM) solutions, most unstable mode (MUM) solutions, and RCE solutions.....229

A.1 Initial vertical profile of $[\theta]$ and the adjusted profile when $[U] < 0$.....252

B.1 T_j after 10,000 time steps from two model runs that are identical except that one calculates T using Form 1 and the other calculates T using Form 2.....256

B.2 A comparison of phase speed spectra computed by the matrix method and by the shooting method.....263

B.3a $N^2(z)$ for three model runs that are alike except that each uses a different grid depth.....271

B.3b Like Figure B.3a, except showing the total eddy flux $\rho(1 + \Lambda)[w^*\theta^*]$.....272

B.3c Like Figure B.3a, except showing the eddy streamfunction amplitude $|\psi|$.....273

B.4 $N^2(z)$ produced by an unfiltered model run.....275

B.5a T(z) for three different times in the integration leading to the solution in Figure B.4.....277

B.5b Like Figure B.5a, only showing the eddy heating.....278

B.6 The filter response functions $R_1(\lambda)$ and $R_2(\lambda)$.....281

Figure Page

B.7 $N^2(z)$ from three model solutions, one with no filter, one using the R_1 filter, and one using the R_2 filter. All model parameters are the same in the three solutions.....283

B.8 $N^2(z)$ for three model solutions which differ in the [U](z) profiles used for their computations.....286

LIST OF TABLES

Table — Page

2.1 Frequently appearing symbols.....39

2.2 The relationship between N_0^2, $N_A^2(0)$, z_A, $\Delta\theta$, and $\Delta Z/Z$ in the N^2 adjustment model. Brunt-Vaisalla frequencies are in units of 10^{-4} sec^{-2}, z_A is in km, $\Delta\theta$ is in K, and $\Delta Z/Z$ is in percent.....65

2.3 The range of heights where $\left| \frac{1}{\rho}\frac{\partial}{\partial z}\rho[w^*\theta^*] \Big/ \frac{\sigma}{\rho}\frac{\partial}{\partial z}\left(\rho\frac{[\theta^{*2}]}{[\theta]_z}\right)\right|$ is much greater than 1, the levels of extreme $\rho[w^*\theta^*]$, and the steering level, as functions of wave number. All All heights are in km.....86

3.1 The ratio |(wave-wave APE exchange)|/(wave-mean flow APE exchange) as a function of wave number, computed from the statistics of Saltzman (1970) and of Tomatsu (1979).....99

3.2 Vertical mean EKE per unit area at 45°N (units: 10^5 J/m^2).....103

4.1 Wave numbers providing the most unstable mode solution (MUM) and the most stabilizing mode solution (MSM) for different choices of EKE and $[U]_z$ in the vertical balance model. The table also shows whether the solution is a strong eddy solution (SE) or a weak eddy solution (WE).....137

4.2 Surface heat flux from Hantel, using on Budyko's data, from the GISS climate model, and from the vertical balance model's (VBM's) 1.5 E_w n_z = 4 solution. All fluxes are in W/m^2.....154

4.3 The net vertical heat flux (W/m^2) by eddies and convection, from computations by Hantel, the GISS climate model, and the vertical balance model (VBM).....157

4.4 Vertical eddy heat fluxes computed by Tomatsu (T), Chen et al. (C+), Chen (C), Schubert and Herman (SH), the GISS model, and the vertical balance model (VBM).....159

4.5 Comparison of computations for summer surface heat fluxes (W/m^2) given by Hantel for Budyko's data and by the vertical balance model for 1.5 E_s solutions using n_z = 4 or n_z = 6.....181

4.6 Comparison of computations for the sum of eddy and convective vertical heat fluxes (W/m^2) for summer.....182

Table Page

4.7 Summer vertical eddy heat fluxes (W/m^2) from the GFDL model, from Tomatsu, and from 1.5 E_s vertical balance model solutions using $n_z = 4$ or $n_z = 6$.....185

4.8 The percentage change of $\tilde{N}^2$, z_T, kc_i, and $\max\{\rho C_p(1+\Lambda)[w^*\theta^*]\}$ when $[U]_z$ or the specified EKE changes by ±50%. The standards for comparison are shown on the first line under the column headings.....192

4.9 Like Table 4.2, only for summer.....196

4.10 The percentage change of $\tilde{N}^2$, z_T, kc_i, and $\max\{\rho C_p(1+\Lambda)[w^*\theta^*]\}$ when the model neglects the vertical latent heat flux. The standards for comparison are the corresponding model runs including the latent heat flux in Tables 4.8 and 4.9. Also shown is the percentage of the original maximum flux due to the latent heat flux,%LH.....198

B.1 The effects of grid resolution upon model solutions. The Brunt-Vaisailla frequency N^2 is in units of 10^{-4} sec^{-2}, the resolution and the level of the flux peak in km, the flux amplitudes in W/m^2, and phase speed in m/sec.....270

CHAPTER I

INTRODUCTION

The vertical temperature structure of the earth's atmosphere is an important feature of the general circulation, influencing both the dynamic and radiative energy transfers. A well-developed understanding of the factors controlling the temperature structure is lacking at present. Although the ultimate source of energy for the atmosphere is solar radiation, dynamic transports are fundamental to the atmosphere's thermal balance (Gierasch et al., 1970). The character of the atmosphere's circulation varies with location, so that, presumably, the role played by dynamics in determining the temperature structure does as well. This thesis focuses on one particular circulation regime, the mid-latitude troposphere. The mid-latitude region is of particular importance for the earth's climate since it is where the total meridional flux of energy per unit area in the atmosphere-ocean system must peak (Stone, 1978a). The main part of this flux occurs in the troposphere, so that the temperature structure in this region exerts an influence over the energy balance for the entire globe.

Guided by observations, earlier models, and a scaling analysis, this thesis presents a simple balance model for the zonally-averaged time mean temperature structure. The model assumes that moist convection and eddies driven by baroclinic instability of the zonal mean circulation provide the most important dynamic contributions to the thermodynamic balance yielding the observed vertical temperature structure. One aim of this work is to determine how successfully the

simple model can reproduce the observed structure. The model's temperature structure does not always match the observed temperature structure, so that a further aim is to understand the reasons for the discrepancy.

The influence of baroclinic instability on the model's temperature structure is especially important in understanding the model's results. Work by Stone (1978b) suggests that the atmosphere's heat and momentum transports maintain the time and zonal mean mid-latitude troposphere near a state of neutrality with respect to baroclinic instability, the baroclinic adjustment hypothesis. This thesis explores the influence baroclinic adjustment has on the vertical temperature structure and the possible limits to its influence due to other physical processes, most notably radiation and convection. The simple model is especially useful in this regard, for it permits an examination of the interaction between vertical eddy heat fluxes and the zonal mean vertical temperature structure in the presence and absence of other physical processes.

The development of a simple model presumes some degree of determinism in the phenomenon studied. Within the mid-latitude troposphere, the atmosphere displays much temporal, as well as spatial variation, a large portion of which appears to be of a turbulent nature. Such a characteristic inhibits a deterministic approach. Stochastic approaches can yield insight into the character of the fluctuations both observationally (e.g. Stone et al., 1982) and theoretically (e.g. Hasselmann, 1976). However, averaged over suitable time and length scales, the atmosphere's temperature field does respond directly to variations in external forcing (Lorenz, 1979), suggesting some form of deterministic behavior. Moreover, the results of Stone et

al. (1982) show that, even on shorter time scales than those yielding the forced response of Lorenz, there is a negative feedback between the zonal mean temperature field and the eddy fluxes with a damping time of a few days. A reasonable hypothesis appears to be that a statistical equilibrium among the relevant internal and external heating processes exists when they are averaged over suitably long time and length scales and that this equilibrium determines the vertical temperature structure.

The model computes the equilibrium among its heat fluxes for the zonal and seasonal mean and determines a corresponding mean vertical temperature structure for summer and winter. The thermal balance under consideration involves difficult to measure vertical fluxes, so that a well-observed assessment of the degree of correspondence between mean transports and mean vertical temperature structure is not available. If the feedbacks between the two are strong enough, then a deterministic relationship does exist between them. This being the case, the balanced state given by the simple model may then correspond to the atmosphere's statistical equilibrium and can provide insight into the physics of the atmosphere.

We may view the model as part of a hierarchy of climate models, ranging from highly-averaged 0- and 1-dimensional models to much more complicated general circulation models (GCM's). Despite being among the more highly-averaged models, the possiblity does exist that such a simple model captures nearly all of the relevant physics of the statistical mean. In that case, more complex models would not yield much further improvement in the understanding or simulation of the phenomenon studied, the mid-latitude vertical temperature structure (Saltzman, 1978).

Figure 1.1 displays the time and zonal mean temperature as a function of height and season, from Oort and Rasmusson (1971). Following their notation, $[(\ )]$ denotes the zonal mean, $(\ )^*$ the departure from the zonal mean, $\overline{(\ )}$ the time mean, and $(\ )'$ the departure from the time mean. The decrease in temperature with height, or lapse rate, is roughly linear in the troposphere. The nearly isothermal layer extending upward from the tropopause is characteristic of the stratosphere. The lapse rate and the tropopause height show only a small change with season compared to the meridional temperature gradient, which changes by about a factor of two between summer and winter. This is remarkable, considering that the energy of the mid-latitude circulation varies considerably over the course of a year (Piexoto and Oort, 1974; Tomatsu, 1979).

Consideration of the spatial and temporal variation of the temperature field shows the degree to which the zonal and seasonal mean represents a statistical equilibrium. The temperature difference between the surface and the tropopause in Figure 1.1 is about 60 K. This temperature difference is a measure of the tropospheric mean lapse rate. For the seasonal and zonal mean, the standard deviation in temperature at some level is about 9 K (Oort and Rasmusson, 1971), so that temperature fluctuations of the size of one standard deviation cause the surface-tropopause temperature difference to vary by about 15%. The relative steadiness of this approximate vertical mean lapse rate indicates the appropriateness of the seasonal and zonal mean vertical temperature structure as an object of study.

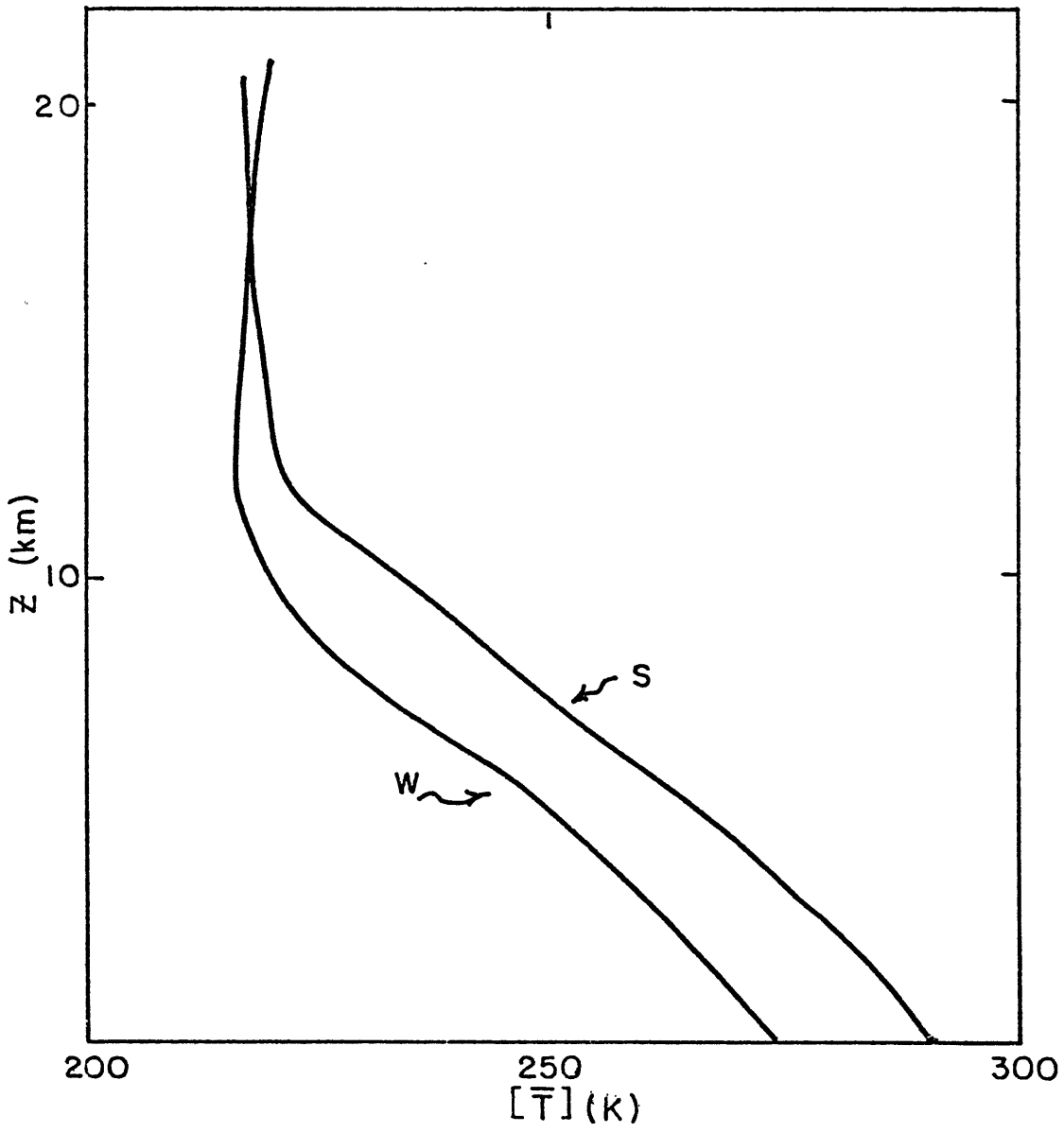


Fig. 1.1 - $\overline{[T]}(z)$ at 45°N for winter (W) and summer (S), from Oort and Rasmusson (1971).

More dynamically relevant measures of the vertical temperature structure's influence upon dynamics than [T](z) are the static stability, $\sigma = \frac{\partial}{\partial z}[\theta]$, and the Brunt-Vaisailla frequency, $N^2 = \frac{g}{[\theta]} \frac{\partial}{\partial z}[\theta]$, where θ is potential temperature and g is the gravitational acceleration. In the troposphere, σ and N^2 are nearly proportional to each other and discussion of the temperature structure in this work uses them interchangeably. The zonal and seasonal mean $N^2(z)$ at 45°N in winter and summer appears in Figure 1.2, also based upon the data of Oort and Rasmusson. These profiles are representative of $N^2(z)$ across the mid-latitudes in their respective seasons. Again, the seasonal variation is relatively small. This well-known fact is often used by climate modelers to justify the assumption, either implicit or explicit, that static stability can be held constant in time. An incomplete understanding of the factors controling static stability precludes assuming any other type of behavior, anyway. Note also that there is a substantial decrease in N^2 between the surface and the tropopause. Simple models of the mid-latitude troposphere often assume that N^2 is constant in the vertical. This assumption could be inaccurate, especially if the phenomenon under consideration is sensitive to the magnitude of N^2 and has a depth scale comparable to that of the troposphere. Baroclinic instability is one possible example.

There are a number of potentially important contributors to the local heat balance determining static stability. Measurement of many is difficult. However, we can obtain some information about which processes are most important from the temperature structure itself. Stone and Carlson (1979) have studied the seasonal and latitudinal variation of lapse rates and compared them to constraints posed by

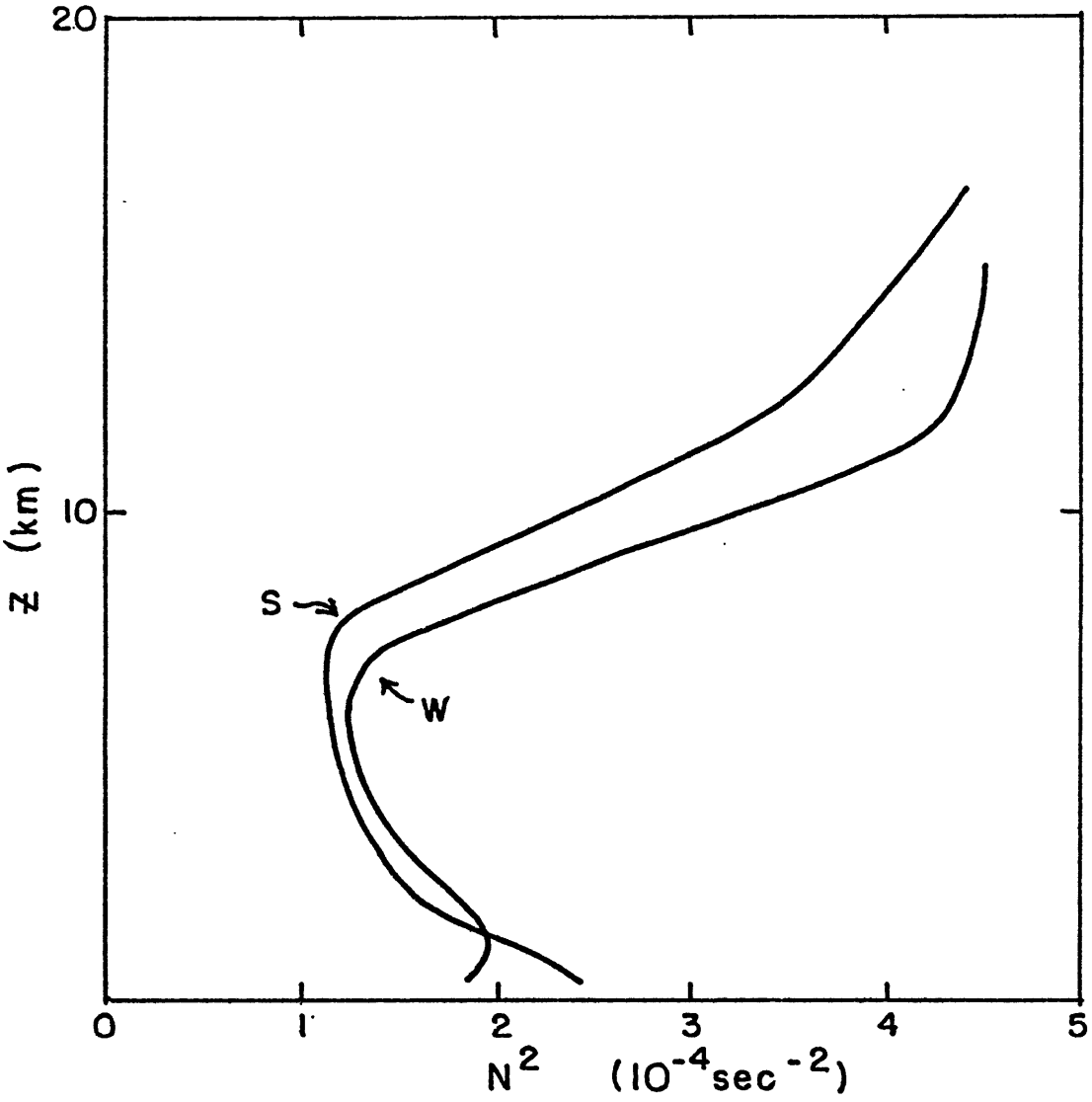


Fig. 1.2 - $N^2(z)$ at 45°N for winter (W) and summer (S), computed from Oort and Rasmusson's (1971) temperature and height data.

physical processes. They conclude that heating due to baroclinic instability and moist convection are two of the most important processes determining the mid-latitude temperature structure.

The study by Stone and Carlson does not delineate the partitioning of local heating between vertical and horizontal flux convergences. Synoptic and planetary scale motions provide most of the contribution to heating by horizontal convergence, so that energy transports in the horizontal, and their accompanying heating, are observable with some accuracy. Vertical motions in the mid-latitudes are generally much smaller than horizontal motions, posing a severe observational difficulty which has inhibited direct measurement of their transports over climatological time and length scales. Hantel (1976) has obtained a value for the net vertical flux of moist static energy due to eddy transports on all scales by calculating it as a residual in a box model for the northern hemisphere. Figure 1.3 displays the heating rates resulting from the divergences of radiation and moist static energy flux in Hantel's mid-latitude boxes. In many of the boxes, there is a rough balance between the heating by radiation and that by the net vertical eddy flux. Of particular importance here is the fact that such a balance exists for both seasons in the mid-latitude boxes between 250 mb and 750 mb, i.e. in the mid-latitude troposphere above the planetary boundary layer.

The exact nature of the motions contributing to Hantel's vertical eddy flux can not be deduced from the box analysis. However, using output from a GCM, he suggests comparable apportionments of the heating between large scale, or grid scale, fluxes and subgrid scale fluxes. This breakdown of the flux is consistent with Stone and Carlson's

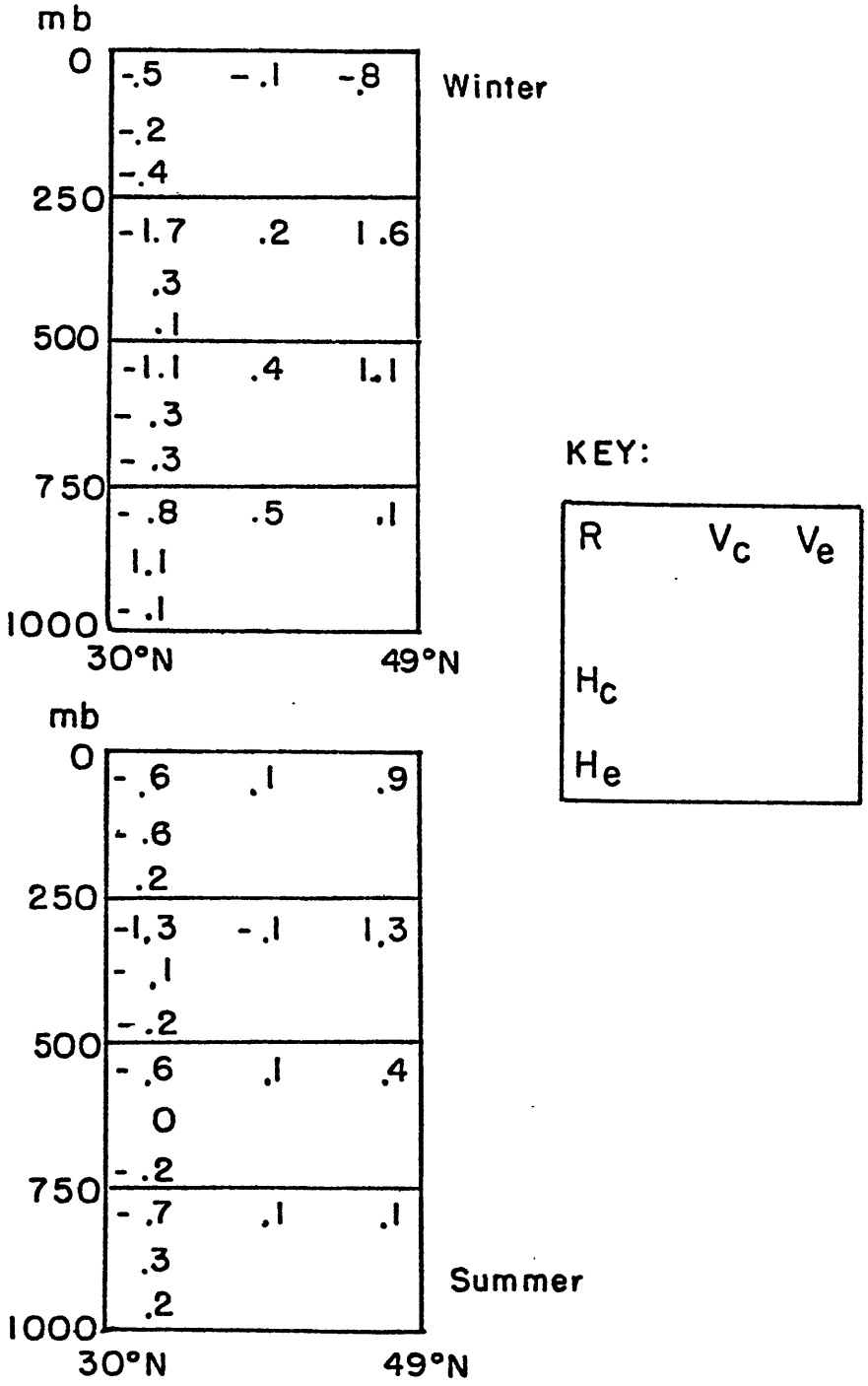


Fig. 1.3 - The heating rates (K/day) in Hantel's (1976) boxes between 30°N and 49°N. The key identifies the location in each box of the heating rate due to radiation (R), the vertical zonal mean cell flux (V_c), the vertical eddy flux (V_e), the horizontal zonal mean cell flux (H_c), and the horizontal eddy flux (H_e).

portrayal of the processes determining the lapse rate. Baroclinic instability is strongest on the synoptic and planetary scales, or the scales resolved by a GCM. Moist convective heating is typically confined to the smaller, or subgrid, scales. The two studies combined imply that the local thermodynamic balance is, as a first approximation, a balance among vertical flux divergences, the principal fluxes resulting from baroclinic instability, moist convection, and radiation.

Other observational evidence, again obtained by various indirect methods, tends to support the importance of eddy vertical fluxes in the local heat balance. Stone et al. (1982) have noted the existence of a relatively short, 1.5 day time scale in atmospheric statistics of a baroclininc stability parameter and have suggested that vertical transports could act this rapidly. Edmon et al (1980) have computed the Eliassen-Palm flux and the residual circulation that it produces. This circulation should have properties similar to a Lagrangian-mean circulation. However, their computations show rising motion throughout much of the mid-latitude troposphere, in disagreement with numerical simulations of Lagrangian motions, which indicate downward motion there (e.g. Kida, 1977). They reconcile the difference by suggesting that the rising motions be attributed to the divergence of the vertical eddy heat flux and estimate that it can produce heating rates on the order of 1 K day^{-1}. They further suggest that this eddy flux is produced by baroclinic instability, although vertical fluxes on both the large and small scale may be responsible.

Despite the difficulties involved, there have been a number of attempts to calculate a form of the atmosphere's vertical eddy sensible heat flux, $[\omega^* T^*]$, where ω is the pressure coordinate vertical

velocity. Although the calculation of $[\omega^*T^*]$ provides an estimate of the size of the flux's heating and its possible influence on the temperature balance, the usual motivation for these studies has been to determine the strength of the conversion between eddy available potential energy and eddy kinetic energy. The calculations of $[\omega^*T^*]$ generally use one of the two following methods. The first method is based solely on observations, using the observed height, wind, and temperature fields and a diagnostic equation for ω to compute the flux. Jensen (1961), for example, applies a form of Panofsky's (1946) adiabatic method. Tomatsu (1979), Chen et al. (1981), and Chen (1982) use the quasi-geostrophic ω-equation and NMC analyses to estimate the flux. The second method uses a numerical model, updated periodically by observations, to produce ω fields. The particular models used range from relatively simple two-layer quasi-geostrophic models (Saltzman and Fleisher, 1961; Berggren and Nyberg, 1967) to more sophisticated primitive equation models (Lau, 1979; Oerlemans, 1980; Schubert and Herman, 1981). The statistics in these cases are hybrids of model and atmospheric climatologies.

Figure 1.4a shows the results of these computations for the transient eddy flux alone, $\overline{[\omega'T']}$, while Figure 1.4b shows the results for the total eddy flux, $\overline{[\omega'T']} + [\overline{\omega^*T^*}]$. The figures use log-pressure coordinates to facilitate comparison with model output in height coordinates. The symbols on the figures distinguish the results produced by the two methods from each other: squares represent model-observation statistics, while circles represent purely observational statistics. Although some of the authors display their results as continuous profiles, Figure 1.4 gives some sense of the

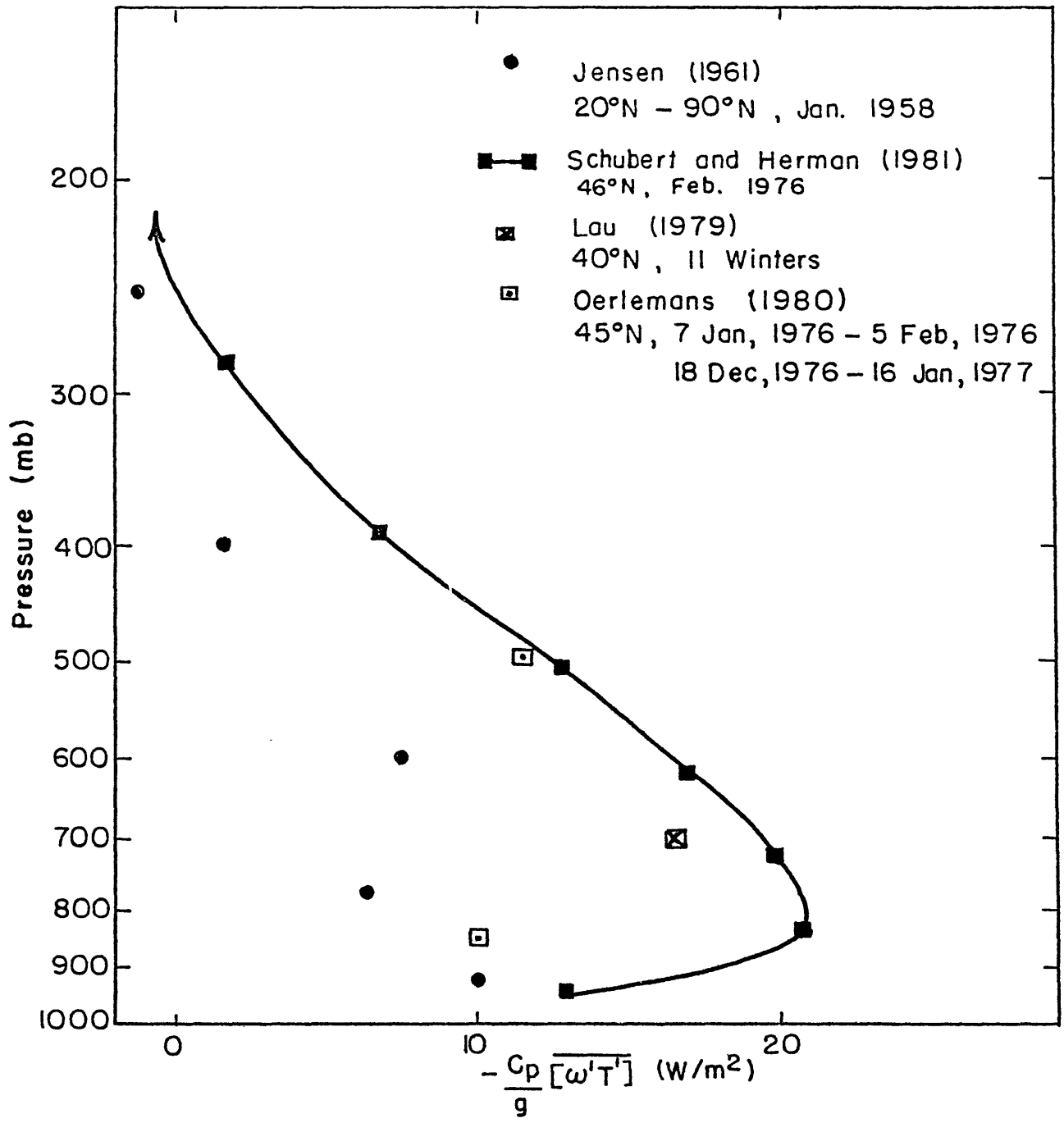


Fig. 1.4a - The transient eddy vertical heat flux in the atmosphere, as obtained by various researchers. The symbols identify the source of data: squares for a combination of observations and numerical model output, circles for observations alone. Here and in Figure 1.4b, symbols placed on curves identify the levels providing temperature data for the referenced work. C_p is the specific heat for dry air at constant pressure and g is the gravitational acceleration.

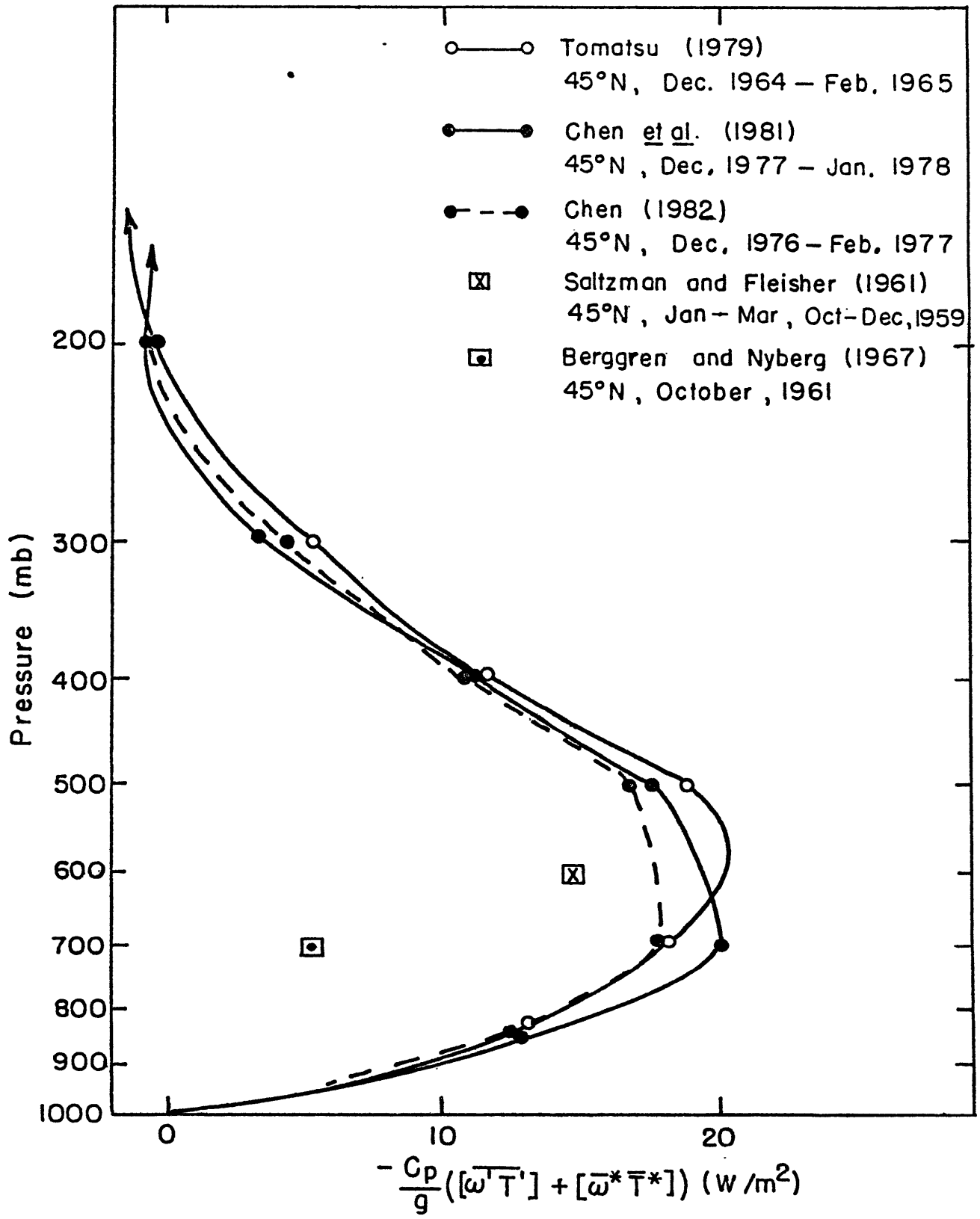


Fig. 1.4b - As in Figure 1.4a, but for the sum of transient and standing eddy fluxes.

vertical resolution in their studies by placing squares or circles at the levels providing the temperature data.

Considering the differences in averaging periods, regions of data coverage, and methods, the results show reasonable agreement, especially among the more recent calculations. The flux peaks below 500 mb and typically changes sign at about 200 mb. The low resolution hinders attempts to determine the level of maximum flux. It also means that the choice of lower boundary condition may influence the location and strength of the peak flux, since the maximum occurs typically two or three data levels above the surface. Chen et al. (1981), for example, assume $\omega = 0$ at the surface, while Tomatsu (1979) attempts to include orographic and viscous effects in his lower boundary condition.

A comparison of Figures 1.4a and 1.4b suggests that the standing eddy vertical sensible heat flux is relatively small. Oort and Rasmusson (1971) estimate that $[\overline{\omega^* T^*}]$ peaks at about 5 W/m^2 during the winter months in mid-latitudes; the peak transient eddy flux given by Schubert and Herman (1981) is about 4 time larger. Chen et al. (1981) and Chen (1982) also indicate that the transient eddy vertical heat flux is significantly larger than the standing eddy vertical heat flux. In contrast, Oort and Rasmusson's (1971) observations show the standing and transient eddy meridional heat fluxes to be the same size in winter.

Berggren and Nyberg (1967) also estimate the eddy latent heat flux in the vertical direction. Their results suggest that, at 700 mb in the mid-latitudes, the transient eddy vertical latent heat flux is about 75% the size of the corresponding sensible heat flux. Oort and Rasmusson

(1971) find a similar, though perhaps smaller, ratio for the standing eddy fluxes in the vertical direction.

The measurements by Lau (1979) and Schubert and Herman (1981) yield an upper troposphere heating rate of about 0.4 K/day from sensible heat transfer by transient eddies alone. Using the works cited above as a guide, we might estimate the net flux of sensible heat, latent heat, and potential energy by both standing and transient eddies to yield a heating rate 2-3 times larger, or about a degree per day. This agrees fairly well with the heating rates computed from Hantel's deduced vertical moist static energy flux by all eddies, considering that small-scale convection may also contribute to Hantel's total flux.

Only a few modeling efforts have studied the interaction between dynamics and temperature structure that leads to the observed time mean behavior. Manabe and Strickler (1964) introduce a convective parameterization intended to represent the effect of all non-radiative processes in a vertical one-dimensional model. However, dynamic transports in this case are merely a passive response to an imposed temperature structure. Stone (1972) has developed parameterizations of the eddy potential temperature flux from baroclinic instability theory, thereby allowing for an active interaction between the static stability and the eddy flux. His model is highly averaged, so it can alter the size of the static stabilty, but not its vertical profile. The form of Stone's parameterizations indicates that the baroclinic stability process acts as a negative feedback in the thermodynamic balance, tending to limit the response of the static stability to changes in external forcing.

An adjustment mechanism such as Stone's (1978b) requires an even stronger feedback than that contained in his earlier parameterizations. Structural change may allow for a stronger feedback. One example is the process presented by Lindzen et al (1980), which stabilizes the zonal mean flow by an alteration of the wind shear profile. Held (1982) has applied this adjustment to a discussion of static stability and the depth of the troposphere. His analysis suggests that, at least in a gross sense, the adjustment hypothesis of Lindzen and coworkers is consistent with that of Stone (1978b), indicating one structural change, that of wind shear profile, that might produce a strong enough feedback.

Stone's (1972) model also does not include explicitly moist convection or other possibly important subgrid scale processes. GCM's can include these processes, albeit in a parameterized form, and also can provide more detail of the temperature structure. However, researchers using GCM's have given little attention to the maintenance of the static stability, though they have noted the static stability's variation under imposed climate changes (e.g. Wetherald and Manabe, 1975; Held, 1978b). Held and Suarez (1978) do look at the maintenance of static stability, though in a two layer model which resolves only a verical mean static stability. Their results display a clear predominance in mid-latitudes of heating by vertical eddy fluxes over that by horizontal eddy fluxes or the mean cell circulation.

The observations and models discussed above indicate that a simple model for the mid-latitude static stability can be constructed that focuses on the vertical transports only. Analysis of the model developed here focuses principally on the vertical eddy heat flux and its interaction with the temperature structure. Although the

interaction of moist convection with the zonal mean state is also important, the eddy transports resulting from baroclinic instability are fundamental to the adjustment hypotheses of both Stone (1978b) and Lindzen et al. (1980). As noted earlier, understanding the degree to which such an adjustment does influence the atmosphere's vertical structure is a goal of this thesis.

The neutralization procedure of Lindzen and coworkers results in an adjustment of the meridional temperature gradient. We could envision an adjustment altering both the meridional and vertical temperature field or, as the opposite extreme, only the vertical structure. The latter possibility, in particular, may be observable as a limiting feature of the atmosphere's and the model's static stability variations with height. Chapter II presents a formulation of the type of temperature profile that occurs in a vertical temperature structure adjustment and a comparison of this structure with observations.

Chapter II also presents a scaling analysis of the thermodynamic equation, in order to identify the principal terms describing the interaction between the heat fluxes and the zonal mean temperature field. In accord with the adjustment hypothesis, baroclinic instability determines the scales appropriate to the large-scale eddy fluxes. The results of theoretical studies of baroclinic instability, supported by observations, guide the choice of length scales. The scaling analysis of the thermodynamic equation serves to indicate the importance in the local temperature balance of vertical eddy heat fluxes resulting from baroclinic instability, complementing Hantel's work. The analysis also shows the type of care that is necessary when averaging previously scaled equations.

Chapter III then presents the development of the vertical balance model, based on the results of Hantel (1976). The representations of the vertical fluxes of heat and moisture are given in detail, with the large-scale eddy fluxes being of particular interest. The mutual interaction between a baroclinically unstable wave and the static stability has been studied by Gall (1976b) and by Simmons and Hoskins (1978) in GCM's and by Saltzman and Tang (1982) in a simpler model. Various researchers (Gall, 1976c; Mak, 1982; Tang and Fichtl, 1983) have studied the interaction between an unstable wave and the moisture field. The concern here, however, is not upon the alteration produced by one wave over one growth cycle, but rather, upon the net effect over many growth cycles. Although there is evidence that the atmosphere displays life cycles representative of growth and decay (Blackmon and White, 1982), the approach here views the observed time and zonal mean unstable state as being indicative of an instability process that is continuous in time. Since the growth and decay cycles are relatively short compared to seasonal periods, this assumption seems reasonable. The longer period is also the one over which a statistical balance of heat fluxes, in particular, the one suggested by Hantel, is more likely to be valid.

Chapter IV presents equilibrium states produced by the interaction between a single wave and the mean state. The most unstable mode is often considered to be the most relevant in modeling eddy fluxes. However, Gall (1976b) has noted a discrepancy between the wave numbers which linear theory predicts to be the most unstable and the wave numbers which reach the largest amplitude in a GCM, a result due in part to the relatively strong interaction between the static stability

and the shorter waves of his study. Thus, this chapter considers model results produced by a variety of single, specified wave numbers.

A broad spectrum of important wave numbers, rather than just one or two, characterizes atmospheric statistics (Saltzman, 1970; Tomatsu, 1979). Thus, Chapter V also looks at solutions produced by ensembles of waves. The results of the two authors cited above suggest that direct interaction between different wavelengths is not as important as their interaction with the mean flow, which simplifies the manner in which many waves are included in the model. While model runs using a spectrum of waves may produce more realistic temperature profiles, the possibility exists that a single wave can simulate the net eddy flux as well as an ensemble. Held and Suarez (1978) note that as they relax the severe spectral truncation of their model from one wave to three, there is relatively little change in the zonal mean statistics of the model. However, the meridional variation of heat fluxes in their model is subject to geometric constraints similar to those discussed by Stone (1978a). The vertical heat fluxes may not be as constrained and the higher vertical resolution in this model compared to Held and Suarez's model affords an opportunity to study the influence of adding in waves with different vertical scales.

Chapter V gives an analysis of the model's equilibrium states in terms of the vertical temperature structure adjustment theory developed in Chapter II. Model runs that neglect one or more of the physical processes contained in the full model reveal the capability of the vertical eddy heat flux to adjust the flow to stability and clarify the restraints imposed on the adjustment by the other processes. In addition, Chapter V presents an analysis of model equilibrium states in

terms of a two-layer model baroclinic stability parameter, illustrating similarities between Stone's (1978b) results for the atmosphere and features of the model's equilibrium states.

Chapter VI reviews the results of the thesis and discusses some of their implications. It also gives some suggestions concerning the modeling and possible observation of vertical eddy heat fluxes.

CHAPTER II

VERTICAL EDDY HEAT FLUXES AND BAROCLINIC ADJUSTMENT

This chapter contains two rather disparate topics loosely joined together by their common basis in baroclinic stability theory. We may expect that baroclinic instablity plays an important role in determining the vertical temperature structure, as the discussion in Chapter I indicates. Although radiation and moist convection are also important, this chapter will delineate the influence the instability may have on the vertical temperature structure and help clarify the nature of the eddy processes involved.

The first section explores a possible effect of the eddy fluxes without actually computing the eddies themselves. Instead, we consider the possibility that the eddy fluxes act to stabilize the zonal mean flow with respect to baroclinic instability, the baroclinic adjustment hypothesis (Stone, 1978b). Baroclinic instability represents an efficient form of heat transport, with fluxes computed from linear instability problems tending to strengthen the static stability and weaken the meridional temperature gradient. Generally such behavior leads to a weaker instability, but it is not obvious a priori that the full nonlinear process should attempt to stabilize the flow completely. Perhaps more importantly, such an adjustment ignores the constraints imposed on the temperature field by other physical processes, which may inhibit considerably any tendency of the eddies to stabilize the zonal mean flow. Nevertheless, work by Stone and coworkers (1978b, 1979, 1982) reveals that a two-layer model stability criterion does describe

the corresponding behavior of the mid-latitude zonal mean flow quite well. This motivates the application of the hypothesis to a continuous atmosphere.

The second section presents a scaling analysis of the zonally-averaged thermodynamic equation, using scales appropriate to baroclinic instability derived by Killworth (1980) and supported by observations. Hantel's (1976) work suggests that synoptic and planetary scale eddies, the large scale eddies, provide an important contribution to the vertical heat flux due to eddies of all scales. The analysis will show that vertical eddy flux heating due to baroclinic instability is large enough relative to the horizontal flux heating to be important in the local temperature balance. It will also show that the magnitude of the heating is large enough to agree with Hantel's computations.

Finally, the third section presents a relationship between the vertical eddy heat flux and the meridional eddy potential vorticity flux. For linearly unstable waves, the latter flux acts to reduce the zonal mean potential vorticity gradient $[Q]_y$. By considering approximate solutions to the Charney problem, this section will indicate where in the atmosphere the heating by the vertical eddy flux may also act to reduce $[Q]_y$. The minimization of $[Q]_y$ is an important aspect of the adjustment hypothesis, so that this last section brings together results from the first two sections. The second section shows that the vertical eddy heat flux driven by baroclinic instability plays a significant role in the local temperature balance. The third section shows that, if the vertical flux is large enough, it may act to achieve the adjustment discussed in the first section.

The presentation in this chapter uses a rather large number of variables and associated symbols. As an aid to the reader, Table 2.1 contains a list of symbols that appear frequently in this chapter.

Table 2.1 Frequently appearing symbols.

c	complex eddy phase speed
C	relative phase factor for scale analysis
f	Coriolis parameter
h_β	$f^2 [U]_z / \beta N^2(0)$
H	vertical scale of motions
H_p	density scale height
H_d	diabatic heating rate for potential temperature
k	zonal wave number
l	meridional wave number
L_a	$\sqrt{L_r L_z}$, meridional scale of eddy amplitude variations
L_r	radius of deformation
L_z	meridional scale for the zonal mean flow
N^2	Brunt-Vaisailla frequency, squared
N_A^2	adjusted N^2
N_m^2	moist adiabatic N^2
N_0^2	a constant N^2
Q	quasi-geostrophic potential vorticity
r	$N_0^2 / N_A^2(0)$
T	temperature
u	zonal velocity
v	meridional velocity
w	vertical velocity
y	meridional coordinate

z	vertical coordinate
z_A	adjustment depth
$\Delta Z/Z$	fractional change of ZAPE
β	latitudinal variation of f
γ	$f^2 [U]_z H_p / \beta N^2(0)$
γ_0	$r\gamma$, $= f^2 [U]_z H_p / \beta N_0^2$
δ	Dirac delta function
η	r-1
θ	potential temperature
ρ	density
ϕ	latitude
ψ	eddy streamfunction

1. Baroclinic Adjustment and the Vertical Temperature Structure.

Computing analytically the linear instability of a given zonal mean flow in a continuous atmosphere can be an extremely difficult, if not impossible task. Even the very basic problem posed by Charney (1947) requires much complicated mathematical manipulation to obtain solutions. However, the theorem derived by Charney and Stern (1962) provides a relatively simple expression of the necessary conditions for instability in a continuous atmosphere. For a quasi-Boussinesq, quasi-geostrophic zonal mean state characterized by some wind field, [U], and temperature structure, N^2, we can form the zonal mean quasi-geostrophic potential vorticity [Q] and its meridional gradient

$$[Q]_y = \beta - \frac{f^2}{\rho}\cdot\frac{\partial}{\partial z}\left(\frac{\rho [U]_z}{N^2}\right) - [U]_{yy} \quad .$$

The flow considered here is on a mid-latitude β-plane, where y is the meridional coordinate, f is the Coriolis parameter, and β its meridional variation. The density ρ is a function of height alone, $\rho = \rho(z)$. For simplicity, N^2 and $[U]$ are also functions of height alone, though the theorem requires no such simplification. In the atmosphere, $[U]_{yy}$ typically gives only a small contribution to $[Q]_y$. To this flow add a wave-like perturbation described by the streamfunction, $\Psi = \psi \exp\{ i(kx+ly-kct)\}$, where the phase speed, $c = c_r + i\, c_i$, is complex, allowing for the possibility of exponential growth. Under the assumption that the eddy's kinetic energy density, $\rho[(\nabla\Psi)^2]$, and vertical energy flux, $\rho[w\Psi]$, vanish as $z \to \infty$, Charney and Stern's derivation yields

$$c_i \left\{ \int_z \int_y \frac{\rho |\psi|^2}{|[U]-c|^2} [Q]_y \, dydz - \int_y \frac{\rho f^2 |\psi|^2}{|[U]-c|^2} \frac{[U]_z}{N^2}\bigg|_{z=0} dy \right\} = 0 \quad . \quad (2.1.1)$$

Instability requires $c_i \neq 0$, which can only occur if the quantity in braces vanishes. This can be the case if the boundary term $([U]_z/N^2)\big|_{z=0}$ is non-zero or if $[Q]_y$ changes sign. For the flow under consideration here, $[Q]_y$ is not a function of y and can only change sign in the vertical direction.

Bretherton (1966) notes that (2.1.1) can assume a slightly more compact form by allowing the term $([U]_z/N^2)$ to jump to zero at the ground. Then (2.1.1) becomes

$$c_i \left\{ \int_z \int_y \frac{\rho |\psi|^2}{|[U]-c|^2} [\hat{Q}]_y \, dydz \right\} = 0 \quad , \quad (2.1.2)$$

where

$$[\hat{Q}]_y = [Q]_y - \left.\frac{f^2 [U]_z}{N^2}\right|_{z=0^+} \cdot \delta(z) \quad . \qquad (2.1.3)$$

Here, $\delta(z)$ is the Dirac delta function. In this form, any instability arises because of a sign change in the effective potential vorticity gradient, $[\hat{Q}]_y$. Bretherton also demonstrates that this formulation of the instability problem is, in effect, identical to the problem in which $([U]_z/N^2)$ is constant everywhere.

Lindzen et al. (1980) find the form of the theorem given by (2.1.2) especially useful, since it permits the interpretation of baroclinic instability as Rossby wave overreflection in a waveguide. In addition, they use (2.1.2) to motivate one type of mean flow adjustment which stabilizes the flow. Like Bretherton, they interpret the δ function in (2.1.3) to result from the vanishing of $[U]_z$ on the lower surface. For quasi-geostrophic flow, this is equivalent to saying that the meridional temperature gradient jumps to zero there. Since $[Q]_y$ is typically positive, especially in simple problems, the discontinuity in the gradient produces the sign change in $[Q]_y$ necessary for instability. They note that a simple way to stabilize the flow is to remove the δ function by adjusting $[U](z)$.

In particular, they assume $[U](z)$ satisfies $[Q]_y = 0$ from the surface up to some adjustment level z_A, where the adjusted wind, $[U]_A$ and wind shear, $([U]_A)_z$, match the original values. They also assume constant Brunt-Vaisalla frequency, N_0^2, and a scale height variation for density, $\rho = \rho_0 e^{-z/H_\rho}$. Figure 2.1 displays schematically the type of adjustment that occurs under this procedure.

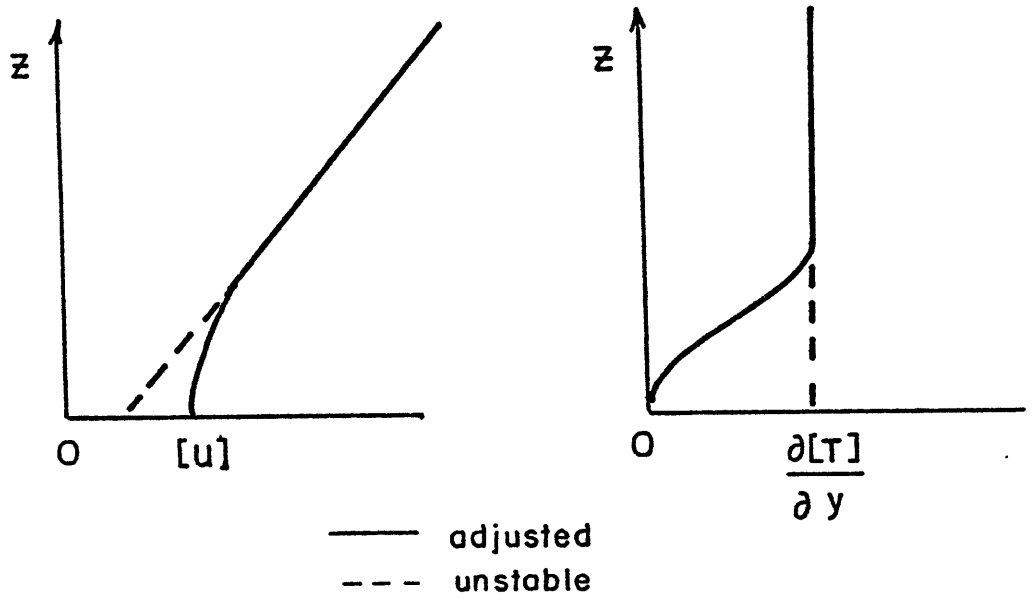


Fig. 2.1 - Schematic representation of $[U]_A(z)$ and $\frac{\partial}{\partial y}[T]_A(z)$ for a baroclinically stable zonal mean flow, under the $[U](z)$ adjustment. Also shown are unstable profiles for a possible unadjusted original state.

For later comparison, Figure 2.1 depicts the meridional temperature gradient $\frac{\partial}{\partial y}[T]_A$ instead of $([U]_A)_z$. The two are proportional to each other in quasi-Boussinesq, quasi-geostrophic flow. As Lindzen et al. (1980) note, the meridional temperature gradient, or equivalently, the zonal mean available potential energy (ZAPE) need not vanish everywhere for the flow to become stable.

Lindzen and Farrell (1980) apply the adjustment in $\frac{\partial}{\partial y}[T]$ to a climate model and show a correspondence between the vertical average of $\frac{\partial}{\partial y}[T]_A$ and the surface temperature gradient in mid-latitudes. For observed values of N_0^2 and H_D, the adjustment typically occurs over 1 - 2 scale heights, essentially the depth of the troposphere. Using observed distributions of $N^2(z)$, Held (1982) shows that there is again a fair agreement given by this adjustment and the depth of the troposphere. He suggests that, climatologically, there is a close relation between the tropopause height and vertical extent of eddy activity, as measured by the depth over which this adjustment occurs. He notes also that atmospheric radiation may provide a strong constraint on the height of the tropopause. Thus, his work implies that the flow maintains N_0^2 to be of such a size that the eddies can have a significant role in the entire troposphere by means of the adjustment.

Because of the correspondence between theory and observations noted above, we might wonder if the vertical profile of $\frac{\partial}{\partial y}[T]$ in the atmosphere resembles the vertical profile of $\frac{\partial}{\partial y}[T]_A$. The resemblance does not appear, however, as a qualitative comparison of the $\frac{\partial}{\partial y}[T]_A(z)$ profile in Figure 2.1 with observed profiles in Figure 2.2 reveals. Figure 2.2 shows the temperature difference between 40°N and 50°N for summer (S) and winter (W), using Oort and Rasmusson's (1971) data. This

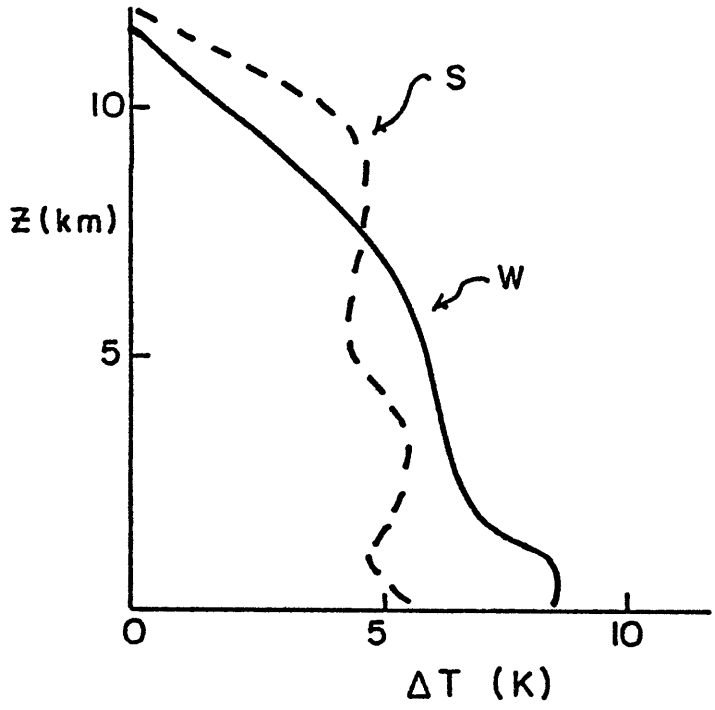


Fig. 2.2 - $\Delta T = \{\overline{[T]}(40°N) - \overline{[T]}(50°N)\}$ as a function of height for summer (S) and winter (W).

difference approximates the mid-latitude temperature gradient. Since the adjustment of $\frac{\partial}{\partial y}[T]_A$ should occur over the troposphere, some resemblance between the observed and schematic profiles should appear if the adjustment does occur. However, while the adjustment theory predicts a minimum in the temperature gradient near the ground, observations show that, if anything, a maximum occurs there. Also, the observed gradients are either roughly constant or else decreasing with height, in contrast to the adjustment profile's gradient, which increases with height.

Lindzen and Farrell (1980) do not compare $\frac{\partial}{\partial y}[T]$ profiles. Instead, they hypothesize that the atmospheric poleward heat transport is the amount of heat that would effect the adjustment, without requiring the details of the adjustment to actually occur. This hypothesis concerns only the net heat transport across a latitude circle and makes no statement about its vertical distribution, hence their comparison of the vertical mean of $\frac{\partial}{\partial y}[T]_A$ with the observed surface temperature gradient. Held (1982) argues that the observed profile would not necessarily need to resemble the adjusted profile. The meridional heat transports which stabilize one latitudinal zone may increase the meridional temperature gradient in adjacent zones, generating instability there. The heat transports adjusting these zones to stability would then increase the temperature gradient of the original zone, destabilizing it. Thus, a cycle occurs and the time mean profile of the meridional temperature gradient can be an average of a stable profile and a highly unstable profile, yielding the observed gradient.

Held's hypothesis does not seem applicable to the effects of large-scale waves, which do the bulk of the meridional heat transport. The scaling arguments presented in the next section show that, if these waves result from baroclinic instability, then they produce a meridional heat flux spanning the entire width of the mid-latitudes, roughly 30°N - 60°N. There is observational support for this limitation, as well. Stone et al. (1982) have studied the correlation between the vertically-integrated meridional eddy heat flux at one latitude, ϕ, and the corresponding simultaneous heat flux at another latitude, $\phi + \Delta\phi$. They note that the fluxes become uncorrelated when $\Delta\phi$ becomes greater than 15° latitude. Since their time series are based on the twice-daily NMC operational analyses, their results imply that the effective width of synoptic scale eddy fluxes is about 30°, or most of the mid-latitudes. Therefore, these waves do not seem to be capable of participating directly in a process whereby eddy activity shifts from zone to zone within the mid-latidudes.

The time mean influence of the meridional heat flux on $[Q]_y$ is also the opposite of that predicted by the $\frac{\partial}{\partial y}[T](z)$ adjsutment. For this adjustment to occur, the meridional eddy flux should tend to decrease the magnitude of $[Q]_y$ in the lower atmosphere, since $[Q]_y$ is zero in the adjustment layer. However, an observational study by Holopainen et al. (1982) shows that, in a layer extending from about 800 mb to 500 mb and between 35°N and 55°N, the meridional eddy heat flux generally increases the already positive $[Q]_y$.

The vertical profile of the meridional temperature gradient does not indicate that the atmosphere adjusts $\frac{\partial}{\partial y}[T]$ to minimize the baroclinic instability of the zonal mean flow. This motivates the

analysis of an adjustment which alters N^2 while holding $\frac{\partial}{\partial y}[T]$ fixed, the opposite extreme from that considered by Lindzen et al. (1980). Further motivation comes from the study of atmospheric lapse rates by Stone and Carlson (1979). They find that the critical lapse rate based on Stone's (1978b) theory of baroclinic adjustment varies with latitude in a very different manner than the moist adiabatic lapse rate does. If baroclinic adjustment affects $\frac{\partial}{\partial y}[T]$ more strongly than N^2, then we might expect to find a broad latitudinal zone where the atmosphere minimizes the instability of the zonal mean flow by altering $\frac{\partial}{\partial y}[T]$ with respect to a lapse rate fixed by moist convection. In that case, the moist adiabatic and the critical lapse rates should vary with latitude in a similar manner. This does not occur. Thus, Stone and Carlson's results suggest that adjustments in the lapse rate are part of the adjustment process observed by Stone (1978b) in two-layer statistics of the atmosphere. The $N^2(z)$ profile may display effects of the adjustment process that are absent in the $\frac{\partial}{\partial y}\overline{[T]}(z)$ profile.

If $[U]_z$ is continuous in height, (2.1.2) still results if there is a jump in N^2 such that $1/N^2$ equals zero there. Thus, we may view the usual baroclinic instability problem as one in which N^2 varies rapidly near the ground, producing the requisite sign change in $[Q]_y$.

An infinite static stability, even if in a thin layer, may seem unrealistic in the atmosphere. Consider, however, the quasi-geostrophic, quasi-Boussinesq thermodynamic equation at a boundary separating two layers of flow with different static stabilities. Defining the interface level as $z = 0$, continuity of vertical velocity there requires

$$\frac{\partial}{\partial t}\Psi_u + J(\Psi_u, \frac{\partial}{\partial z}\Psi_u) = \left(\frac{N_u^2}{N_\ell^2}\right)\left\{\frac{\partial}{\partial t}\Psi_\ell + J(\Psi_\ell, \frac{\partial}{\partial z}\Psi_\ell)\right\} \quad ,$$

where Ψ is the the streamfunction, $J(\ ,\ )$ is the Jacobian operator, and the subscripts u and ℓ refer to the upper and lower layers, respectively. In the limit as $N_\ell^2 \to \infty$, the equation becomes

$$\frac{\partial}{\partial t}\Psi_u + J(\Psi_u, \frac{\partial}{\partial z}\Psi_u) = 0$$

at $z = 0$, the usual rigid surface boundary condition for inviscid, quasi-geostrophic theory (cf. Charney and Stern, 1962). Thus, we can interpret the boundary condition at a rigid surface to be the result of a jump in static stability such that $(1/N^2)\big|_{z=0^-} \to 0$.

Temperature profiles also occur in the observed atmosphere for which a jump in static stability is a reasonable limiting case. This behavior will motivate a simple model for studying an adjustment of N^2. In the atmosphere, $[Q]_y$ is generally positive, but Fullmer (1982a) has found regions of negative values in the monthly mean flow, using the observed $[U](y,z)$ and $[T](y,z)$ distributions. At levels where the thermal wind relation is not reliable, such as near the ground, the observation of negative $[Q]_y$ based on $[U](z)$ measurements may be spurious, as Fullmer notes. However, $[Q]_y$ can change sign there if N^2 varies rapidly. Such behavior occurs at the top of the well-mixed boundary layer (e.g. Lilly, 1968) and at the bottom of the stable boundary layer (e.g. Melgarejo and Deardorff, 1974). We can construct idealized profiles of $N^2(z)$ and potential temperature $\theta(z)$ for these two cases, as shown in Figure 2.3. $[Q]_y$ probably will be negative in the layer of rapidly decreasing N^2. As this layer diminishes in thickness,

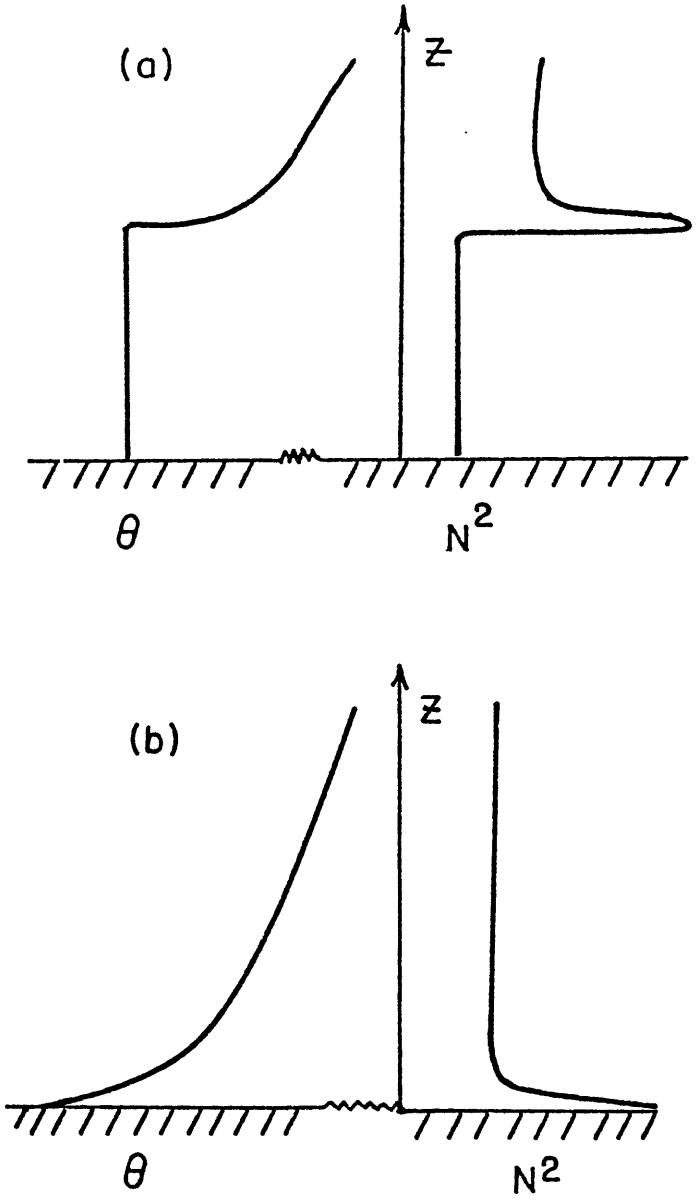


Fig. 2.3 - Idealized vertical profiles of θ and N^2 in a) the well-mixed planetary boundary layer and b) the stable planetary boundary layer.

$1/N^2 \rightarrow 0$ within the layer, with N^2 decreasing more and more rapidly just above the peak in N^2. In the limit, the interface condition obtained in the previous paragraph occurs. The limiting $N^2(z)$ profile is not necessary for $[Q]_y$ to change sign, but it shows how the interior of the atmosphere can approximate the boundary condition appropriate for a rigid lower surface.

One might argue that the instability generated by the temperature structure at the top of the boundary layer should not be as important a source of instability as the meridional temperature gradient at the ground. However, the theory presented by Lindzen et al. (1980) and employed here is quasi-geostrophic and the adjustment toward neutrality by quasi-geostrophic motions may not even occur in the highly non-geostrophic boundary layer. Viewing the top of the boundary layer as the bottom of the layer of atmospheric quasi-geostrophic motions, this level becomes a lower surface for adjustment by quasi-geostrophic motions and the variation of $[Q]_y$ with height due to the vertical temperature structure at the top of the boundary layer becomes especially pertinent.

The well-mixed planetary boundary layer temperature structure may explain why Charney's (1971) theory of geostrophic turbulence approximates observed eddy spectra well. He sets a lower boundary term in his derivation to zero by assuming that $[\theta]_y$ vanishes there. This assumption is often cited as a weakness in the theory. However, the lower boundary term will vanish if $1/N^2 \rightarrow 0$ there. Thus, the lower boundary of the quasi-geostrophic layer in the atmosphere can satisfy the boundary constraint and preserve the essence of his theory.

The boundary layer structure motivates a simple model which is useful for studying an adjustment of vertical temperature. Given that one source of instability is a sharp variation in the vertical temperature structure, we would like to know what smoothing removes this source of instability. Consider the idealized situation in which potential temperature jumps from a value of $[\theta](0)$ at the surface to $[\theta](0) + \Delta\theta$ just above and N^2 is constant, $N^2 = N_0^2$, except in the region of the jump. This is depicted in Figure 2.4, along with the N^2 and $[Q]_y$ that result if $[U]_z$ is constant and $\rho = \rho_0 e^{-z/H_\rho}$. The assumption of constant N_0^2 above the surface simplifies the presentation, though it is not necessary. Assuming $N_0^2 = N_0^2(z)$ adds little additional insight to the adjustment presented here. Later discussion will consider briefly the modifications allowed when N_0^2 becomes a function of height. Also, the discussion in this section considers only solutions with $[U]_z > 0$. Solutions may exist for $[U]_z < 0$, but they are not relevant to the mid-latitude troposphere. For completeness, consideration of the $[U]_z < 0$ case appears in Appendix A.

Although the adjustment will eliminate one source of instability, the flow will not necessarily become stable, for the boundary term in the form of Charney and Stern's theorem given by (2.1.1) may be non-zero. Nonetheless, the simple model considered here will show the conditions under which the flow is rigorously stable and also indicate how the flow may become effectively stable when it is not rigorously stable. Neither the atmosphere nor the model developed in Chapter III can attain the rigorously stable state, but results presented in Chapter V will show that the model can attain an effectively stable state.

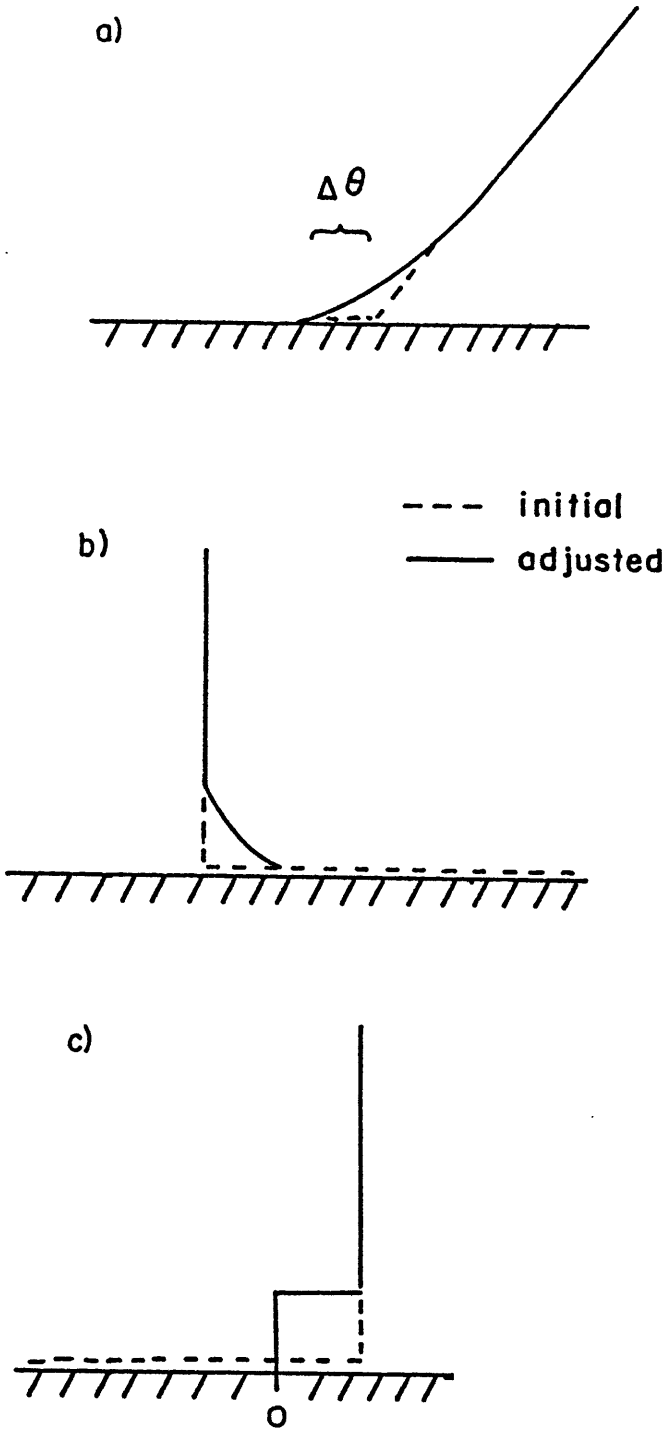


Fig. 2.4 - Initial and adjusted vertical profiles of $[\theta]$, N^2, and $[Q]_y$ in the temperature jump model.

The results will also indicate that we can understand features of the atmosphere's and the model's vertical temperature structures in terms of the adjustment.

The hypothesized adjustment process eliminates a negative in $[Q]_y(z)$ by altering $N^2(z)$ such that $[Q]_y = 0$ in a layer extending from the surface to a level z_A where the new and old values of $[\theta]$ and N^2 match. $[\theta](0)$ remains fixed to its initial value. We might consider $[\theta](0)$ to change during the adjustment, but the most likely change in $[\theta](0)$ is some decrease in size of the order of $\Delta\theta$ or less: such a change in $[\theta](0)$ has little influence on the properties of the adjustment described below. As the $[\theta]$ profiles in Figure 2.4 indicate, the adjustment described here causes a loss of heat in the lower atmosphere. We can consider the vertical eddy heat flux to cause the loss, transporting the heat to higher levels and perhaps causing N_0^2 to change there. Unless the heat causes N^2 to change greatly at z_A, changes in N_0^2 at higher levels have little influence on the adjustment properties described here. Analysis in Chapter V of the model's effective stability supports this contention.

The adjusted Brunt-Vaisalla frequency, $N_A^2(z)$ is a solution of

$$\frac{\partial}{\partial z}\left(\frac{1}{N^2}\right) - \frac{1}{H_\rho}\frac{1}{N^2} = \frac{\beta}{f^2 [U]_z} \quad . \tag{2.1.4}$$

A simple solution is $N_A^2 = -f^2 [U]_z / \beta H_\rho$. Since $[U]_z$ is positive, this solution is unstable with respect to dry convection; it would not appear in monthly or seasonal mean atmospheric statistics. The height dependent solution is

$$N_A^2(z) = \frac{N_A^2(0)e^{-z/H_p}}{\{1 + \gamma(1 - e^{-z/H_p})\}} , \qquad (2.1.5)$$

where $\gamma \equiv \frac{H_p}{h_\beta}$, and $h_\beta \equiv \frac{f^2[U]_z}{N_A^2(0)\beta}$. With $N^2 = g\frac{\partial}{\partial z}\ln[\theta]$, then

$$[\theta]_A(z) = [\theta](0)\{\left|\gamma e^{-z/H_p} - (1 + \gamma)\right|\}^{N_A^2(0)H_p/g\gamma} . \qquad (2.1.6)$$

The z-dependence of N_A^2 is an exponential decay with height arising from the two terms on the left side of (2.1.4), modified by the term on the right side of (2.1.4), which causes $N_A^2(z)$ to decrease more rapidly with height than exponentially.

Note that the scales H_p and h_β appear, a consequence of assuming that the quasi-geostrophic potential vorticity gradient governs the flow. In the Charney stability problem, the ratio H_p/h_β determines the depth scale for the Charney modes (Held, 1978a; Branscome, 1983), while here, it provides a scale for the vertical decay of N_A^2. The decay scale appears more explicitly by considering the logarithmic derivative of N_A^2,

$$\frac{\partial}{\partial z}(\ln N_A^2) = -\left(\frac{1 + \gamma}{H_p}\right)\left\{\frac{1}{1 + \gamma(1 - e^{-z/H_p})}\right\} .$$

For $\gamma \ll 1$, or $H_p \ll h_\beta$, $\frac{\partial}{\partial z}(\ln N_A^2) \approx \frac{-1}{H_p}$. In this case, the term on the right-side of (2.1.4) is relatively weak and, correspondingly, the height dependence of N_A^2 is simple exponential decay on the scale H_p. For $\gamma \gg 1$, or $h_\beta \ll H_p$, there are three height ranges to consider. Near the surface, where $z \ll h_\beta$, $\frac{\partial}{\partial z}(\ln N_A^2) \approx \frac{-1}{h_\beta}$. Far away, where $z \gg H_p$, $\frac{\partial}{\partial z}(\ln N_A^2) \approx \frac{-1}{H_p}$. In between, where $h_\beta \ll z \ll H_p$, the derivative is independent of either scale, $\frac{\partial}{\partial z}(\ln N_A^2) \approx \frac{-1}{z}$. With $\gamma \gg 1$,

the decay is roughly exponential near the surface, but on a much smaller scale than H_p. Thus, near the surface, $N_A^2(z)$ decreases on the smaller of the two scales, h_β and H_p, while at higher levels, the decay scale is always H_p. $N_A(z)$ can decrease very rapidly away from the surface when h_β is small. This is particularly the case when $N_A^2(0)$ is very large, which has important consequences for the adjustment depth, z_A.

Using the matching conditions that N^2 and $[\theta]$ be continuous at z_A, we can obtain z_A and $N_A^2(0)$ in terms of N_0^2 and the jump, $\Delta\theta$. In practice, calculating z_A and $\Delta\theta$ as functions of $N_A^2(0)$ and N_0^2 is easier. Thus,

$$\frac{\Delta\theta}{[\theta](0)} = \left\{1 + \gamma\left(1 - \frac{r(1+\gamma)}{(1+r\gamma)}\right)\right\}^{N_A^2(0)H_p/g\gamma} \times \left\{\frac{r(1+\gamma)}{(1+r\gamma)}\right\}^{N_0^2 H_p/g} - 1 \quad , \tag{2.1.7}$$

and

$$\frac{z_A}{H_p} = \ln\left\{\frac{(1+r\gamma)}{r(1+\gamma)}\right\} \quad . \tag{2.1.8}$$

Here, r is the ratio of Brunt-Vaisalla frequency above z_A to that at the surface, $r = N_0^2/N_A^2(0)$. Since $N_A^2(z)$ decreases with height, $r \leq 1$. For later reference, note that $\Delta\theta$ increases as r decreases: for $r \to 1$,

$$\frac{\Delta\theta}{[\theta](0)} \to \left\{\left(1 + \frac{(1-r)\gamma}{(1+\gamma)}\right) \times \left(1 - \frac{(1-r)}{(1+\gamma)}\right)\right\}^{(2-r)/\gamma} \quad - 1 \to 0 \quad ,$$

while in the opposite limit, for $r \to 0$,

$$\frac{\Delta\theta}{[\theta](0)} \to \left\{(1+\gamma)^{1/\gamma r} r(1+\gamma)\right\}^{N_0^2 H_p/g} \times \left\{1 - \frac{N_0^2 H_p}{g}\right\} - 1 \to \infty \quad .$$

Thus, small $\Delta\theta$ implies $N_A^2(0) \approx N_0^2$ and large $\Delta\theta$ implies $N_A^2(0) \gg N_0^2$.

The scaling for z_A under various limiting sizes of γ and r is of interest. If $N_A^2(0) \approx N_0^2$, then $r = 1 - \eta$, $\eta \ll 1$, and

$$z_A \approx \eta H_\rho \qquad (\gamma \ll 1) \quad ,$$

$$z_A \approx \eta h_\beta \qquad (\gamma \gg 1) \quad .$$

If $N_A^2(0) \gg N_0^2$, then $r \ll 1$ and

$$z_A \approx H_\rho \ln(1/r) \qquad (\gamma \ll 1) \quad ,$$

$$z_A \approx h_\beta / r \qquad (\gamma \gg 1) \quad .$$

Since $\gamma = H_\rho / h_\beta$, the appropriate length scale in each case is the shorter of H_ρ and h_β. Thus, the depth of the adjustment layer tends to scale in the same manner as the vertical decay of N_A^2. Also, the depth of the adjustment depends strongly on r, as may be expected. When $N_A^2(0) \approx N_0^2$, $r \approx 1$ and z_A is relatively shallow. If $N_A^2(0) \gg N_0^2$, then $r \ll 1$ and z_A is relatively deep.

There is also a third limit to consider, in which $N_A^2(0) \to \infty$. If all parameters are fixed except for $N_A^2(0)$, then as $N_A^2(0)$ becomes large, $r \to 0$, $\gamma \to \infty$, but $\gamma_0 = r\gamma = \frac{\beta N_0^2 H_\rho}{f^2 [U]_z}$ remains finite. In this case, $z_A \to H_\rho \ln\left(\frac{1 + \gamma_0}{\gamma_0}\right)$, a finite depth. The adjustment depth can be finite even for infinitely large values of $N_A^2(0)$ because as $N_A^2(0)$ approaches infinity, the decay scale near the surface, h_β, approaches zero, causing $N_A^2(0)$ to decay very rapidly with height.

The process of baroclinic instability causes a transfer of energy from the zonal mean flow to the eddies. As noted above, for this adjustment to be realized, the adjusted state should have a lower zonal available potential energy (ZAPE) than the original state. Within the

layer $0 < z < z_A$, the approximation

$$\text{ZAPE} \propto \int_0^{z_A} \rho(z) \frac{([U]_z)^2}{N^2} \, dz$$

provides a measure of the zonal mean available potential energy. The original state has constant N^2 and $[U]_z$, so that

$$(\text{ZAPE})_0 \propto \frac{([U]_z)^2}{N_0^2} \rho_0 H_p \{ 1 - \exp(-z_A/H_p) \} \quad .$$

Use of (2.1.5) yields for the adjusted state

$$(\text{ZAPE})_A \propto \frac{([U]_z)^2}{N_A^2(0)} \rho_0 H_p \{ (1 + \gamma) \frac{z_A}{H_p} - \gamma (1 - \exp(-z_A/H_p)) \} \quad .$$

The fractional change of available potential energy is then

$$\frac{(\text{ZAPE})_0 - (\text{ZAPE})_A}{(\text{ZAPE})_0} \propto \Delta Z/Z = 1 - r\{ \frac{(1+\gamma)(1+\gamma r)}{(1-r)} \frac{z_A}{H_p} - \gamma \} \quad . \quad (2.1.9)$$

We can obtain some understanding of the dependence of $\Delta Z/Z$ upon its parameters by considering the form of $\Delta Z/Z$ for extreme values of r and γ. When $N_A^2(0) \approx N_0^2$, $r = 1 - \eta$, where $\eta \ll 1$, and to lowest non-vanishing order in η

$$\Delta Z/Z \approx \frac{1}{2} \eta \quad .$$

In this limit, $\Delta Z/Z$ is independent of γ to lowest order in η and the adjustment causes very little change in ZAPE, since $N_A^2(0) \approx N_0^2$. Also, the adjustment depth is shallow, so that there is little overall change in ZAPE.

When $N_A^2(0) \gg N_0^2$, $r \ll 1$ and

$$\Delta Z/Z \approx 1 - r \cdot \ln(1/r) \qquad (\gamma \ll 1) \quad ,$$

$$\Delta Z/Z \approx \frac{1}{2} - \frac{1}{2} r \qquad (\gamma \gg 1/r^3) \quad .$$

The relatively large lower bound in the latter case helps to simplify the final result and clarify the behavior for the largest values of γ. As r becomes very small, $\Delta Z/Z$ in each of these two cases is a non-zero constant. The transfer of energy may be considerable, since z_A may be relatively deep in both cases. When $\gamma \ll 1$, or $H_p \ll h_\beta$, the adjustment removes nearly all of the ZAPE from the flow. For large γ, or $h_\beta \ll H_p$, there is also a large percentage change of ZAPE, though not all of it is lost. The difference in $\Delta Z/Z$ between the two occurs because N_A^2 may have a more complicated height dependence when γ is very large. Figure 2.5 shows N_A^2 for two cases in which r = 0.05. In the first, H_p = 1 km and h_β = 20 km, giving γ = 0.05. In the second, H_p = 20 km and h_β = 1 km, giving γ = 20. In the lowest 2 km, the decay scale is about 1 km for each curve, but when $\gamma \gg 1$ ($h_\beta \ll H_p$), N_A^2 has a much slower decay with height at higher levels than when $\gamma \ll 1$, as the discussion of $\frac{\partial}{\partial z}(\ln N_A^2)$ says should occur. Consequently, when $\gamma \gg 1$ there is a relatively deep layer below z_A where $N_A \approx N_0^2$. The adjustment produces almost no change in this layer's contibution to the ZAPE integral because the adjustment alters $N^2(z)$ very little in the layer. Thus, the net change in ZAPE is only some fraction of the total. In contrast, when $\gamma \ll 1$, N_A decays relatively rapidly to N_0^2 and there is only a thin layer below z_A where $N_A \approx N_0^2$.

For the third limit considered, $1/N_A^2(0) \to 0$ with γ_0 constant, the change of ZAPE is

$$\Delta Z/Z \approx 1 - \{\gamma_0(1 + \gamma_0)\ln\left(\frac{1 + \gamma_0}{\gamma_0}\right) - \gamma_0\} \quad .$$

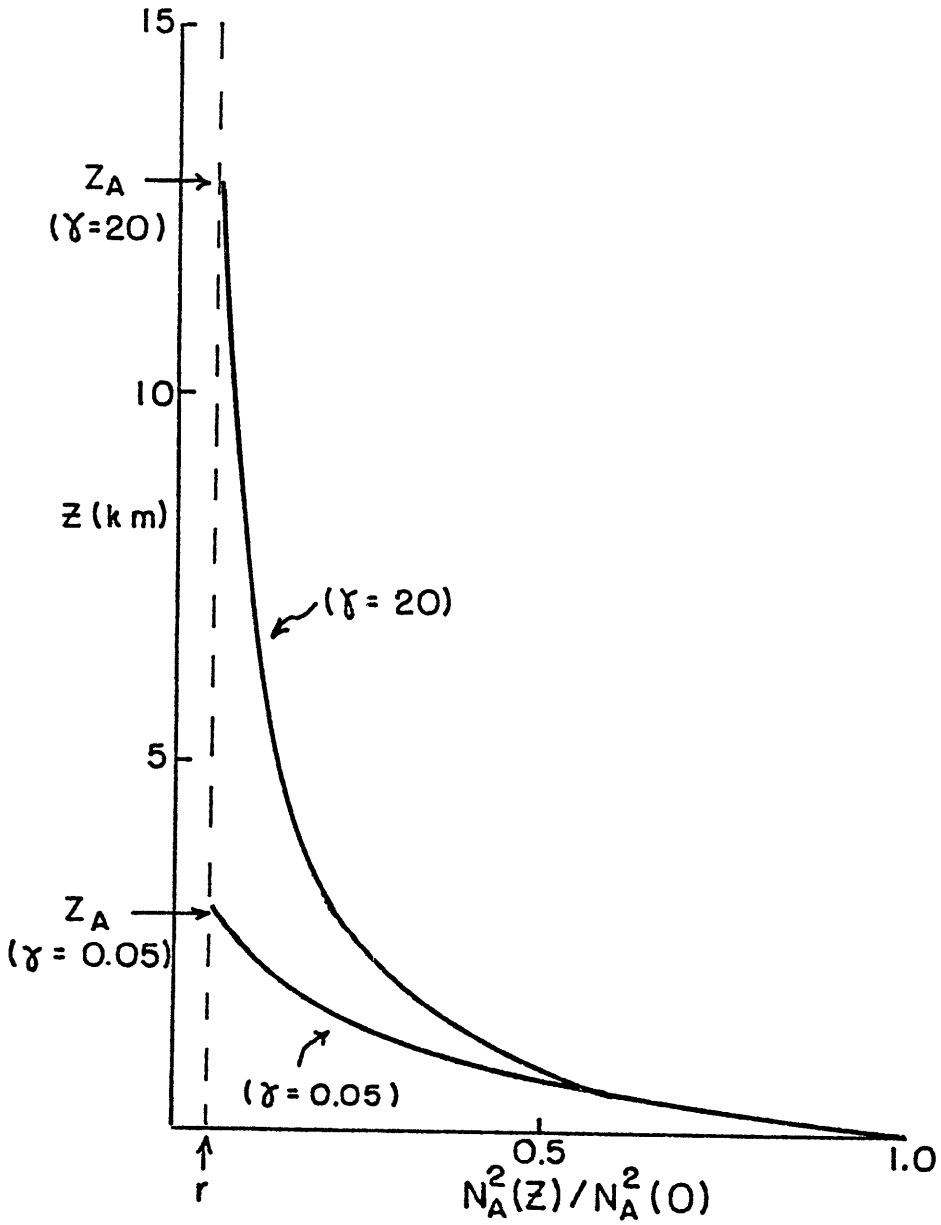


Fig. 2.5 - $N_A^2(z)/N_A^2(0)$ for two choices of γ. Also shown is the matching level, z_A, for each case and $r = N_0^2/N_A^2(0)$.

Figure 2.6 shows $\Delta Z/Z$ as a function of γ_0. Note that for γ_0 of order 1 or larger, $\Delta Z/Z$ is approximately 1/2. The flux parameterizations of Branscome (1980) assume that the eddy grows until its kinetic energy (EKE) is equal to the ZAPE measured over its meridional oscillation scale. If the ZAPE lost during the adjustment transfers to EKE, then the $\Delta Z/Z$ dependence on γ_0 is consistent with his assumption as long as γ_0 is not small.

This adjustment assumes $[Q]_y = 0$ in the adjustment layer, but any value of $[Q]_y$ is permissible, so long as $[Q]_y \geq 0$ everywhere. While setting $[Q]_y = 0$ may yield some minimal adjustment necessary to remove the negative potential vorticity gradient, the possibility exists that setting $[Q]_y = f_A(z)$, $f_A > 0$, may alter the zonal mean flow even less. We can look for the minimal alteration by considering a slightly more general form of the adjustment, where $[Q]_y = \beta_0 \geq 0$, in the adjustment layer. Then, (2.1.4) becomes

$$\frac{\partial}{\partial z}\left(\frac{1}{N^2}\right) - \frac{1}{H_p}\frac{1}{N^2} = \frac{(\beta - \beta_0)}{f^2 [U]_z} \quad . \tag{2.1.10}$$

This equation is identical in form to (2.1.4). Solutions of the latter become solutions of (2.1.10) simply by replacing β by $(\beta-\beta_0)$ everywhere, most particularly in the parameter γ. As β_0 increases, γ decreases and vice versa. This allows us to consider in a fairly simple manner the influence β_0 has upon solutions. Two ways of measuring the influence are by the dependencies upon γ of the adjustment depth, z_A, and the fractional ZAPE change, $\Delta Z/Z$.

Consider first the adjustment depth. The derivative of z_A/H_p with respect to γ is

$$\frac{\partial}{\partial \gamma}\left(\frac{z_A}{H_p}\right) = \frac{r - 1}{(1 + \gamma)(1 + \gamma r)} \quad .$$

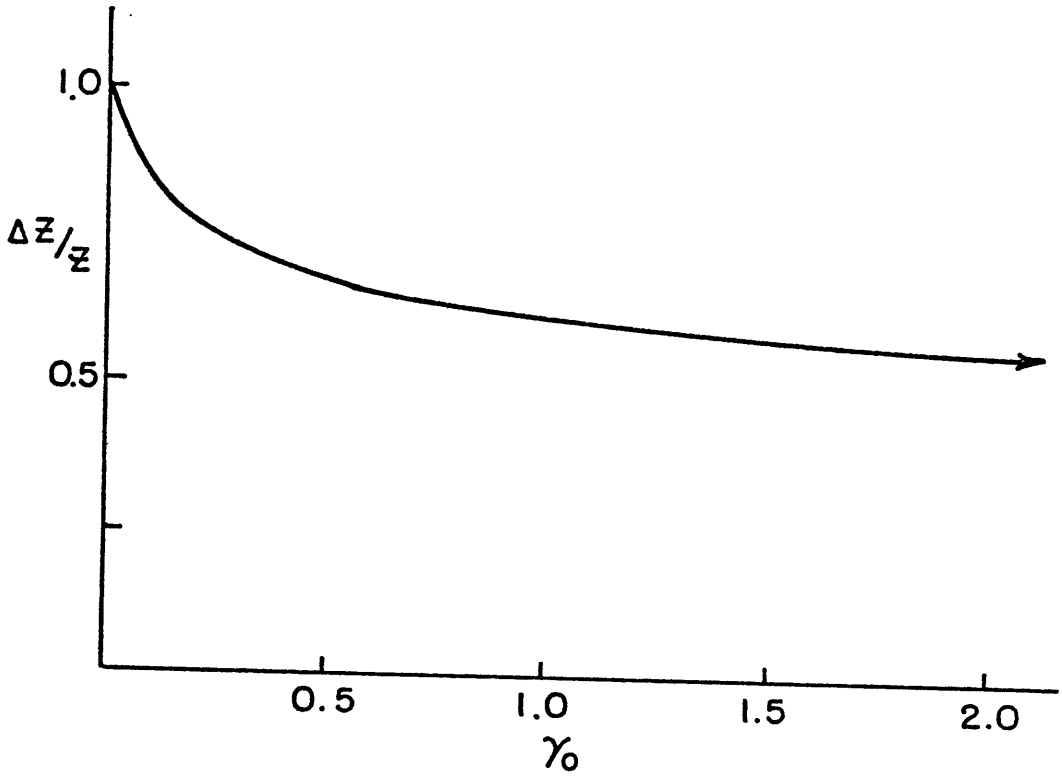


Fig. 2.6 - $\Delta Z/Z$ vs. γ_0

The derivative is less than zero for all r less than 1. If r = 1, then there is no adjustment. Thus, for the r values of interest, the adjustment depth decreases as γ increases, meaning that z_A decreases as β_0 decreases, and vice versa.

The derviative of $\Delta Z/Z$ with respect to γ is

$$\frac{\partial}{\partial \gamma}\left(\frac{\Delta Z}{Z}\right) = r\left\{2 - \frac{z_A}{H_p}\frac{(1 + 2\gamma r + r)}{(1 - r)}\right\} \quad .$$

The quantity on the right side of this equation is almost always negative. The exceptions are the extreme cases of $r \to 0$ for fixed γ and $\gamma \to \infty$ for fixed r, and then the quantity approaches zero. Thus, except for certain extreme values of r or γ, $\Delta Z/Z$ decreases as β_0 decreases.

For the limit where $r \to 0$ and $\gamma \to \infty$ while γ_0 remains fixed,

$$\frac{\partial}{\partial \gamma}\left(\frac{z_A}{H_p}\right) = \frac{-1}{\gamma_0(1 + \gamma_0)} < 0 \quad ,$$

and

$$\frac{\partial}{\partial \gamma}\left(\frac{\Delta Z}{Z}\right) = -\left\{(1 + 2\gamma_0)\ln\frac{1 + \gamma_0}{\gamma_0} - 1\right\} < 0 \quad .$$

Thus, this particular case of extreme r and γ values also has z_A/H_p and $\Delta Z/Z$ decreasing when β_0 is decreasing.

These results show that the change in ZAPE is the least and the adjustment depth is the shallowest when $\beta_0 = 0$. By these measures, then, the minimal adjustment occurs when $[Q]_y = 0$ in the adjustment layer. As noted above, there may still be some function of height $f_A(z)$ for which $[Q]_y = f_A(z)$ in the adjustment layer yields an even smaller alteration of the zonal mean state. However, for $[Q]_y$ constant, $[Q]_y = \beta_0$, the minimal adjustment occurs at the extremum, β_0

= 0. This suggests that the extreme function, $f_A(z) \equiv 0$, would yield the minimal adjustment if we allowed $[Q]_y$ to be a function of height in the adjustment layer.

In order to compare this adjustment with observations, first consider the range of $N_A^2(0)$, z_A, and $\Delta Z/Z$ values given by various choices of N_0^2 and $\Delta\theta$. Table 2.2 displays values of these quantities, using a surface temperature which is representative of typical mid-latitude mean surface temperatures, $[\theta](0) = 290$ K. N_0^2 is 10^{-4} sec^{-2} or 10^{-5} sec^{-2}. The former is appropriate if we consider the upper layers of the observed troposphere to be an ambient state with instability initiated by lower level processes. The latter is a smaller value used for comparative purposes. We might consider it to be an upper bound on the size of N^2 that would occur if convection determined the temperature structure in the initial state's upper troposphere. The other parameters assume typical mid-latitude values: $[U]_z = 2 \cdot 10^{-3}$ sec^{-1}, $H_p = 9$ km, $f_0 = 10^{-4}$ sec^{-1}, and $\beta = 1.6 \cdot 10^{-11}$ $m^{-1} sec^{-1}$.

For $N_0^2 = 10^{-4}$ sec^{-2}, the adjustment depth is less than the depth of the troposphere and the adjustment removes only a fraction of the zonal available potential energy originally present. The choice of $N_0^2 = 10^{-5}$ sec^{-2}, on the other hand, gives a much deeper adjustment depth and most of the ZAPE is lost. Furthermore, as $N_0^2 \to 0$, $z_A \to \infty$ and $\Delta Z/Z \to 100\%$. In the atmosphere, eddies do not adjust the zonal mean flow to a state of negligble ZAPE, and they cause N^2 to decrease with height only over the depth of the troposphere, at most. Thus, an adjustment with $N_0^2 \sim 10^{-4}$ sec^{-2} seems more acceptable in comparison to the atmosphere than one with $N_0^2 \ll 10^{-4}$ sec^{-2}. In addition, typical values for the temperature jump at the top of the mixed layer range up

Table 2.2 The relationship between N_0^2, $N_A^2(0)$, z_A, $\Delta\theta$, and $\Delta Z/Z$ in the N^2 adjustment model. Brunt-Vaisalla frequencies are in units of 10^{-4} sec^{-2}, z_A is in km, $\Delta\theta$ is in K, and $\Delta Z/Z$ is in percent.

N_0^2	$N_A^2(0)$	z_A	$\Delta\theta$	$\Delta Z/Z$
1	1	0	0	0
	2	3.1	3.8	28
	3	4.4	9.6	39
	4	5.2	15.2	45
.1	1	16.	13.	70
	2	20.	26.	77
	3	21.	36.	80
	4	23.	44.	82

to about 10 K. If such a jump is closely tied to the occurrence of baroclinic instability in the atmosphere, then $N_0^2 = 10^{-4}$ sec^{-2} yields realistic $\Delta\theta$ values, while $N_0^2 = 10^{-5}$ sec^{-2} does not.

The adjustment considered here is of greatest interest, of course, if it produces a vertical temperature structure similar to the observed structure. The comparison of the adjustment's $N^2(z)$ with the atmosphere's is hindered by the limited vertical resolution of climatological statistics; the comparison should be considered suggestive. Figure 2.7a displays $N^2(z)$ for winter at 45°N from Oort and Rasmusson (1971), along with the neutralized structure for one choice of the input parameters. The most appropriate values for $N_A^2(0)$ and the z = 0 height are not obvious. The curve shown uses $N_A^2(0) = 2 \cdot 10^{-4}$ sec^{-2} and has z = 0 at 2 km above the ground. The other parameters have the same values as in Table 2.2. As a first approximation to the structure, the adjustment curve does well in the range 2 - 7 km. The adjustment requires N^2 to decrease with height,

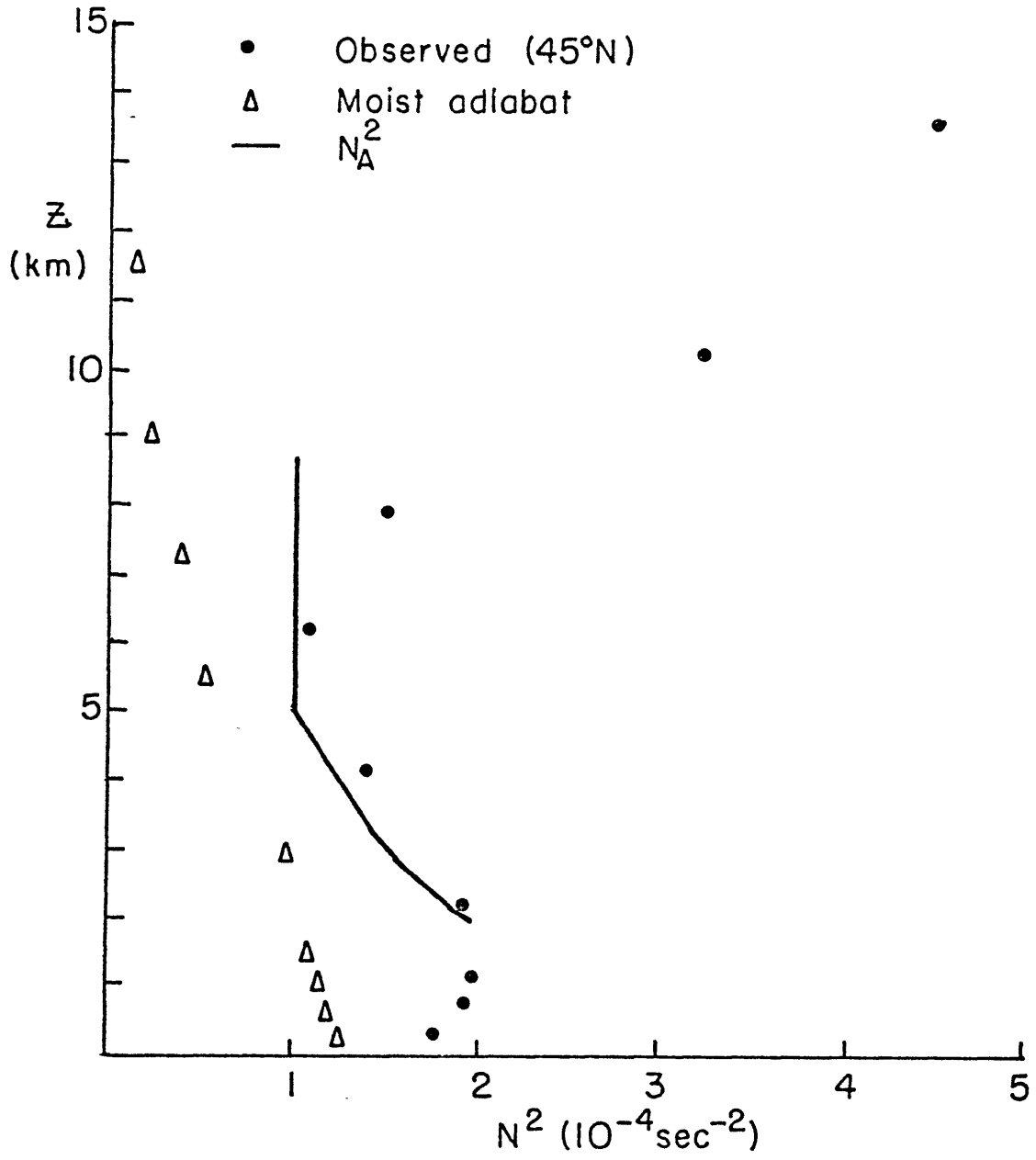


Fig. 2.7a - $N^2(z)$ given by observations for winter (Oort and Rasmusson, 1971) and by the adjustment. Also shown is the N^2 given by a moist adiabat using observed temperatures and pressures.

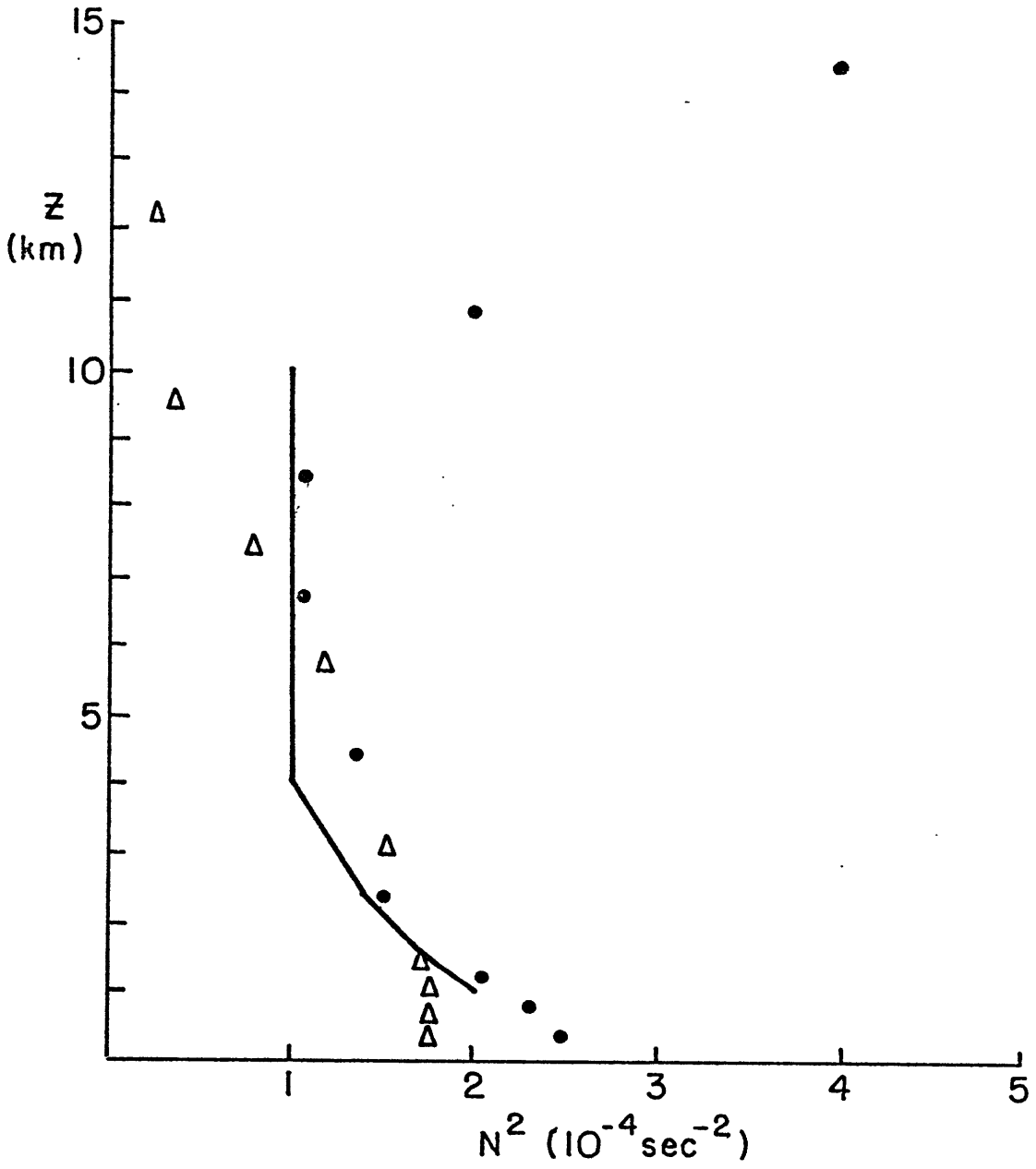


Fig. 2.7b - As in Figure 2.7a, except for summer.

which is a feature of the observed $N^2(z)$ in the lower atmosphere. The depth of the layer where the observed N^2 decreases with height agrees well with the depth z_A for this choice of $N_A^2(0)$ and N_0^2 in Table 2.2. Figure 2.7b compares the same adjustment curve with summer data, only here the z = 0 level is at 1 km. The trends in N_A^2 and the observed N^2 as z approaches the ground suggest a correspondence between the two within the boundary layer, though a quasi-geostrophic approximation should not apply all the way down to the ground.

Also shown in Figure 2.7 are the values N_m^2 computed from a moist adiabat for the temperature at the given level in Oort and Rasmusson. Using the formula of Hess (1959),

$$N_m^2 = \left(\frac{g\Gamma_d}{T}\right)\left\{ 1 - \frac{1 + \varepsilon L_v e_s/pRT}{1 + \frac{\varepsilon L_v e_s}{pRT}\frac{\varepsilon L_v}{C_p T}} \right\} \quad . \qquad (2.1.11)$$

In (2.1.11), Γ_d is the dry adiabatic lapse rate, ε is the ratio of the mass of water vapor to that of dry air, e_s is the saturation vapor pressure, R is the gas constant for dry air, p is pressure, and L_v is the latent heat of vaporization. In winter, the moist adiabatic values are substantially less than the observed, and the adjustment values yield a better approximation through a depth z_A. In summer, the adjustment values yield a good approximation only up to the level where the moist adiabatic values are larger. This result is in agreement with Stone and Carlson (1979). For both seasons, the lower troposphere displays a static stability structure consistent with the adjustment, except where moist convection yields a larger static stability.

Neither process, however, explains the behavior of N^2 above 7 km in either season. Hantel's (1976) study shows that there is considerable vertical eddy flux heating in the layer between 7 and

10 km. The level z_A may be thought of as a transition region between layers with different temperature structures and different processes controling them. In the lower layer during winter, despite the need to balance the heating by other processes, the eddies exert considerable control, yielding the adjustment profile. The eddies may play a significant role in determining the upper layer's temperature structure, as well. However, they do not predominate as in the lower layer, so that other processes, such as radiation, presumably have as large an influence or larger in determining the temperature structure. In the summertime, a modification of this picture is necessary. Then, moist convection becomes as important as the eddies in determining the temperature structure of the lower layer. The actual static stability in this case is the larger value given by either process.

We can view N_0^2 as the Brunt-Vaisalla frequency in a matching region separating the lower and upper layers. The adjustment presented here could have assumed from the beginning that $N_0^2 = N_0^2(z)$, since $N_A^2(z)$ does not depend upon N_0 except where the two profilesmust match. Having $N_0^2 = N_0^2(z)$ complicates the matching procedure but the matching requirements remain the same. This is outlined in Figure 2.8. For some $N_0^2(z)$ and $\Delta\theta$, the $[\theta]_A(z)$ profile must match the $[\theta]_0(z)$ profile in a tangential manner, so that $N_A^2(z_A) = N_0^2(z_A)$. By altering the choice of $N_A^2(0)$, we can obtain the correct match. For complicated profiles, more than one matching level may be possible, but such details do not appear to be of any particular importance. The simple scenario provided by the PBL analogy captures the essence of the $N^2(z)$ adjustment.

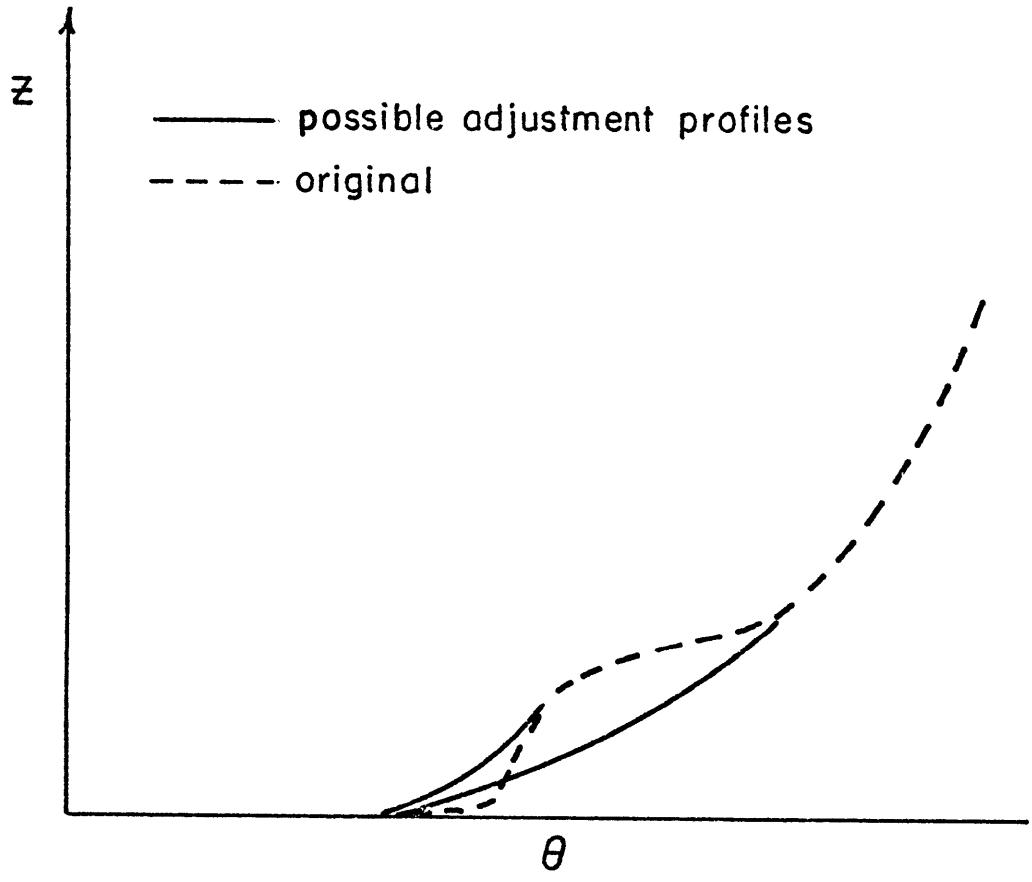


Fig. 2.8 - Matching of $\theta_A(z)$ and $\theta_0(z)$ when $N_0^2 = N_0^2(z)$.

The parameters used in Figure 2.7 yield $\gamma_0 = 0.72$, so that $z_A \to 9\ \text{km} \cdot \ln(1.72/0.72) = 7.8\ \text{km}$ when $N_A^2(0) \to \infty$. As noted previously, the adjustment depth can be finite if all other parameters are fixed when $N_A^2(0) \to \infty$. For typical mid-latitude parameter values, the limiting depth is roughly the same as the tropospheric depth, so that an adjustment of this sort can fit into the layer of the atmosphere where eddies resulting from baroclinic instability play a significant role. This may imply that the flow maintains N_0^2 and $\frac{\partial}{\partial y}[T]$ at values such that the limiting depth is of that size.

The consistency between theory and observations in Table 2.2 and Figure 2.7 suggests a physical connection between boundary layer dynamics and baroclinic instability in the atmosphere. However, the planetary boundary layer fluctuates greatly over the course of a day, so that we might question its efficacy in generating instability and maintaining growth over the longer periods associated with eddy lifecycles. Note also that $N_A^2(0) \to \infty$ implies $\Delta\theta \to \infty$. The adjustment in this simple model smooths a temperature jump, but the resulting temperature structure must span at least the range of temperatures given by $\Delta\theta$, so that a state eliminating the jump but with $1/N^2(0) = 0$ is not realizable. Thus, the $N^2(z)$ structures shown in Figure 2.7 do not represent a strict stabilization of the flow, for $[U]_z(0) \neq 0$ and the boundary term in Charney and Stern's (1962) form of the stability theorem, (2.1.1), does not vanish.

The requirement that $\Delta\theta \to \infty$ for $N_A^2(0) \to \infty$ limits the applicability of the temperature jump model to the atmosphere. It does not limit the applicability of the adjustment itself, since none of (2.1.5), (2.1.6), (2.1.8), and (2.1.9) depend explicitly on $\Delta\theta$. An

adjustment of N^2 that stabilizes the flow occurs in the model developed in Chapter III even though the model has no detailed boundary layer physics and the model's initial state has no explicit temperature jump. The more abstract notion that a rigid lower boundary appears to the flow as a jump to infinite static stability may be a more appropriate causal feature for instability, especially since the lower boundary condition does not invlove a jump in temperature and therefore places no limit on the size of $N_A^2(0)$. Thus, the ability of the adjustment to give finite non-zero limits for z_A and $\Delta Z/Z$ as $1/N_A^2(0) \to 0$ is of interest because it shows that an adjustment of the vertical temperature structure can stabilize the flow without having to alter the entire atmosphere or eliminate all of the zonal available potential energy.

Since $N_A^2(0) \to \infty$ yields a strict stability, finite but large values of $N_A^2(0)$ may allow only weak instability. The surface temperature gradient permits instability via Eq. (2.1.1), but the size of the boundary term diminishes as $N_A^2(0)$ approaches ∞. Fullmer's (1982b) results indicate that the strength of the instability varies with the degree to which the flow violates the stability criteria in the Charney-Stern theorem. In his work, the more negative $[Q]_y$ becomes or the broader the region of $[Q]_y < 0$ becomes, the stronger the instability associated with that particular sign change. For $N_A^2(0)$ finite but large, the boundary term becomes relatively small, so that the linear stability problem may give only weakly unstable waves. Viscous effects in the atmosphere or grid resolution in a model may prevent the growth of these waves and the flow is then effectively stable. The temperature structure for an effective stability due to large $N^2(0)$ should resemble the temperature structure in the $N_A^2(0)$

$\rightarrow \infty$ limit. Some of the model states analyzed in Chapter V do show an effective instability, and their $N^2(z)$ profiles do resemble the N^2 adjustment's profile for $N_A^2(0) \rightarrow \infty$.

The results of this section suggest that atmospheric processes do attempt to adjust the time and zonal mean flow to a configuration that is stable with respect to baroclinic instability. The adjustment appears in the static stability's vertical profile, but not in the meridional temperature gradient's, providing another motivation besides Hantel's (1976) results for the static stability model developed in Chapter III. Since the eddies appear to decrease the instability of the time and zonal mean flow more by their influence on the vertical rather than meridional temperature gradient, the results here suggest that a model that alters the vertical temperature structure relative to a given meridional temperature structure provides a reasonable first approximation to the mid-latitude atmosphere's heat flux balance.

2. Baroclinic Instability and Eddy Flux Scales.

One form of the quasi-geostrophic thermodynamic equation is

$$\frac{\partial}{\partial t}\theta + u\frac{\partial}{\partial x}\theta + v\frac{\partial}{\partial y}\theta + w\frac{\partial}{\partial z}[\theta]_0 = H_d \quad , \tag{2.2.1}$$

where u is the zonal velocity, v is the meridional velocity, and $[\theta]_0 = [\theta]_0(z)$ is the vertical temperature profile of a reference state. H_d is the diabatic heating rate for potential temperature, θ. Using the quasi-geostrophic continuity equation and zonally averaging, (2.2.1) becomes

$$\frac{\partial}{\partial t}[\theta] + \frac{\partial}{\partial y}[v^*\theta^*] + [w]\frac{\partial}{\partial z}[\theta]_0 = [H_d] \quad . \qquad (2.2.2)$$

As in section 1, the flow is quasi-Boussinesq, with density a function of height only. For the purposes of this thesis, (2.2.2) is inadequate, for it fails to show explicitly the heating due to the vertical eddy flux. Edmon et al. (1980) use a form of (2.2.2) in their study of the quasi-geostrophic Eliassen-Palm flux and they conclude that for (2.2.2) to include the predominant sources of atmospheric heating, they must modify the definition of $[H_d]$ to include non-diabatic heat sources, in particular, the vertical eddy heat flux. This section will show that typical scale choices used to develop the quasi-geostrophic system of equations can give a zonal mean thermodynamic equation where $[v^*\theta^*]$ appears explicitly, provided that the analysis uses scales appropriate to baroclinic instability.

The quasi-Boussinesq primitive equation form of the thermodynamic equation, written in flux form and zonally averaged, is

$$\frac{\partial}{\partial t}[\theta] + \frac{\partial}{\partial y}[v][\theta] + \frac{\partial}{\partial y}[v^*\theta^*] + \frac{1}{\rho}\frac{\partial}{\partial z}\rho[w][\theta] + \frac{1}{\rho}\frac{\partial}{\partial z}\rho[w^*\theta^*]$$

$$= [H_d] \quad . \qquad (2.2.3)$$

Oort and Rasmusson's (1971) compilation suggests the following scale sizes for some of the dependent variables:

$$[v] \sim 1 \text{ m/sec} \qquad [w] \sim 10^{-3} \text{ m/sec}$$

$$v^* \sim 10 \text{ m/sec} \qquad \theta^* \sim 10 \text{ K} \quad .$$

The mean cell terms, those involving $[\theta]$, will appear to be relatively large unless we recognize that the varying part of $[\theta]$ is only a fraction of the total potential temprature. Use of the zonal mean continuity equation

$$\frac{\partial}{\partial y}[v] + \frac{1}{\rho}\frac{\partial}{\partial z}\rho[w] = 0$$

permits the subtraction of a constant temperature θ_{00} from the mean cell terms in (2.2.3). Then, with $[\theta]' \equiv [\theta] - \theta_{00}$,

$$\frac{\partial}{\partial t}[\theta]' + \frac{\partial}{\partial y}[v][\theta]' + \frac{\partial}{\partial y}[v^*\theta^*] + \frac{1}{\rho}\frac{\partial}{\partial z}\rho[w][\theta]' + \frac{1}{\rho}\frac{\partial}{\partial z}\rho[w^*\theta^*] = [H_d] \quad . \quad (2.2.4)$$

In the mid-latitude Ferrel cell, $\theta_{00} \sim 310$ K and $[\theta]' \sim 20$ K.

Meridional scales for the mid-latitude eddies are determined by their primary driving mechanism, baroclinic instability. Killworth (1980) identifies three important horizontal scales in a study of linear quasi-geostrophic baroclinic instability in a meridionally varying zonal flow. The first two are the meridional scale of the zonal mean state, L_z, and the radius of deformation, L_r. If $L_z \gg L_r$, then unstable waves have two scales of variation: they oscillate horizontally on the scale L_r and they display an amplitude modulation on a geometric mean scale, $L_a = \sqrt{L_r \cdot L_z}$. Pedlosky (1975), Kim (1978), and Lin (1980) also identify the radius of deformation as a scale for the meridional oscillations of a baroclinically unstable wave when the basic state flow consists of a baroclinic wave superimposed upon a zonal mean flow. Furthermore, we may consider L_a to be the appropriate meridional scale for zonally-averaged quadratic eddy terms, as follows. If Y represents the amplitude modulation on the scale L_a, then for some eddy quantity Ψ,

$$\Psi \sim \psi(Y,z,t)\exp\{i(kx + ly)\} \quad (2.2.5)$$

where $k \sim 2\pi/L_r$ and $l \sim 2\pi/L_r$ are the zonal and meridional wave numbers, respectively. The zonal mean of two such variables is

$$[\Psi_i \Psi_j] = \frac{1}{2} \mathrm{Re}\{\Psi_i \mathrm{conj}(\Psi_j)\} \sim \frac{1}{2} \mathrm{Re}\{\psi(Y,z,t)\mathrm{conj}(\psi(Y,z,t))\}$$

The shortest remaining horizontal scale is L_a.

The scaling values for the meridional lengths are

$$\left.\begin{aligned} L_r &\sim 10^6 \text{ m} \\ L_z &\sim 10^7 \text{ m} \end{aligned}\right\} \quad \rightarrow \quad L_a \sim \sqrt{10} \cdot 10^6 \text{ m}$$

The value of L_a gives a scale for the meridional eddy heat flux of about 30° latitude. This is the same size as the observed latitudinal width deduced from the latitude-lagged flux correlations of Stone et al. (1982).

There are two vertical scales present in (2.2.4), the depth of the fluid motions, H, and the density scale height, H_ρ. For the flow under consideration, $H \sim H_\rho \sim 10^4$ m.

Quasi-geostrophic scaling suggests that $w^* \sim \frac{H}{f}\left(\frac{v^*}{L_r}\right)^2$. Using the above scales and $f = 10^{-4}$ sec^{-1}, $w^* \sim 10^{-2}$ m/sec.

An additional scaling coefficient arises when nonlinear eddy terms are zonally-averaged. Viewing eddies as simple sine waves, the product of two eddy variables has a zonal mean which depends upon the relative phases of the two waves involved as well as the waves' amplitudes. Thus, eddy flux estimates should include the relative phase factor $C_{\psi_i\psi_j}$ $\frac{1}{2}\cos(\phi_{ij})$, where here ϕ_{ij} is the relative phase difference between the two eddy variables, ψ_i and ψ_j. The correlation coefficients computed by Oort and Rasmusson (1971) for the meridional eddy flux suggest $C_{v^*\theta^*} \sim \frac{1}{4}$; calculations using Eady's (1947) model for baroclinic instability suggest $C_{v^*\theta^*} \sim \frac{1}{4}$ and $C_{w^*\theta^*} \sim \frac{1}{2}$. The computations performed by the model presented in Chapter III using realistic temperature profiles on a β-plane give $C_{v^*\theta^*} \sim C_{w^*\theta^*} \sim \frac{1}{2}$, though generally $C_{w^*\theta^*} > C_{v^*\theta^*}$ below 9 km. The discrepancy between the value based on Oort and Rasmusson's

data and the linear instability value may be due to finite amplitude effects which cause $\phi_{v^*\theta^*} \to 90°$ as eddy growth ceases. Since both $C_{v^*\theta^*}$ and $C_{w^*\theta^*}$ appear to be larger than 10^{-1}, the estimates here simply assume that $\phi_{ij} = 0$ for both components of the heat flux. This assumption may produce estimates that are too large, especially for the meridional flux, so that it gives an upper bound on the $C_{\psi_i\psi_j}$.

Inserting these scales into their respective variables then yields as estimates for the sizes of individual terms

$$\frac{\partial}{\partial y}[v][\theta] \sim \frac{[v][\theta]'}{L_z} \sim 0.2 \text{ K/day},$$

$$\frac{\partial}{\partial y}[v^*\theta^*] \sim C_{v^*\theta^*}\frac{v^*\theta^*}{L_a} \sim 1.4 \text{ K/day},$$

$$\frac{1}{\rho}\frac{\partial}{\partial z}\rho[w][\theta] \sim [w][\theta]'\left(\frac{1}{H} + \frac{1}{H_p}\right) \sim 0.3 \text{ K/day},$$

$$\frac{1}{\rho}\frac{\partial}{\partial z}\rho[w^*\theta^*] \sim C_{w^*\theta^*}\, w^*\theta^*\left(\frac{1}{H} + \frac{1}{H_p}\right) \sim 0.9 \text{ K/day}.$$

The largest heating results from the two components of the eddy flux. The eddy terms are roughly the same magnitude and are about the size of typical values for radiative cooling, on the order of a degree per day. As a first approximation, the scaling suggests that the appropriate zonal mean thermodynamic equation when the eddy fluxes result from baroclinic instability is

$$\frac{\partial}{\partial t}[\theta] + \frac{\partial}{\partial y}[v^*\theta^*] + \frac{1}{\rho}\frac{\partial}{\partial z}\rho[w^*\theta^*] = [H_d] \quad . \quad (2.2.6)$$

An important feature of (2.2.6) is that the vertical eddy heat flux is a significant part of the heating balance. This equation is essentially the same as that used by Stone (1972) for his radiative-dynamic equilibrium model, so that the analysis here supports Stone's choice of terms to balance in his model.

The scale choices here for the eddies are of the size used to develop the quasi-geostrophic system of equations (cf. Charney, 1973; Pedlosky, 1979b), so that the eddies follow the quasi-geostrophic equations of motion. In particular, the eddies obey the conservation of quasi-geostrophic potential vorticity

$$\{\frac{\partial}{\partial t} + [U]\frac{\partial}{\partial x} + \frac{g}{f}J(\Psi, \ )\}\{\nabla^2\Psi + \frac{f^2}{\rho}\frac{\partial}{\partial z}(\frac{\rho\Psi_z}{N^2})\} + \Psi_x\{\beta - \frac{f^2}{\rho}\frac{\partial}{\partial z}(\frac{\rho[U]_z}{N^2}) - [U]_{yy}\}$$

$$= 0 \quad . \qquad (2.2.7)$$

where Ψ is an eddy streamfunction. For later reference, the zonal, meridional, and vertical eddy velocities are

$$u^* = -\frac{g}{f}\Psi_y \quad ,$$

$$v^* = \frac{g}{f}\Psi_x \quad ,$$

$$w^* = -\frac{g}{N^2}\{(\frac{\partial}{\partial t} + [U]\frac{\partial}{\partial x} + J(\Psi, \ ))\Psi_z - [U]_z\Psi_x\} \quad .$$

and the eddy temperature is $\theta^* = [\theta]\Psi_z$. In addition to β-plane quasi-geostrophy, this set also assumes that the flow is quasi-hydrostatic, $H/L_r \ll 1$, and quasi-Boussinesq, $H[\theta]'/[\theta] \ll 1$, $f^2L_r^2/gH \ll 1$, and $\frac{H}{\varepsilon_s}(\frac{g}{R\theta_{00}}) \lesssim 1$, where $\varepsilon_s = C_p/C_v$, the ratio of specific heats. The scale choices used here satisfy each of the inequalities.

When the set of quasi-geostrophic equations includes the zonally-averaged thermodynamic equation given by (2.2.2), then the set is energetically consistent: for inviscid, adiabatic flow described by the set, the the total energy of the flow remains constant in time. If the quasi-geostrophic system of equations includes (2.2.6) instead of (2.2.2), then the condition of energetic consistency most likely is violated. In a nonadiabatic, dissipative fluid, such an inconsistency

may not be important, however, especially if the heating or dissipation produces a negative feedback limiting the degree to which any quantity such as temperature or energy can change.

The differences between (2.2.6) and (2.2.2) occur primarily because the analysis leading to the former distinguishes the various meridional scales occurring in baroclinically unstable flow. Scaling the advective form of the thermodynamic equation to arrive at (2.2.1) and then zonally averaging does not elicit the appropriate meridional flux scale. If left in advective form, terms such as $[v^*\frac{\partial}{\partial y}\theta^*]$ and $[u^*\frac{\partial}{\partial x}\theta^*]$ appear, which individually have sizes of $C_{w^*\theta^*}\frac{v^*\theta^*}{L_r}$ ~ 4.5 K/day. However for motions described by the streamfunction in (2.2.5), their net heating is zero, unless there is an amplitude modulation on the scale L_a. With $\Psi \neq \Psi(Y)$,

$$u^*\frac{\partial}{\partial x}\theta^* + v^*\frac{\partial}{\partial y}\theta^*$$

$$= \frac{g[\theta]}{4f}\{-(\Psi_y + \mathrm{conj}(\Psi_y))(\Psi_z + \mathrm{conj}(\Psi_z))_x + (\Psi_x + \mathrm{conj}(\Psi_x))(\Psi_z + \mathrm{conj}(\Psi_z))_y\} \quad ,$$

$$= -\frac{g[\theta]}{f}\mathrm{Im}(\Psi)\mathrm{Im}(\Psi_z)\cdot(lk - kl) \quad ,$$

$$= 0 \quad .$$

The complex conjugates appear because only the real part of a quantity is of interest, i.e. $v^* = \frac{g}{f}\frac{\partial}{\partial x}\mathrm{Re}(\Psi)$. Also, derivatives of $[\theta]$ do not appear above since $[\theta]$ varies only on the much longer scale, L_z. The important scale for the meridional eddy flux's influence on the zonal mean flow is not the scale of the streamfunction's oscillations but the scale of the flux divergence, the scale of the streamfunction's amplitude variation. A scaling analysis of the zonal mean thermodynamic

equation written in flux form can use the appropriate scale for the divergence of the meridional eddy heat flux, which is not L_r, but the larger scale, L_a. Because the divergence of $[v^*\theta^*]$ occurs on the scale L_a, the zonal averaging operation effectively reduces the size of the meridional eddy flux heating, allowing the vertical flux heating to assume a role of equal importance in the temperature balance.

Neither eddy flux is important, however, if the zonal averaging operator leaves unchanged the size of the vertical advection term, $[w]\frac{\partial}{\partial z}[\theta]$. Equation (2.2.2) states that both $\frac{\partial}{\partial y}[v^*\theta^*]$ and $[w]\frac{\partial}{\partial z}[\theta]$ are important in balancing the diabatic heating. If $\frac{\partial}{\partial y}[v^*\theta^*]$ is actually smaller than originally suggested by quasi-geostrophic theory, then $[w]\frac{\partial}{\partial z}[\theta]$ alone may balance the diabatic heating. This possibility does not appear to occur since observations and the scale choices above indicate that $[w] \ll w$. Thus, the zonal averaging operator leaves both $\frac{\partial}{\partial y}[v^*\theta^*]$ and $[w]\frac{\partial}{\partial z}[\theta]$ smaller than originally indicated by quasi-geostrophic theory, so that the zonal mean vertical eddy heat flux can be an important part of the zonal mean thermodynamic balance.

The scale L_a typically does not arise in scaling analyses (e.g. Charney, 1948) or perturbation analyses (e.g. Pedlosky, 1979b) leading to the quasi-geostrophic system, yet it becomes an important scale in zonally-averaged equations. This suggests that one must proceed with caution when averaging a previously scaled set of equations, for the averaging operator may remove certain scales. In the case here, the zonal average eliminates the oscillatory scale L_r. Edmon _et al._ (1980) implicitly recognize this difficulty by noting that their diabatic heating term must be modified to include adiabatic sources of heating, such as the vertical eddy flux.

Further difficulties can arise if the physics of the problem forces two waves to be nearly 90° out of phase with each other. Then, the zonal mean of a quadratic term involving the two waves is much smaller than indicated by the product of their amplitudes. The relative phase coefficient $C_{\psi_i\psi_j}$ represents an accounting for the phase differences. $C_{\psi_i\psi_j}$ is order one for baroclinically unstable waves near the growth rate peak, so that the phase difference is relatively unimportant here. For waves that become progressively less unstable, $C_{\psi_i\psi_j} \to 0$.

The scale of the meridional eddy flux being L_a rather than L_r acts to weaken Held's conjecture that eddy fluxes shift a zone of maximum instability back-and-forth across the mid-latitudes. The scales used above imply that the eddy flux spans about 30° of latitude. If the meridional wavelength is exactly the same as the zonal wavelength, then the flux spans an even larger region. For example, a synoptic scale eddy of zonal wave number 6 at 45°N then has a meridional wavelength $\approx 5 \cdot 10^6$ m. If the meridional length scale for the amplitude is at least as large as this wavelength, then the flux has a meridional width of at least 45° of latitude. For synoptic and longer scale waves, the meridional eddy flux then spans the mid-latitudes. Such a meridional width, as noted previously, can inhibit the appearance of zones of large instability within the mid-latitudes.

3. Vertical Eddy Heat Flux and the Potential Vorticity Gradient.

The previous section shows that the vertical eddy heat flux may play a significant role in the local temperature balance. Since this

flux can alter the vertical temperature structure, it also can alter the vertical profile of $[Q]_y$, the zonal mean quasi-geostrophic potential vorticity gradient. A short derivation in this section will show how the vertical eddy flux heating can act like a down-gradient potential vorticity flux when the flow is unstable. Computations using approximate solutions to the Charney instability problem will show where this behavior might be expected in the model. The derivation will also provide a diagnostic for use with the model's solutions, in which the temperature structure is more complicated than in the Charney problem.

For linear, quasi-geostrophic perturbations about a zonal mean state, the thermodynamic equation for the perturbation temperature is

$$\frac{\partial}{\partial t}\theta^* + [U]\frac{\partial}{\partial x}\theta^* + v^*\frac{\partial}{\partial y}[\theta] + w^*\frac{\partial}{\partial z}[\theta]_0 = 0 \quad . \qquad (2.3.1)$$

For simplicity, we can assume that the perturbation is adiabatic. Multiplying (2.3.1) by θ^*, and zonally-averaging then gives

$$\frac{1}{2}\frac{\partial}{\partial t}[\theta^{*2}] + [v^*\theta^*]\frac{\partial}{\partial y}[\theta] + [w^*\theta^*]\frac{\partial}{\partial z}[\theta]_0 = 0 \quad . \qquad (2.3.2)$$

which provides a relationship between the vertical and merdional heat fluxes, subject to modification by the time derivative term.

Using the definition of the perturbation potential vorticity $Q^* = v_x^* - u_y^* + \frac{f}{\rho}\frac{\partial}{\partial z}\left(\frac{\rho\theta^*}{([\theta]_0)_z}\right)$, we can obtain a relationship between the meridional fluxes of potential vorticity, momentum, and heat (e.g. Held, 1978a):

$$[v^*Q^*] = -\frac{\partial}{\partial y}[v^*u^*] + \frac{f}{\rho}\frac{\partial}{\partial z}\left(\frac{\rho[v^*\theta^*]}{([\theta]_0)_z}\right) \quad . \qquad (2.3.3)$$

For a β-plane flow in which [U] is not a function of the meridional coordinate, $\frac{\partial}{\partial y}[v^*u^*] = 0$ (Held, 1978a). Assuming this and also $\frac{\partial}{\partial z}\left(\frac{\partial}{\partial y}[\theta]\right) = 0$ then gives upon combining (2.3.2) and (2.3.3)

$$\frac{1}{\rho}\frac{\partial}{\partial z}\rho[w^*\theta^*] + \frac{1}{2\rho}\frac{\partial}{\partial z}\left(\frac{\rho\frac{\partial}{\partial t}[\theta^{*2}]}{([\theta]_0)_z}\right) = \left(\frac{-[\theta]_y}{f}\right)[v^*Q^*] \quad .$$

If the perturbations are growing exponentially as $e^{\sigma t}$, then $\frac{\partial}{\partial t}[\theta^{*2}] = 2\sigma[\theta^{*2}]$. Thus,

$$\frac{1}{\rho}\frac{\partial}{\partial z}\rho[w^*\theta^*] + \frac{\sigma}{\rho}\frac{\partial}{\partial z}\left(\frac{\rho[\theta^{*2}]}{([\theta]_0)_z}\right) = \left(\frac{-[\theta]_y}{f}\right)[v^*Q^*] \quad . \quad (2.3.4)$$

For growing perturbations, $[v^*Q^*] \propto -[Q]_y$, or the eddy potential vorticity flux is down the gradient of the zonal mean potential vorticity. When $\frac{\sigma}{\rho}\frac{\partial}{\partial z}\left(\frac{\rho[\theta^{*2}]}{([\theta]_0)_z}\right) \ll \frac{1}{\rho}\frac{\partial}{\partial z}\rho[w^*\theta^*]$, then the heating by the vertical eddy flux acts like the eddy potential vorticity flux. If $[Q]_y$ is positive, then negative $\frac{\partial}{\partial z}\rho[w^*\theta^*]$, or positive positive eddy heating, reduces $[Q]_y$ at those levels where the second term on the left is relatively small.

We can obtain a sense of where the eddy flux heating may reduce $[Q]_y$ by observing how the terms on the left side of (2.3.4) vary with height in the Charney stability problem. Branscome (1983) has derived an approximate solution for the eddy streamfunction ψ and complex phase speed c by means of an asymptotic analysis in the vicinity of the neutral point separating Charney and Green modes. His first-order approximation for the streamfunction appears to compare well with numerical solutions for Charney modes even when his expansion parameter becomes order 1. Branscome obtains more accurate values of the phase speed using a short wavelength approximation, so that the calculations in this section use the expansion near the neutral point to give the vertical structure of the streamfunction and the short-wave approximation to give the phase speed.

The ratio of $\frac{1}{\rho}\frac{\partial}{\partial z}\rho[w^*\theta^*]$ to $\frac{\sigma}{\rho}\frac{\partial}{\partial z}\left(\rho\frac{[\theta^{*2}]}{([\theta]_0)_z}\right)$ is more important here than the magnitudes of the individual terms. Branscome's solution gives for the absolute value of their ratio

$$\left|\frac{\frac{1}{\rho}\frac{\partial}{\partial z}\rho[w^*\theta^*]}{\frac{\sigma}{\rho}\frac{\partial}{\partial z}\left(\frac{[\theta^{*2}]}{([\theta]_0)_z}\right)}\right| = \frac{1}{c_i'}\,\frac{\left\{1 - \frac{z}{2d} + \frac{d}{D}\left(\left(\frac{z}{2d}\right)^2 - \frac{z}{d}\right)\right\}}{\left\{1 - \frac{z}{2d} + \frac{d}{D}\left(1 - \frac{z}{2d}\right)^2\right\}}\quad , \qquad (2.3.5)$$

where $d = H_\rho/(\sqrt{4K'^2 + 1} - 1)$ and $D = dH_\rho/(d + H_\rho)$. K' is a non-dimensional wave number, $K' = \frac{N_0 H}{f}\sqrt{k^2 + l^2}$, and c_i' is a non-dimensional imaginary phase speed, $c_i' = (K'/[U]_z H_\rho)c_i$. For the computations shown here, k is the zonal wave number at 45°N, l = k, and $N_0^2 = 1.6\cdot10^{-4}$ sec^{-2}. The other parameters have the same values as in section II.1, giving $[Q]_y \approx 3\cdot10^{-11}$ m^{-1}sec^{-1} > 0 everywhere. Figure 2.9 shows the height dependence of the ratio in (2.3.5) for a wave number near the neutral point, zonal wave number 3. There is a region between 10 km and 25 km where $\frac{1}{\rho}\frac{\partial}{\partial z}\rho[w^*\theta^*] \gg \frac{\sigma}{\rho}\frac{\partial}{\partial z}\left(\rho\frac{[\theta^{*2}]}{([\theta]_0)_z}\right)$. The ratio goes to zero at the level of the flux maximum (~3 km) and the level of the flux minimum (~30 km). Since $[Q]_y$ is positive, the ratio is much greater than 1 in a layer where $\frac{1}{\rho}\frac{\partial}{\partial z}\rho[w^*\theta^*] < 0$.

Figure 2.9 also shows the steering level for this wave, where the steering level = $\frac{\mathrm{Re}(c)}{[U]_z} = \frac{H_\rho}{K'}\left\{1 - \frac{1 + \gamma_0}{2K'}\left(1.34 - \frac{1}{1 + \gamma_0}\right)\right\}$, using Branscome's short-wave approximation. The dimensionless parameter $\gamma_0 = \beta N_0^2 H_\rho/f^2[U]_z = 1.15$. For this wave number, the steering level is well below the layer where the vertical eddy flux heating tends to reduce $[Q]_y$.

Table 2.3 shows the depth of the layer where the eddy flux heating dominates the left side of (2.3.4), as a function of wave number. The

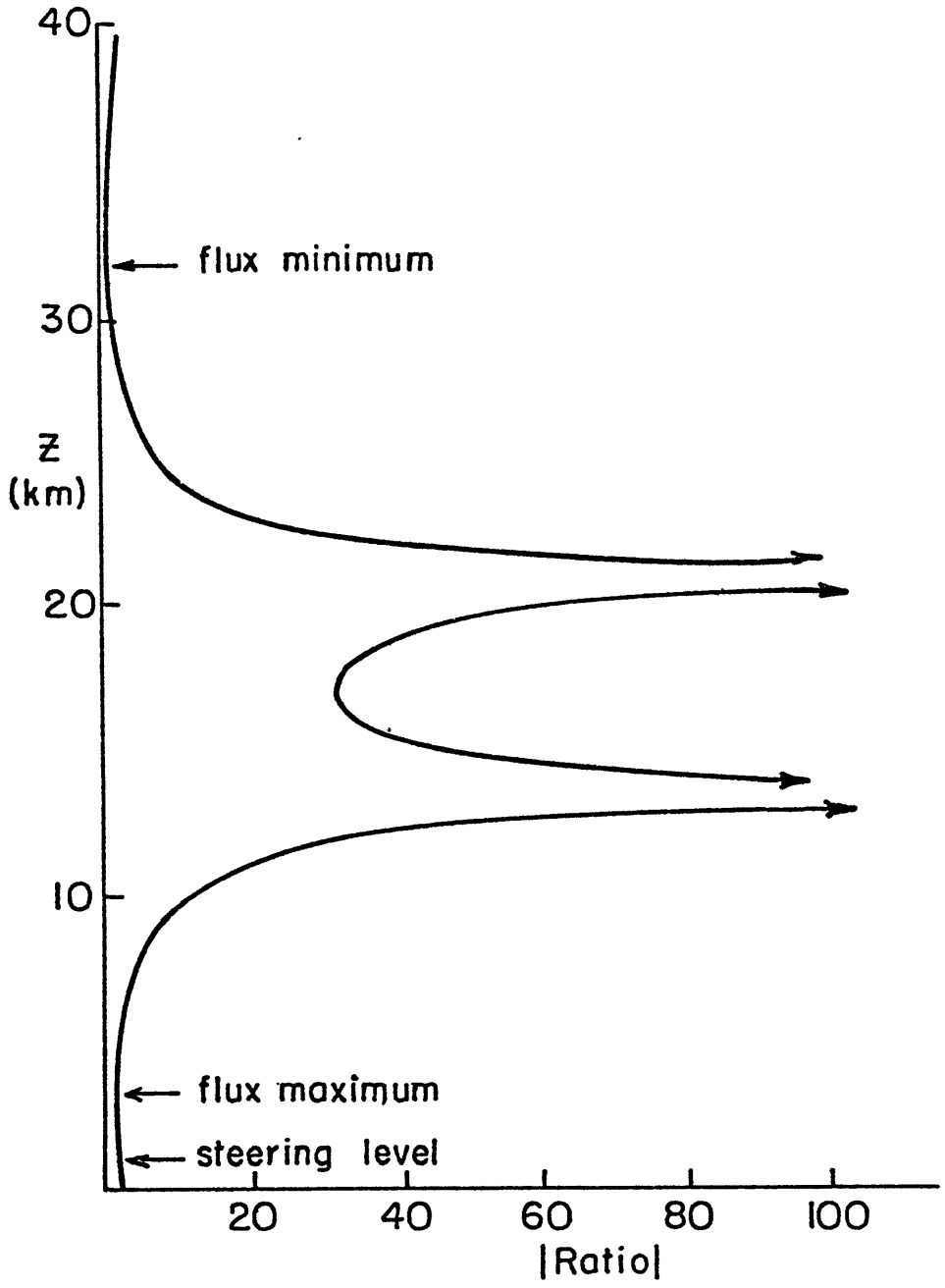


Fig. 2.9 - The ratio in (2.3.5) as a function of height for wave number 3.

Table 2.3 The range of heights where $\left| \frac{1}{\rho}\frac{\partial}{\partial z}\rho[w^*\theta^*] \Big/ \frac{\sigma}{\rho}\frac{\partial}{\partial z}\left(\rho\frac{[\theta^{*2}]}{([\theta]_0)_z}\right)\right|$ is much greater than 1, the levels of extreme $\rho[w^*\theta^*]$, and the steering level, as functions of wave number. All heights are in km.

zonal wavenumber	3	6	9
min($\rho[w^*\theta^*]$) level	31	13	8
ratio $\gg$ 1	10-24	4-11	2.5-7
max($\rho[w^*\theta^*]$) level	3	1.5	1
steering level	1	2.5	2

table also shows the steering level in each case and the levels where $[w^*\theta^*]$ has its maximum and minimum. For wave numbers 6 and 9, Branscome's expansion parameter in the near-neutral point approximation becomes order 1 in size, which may seem too large for the results to be reliable. However, Branscome's analysis appears to capture at least in a qualitative manner the change in the streamfunction as wave number increases. Low-order perturbation series often remain remarkably accurate even as the perturbation parameter becomes order one in size (e.g. Bender and Orzag, 1978). There is, of course, no way of guaranteeing when this accuracy will exist.

For each wave number in Table 2.3, there is always a layer where the vertical eddy flux heating tends to reduce the positive $[Q]_y$. The layer appears at lower levels as wave number increases. For wave numbers 6 and 9, it overlaps the layer where Figure 2.7 suggests that an adjustment does occur. For later reference, note that in each case, the steering level and the level of eddy flux maximum are 2 km apart or

less, while the layer of relatively strong eddy flux heating is centered a few kilometers or more above the steering level.

The height dependence of the approximate solutions suggests that there is a layer in the middle troposphere where the eddy flux heating tends to reduce $[Q]_y$. In the atmosphere and in the model, the eddy flux does not act alone upon the temperature structure and other sources of heating could counteract its tendency to lower $[Q]_y$. Table 2.3 suggests that in the middle troposphere, at least, the heating is strong enough to render the magnitude of $[Q]_y$ small compared to its size at other levels.

CHAPTER III

A VERTICAL BALANCE MODEL

The discussion in the first chapter concludes that three particular vertical transport processes are the most important for determining the local heat balance and temperature structure: radiation, moist convection, and large scale eddy fluxes. This chapter presents a balance model incorporating parameterizations for each of these processes. For balanced states, the parameterizations need only represent time mean effects, rather than an evolutionary process, which simplifies the formulation of the model. The atmosphere, of course, is not in a state of equilibrium, but averaged over suitably long time scales it does maintain a statistical equilibrium, as noted in Chapter I. If the model includes the predominant processes, then it should be capable of representing the atmosphere's time-averaged structure in its balanced states. Since this thesis focuses on the interaction between the thermal field and the large scale eddies, the representation of the eddy flux is the most complex. Although the model developed here is relatively simple compared to, for example, a GCM, the nonlinearity of the system of equations to be solved, in essence, (2.2.6) and (2.2.7), is sufficiently complex that a numerical procedure is necessary to determine equilibrium solutions.

The model ignores certain interactions between the eddy fluxes and the zonal mean state by including explicitly only vertical heat transports, so that the sizes and distributions of certain quantities, most notably the zonal mean zonal wind, are specified rather than

determined internally. Thus, the model performs a consistency check of the hypothesis that, as a first approximation, a balance between vertical heat tranports determines the vertical temperature structure. Using the observed sizes and distributions for specified quantities, we can see how well the model reproduces the observed vertical temperature structure. The most interesting equilibrium states are those whose temperature and flux distributions resemble the observed distributions. Similarities of the equilibrim states with observations should reveal the model's strengths and discrepancies should reveal the model's weaknesses.

The requirement of consistency with observations simplifies the development of heating parameterizations, for the parameterizations need only be appropriate for [T](z) profiles near the observed temperature distribution. Since the model does not need parameterizations which are applicable to a wide range of temperature distributions, it can use relatively simple parameterizations of the radiative and convective heatings. One immediate simplification is that the model does not solve an equation for the surface heat balance. Instead, the model uses a fixed surface temperature given by the observed seasonal mean surface temperature, so that consistent model results should give parameterized surface heat fluxes into the atmosphere which match the observed.

1. The Thermal Balance Equation.

Hantel's (1976) calculation includes the flux of moist static energy. To properly apply his results, the model's eddy flux should represent the same quantity. The thermodynamic equation derived in the

last chapter, (2.2.6), does not have an explicit eddy moisture convergence, but this is added fairly easily. One form of the thermodynamic equation is

$$\rho C_p \frac{d\theta}{dt} = \rho \frac{\theta}{T}(Q_R + Q_C) - \rho \frac{L_v \theta}{T} \frac{dm}{dt} \approx \rho \frac{\theta}{T}(Q_R + Q_C) - \rho L_v \frac{d}{dt}\left\{\left(\frac{p_0}{p}\right)^{\kappa} m\right\} . \quad (3.1.1)$$

Here, Q_R is the radiative heating, m is the mixing ratio for water vapor, and $\kappa = R_a/C_p$, where C_p is the heat capacity of air at constant pressure, and R_a is the gas constant for dry air. Q_C is the heating due to Hantel's (1976) subgrid scale eddy transports of moisture and sensible heat, so that the explicit transports in (3.1.1) are by the large scale eddies and the zonal mean circulation. The approximate equality on the far right occurs because, although p is a function of z, $(p_0/p)^{\kappa}$ varies much more slowly with height in the atmosphere than m does. Performing a zonal average guided by (2.2.6),

$$\frac{\partial}{\partial t}\left\{\rho C_p [\theta] + \rho L_v \left(\frac{p_0}{p}\right)^{\kappa} [m]\right\} + \frac{\partial}{\partial y}\left\{\rho C_p [v^*\theta^*] + \rho L_v \left(\frac{p_0}{p}\right)^{\kappa} [v^* m^*]\right\}$$

$$+ \frac{1}{\rho}\frac{\partial}{\partial z}\left\{\rho C_p [w^*\theta^*] + \rho L_v \left(\frac{p_0}{p}\right)^{\kappa} [w^* m^*]\right\} = \frac{\theta}{T}\left(Q_R + Q_C + Q_{mZ}\right) , \quad (3.1.2)$$

where Q_{mZ} represents the convergence of m by the zonal mean circulation. Since [m] and m^* are the same order of magnitude (Oort and Rasmusson, 1971), the scaling analysis in Chapter II indicates that Q_{mZ} is relatively unimportant; the model may ignore it as a first approximation. Dropping the factor $(p_0/p)^{\kappa}$ would introduce little error, but its retention allows for a slight simplification later.

Equation (3.1.2) describes the balance sought, except that it has a horizontal flux term. In a purely theoretical sense, we may view the

model as having a radius of deformation many orders of magnitude smaller than the horizontal scale of the zonal mean flow. Then, in terms of the analysis in Chapter II, L_r/L_z and $L_a/L_z \to 0$ and the meridional flux divergence vanishes. In the atmosphere, L_r and L_z are only a single order of magnitude different. Hantel's (1976) results suggest that the horizontal flux contribution to the thermal balance is still relatively small, at least for the scales of his box model. Alternatively, we may average (3.1.2) over a meridional domain between latitudes ϕ_+ and ϕ_-. If the two boundaries have the same flux across them at each level, then the averaging removes the horizontal flux convergence.

A trivial choice of ϕ_+ and ϕ_- is the two poles. Radiative-convective models of the type originally developed by Manabe and Strickler (1964) usually assume such a global average. Noting that the horizontal flux of moist static energy peaks in mid-latitudes, we can choose ϕ_+ and ϕ_- to be points on either side of the peak which satisfy the condition of no net flux convergence. One possibility is to apply the equation at the location of the peak, or $\phi_+ = \phi_-$.

Figure 3.1 displays the zonal and annual mean heating rate resulting from the total meridional transport of moist static energy, based upon the Oort and Rasmusson's (1971) compilation. The distribution of the heating above 900 mb suggests that one appropriate choice of walls is $\phi_+ = \phi_- = 45°N$, so that the model results presented in Chapter IV use observed temperature and flux distributions at 45°N as a standard for evaluating the model's performance. The horizontal flux heating is relatively strong at 45°N below 900 mb, indicating that the horizontal flux convergence is an important part of the heat balance near the surface. In the model, moist convection controls the

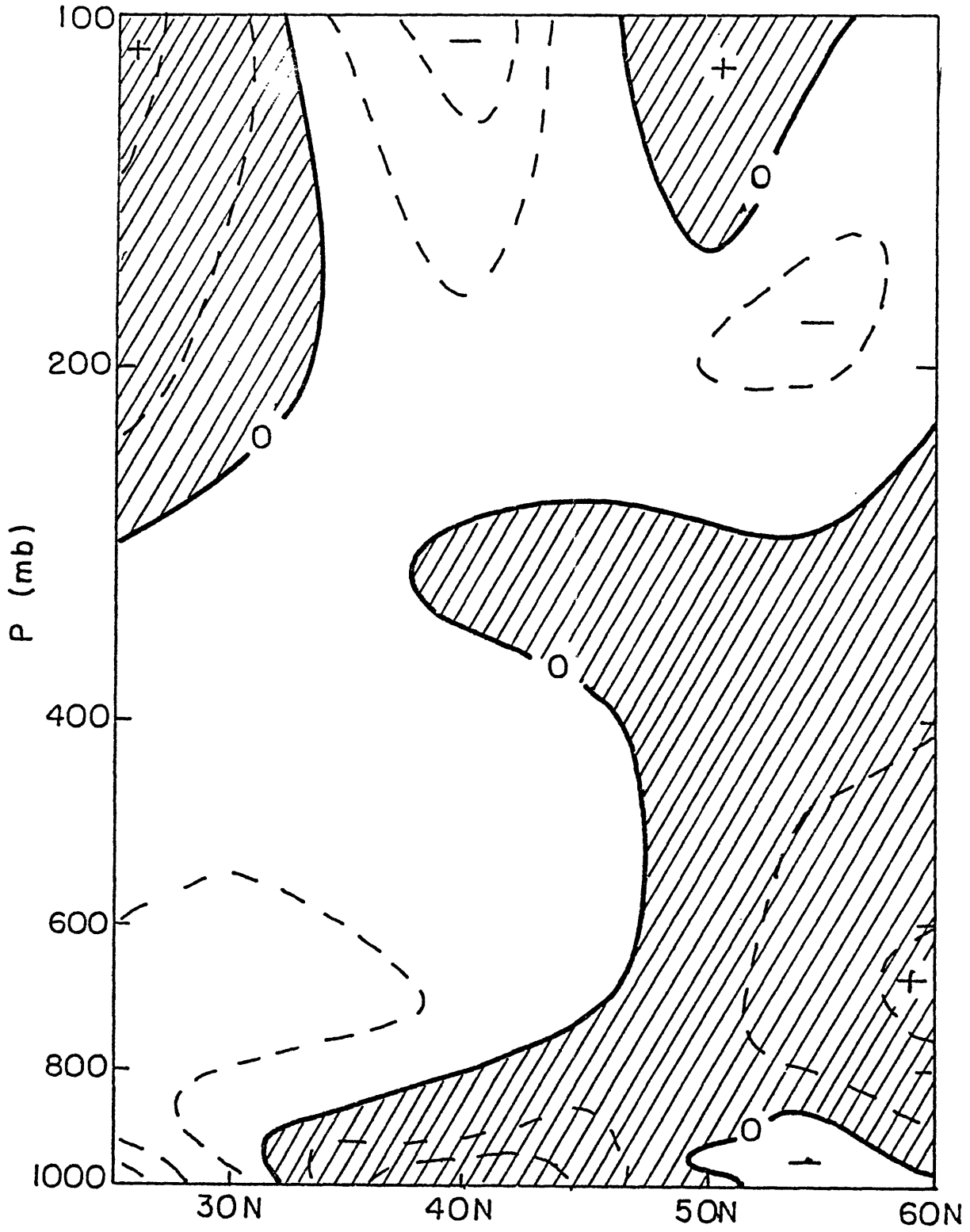


Fig. 3.1 - The annual mean heating rate due to the meridional transport of moist static energy $C_p\overline{[v\theta]} + L_v\overline{[vq]}$, using the data of Oort and Rasmusson (1971). q is the specific humidity. The contour spacing is 0.4 K/day, and positive heating is hatched.

temperature structure in this region through a convective adjustment. The horizontal flux heating below 900 mb in Figure 3.1 is much smaller than the model's typical vertical eddy flux cooling below 900 mb, so that even if the horizontal flux heating were included in the model's thermodynamic balance, it would have no direct influence on the model's vertical temperature structure: the net temperature tendency by all eddy divergences would be still be negative below 900 mb, convective heating would still be necessary for a thermodynamic balance to occur there, and a convective adjustment would still determine [T](z) there. Therefore, the horizontal heat flux, whether included in the model's balance or not, has no direct influence on the temperature structure of the model. The horizontal fluxes do provide energy, which can be distributed vertically. The model assumes that the vertical eddy fluxes draw upward whatever energy is necessary to achieve a balance in the model's upper layers, a flux across the lower surface supplying this energy. The observed horizontal flux convergence near the surface may be modeled simply by subsuming it into the heating resulting from the surface energy flux.

The vertically-averaged climate model developed by Saltzman and Vernekar (1971) uses an assumption about the vertical heating balance similar to this model's. They obtain a closure for the amplitude of the eddy fluxes in their model by hypothesizing that the vertical mean eddy flux heating above 500 mb matches the vertical mean radiative cooling there. Under this assumption, the amplitudes of their model's horizontal eddy fluxes of heat, water vapor, and momentum agree well with observations. The model presented here determines the eddy amplitude by other means, but in effect it assumes the same type of balance in the upper troposphere.

2. Large Scale Eddy Flux

Observations of eddies often divide them into two categories: transient and stationary. The model computes only a transient eddy flux and neglects the standing eddy flux. The observational results discussed in Chapter I show that the standing eddy vertical flux is relatively small, so that the transient eddy flux alone accounts for most of the vertical eddy heat flux. Also, in Kasahara and Washington's (1971) GCM experiments, the net vertical eddy heat transport changes very little when they eliminate standing eddy fluxes by removing all mountains from their model: the vertical transient eddy heat flux increases to compensate for the loss of the vertical standing eddy heat flux. Such compensation may occur if there is a negative feedback between the size of N^2 and the strength of the vertical eddy heat flux. The model developed here assumes that the large scale vertical eddy heat flux results from the baroclinic instability of the zonal mean flow. For such a flux, the negative feedback seems likely to occur, since a decrease in N^2 causes the instability of the zonal mean flow to increase, causing the vertical eddy heat flux to increase and counteract the decrease in N^2. The relative sizes of the observed transient and standing vertical eddy heat fluxes indicates that only a small amount of compensation should be necessary for the transient eddy heat flux to account for the neglect of the standing eddy heat flux in the model.

We also might expect that similar compensation involving N^2 exists between the vertical eddy sensible and latent heat fluxes and thereby eliminate the moisture flux from the model. However, a relatively

simple expression exists for the latent heat flux in terms of the sensible heat flux. Therefore, the model can check for compensation, rather than assume it, by computing equilibrium states with and without latent heat fluxes.

a) Sensible heat flux.

The model uses the quasi-geostrophic approximation to compute the eddy sensible heat flux. Gall (1977) and Mudrick (1982) have studied the eddy heat fluxes produced by a baroclinically unstable wave using both quasi-geostrophic and primitive equation models. The results of both studies indicate that the zonally-averaged vertical eddy heat flux given by the quasi-geostrophic equations is a good approximation to the same flux given by the primitive equations.

The model determines the sensible heat flux profile by solving a linear baroclinic instability problem based upon (2.2.7). For a wave-like perturbation, $\Psi = \psi(z)\exp\{i(kx+ly-kct)\}$, and a basic state given by the zonal mean flow, the perturbation must be a solution of

$$\left\{\frac{d^2}{dz^2} - T\frac{d}{dz} - \mu^2\right\}\psi(z) + \left\{\beta_* + T[U]_z - [U]_{zz}\right\}\frac{\psi(z)}{([U] - c)} = 0 \ . \quad (3.2.1)$$

Here, $T = \frac{d}{dz}\ln\left(\frac{N^2}{\rho}\right)$, $\beta_* = \frac{N^2}{f^2}\beta$, and $\mu^2 = \frac{N^2}{f^2}(k^2 + l^2)$. k and l are the zonal and meridional wave numbers, respectively, while β is the variation with latitude of the Coriolis parameter, f. Guided by Killworth's (1980) results, the model uses l = k for all computations. The zonally-averaged vertical eddy sensible heat flux is $0.5 \cdot \mathrm{Re}\{w^* \mathrm{conj}(\theta^*)\}$, where the vertical velocity of the unstable wave, w^*, is

$$w^* = \frac{-igk}{N^2} \{([U] - c)\psi_z - [U]_z\psi\} \quad ,$$

and temperature perturbation, θ^*, is

$$\theta^* = [\theta]\psi_z \quad .$$

With boundary conditions of $w^* = 0$ at the top and bottom, (3.2.1) becomes an eigenvalue problem for phase speed c. The upper boundary condition is not realistic, but by choosing the top at a high enough level, the strong increase in static stability at the tropopause should limit the influence of the upper lid (Green, 1960). Appendix B4 shows that a lid at 25 km has negligible influence upon the model's troposphere.

Given specified distributions of zonal wind shear and density and the model generated temperature structure, (3.2.1) provides the vertical structure equation for the streamfunction of an unstable wave. For one wave number, there may be a number of linearly unstable modes (e.g., Fullmer, 1982b). The model chooses the one with the largest growth rate, under the assumption that, given a random perturbation, such mode ultimately will determine the vertical distribution of that particular wave number's heat fluxes. Neutral modes may dominate early eddy growth in an initial value problem (Farrell, 1982), but the parameterization aims at modeling the time mean eddy heat transport and neutral modes do not yield a net heat transfer.

Analytic studies of weakly nonlinear, viscous baroclinic instablility (Pedlosky, 1970, 1971, 1979a; Drazin, 1972) show that the lowest-order streamfunction for equilibrated flows is given by the linear instability problem, which indicates that the height distribution of the vertical eddy heat flux may be well-approximated by the linear

instability problem. This result for the streamfunction's vertical structure in weakly nonlinear flow occurs merely by definition of the problem, however, and may be suspect for flows which are more strongly supercritical. Simmons and Hoskins (1978), for example, note that the time and zonal mean eddy kinetic energy density in their wave-mean flow studies can have a considerably different vertical structure than that given by linear instability. The distribution of eddy kinetic energy in the atmosphere is subject to rearrangement after being generated by conversion processes (Gall, 1976b; Simmons and Hoskins, 1978). The conversion processes themselves die away as growth ceases, so that nonlinear effects may not appear as strongly in the time mean vertical structure of a conversion process as they do for non-vanishing quantities, such as kinetic energy. The model requires a parameterization of the time mean vertical eddy heat flux, which is proportional to the conversion of eddy available potential energy (EAPE) to eddy kinetic energy. Thus, the linear instability structure may still give a good approximation of the time mean heat flux.

Numerical work by Gall (1976b) suggests that the linear instability structure does give a good approximation for the vertical structure of the time mean vertical eddy heat flux. Gall (1976b) follows the development of a wave in a GCM which retains only the single wave and the zonal mean flow, the model running until the growth of eddy kinetic energy ceases. The term representing conversion of eddy available potential energy into eddy kinetic energy, $[\omega^*\alpha^*]$, where $\alpha = 1/\rho$, is proportional to the vertical eddy heat flux. Figure 3.2 reproduces Gall's figure showing the time development of $[\omega^*\alpha^*](z)$ in his experiment using wave number 7. Gall's data have been averaged

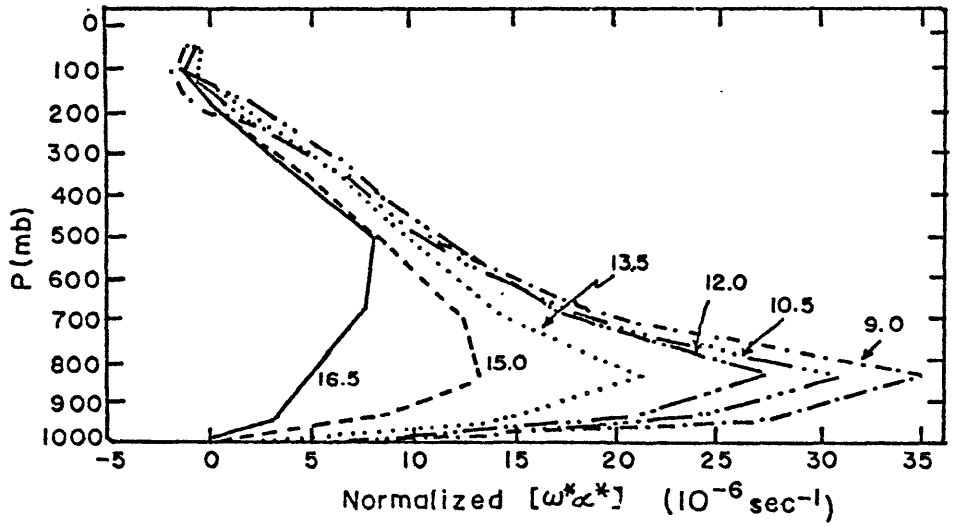


Fig. 3.2 - $[\omega^*\alpha^*](z)$ as a function of time in Gall's (1976) wave-mean flow interaction experiment using wave number 7. The numbers on each curve refer to the time in days from the beginning of the experiment. Each $[\omega^*\alpha^*]$ curve is normalized by the total kinetic energy of the wave at the corresponding time.

over the mass of the atmosphere, but the experiment's eddy activity is concentrated between 35°N and 60°N, so that the profiles in Figure 3.2 are essentially mid-latitude horizontal mean profiles. The flux at each time in the figure is normalized by the eddy's current kinetic energy, and the maximum renormalized flux occurs on day 12. $[\omega^*\alpha^*]$ shows litttle gross structural change during the experiment until the end of the growth phase on day 15, at which point $[\omega^*\alpha^*]$ becomes relatively small. The behavior of the flux suggests that the time mean structure of the vertical flux over the period of substantial transport is well-approximated by the linear instability structure.

In the atmosphere, wave-wave interactions could also modify the flux structure during the period of substantial transport. However, statistics for atmopheric spectral energetics presented by Saltzman (1970) and Tomatsu (1979) show that for wave numbers smaller than zonal wave number 9, the exchange of APE between a wave and the zonal mean flow tends to be much larger than the exchange of APE between that wave and all other waves. Table 3.1 shows the ratio $\left|\text{(wave-wave APE exchange)}\right|$/(wave-mean flow APE exchange) for zonal wave numbers 1 through 10 in the atmosphere, computed from the statistics of Saltzman (1970) and Tomatsu (1979). The relative sizes of the transfers indicate that the wave-mean flow interaction is the most important process influencing the nonlinear evolution of the wave. The wave-wave energy exchange tabulated by Saltzman and by Tomatsu is the sum over all wave-wave interactions involving a particular wave; there may be much larger wave-wave exchanges of energy than indicated by the sum, due to cancellation. However, weakly nonlinear studies with more than one unstable wave (Hart, 1981; Pedlosky, 1981) suggest that the primary

Table 3.1 - The ratio |(wave-wave APE exchange)|/(wave-mean flow APE exchange) as a function of wave number, computed from the statistics of Saltzman (1970) and of Tomatsu (1979).

zonal wave number	1	2	3	4	5	6	7	8	9	10
(from Saltzman)	.4	.9	.6	.1	.2	0	.1	.2	.4	.8
(from Tomatsu)	.1	.6	.5	.1	.1	.2	.5	.5	.9	.5

nonlinear interaction is between the wave and the zonal mean flow.

During the eddy decay phase, the conversion term could possibly change sign. The reverse conversion ought to be relatively weak, since observational data show a strong net transfer of eddy available potential energy to eddy kinetic energy (Oort and Piexoto, 1974; Tomatsu, 1979). Furthermore, the observational evidence on the existence of lifecycles in atmospheric eddies (Blackmon et al., 1977; Blackmon and White, 1982) indicates that the growth phase tends to occur in the zone from 35°N to 50°N, while the decay phase occurs farther north. This being the case, for a mid-latitude simulation centered at 45°N, the influence of decay phase characteristics on the vertical flux structure should be relatively small.

Edmon et al. (1980) have compared zonal mean fluxes averaged over an eddy lifecycle with those given by linear instability and have concluded that the linear instability flux does not yield a good approximation to the time mean flux. However, their results are based upon the GCM study of Simmons and Hoskins (1980). In the Simmons and Hoskins model, the conversion of eddy kinetic energy to zonal mean kinetic energy is about the same size as the conversion between eddy available and eddy kinetic energies. In the atmosphere, the former is much smaller (Oort and Piexoto, 1974; Tomatsu, 1979). Thus, the GCM's

energy cycle does not match the atmosphere's, and their observation that the linear instability fluxes do not have the same vertical structure as the time mean fluxes may not apply to the atmosphere. Figure 3(c) in Edmon et al. (1980) shows the spatial distribution of the zonal mean meridional eddy fluxes at the time in the GCM when the eddy kinetic to zonal kinetic energy conversion is greatest, the time when the GCM's eddies are decaying. At this point, the heat flux in the lower atmosphere is very weak, even equatorward at some points, but still poleward above. This indicates that the unrealistically strong kinetic energy conversion phase of the GCM indeed can change the vertical structure of the time mean flux so that it is different from the linear instability structure. The atmospheric decay phase regions identified by Blackmon et al. (1977) show generally poleward, rather than equatorward, eddy heat fluxes in the time mean. Thus, even within decay phase zones that are spatially separate from zones of growth, Edmon et al.'s (1980) conclusion that linear instability fluxes are inappropriate for modeling the time mean fluxes may not apply. Note also that, in a strict sense, their conclusion does not apply to the vertical eddy heat flux since they study only the meridional component of the eddy heat flux.

After obtaining the sensible heat flux profile from a linear computation, the model must still make some closure assumption. The model uses one of two different methods to determine the sensible heat flux amplitude. The methods are the same for runs using a single wave or an ensemble of waves; the discussion here will only present the closure for the single wave case.

One approach is to use the results from studies of the weakly nonlinear evolution of baroclinically unstable waves. Branscome (1980) has used these studies to develop a closure based on the amplitude they give for equilibrated waves. The nonlinear effects cause the growth of the wave to cease at some point. If there is sufficient damping in the model, the wave equilibrates at a steady amplitude, resulting in a balance between the damping of eddy energy and the conversion of zonal available potential energy into eddy energy, similar to the atmosphere (Oort and Piexoto, 1974). The most realistic of the models is Pedlosky's (1979a) study, which uses β-plane geometry and which includes damping of the temperature perturbation by Newtonian cooling. His results show that at equilibration the amount of eddy kinetic energy is approximately the same size as the zonal available potential energy. Thus, Branscome uses EKE ≈ ZAPE for a closure. For the model,

$$\text{EKE/(area)} = \frac{gK^2}{4f^2} \int_0^{z_{top}} \rho(z) \left|\psi\right|^2(z)\, dz \ , \qquad (3.2.2)$$

and

$$\text{ZAPE/(area)} \approx \frac{1}{6}(L_y f)^2 \int_0^{z_{cl}} \rho(z) \frac{([U]_z)^2}{N^2} dz \ , \qquad (3.2.3)$$

where K is the total horizontal wave number, z_{top} is the top of the model, and L_y is the meridional extent of parcel motions. L_y is the length over which the eddy draws upon the zonal available potential energy, under a mixing hypothesis. The height z_{cl} measures the depth over which the mixing occurs such that there is a conversion from eddy available to eddy kinetic energy, the depth over which $[w^*\theta^*]$ is positive. For some flux profiles, $[w^*\theta^*]$ is positive at all heights, but it becomes very small above some level. In order to

measure the ZAPE only over the depth where significant conversion is occurring, z_{cl} in the model is the level above the flux maximum where $\rho C_p[w^*\theta^*]$ becomes less than 10^{-2} W/m^2. Above z_{cl}, the model's vertical eddy heat flux is always negative, very small, or both.

We can estimate L_y from the meridional length scale for Lagrangian motions in a wave field. For a travelling wave described by $\Psi \sim \psi\exp\{i(kx+ly-kc_rt)\}$, where c_r is the real part of the phase speed, the Lagrangian motion in the meridional direction is an oscillation with approximate amplitude V/kc_r, where V is the streamfunction's velocity scale. Viewing the transfer of ZAPE to the eddy as an exchange of parcels described by the Lagrangian motion, then $L_y \sim V/kc_r$. A choice consistent with the assumption that EKE $\approx$ ZAPE is $V \sim [U]$, so that $V \sim V \sim [U]$, so that $V \sim c_r$ and $L_y \sim 1/k$. L_y thus scales with the radius of deformation, since 1/k does. Pedlosky (1975), Kim (1978) and Lin (1980) have shown that, for a basic state baroclinic wave, the eddy draws available potential energy from this scale. Also, Kida's (1977) tracer experiments show particles in mid-latitudes oscillating in the meridional direction with a length scale of $\sim 10^3$ km, about the size of the radius of deformation. The model uses $L_y = 1/k$ in the EKE $\approx$ ZAPE closure.

Since the model aims at reproducing features of the general circulation resulting from eddies, another closure choice is to simply specify the EKE from observations. The eddy kinetic energy level in the atmosphere is readily available from the zonal mean velocity variance statistics of Oort and Rasmusson (1971) and this closure uses the observed EKE per unit area to determine an amplitude for the streamfunction, ψ, by means of (3.2.2). Table 3.2 shows the observed

Table 3.2 - Vertical mean EKE per unit area at 45°N (units: 10^5 J/m^2)

Winter (DJF)	15.4
Summer (JJA)	9.1

mass-weighted vertical mean values of EKE per unit area. As previously noted, the time mean distribution of eddy kinetic energy throughout the atmosphere will probably not be well-modeled by the linear instability streamfunction. The closure simply assumes that the model's vertical mean EKE computed from $\psi(z)$ matches the observed EKE even if the model's and the atmosphere's distributions of EKE are different.

Computations in Chapters IV and V use a variety of specified vertical mean EKE's and the atmospheric values in Table 3.2 provide reference points for the range of EKE values covered by the model. Discussion in these chapters of model runs using a specified eddy amplitude refers to the size of the amplitude by the size of the model's EKE relative to the observed EKE in the appropriate season. Thus, a $2E_w$ model run means the model uses an eddy amplitude of such size that the model's EKE is twice the observed wintertime EKE.

b) Latent heat flux.

Given the sensible heat flux, we can compute the latent heat flux from a parameterization developed by Leovy (1973) for Mars. Mullan (1979) has demonstrated its applicability to the earth's atmosphere. With relative humidity R(z) constant in time at each level, a temperature perturbation applied to the Clausius-Clapeyron equation leads to

$$L_v\left(\frac{p_0}{p}\right)^{\kappa}[w^*q^*] = \Lambda(z)C_p[w^*\theta^*] \quad , \tag{3.2.4}$$

where

$$\Lambda(z) = \frac{L_v R}{C_p}\left(\frac{\varepsilon}{p}\right)\frac{\partial e_s}{\partial T} \quad ,$$

and q is the specific humidity. To a very good approximation in the atmosphere, $q \approx m$, so that (3.2.4) gives a parameterization for the eddy latent heat flux in (3.1.2) in terms of the eddy sensible heat flux.

The assumption of constant R(z) actually may be more appropriate for the earth than Mars, since the earth's surface is mostly covered by ocean, providing a ready source of moisture. The Martian surface does not appear to supply moisture so easily, except possibly over the northern ice cap (Davies, 1979). For the earth, Telegadas and London (1954) have found that relative humidity shows little variation between winter and summer. Mullan notes that a simple model of the tropics by Sarachik (1978) gives only a 10% variation of relative humidity when the solar forcing changes by a factor of 2.

The assumption of constant relative humidity may seem weaker for a time scale shorter than a season, such as that for an eddy lifecycle. Mullan has compared the vertically-averaged meridional latent heat flux predicted by the parameterization with the observed flux, obtaining a good agreement in mid-latitudes. This comparison appears in Figure 3.3, reproduced from Figure 1.3 of Mullan (1979). Mullan uses R = 1 for his computations, but a more appropriate choice is $R \approx 0.8$, the atmosphere's relative humidity at the levels where the meridional latent heat flux peaks. Using R = 0.8 improves the agreement between observed and parameterized fluxes in January, though it weakens the agreement in July.

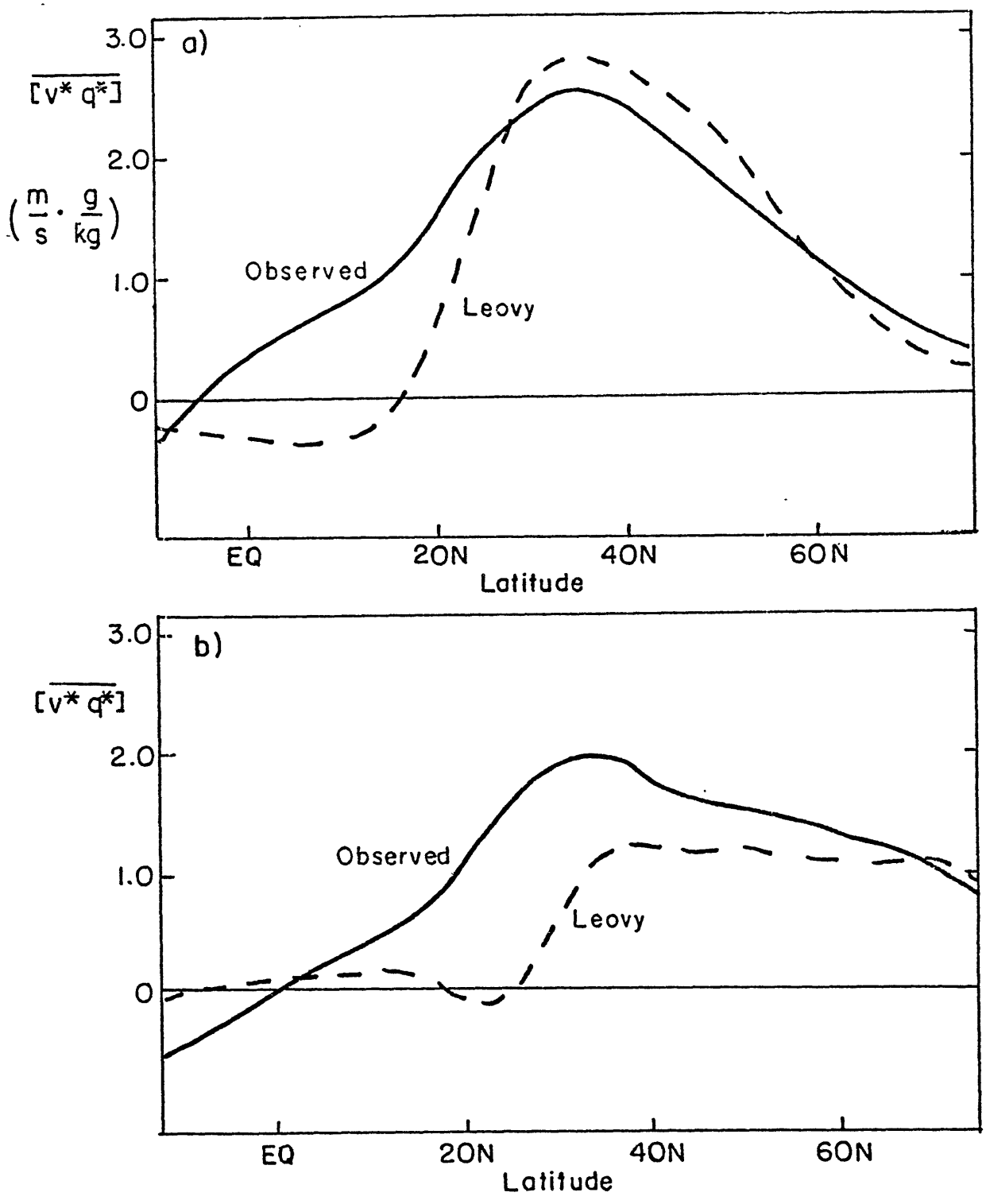


Fig. 3.3 - Mullan's (1979) comparison of the Leovy parameterization for meridional latent heat flux with the observed eddy latent heat flux from Oort and Rasmusson (1971), for a) January and b) July. All fluxes are vertically-averaged.

As long as $T' \ll \overline{T}$, the above parameterization is very accurate at each pressure level if R is strictly constant in time. It should still work well for a perturbation R' about $\overline{R}$, if

$$\left(\frac{R'}{\overline{R}}\right) \ll \left(\frac{e_s'}{\overline{e}}\right) \approx \frac{T'}{\overline{e}} \cdot \frac{\partial \overline{e}_s}{\partial T}(T) \quad . \tag{3.2.5}$$

For January, the variance data of Oort and Rasmusson (1971) give in the lower atmosphere at 40°N, $T' \approx 7$ K. With the observed $\overline{T} \approx 275$ K, then (3.2.5) requires $R'/\overline{R} \ll 0.5$. For July, the data give $T' \approx 4.5$ K and $\overline{T} \approx 290$ K, which requires $R'/\overline{R} \ll 0.3$. Measurements of R' are not available, but we can see that a greater range of R' values is acceptable in winter than in summer due to larger temperature perturbations about a cooler mean temperature. This appears to be evident in the accuracy of the parameterization as shown in Fig. 3.3. The closer $\overline{R}$ is to 100%, the more likely it is that R' variations will be acceptably small. The barrier of 100% relative humidity also has the favorable effect of restricting the range of R' variations.

c) Vertical heat flux from an ensemble of waves.

The depths of unstable waves tend to vary with wave number. A single wave may provide a reasonable first approximation to the height dependence of the atmosphere's vertical eddy heat flux, but the height dependence may be better approximated by calculating it from a spectrum of waves similar to the observed spectrum. The wave ensemble runs discussed in this thesis use a spectrum consisting of zonal wave numbers 1 through 10. As suggested by the discussion of Table 3.1, the wave-mean flow interaction for each individual wave is more important than wave-wave interactions. Thus, the model obtains the vertical

structure of the ensemble's heat flux by computing the linear instability flux for each wave separately using the zonal mean flow as the basic state for the computation. The total flux is then a weighted sum over all of the individual fluxes.

The determination of the amplitude of the total flux follows from the same procedures outlined above, only for wave ensembles, the EKE calculation (3.2.2) includes a weighted sum over all the waves in the spectrum. The weighting factor for each wave is chosen to make the spectral distribution of sensible heat flux amplitudes match the observed spectral distribution of EAPE → EKE conversions, since the conversion varies in strength approximately with the amplitude of the vertical eddy sensible heat flux. Figure 3.4a shows the energy conversion rates computed by Tomatsu (1979) and by Chen (1982) for the winter troposphere north of 15°N. The figure shows the mean of the two studies for each wave number, as well. Wave numbers beyond $n_z = 10$ have relatively insignificant conversion rates. Thus, an ensemble of wave numbers 1 through 10 should include the most important waves. The dots in Figure 3.4a show the model's spectral distribution for the relative sizes of vertical eddy flux maxima in wintertime runs. Any stable wave has no flux and it is ignored when computing the ensemble's EKE. The distribution ignores the possible dependence of an individual wave's flux upon that wave's growth rate. However, the total flux does tend to vary with the ensemble averaged growth rate, so that the total flux can respond to changes in temperature structure through changes in the growth rate.

Saltzman and Fleisher (1961) and Tenenbaum (1976) also compute spectral distributions of the conversion rate. Their data sets are more

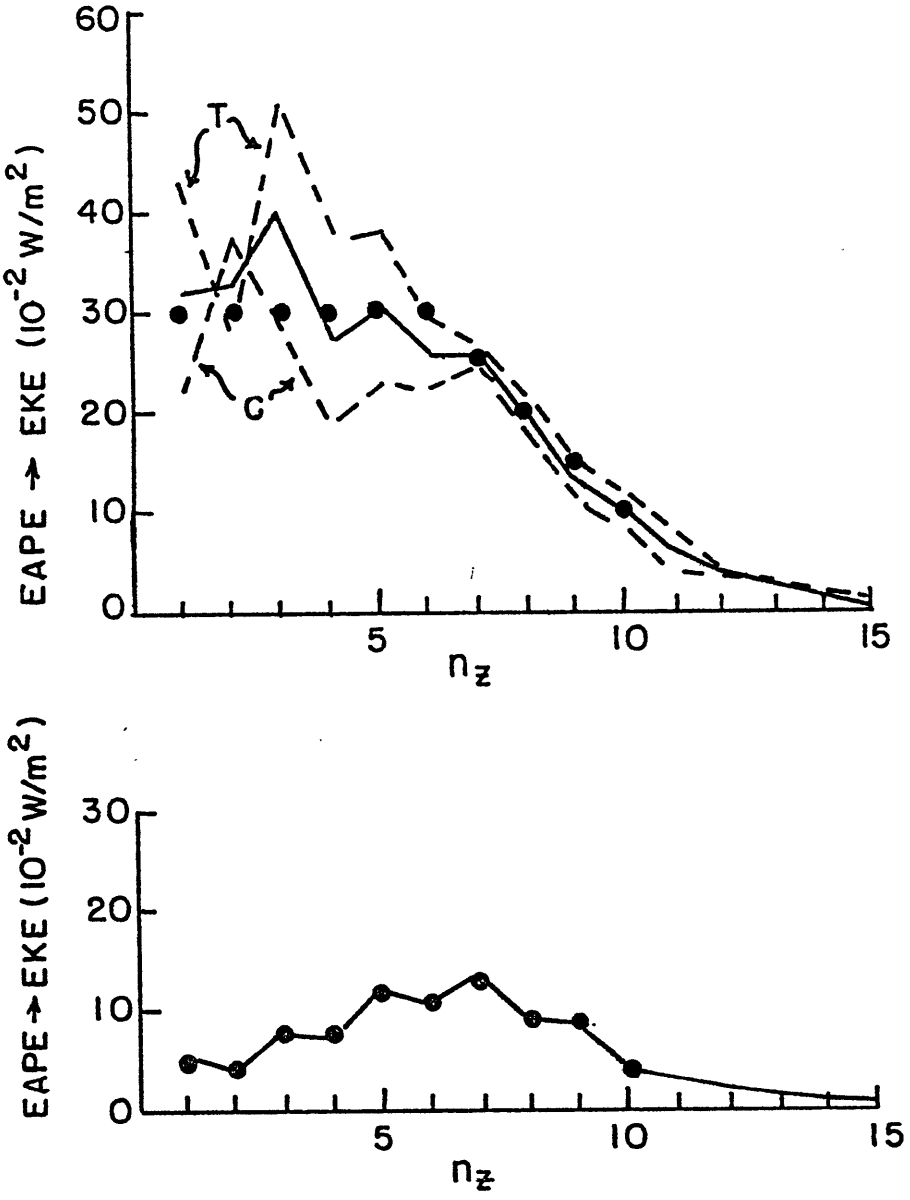


Fig. 3.4 - a) Winter EAPE → EKE conversion rates calculated by Tomatsu (T) and by Chen (C), as a function of zonal wave number n_z. Also shown is the mean of the two calcuations (solid line) and the relative sizes of the peak sensible heat fluxes in the model's wave ensemble runs for winter conditions (dots). b) Summer EAPE → EKE conversion rates calculated by Tomatsu (solid line) and the relative sizes of the peak sensible heat fluxes in the model's wave ensemble runs for summer conditions (dots).

limited in either space or time compared to the data sets used by Tomatsu and by Chen. Therefore, the conversion rates of Saltzman and Fleisher and of Tenenbaum are not included in Figure 3.4. Including them would not have caused the mean conversion rates in the figure to change significantly.

Tomatsu (1979) also computes summer spectral energetics. His results (Figure 3.4b) show shorter wave numbers being relatively strong compared to their sizes in the winter spectral distribution of conversion rates. The model uses the spectral distribution of relative sizes for wave flux maxima in summertime runs as shown by the dots in the figure.

3. Radiation

Radiative flux within the mid-latitude troposphere generally tends to be cooling, counterbalancing the heating due to motions and moisture condensation. The effect of radiation varies with temperature and with the amount of absorbers. The model's parameterization uses a fixed distribution of the latter and attempts to include some effect of the former. As noted previously, work using the model attempts to determine how well the model can produce equilibrium states which are consistent with the sizes and distributions of observationally-based specified parameters. The radiative cooling is one such specified parameter. The model uses results from Dopplick's (1979) radiative transfer computations, an update of results reported earlier (Dopplick, 1972). His computations have been performed as a function of latitude and season for observed distributions of the temperature and the principal absorbers, including clouds.

The parameterization consists of two parts. The primary net radiative cooling is that computed by Dopplick for 45°N. The model's temperature profile usually differs from the one used by Dopplick, so the parameterization uses a Newtonian damping based on the temperature difference to provide a correction to Dopplick's values. Thus, at some height z, the net radiative cooling of [θ] is

$$Q_R = \{Q_{Do}(z) + (T_{Do}(z) - [T](z))/\tau_R\} \quad ,$$

where $T_{Do}(z)$ and $Q_{Do}(z)$ are the distributions of temperature and net cooling from Dopplick, and τ_R is a damping time. Dickinson (1973) has proposed a similar treatment of radiation for the stratosphere.

Prinn (1977) has shown that the damping time for a perturbation $(T_{Do}-[T])$ in the troposphere can vary greatly, depending on the vertical length scale of the perturbation, its distance from the surface, and the type of surface. For the purposes of the model, a damping time representative of the middle troposphere is sufficient. The model uses an approximation to τ_R, based on non-grey calculations by Prinn and Visconti (private communication), $\tau_R(\text{days}) = 11.4 + 1.7z_R$, where z_R is the depth of the layer in kilometers for which $[T] \leq T_{Do}$ in the troposphere. This approximation assumes that there is a single dominant vertical wavelength for $(T_{Do}-[T])$ in the troposphere, with wavelength $2z_R$, which is typically the case in model solutions. Since the model's convective adjustment procedure maintains $\frac{\partial}{\partial z}[T] < \frac{\partial}{\partial z}(T_{Do})$ near the surface, the level z_R is the lowest level above the surface where $[T] \geq T_{Do}$, which the model can determine quickly. Perhaps a more sophisticated procedure would Fourier analyze $(T_{Do}-[T])$ and assign different damping times to each mode, but such refinement does not seem to be necessary.

There are two extreme cases where $2z_R$ may not be a representative wavelength. For some summer condition runs, $2z_R$ may be about 2 km, but the more appropriate wavelength may be 10 - 12 km, or about 5 times larger. The error in $(1/\tau_R)$ using the formula above is roughly 100%. However, in these cases, $T_{Do} - [T] \leq 2$ K through most of the troposphere, so that the error is only about 0.1 K/day, relatively insignificant. For weak eddy flux, the model gives $[T] < T_{Do}$ everywhere. Thus, the damping time depends upon the depth of the model atmosphere. In most cases, the depth is 25 km, yielding a damping time of about 50 days, which is within the range of τ_R values given by Prinn and Visconti for long (> 30 km) vertical perturbation wavelengths in the lower troposphere.

The primary upper-boundary of the model is sufficiently high that the eddy flux typically decays to relatively small size well below the lid. Thus, although the net heating in Dopplick's computations, Q_{Do}, is non-zero at these heights, in the model this heating would be balanced primarily by $(T_{Do}-[T])/\tau_R$. Consequently, the model uses a Q_{Do} smoothed to zero above 15 km. Figure 3.5 displays the functions $Q_{Do}(z)$ and $T_{Do}(z)$ for summer and winter, both before and after alteration. The alteration occurs in the model stratosphere, so that it should have little influence on the model's troposphere.

4. Subgrid Scale Fluxes

As noted previously, interaction between the subgrid or subsynoptic scale fluxes and the zonal mean environment is a complex problem in itself. No attempt is made here to model explicitly these

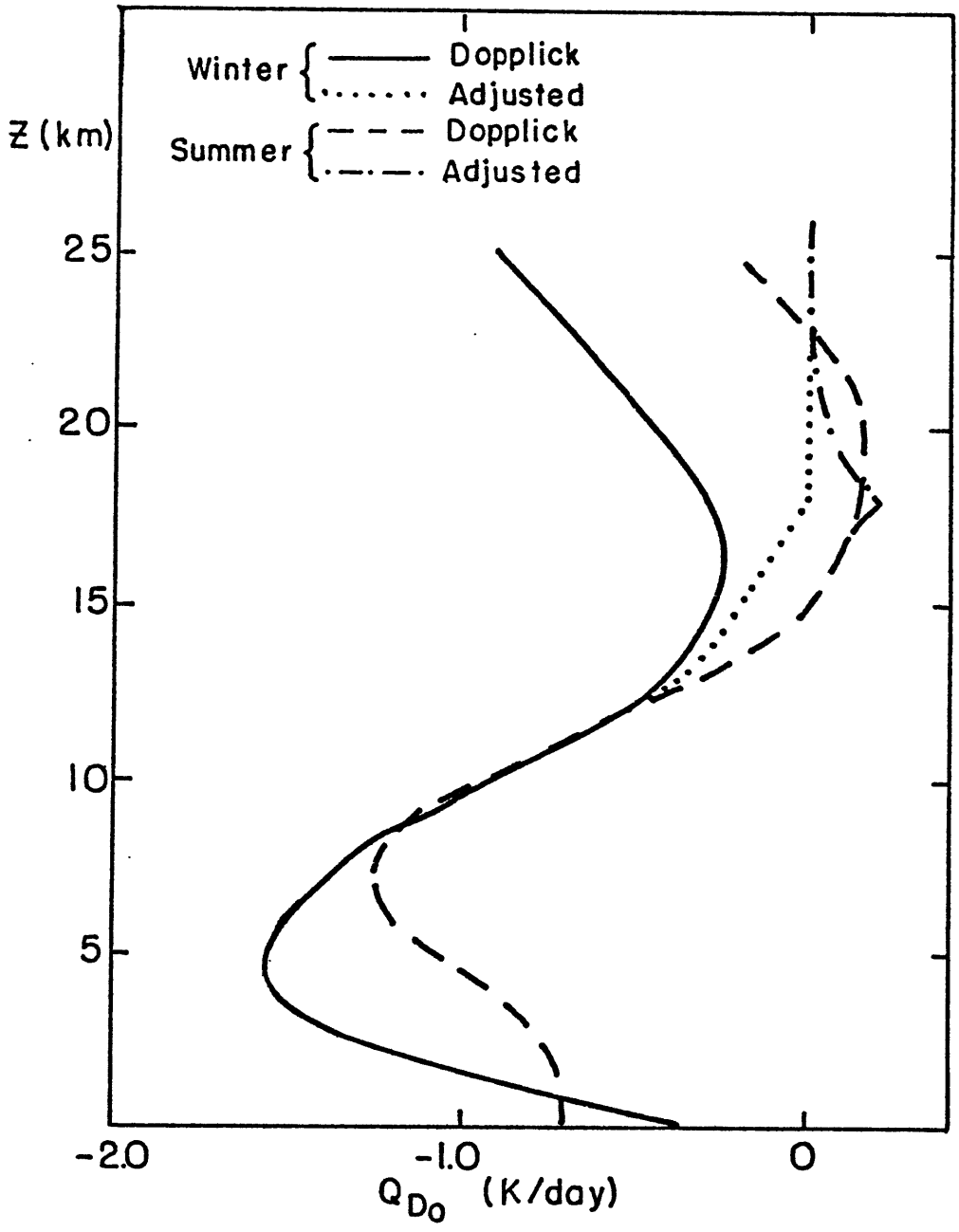


Fig. 3.5a - Specified radiative cooling rates, Q_{Do}. The figure shows the cooling profiles for winter and summer at 45°N computed by Dopplick (1979) and the adjusted profiles for each season used by the model.

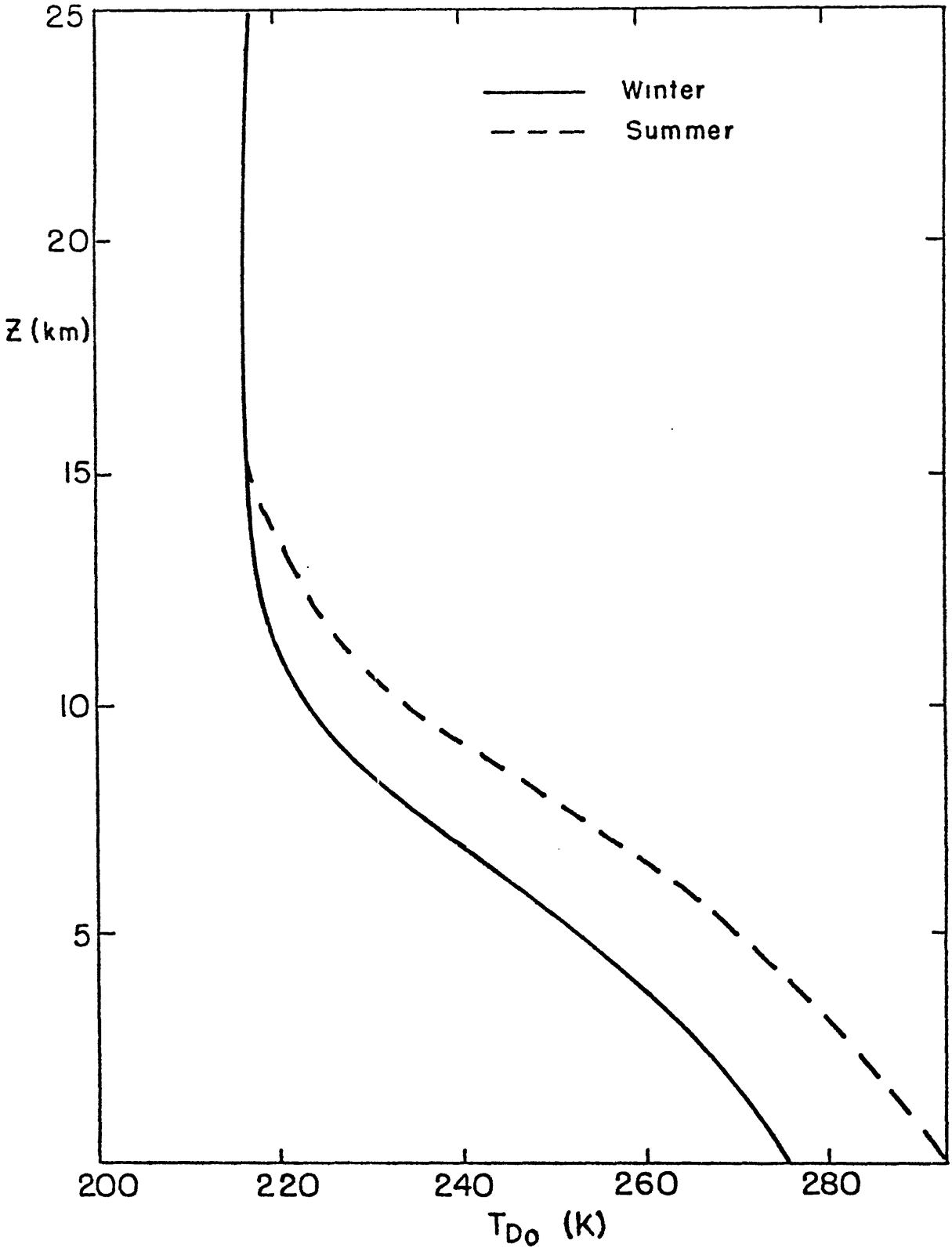


Fig. 3.5b - $T_{Do}(z)$ for winter and summer.

processes. Drawing from Stone and Carlson (1979), the model assumes that a moist adiabat provides a reasonable approximation to the net effect that subgrid scale fluxes have upon the zonal mean temperature structure. The appropriate moist adiabat to use is suggested by Figure 3.6, which compares the observed $[T](z)$ at 45°N in winter and summer with $T_m(z)$, the temperature profile of a saturation moist adiabat that intersects the observed temperature profile at 1000 mb. With respect to saturated air parcels near the surface, $[T](z)$ for both winter and summer at 45°N is conditionally stable at all levels, but only marginally so in summer. The appropriateness of the particular adiabat described here is also suggested by Figure 3.7, which compares $N^2(z)$ profiles computed from $[T](z)$ and $T_m(z)$ for summer in Figure 3.6. The observed N^2 is never less than the moist adiabat's N^2, the two being nearly equal between 2 and 7 km.

The comparison suggests the treatment of moist convection as a rapid adjustment in which the temperature at any level is never allowed to be less than the value of T_m at that level. In the model, $T_m(z)$ is given by the saturation moist adiabat whose temperature at the surface is the same as the specified surface temperature. The model calculations are actually performed in terms of potential temperature, θ, and the model obtains the moist adiabat for θ_m corresponding to T_m by integrating (2.1.11) upward from the surface. At any level where $\theta < \theta_m$, the model increases the temperature so that $\theta = \theta_m$. The adjustment implies that there is a flux of heat into the atmosphere. The model interprets the flux as one coming across the bottom surface, though we may interpret the heating it produces to include a contribution from horizontal flux divergence as well.

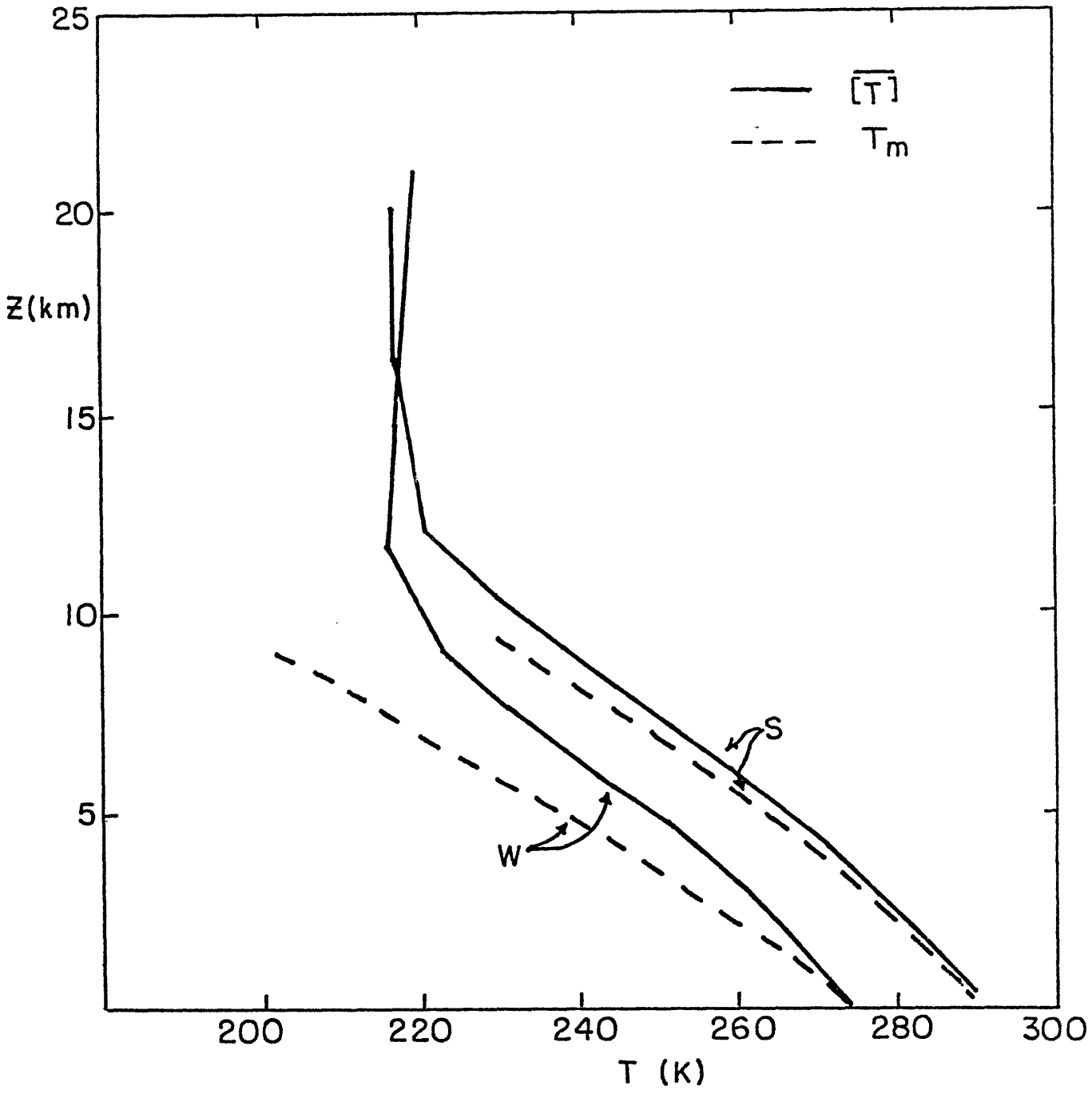


Fig. 3.6 - Observed $\overline{[T]}(z)$ for winter (W) and summer (S) at 45°N (Oort and Rasmusson, 1971) compared with $T_m(z)$, the temperature profile for a moist adiabat intersecting the observed temperature at 1000 mb.

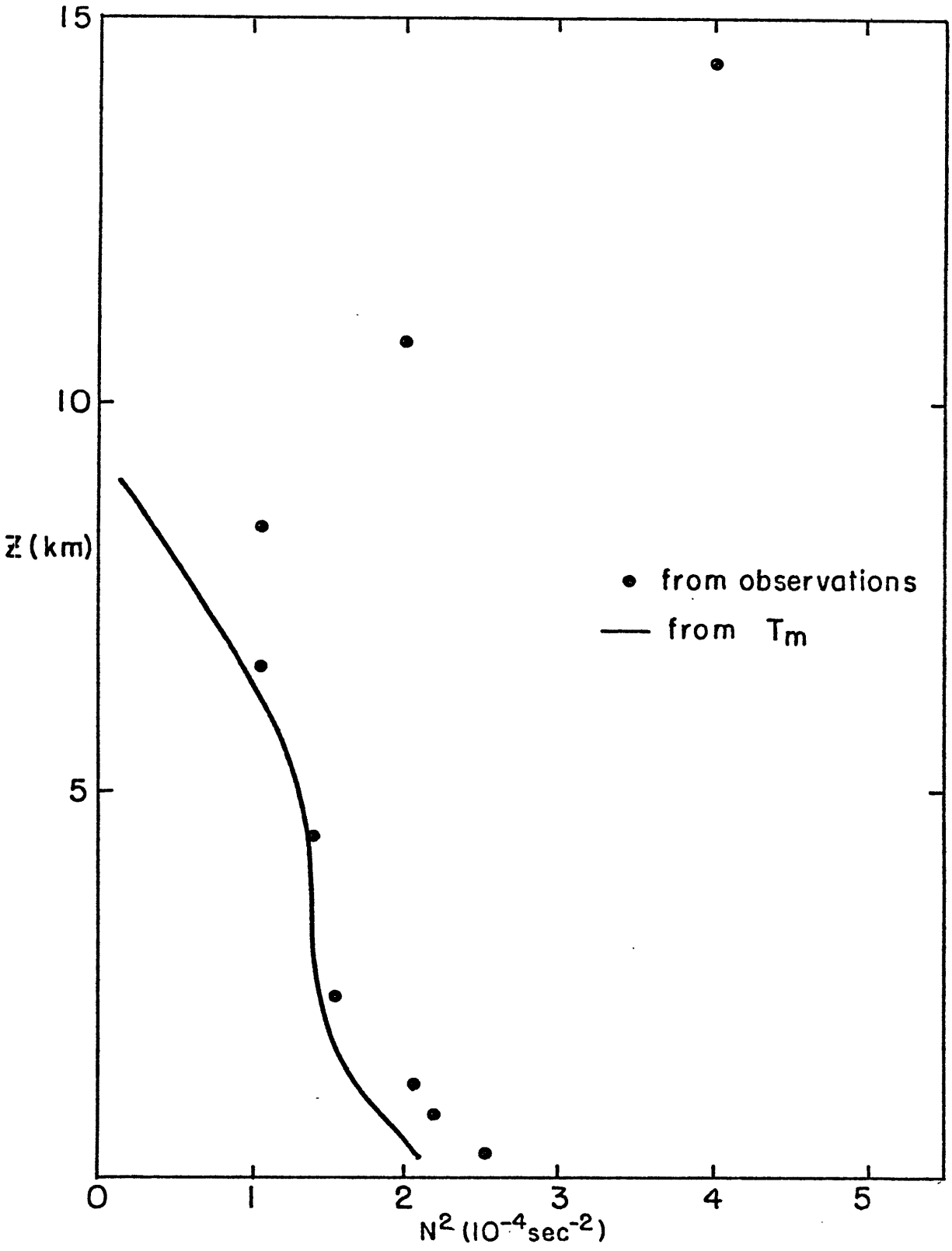


Fig. 3.7 - Observed summer $N^2(z)$ at 45°N compared with $N^2(z)$ calculated from the summer $T_m(z)$ in Figure 3.6.

The surface flux is an unspecified combination of sensible and latent heat fluxes. In the atmosphere, the latent heat flux is typically much larger than the sensible heat flux. No precise differentiation between the two is necessary here, but the adjustment does assume that there is a large enough water vapor flux into the atmosphere to maintain some portion of the air in the vicinity of the surface near saturation. The adjustment also assumes that vertical velocities on the subsynoptic scale occur with enough strength and persistence to initiate convection whenever conditional instability appears, so that the time and zonal mean temperature structure cannot be conditionally unstable. Stone and Carlson's (1979) results and Figures 3.6 and 3.7 indicate that both assumptions are reasonable in mid-latitudes.

If the convection reaches heights greater than about 10 km, the moisture level becomes so low that the moist adiabat approaches a dry adiabat, or $\frac{d}{dz}\theta_m \to 0$. A static stability approaching zero implies large vertical velocities. As a response to the resulting large heat flux, the model may integrate very slowly in time (Appendix B3). The model, therefore, restricts $\frac{d}{dz}[\theta]$ to be greater than a minimum value, $(\frac{d}{dz}[\theta])_{min} = 0.3$ K/km, at all times. This particular minimum value gives a very small increase in temperature with height, while allowing the model to maintain an adequate rate of integration through time. The model's static stability approaches the minimum static stability only at levels above 10 km where convection maintains the temperature structure, so that the model implements the constraint on the size of $\frac{d}{dz}[\theta]$ by by prohibiting $\frac{d}{dz}\theta_m$ from being less than 0.3 K/km when integrating (2.1.11) to obtain $\theta_m(z)$.

The value of L_v changes slowly with temperature, but not so much that it is important to include such dependency here. For temperatures below the freezing point of water, the latent heat of sublimation might seem more appropriate. However, the difference between the two latent heats is only about 13%, an error which should be well within the accuracy of the parameterization.

5. Other Specified Distributions and Parameters

The model uses specified distributions of pressure p(z), density $\rho(z)$, relative humidity R(z) and zonal mean zonal wind [U](z). Each of these may have some dependence upon the vertical temperature distribution, but likely variations of any due to temperature changes are small. Thus, their temperature dependencies should not influence significantly the interaction between the vertical eddy heat flux and the vertical temperature structure. As discussed in the introduction to this chapter, observations determine the values for each of these distributions.

For pressure and density, the model uses,

$$p(z) = 1013 \text{ mb} \times e^{-z/(7.5 \text{ km})}$$

$$\rho(z) = 1.25 \frac{\text{kg}}{\text{m}^3} \times e^{-z/(9 \text{ km})}$$

The compilations of zonal mean temperature and geopotential height as functions of pressure by Oort and Rasmusson (1971) provide the basis for these distributions. The density distribution in particular is obtained by assuming that Oort and Rasmusson's data obey the ideal gas law, so

that from observations of T(p) and z(p), one can compute $\rho(z) = p(z)/R_a T(z)$, where R_a is the gas constant for dry air.

The distribution of zonal and seasonal mean relative humidity presented by Telegadas and London (1954) does not display much variation in time or in latitude. For mid-latitudes, a good approximation is

$$R(z) = 0.8\ e^{-z/(7.5\ km)}$$

Given the model's p(z), this distribution is nearly the same as that used by Manabe and Wetherwald (1967) in their radiative-convective model study with fixed relative humidity. The model uses the relative humidity distribution only in the eddy latent heat flux parameterization and assumes that the profile appropriate for that parameterization is the time and zonal mean R(z).

The surface relative humidity may appear to be too low to satisfy one of the assumptions implicit in the moist convective adjustment. As discussed in the previous section, the adjustment assumes that atmospheric processes near the surface generate enough saturated air parcels over the temporal and spatial averaging lengths that moist convection prevents the lapse rate from being greater than a moist adiabat. This assumption only requires that a sufficient portion of the air be saturated to prevent conditional instability from appearing in $\overline{[T]}(z)$; the time and zonal mean relative humidity may be less than saturated.

Although $[U]_z$ is negative above the tropopause in the mid-latitude atmosphere, the model uses a positive wind shear at all levels for most runs. The original motivation for such a shear was the occasional appearance of undesirable growing grid-scale oscillations in

the model's stratospheric temperature profile. Positive $[U]_z$ in the model stratosphere seemed to suppress the oscillations, while negative $[U]_z$ seemed to enhance them. The model used a positive $[U]_z$ to prevent their appearance. The stratosphere's zonal mean flow appears to have little influence on the tropospheric behavior of the baroclinically most unstable modes (Staley and Gall, 1977), so that the actual wind shear there should be of little consequence. This seems reasonable since the modes of greatest instability, the Charney modes, are external and generally decay rapidly with height above the tropopause, if not at lower levels. The model's adoption of a filter, discussed in section 6 and Appendix B5, suppresses the grid-scale oscillations, so that the model is able to perform computations with a variety of stratospheric wind shears. Results presented in Appendix B6 confirm the assumption that the actual stratospheric wind shear is of little consequence in a model of the tropospheric temperature structure.

The model's standard zonal wind profile for winter conditions is $[U](z) = (2.0 + 2.5z)$ m/sec, where z is in kilometers. For summer conditions, the model uses $[U](z) = (2.0 + 1.7z)$ m/sec. The observed winds at 45°N in Oort and Rasmusson (1971) provide the bases for these profiles. The linear stability problem (3.2.1) is Galilean invariant, so that the height independent part of [U] affects only the value of Re(c), but not the growth rate or streamfunction. Otherwise, in the context of the model, the height independent part of the wind has no significance and appears only to provide a correspondence between the observed and modeled [U](z).

Latitude dependent constants have their values at 45°N. Thus, $f = 10^{-4}$ sec^{-1} and $\beta = 1.6 \cdot 10^{-11}$ m^{-1}sec^{-1}. $[T](0) = T_{Do}(0)$ in the season

modeled. In winter, [T](0) = 274 K, while in summer, [T](0) = 291 K. Eddies have cyclic continuity on a 45°N latitude circle, so that for zonal wavenumber k, $k(m^{-1}) = 2.22 \cdot 10^{-7} \times n_z$, where n_z is the integer zonal wave number. Later discussion identifies a particular eddy by its value of n_z.

6. Numerical Integration

The model solves the eigenvalue problem, (3.2.1) plus boundary conditions, using the shooting method (e.g. Dahlquist and Bjorck, 1974) with a fourth-order Runge-Kutta scheme. For all computations involving vertical derivatives, the model computes finite differences on a vertical grid with equal intervals in height z (Appendix B1). For single mode computations, the grid is 25 km deep and has a spacing of 0.5 km. For the wave ensemble calculations, the grid extends to 35 km and has a spacing of 1 km. The lower resolution for the ensemble runs is to prevent the computing time from being excessively long. The deeper grid for wave ensemble runs is to provide a better representation of the typically deep $n_z = 1$ and $n_z = 2$ streamfunctions included in the ensemble. Even a vertical domain of 35 km may not always be deep enough to compute the linear instability of wave numbers 1 and 2 with high accuracy, but these two wave numbers provide only 20% of the total flux or less, so that the grid depth should be adequate for computing the total eddy flux. Appendix B4 discusses the influences of grid depth and grid resolution on model solutions.

Matrix methods also can solve the eigenvalue problem and can yield, as well, all of the unstable vertical modes that may exist for a

given wave number, but they are much slower than the shooting method. Test computations comparing one such method, the QR algorithm (Dahlquist and Bjorck, 1974), and the shooting method indicate that the two are of similar accuracy. The model uses the QR algorithm at the end of an integration as a check on the shooting method's eigenvalue. Besides serving as an indicator of relative accuracy, the QR algorithm also assures that the shooting method has computed the eigenvalue of the most unstable vertical mode. Appendix B2 presents the details of both the shooting method and the QR algorithm as used by the model.

The parameterized eddy flux tends to smooth out large variations in $T = \frac{d}{dz}\ln(\frac{N^2}{\rho})$ as the model integrates forward in time. If the model uses a fixed time step, the eddy heating may tend to overcorrect, resulting in very erratic behavior. Therefore, the model alters the size of the time step at each iteration. The criterion for adjustment is that time step be small enough that large changes in T do not occur, most especially those involving a change of sign. The details are in Appendix B3.

In the course of integration for some parameter choices, substantial grid scale oscillations appear in the model stratosphere. Sometimes the oscillations grow unchecked and the integration breaks down. To prevent the appearance of these oscillations, the model uses a modified form of the smoothing filter studied by Shapiro (1970). A more detailed description of the oscillations and the filter appears in Appendix B5. The filter selectively damps short vertical wavelength oscillations in the temperature structure by producing temperature changes ΔT_j at each level j. The model uses the ΔT_j in the form of a radiative damping, dividing the filter's temperature change at a given

level by a decay time, to produce a heating rate. The decay time is one appropriate for the radiative damping of short vertical wavelength temperature perturbations, 10 days. Thus, the vertical distribution of the filter's heating rate has roughly the same effect on these wavelengths that radiation would have if the model computed radiative heating by solving a radiative transfer equation.

Aside from any physical interpretation, the application of the filter's smoothing as a damping rate also renders the filter compatible with the model's variable time step. The time step may change by orders of magnitude between iterations, while the ΔT_j tend to change less. Simply applying a smoothing operator after each time step can mean that if the time step is small enough, the smoothing operator's effective heating rate at a given level will be as large as the physical heating rates. The smoothing operator's heating rate then may become a major part of the model's heat balance. Since the model incorporates the filter's smoothing as a heating distribution, the size of the time step has no direct influence on the size of the heating rate produced by the filter. The filter's heating rate then can be very small compared to the physical processes.

The model finds an equilibrium state by integrating forward in time until it can satisfy a convergence criterion implying a balance among the different transports. The procedure follows the flow chart appearing in Figure 3.8. First, the model computes the derivatives of the temperature structure and quantities depending upon the derivatives, such as $N^2(z)$ and $[Q]_y(z)$. Next, the model determines the net potential temperature heating Q_N at each level due to the eddy flux, radiation, and the filter. After calculating the size of the time step

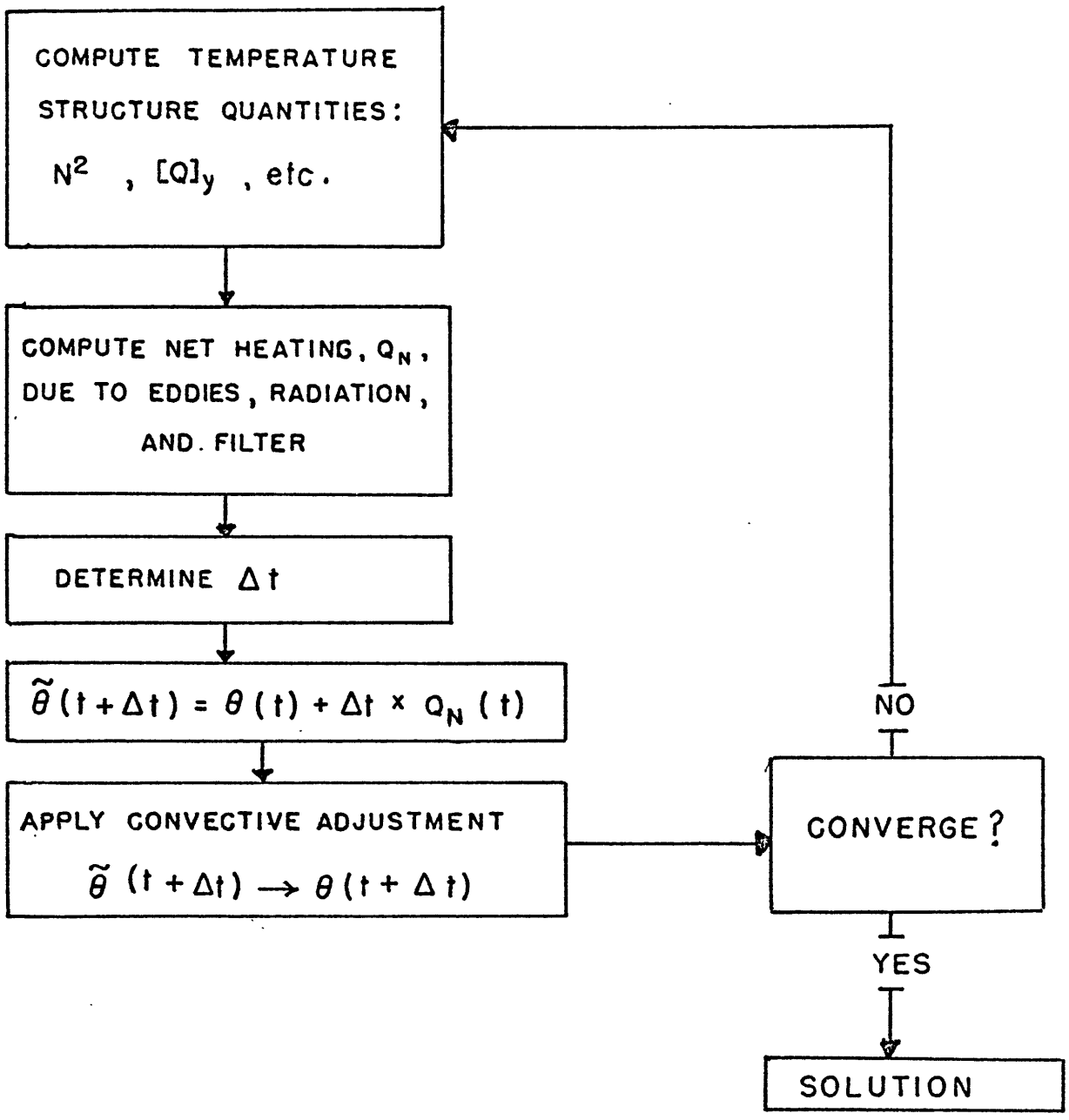


Fig. 3.8 - A flow chart of the model's integration procedure.

Δt, the model steps forward, adding to the temperature structure $\theta(z)$ the temperature change $\Delta t \cdot Q_N(z)$. Finally, the model applies the convective adjustment, completing the process.

The model assumes convergence when the rate of temperature change over one time step is less than 10^{-3} K day^{-1} at all levels. Subsequent discussion refers to the convergent state as the model solution for the particular set of input parameters. Occasionally, the model appears to converge toward a steady state, but the rate of temperature change does not become small enough to satisfy the convergence criterion. This may occur, for example, if there are small oscillations in temperature at some levels. In this case, the model considers the solution to be a time mean over the last 30 days of integration time. For time-averaged solutions, the standard deviation of temperatures about their mean at each level is typically very small, much less than a degree.

The possiblity exists that the model does not reach convergence because of a relatively slow but persistent process, such as radiative damping or some dynamic adjustment. If this process is to be significant in the model's simulation of the atmosphere, then the slow process should produce standard deviations in the temperature profile on the order of a degree or larger over the 30 day averaging period. Smaller deviations imply such a small change due to the process that other processes not modeled, most notably the seasonal cycle of radiation, probably produce larger changes in the atmosphere. Thus, a slow process may not have much significance in the model anyway. The longest explicit time scale in the model is the damping time for the Newtonian part of the radiation parameterization. Non-convergent model runs which might display a slow damping due to this radiative effect have not appeared.

A slow process might also reveal itself if two model runs with the same set of input parameters but different initial conditions produce different solutions. In this case, each solution satisfies the convergence criterion, but only one, or perhaps neither, truly represents a balance among the different flux convergences. Further adjustment by the slow process might be necessary before the model reaches a true balance. The existence of multiple nearly-balanced states would be interesting, but model runs have not produced them.

The forward differencing procedure is rather crude compared to more sophisticated methods which use the integration run's recent history, such as various forms of the leapfrog method. However, a variable time step appears to be necessary for the model to integrate smoothly to an equilibrium and the forward differencing procedure incorporates this more readily than other schemes. The more sophisticated methods may require elaborate bookkeeping in order to use a variable time step, especially if the computation of the time-averaged statistics is necessary. Since the model runs smoothly using the relatively simple procedure of forward differencing with variable time step, there does not seem to be any compelling reason to use more complicated techniques.

CHAPTER IV

MODEL RESULTS: COMPARISON WITH OBSERVATIONS AND OTHER MODELS

Some degree of correspondence between the model solutions and the atmosphere is desirable if the vertical balance model is to provide insight into the physics of the atmosphere. This chapter compares the results from vertical balance model runs using winter or summer conditions with results from observational and numerical model studies. Unless stated otherwise, the model runs presented here use a specified eddy amplitude, guided by the observed eddy kinetic energy for the apporpriate season (Table 3.1). Specified quantities such as the zonal mean wind, radiative heating, and the surface temperature have values suggested by observations or computations for the appropriate season at 45°N.

Some of the model results discussed in this chapter are from solutions produced by ensembles of waves, but the most extensive discussion is of solutions produced by a single mode, for reasons the discussion will make apparent. We can consider the single mode to represent the net effect of all eddies, though the most appropriate wavelength to use is not always evident. Stone (1972) and Branscome (1980) assume that the most unstable mode is the representative wavelength in the parameterizations they develop for their simple global heat balance models. Mullan (1979) and Branscome (1980) also use these parameterizations in zonally symmetric numerical models. All the models reproduce features of the zonal mean circulation governed by heat transports, supporting the use of a single wave parameterization using

the most unstable mode. Held and Suarez (1978) have similar success using a single eddy in their numerical climate model, although they specify a particular wave number for their model runs, the wave not necessarily being the most unstable mode.

Some type of selection criterion for choosing the most relevant single wave, if such a wave exists, is desirable. Having such a criterion would allow the vertical balance model to be used under a variety of climatic conditions. Such a selection criterion is not necessary for the work presented here. Instead, the comparison with observations and other models, the consistency check, permits an evaluation of different possible selection criteria. Neither of the two selection criteria considered here chooses a particular mode before performing model runs. Rather, each provides a means of selecting the most relevant single mode solution from a set of solutions using a variety of wave numbers.

The rationale behind using the most unstable mode is that, for random perturbations of equal magnitude, we might expect the mode with the largest linear growth rate to eventually become the dominant eddy at finite amplitude. Eddy flux scales and structures given by the most unstable mode then would govern interactions between the eddies and zonal mean flow. If the peak in the growth rate spectrum is fairly flat, some band of wavelengths centered about the peak may be important. However, for simple zonal mean states at least, the vertical structure of the eddy fluxes varies relatively slowly about the growth rate peak (e.g., Branscome, 1983), so that the most unstable mode remains representative.

One potential difficulty with using the most unstable mode is that, while eddy structures may vary slowly about a growth rate maximum, there may not be a single most unstable mode and the wave structure may vary significantly from one growth rate peak to another. A relatively simple f-plane model with two layers of different static stability studied by Blumen (1979) can yield two peaks in the growth rate spectrum. The difference in eddy structure between the two growth rate peaks in Blumen's model is considerable. At the long wavelength peak, the eddy fills the depth of the fluid, in contrast to the short wavelength peak, where the eddy is confined to the layer with lower static stability. In Blumen's model, the zonal mean state where the two maxima have equal growth rates is very special. For more complicated temperature structures, though, there may be multiple peaks and the determination of a single most unstable mode may not be feasible.

Perhaps a more important potential difficulty is that the most unstable mode in the linear problem may not be the one which ultimately reaches the largest amplitude and has the greatest impact on the zonal mean state. In Gall's (1976b) GCM study of baroclinic instability and wave-mean flow interaction, the linear instability computation for his initial state yields maximum growth rates at about zonal wave number 13. Yet when he allows individual waves to interact with the zonal mean flow, the short modes (zonal wave number $\geq$ 9) stabilize themselves relatively quickly compared to the longer modes, so that the waves which reach the largest amplitude and are therefore able to cause the greatest change of the zonal mean flow are the longer, slower growing waves. Pedlosky (1981) finds the same behavior for a weakly unstable ensemble of waves: except for the special case where only one wave is initially

unstable, the wave capable of reaching the largest amplitude is always larger than the linearly most unstable mode of the initial state.

In the single mode runs, the model finds a balanced state for a specified wave number, so that it generally does not use the most unstable mode when computing the eddy heat flux. The following procedure, however, permits us to obtain a solution defined to be the most unstable mode run. After the model finds a solution, it computes the growth rate spectrum for that temperature structure. The most unstable mode run is defined to be the one for which the growth rate peaks at the same wave number as that specified for the model's run. One can review the growth rate spectra for solutions produced by different wave numbers and, usually, select the most unstable mode solution.

An additional stipulation is sometimes necessary if more than one growth rate peak appears in the spectrum. As in Blumen's (1979) study, relatively shallow, short wavelength modes may have higher growth rates than longer, deeper modes do. Gall's (1976b) wave-mean flow interaction study shows that shallow, fast-growing modes do not grow as large in amplitude as deeper modes. Thus, despite having large growth rates, the shallow modes probably have a relatively small influence on the zonal mean state and are not as important as the deeper modes in determining the vertical temperature structure. The procedure to determine the most unstable mode uses only those modes in the solution's growth rate spectrum which are deeper than a minimum depth, the minimum depth being the smaller of ten kilometers or one half the depth of the solution's troposphere. In the model, a mode's depth is the lowest level above the flux maximum where the upward flux is smaller than 10^{-2} W/m^2, the level

z_c defined in Chapter III, Section 2. When the model finds solutions for the short, potentially more unstable modes, they do behave as expected. They produce relatively weak eddy heat fluxes and they play only a relatively small role in the heating balance that determines the vertical temperature structure.

The model uses a discrete wave number spectrum determined by the wavelengths that will fit on a latitude circle at 45°N, so that solutions for two adjacent wavelengths in the spectrum may have the most unstable mode for each wavelength's solution being the other wave number. This may occur, for example, because the two wave numbers are on opposite sides of the growth rate peak that would occur for a continuous spectrum. There are differences in the solutions produced by each wave number, but since both wave numbers are associated with the same growth rate peak, there are no gross differences in their solutions or the associated heat fluxes. We might consider the solution to be some mean of the two, though either is representative.

Pedlosky's (1981) work suggests another possible selection criterion. In his study, the mode which can attain the largest amplitude is also the one which can cause the largest decrease in the size of the zonal mean zonal wind shear, $[U]_z$, in the middle latitudes of his model. The reduction of $[U]_z$ occurs because the wave alters the zonal mean flow so that the rate at which it draws energy from the zonal mean flow balances the rate at which is loses energy by dissipation: the wave alters the zonal mean flow so that the wave is less unstable. Pedlosky does not compute growth rate spectra for the equilibrated states produced by individual waves, but a reasonable hypothesis appears to be that the most relevant single mode in his model

is the one whose equilibrated state has the smallest growth rate maximum, since it has the smallest $[U]_z$. Thus, we can consider the most appropriate single mode in the vertical balance model to be the one whose solution has the lowest peak in its growth rate spectrum. Since growth rate tends to decrease as the Brunt-Vaisalla frequency, N^2, increases, we might expect that the mode chosen by this criterion would also tend to produce the warmest troposphere. However, growth rates may depend strongly upon the details of the Brunt-Vaisalla frequency's height dependence: a correspondence between a warmer troposphere and slower growth rates is not necessary. Also, the dependence of growth rates on the details of $N^2(z)$ means that a criterion based on the smallest growth rate rather than on $N^2(z)$ should be simpler to apply. The maximum growth rate is a global property of a solution and is perhaps a more complete measure of a single mode's influence upon the model's temperature structure than, say, the value of N^2 at some level or the mean of N^2 over some depth. Solutions selected by the smallest peak growth rate criterion are termed most stabilizing solutions. As with the determination of the most unstable mode solution, only the modes in a solution's growth rate spectrum deeper than a minimum depth are considered when determining the most stabilizing mode solution, the minimum depth again being the smaller of ten kilometers or one half the depth of the solution's troposphere.

Despite the different motivations for each selection criterion, the discussion of model solutions will show that the two tend to select nearly the same wave number as the most relevant single mode. Solutions selected by both criteria are called most relevant mode solutions.

The remainder of the chapter is divided into three parts. The first section compares model solutions using winter conditions with winter observations. The second section has a similar comparison, but between summer conditions solutions and summer observations. The comparisons reveal the model's strengths and weaknesses, while also providing insight into the size and distribution of the eddy fluxes. Finally, a third section gives the results of some simple sensitivity tests, which demonstrate the strength of the feedback between the eddy flux and the temperature structure.

1. Winter conditions solutions.

The vertical balance model's solutions for winter conditions almost always fall into one of two categories. A way of distinguishing the two is that solutions in one category, termed strong eddy solutions, always have a local maximum in the $N^2(z)$ profile between the surface and 5 km (Figure 4.1a); solutions in the other category, termed weak eddy solutions, do not (Figure 4.1b). This simple morphological distinction is indicative of the degree to which eddy fluxes regulate the vertical temperature structure of the lower atmosphere. The discussion below will show that for strong eddy solutions, the vertical eddy flux heating plays a dominant role in determining the vertical temperature structure of the lower atmosphere. The heat flux balance for these solutions is primarily between radiation and the vertical eddy flux, a radiative-dynamic equilibrium (RDE). For weak eddy solutions, the eddy flux heating is relatively weak and the vertical temperature structure is similar to that produced by a balance between radiation and convection

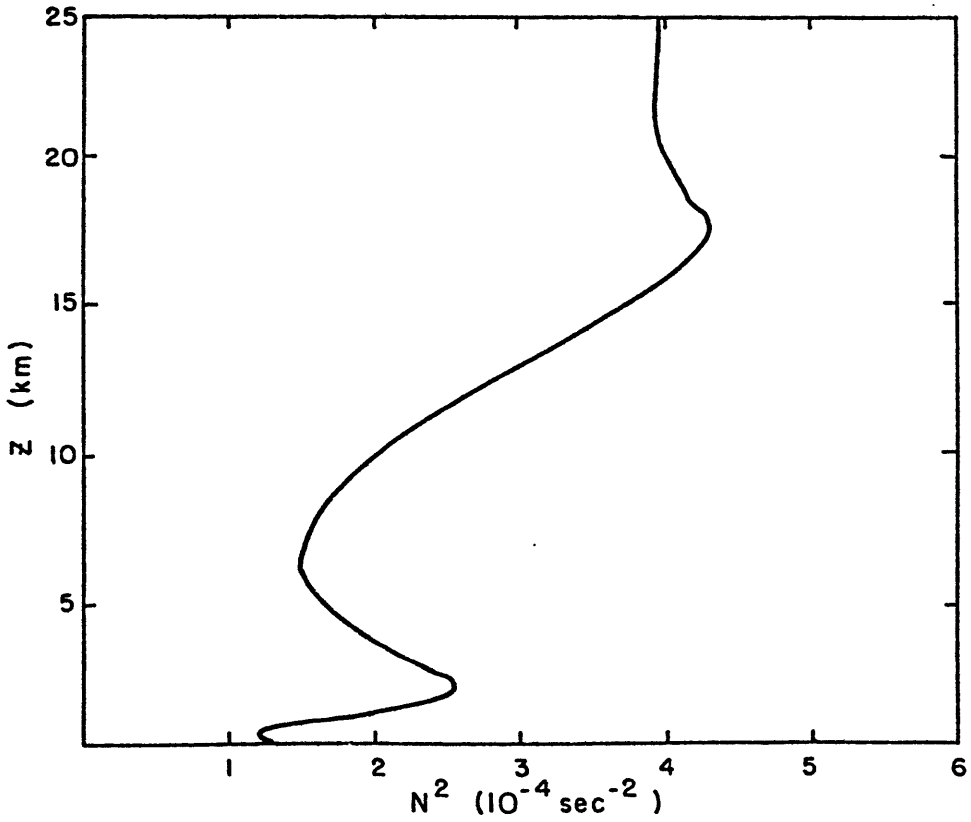


Fig. 4.1a - Typical $N^2(z)$ for a strong eddy solution.

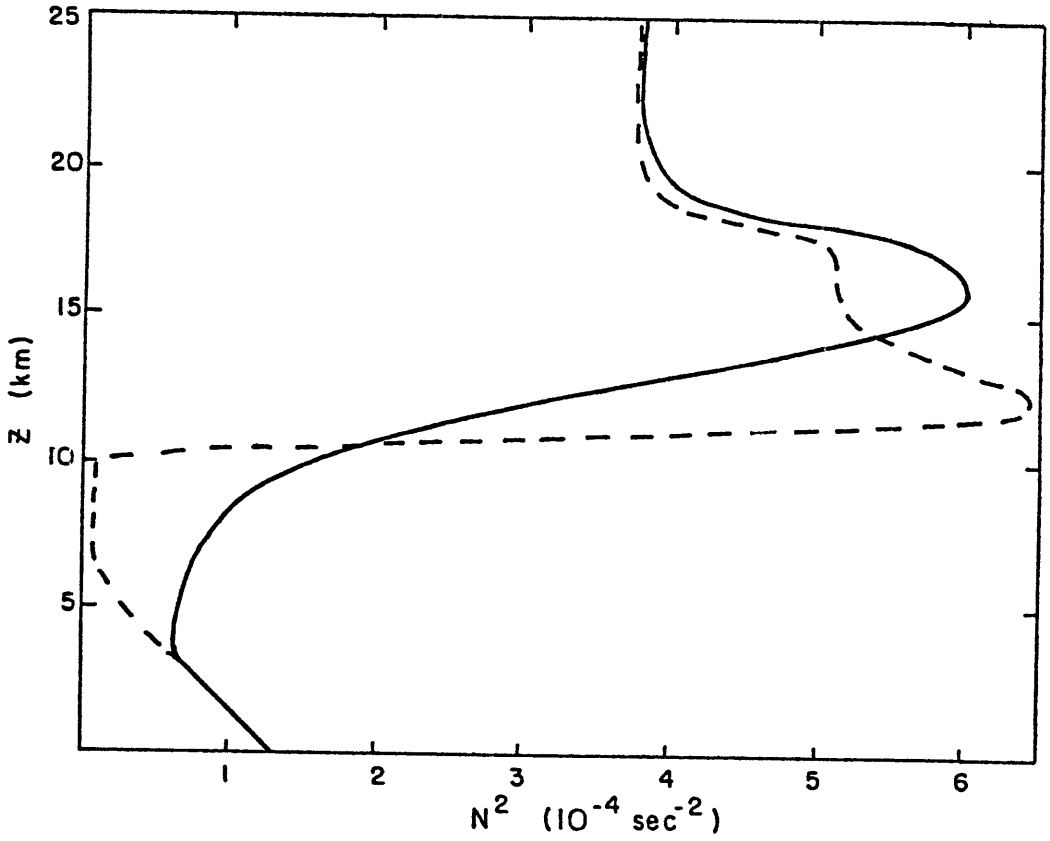


Fig. 4.1b - Typical $N^2(z)$ for a weak eddy solution (solid) and $N^2(z)$ for RCE (dashed).

with no eddy flux, a radiative-convective equilibrium (RCE). The similarity with the RCE temperature structure does not mean that the weak eddy solutions have only a negligible eddy flux heating. The example shown in Figure 4.1b still has a RDE balance between 3.5 and 10 km, and the temperatures in this layer are warmer than those given by the RCE solution. The interesting feature of this division is that for a wide range of input parameters, all solutions with sufficiently strong eddy flux always display the characteristics shown in Figure 4.1a: a local maximum near 3 km and a local minimum near 7 km. The discussion in this chapter and the one following will show that these characteristics are indicative of the manner in which eddies interact with the zonal mean flow through the vertical eddy heat flux.

The two procedures for choosing the most relevant single mode tend to select the same wave number. Table 4.1 lists the wave number of the most unstable mode solution and of the most stabilizing mode solution for model runs using a variety of parameter choices under both closure assumptions. The table also shows whether the solution is a strong eddy solution, a weak eddy solution, or a transition solution between the two. The 1 E_w and 1 $[U]_z$ values are the EKE and zonal wind shear, respectively, for winter given in Chapter III. For the 1.5 $([U]_z)_w$ specified EKE solutions, the $n_z = 4$ solution's growth rate spectrum gives wave number 3 as the most unstable mode, and the $n_z = 3$ solution's growth rate spectrum gives wave number 4 as the most unstable mode. For the specified EKE solutions, the most unstable mode solution and the most stabilizing mode solution are the same over the range of parameter changes considered. For the EKE ≈ ZAPE closure, the two selection procedures select nearly the same wave numbers for strong eddy

Table 4.1 - Wave numbers providing the most unstable mode solution (MUM) and the most stabilizing mode solution (MSM) for different choices of EKE and $[U]_z$ in the vertical balance model. The table also shows whether the solution is a strong eddy solution (SE) or a weak eddy solution (WE).

Specified EKE closure:

	MUM	(type)	MSM	(type)
0.5 $[U]_z$	7	WE	7	WE
0.5 E_w	6	WE	6	WE
1 E_w, 1 $[U]_z$	4	WE/SE	4	WE/SE
1.5 $[U]_z$	3↔4	WE/SE↔SE	4	SE
1.5 E_w	4	SE	4	SE

EKE ≈ ZAPE closure:

	MUM	(type)	MSM	(type)
0.5 $[U]_z$	11	WE	5	WE
1.0 $[U]_z$	7	WE	4	WE
1.5 $[U]_z$	3	SE	3	SE
2.0 $[U]_z$	2	SE	3	SE

solutions, but they select very different wave numbers for weak eddy solutions, with the most stabilizing mode solution using a longer wavelength than the most unstable mode solution. Thus, when the eddy flux plays a dominant role in determining the temperature structure in the lower atmosphere, the two selection criteria choose the same or nearly the same wave number.

Figure 4.2 compares the observed wintertime [T](z) with solutions for three different choices of eddy amplitude. The observed temperature profile is taken from Oort and Rasmusson (1971). The EKE ranges from 1 to 2 times the observed EKE, and in each case, zonal wave number 4 gives both the most unstable mode solution and the most stabilizing mode solution: both selection criteria choose wave number 4 as the most

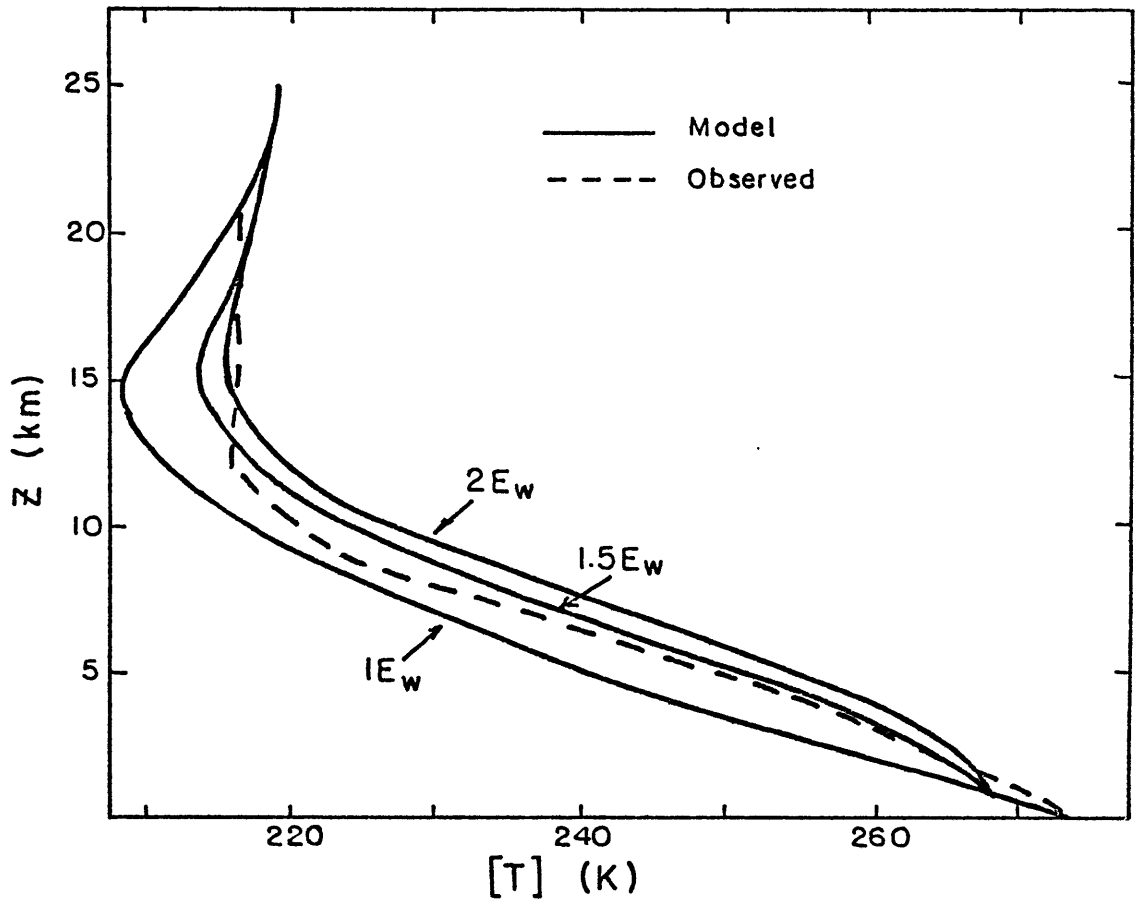


Fig. 4.2 - Winter [T](z) from observations and from three most relevant mode solutions. The labels on the curves refer to the size of the specified EKE.

relevant single mode. The temperature profile for the 1.5 E_w model run compares most favorably with the observed [T](z), but each of the profiles agreees fairly well with the observed profile in this figure. That the specified EKE values giving [T](z) profiles like the observed [T](z) are about the same size as the observed EKE and not orders of magnitude different is encouraging.

The agreement between the most relevant single wave computation and the observations indicates that a single eddy can represent the heat transport of all eddies combined. Figure 4.3 illustrates the effectiveness of the most relevant single wave in simulating the atmosphere compared to other wavelengths. This figure shows solutions for different wave numbers using a 1.5 E_w amplitude, since this gives the best comparison with the observed [T](z) for the most relevant mode. Model runs using wave number 1 or 2 do not produce solutions in which the specified wave is unstable; the model produces RCE solutions when using either of these wave numbers. The results for n_z = 1 or 2 could be because the model's grid is not deep enough to adequately resolve either of these waves, but even when the model uses grids up to 69 km deep, these waves remain stable.

As wave number increases or decreases away from n_z = 4, the growth rate at equilibrium of the specified wave and the vertical heat flux both decrease, which causes a decrease in temperature below 10 km. Above 10 km, the wave number 3 solution is warmer than the most unstable mode solution. This occurs because baroclinically unstable modes tend to become progressively deeper as wave number decreases. Wave number 3 thus transports more heat to the levels above 10 km than wave number 4 does, producing warmer temperatures. Note also that the level of

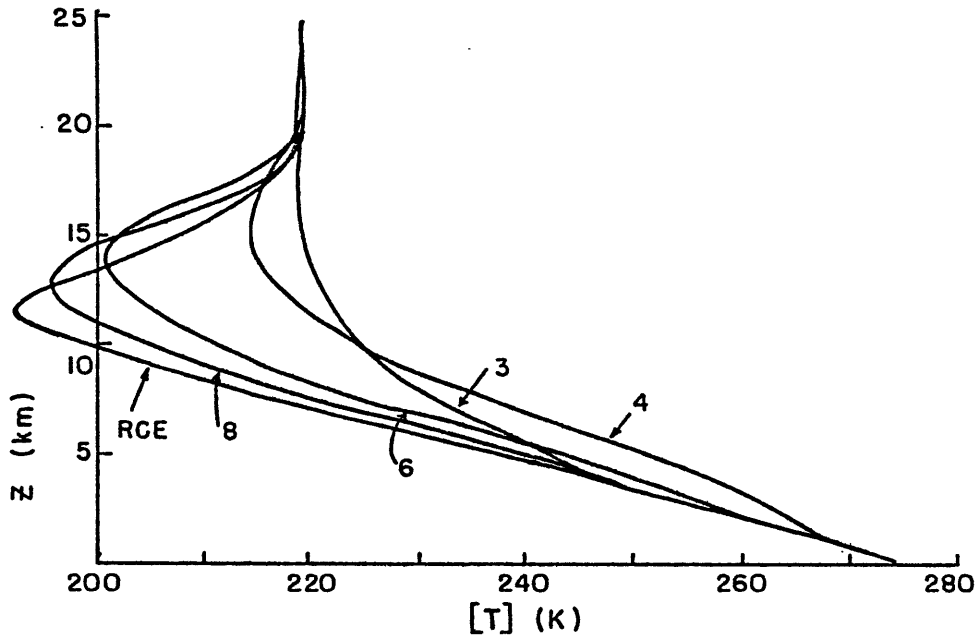


Fig. 4.3 - [T](z) from 1.5 E_w single mode solutions using different wave numbers and from the RCE solution. The number identifying a curve refers to the zonal wave number used to compute the particular solution.

minimum temperature for the solutions in Figure 4.3 becomes higher as wave number decreases, again due to the increase in eddy depth as wave number decreases.

Solutions produced by shorter waves than the most relevant mode could have temperatures just as warm as those for the most relevant mode solution, but the shorter waves would need a specified amplitude larger than the most relevant mode's amplitude. Since shorter wavelength eddies tend to be shallower and less unstable, the increase in amplitude that would allow their solutions to be as warm as the most relevant mode's at all levels could be quite substantial. The amplitude necessary for the most relevant mode to produce a [T](z) as warm as the observed [T](z) is smaller than the amplitude necessary for any other mode to produce a [T](z) as warm. The most relevant mode thus makes the most efficient use of the specified amplitude.

In Figure 4.3, the lapse rate varies more between solutions than the tropopause height z_T does. The Meteorological Glossary (McIntosh, 1972) defines the tropopause as "the lowest level at which the lapse rate decreases to 2 degC/km or less,..." The model does not compute the lapse rate in the course of its calculations, but it does compute $N^2(z)$. Therefore, the vertical balance model uses as a definition of the tropopause the level above 5 km where N^2 equals $3.5 \cdot 10^{-4}$ sec^{-2}. Usually, though not always, this is the lowest level where N^2 equals the tropopause value. In practice, for computations requiring the tropopause level, the model uses data from the grid level immediately below the tropopause. The temperature in the vicinity of the model's tropopause is usually about 200 K, so that at the tropopause $\frac{\partial \theta}{\partial z} \approx 7$ K/km and $-\frac{\partial T}{\partial z} \approx \frac{g}{C_p} - \frac{\partial \theta}{\partial z} \approx 3$ K/km, which means that the model's

definition is equivalent to the definition in the Meteorological Glossary. In Figure 4.3, as wave number increases, the lapse rate increases, changing from 4.9 K/km for wave number 4 to 6.8 K/km for wave number 8, a 40 % increase. The tropopause height, on the other hand, decreases from 14 km for wave number 4 to 12.5 km for wave number 8, a decrease of 10%, which is smaller than the change in lapse rate. The profiles in this figure thus support Held's (1982) contention that radiation determines the tropopause, as a first approximation, with eddies adjusting the lapse rate so that dynamic transports can span the depth of the troposphere. Later discussion, however, will show that his contention does not apply universally and is valid only for a range of eddy flux strengths.

Figure 4.3 also displays the RCE solution. As the flux decreases, the RDE solution approaches the RCE solution. The region of greatest temperature change as wave number increases occurs between 10 and 15 km. This occurs for two reasons. First, the eddy heating in this layer decreases substantially as wave number increases, because the specified eddy's flux becomes both weaker and shallower. Second, the radiative damping time in the Newtonian damping term increases, since the vertical wavelength of $(T_{Do} - [T])$ increases. As τ_R increases, any imbalance between eddy flux heating and Q_{Do}, the specified radiative cooling, requires a larger temperature difference for the Newtonian term to match the imbalance. For $n_z = 4$, $\tau_R = 23$ days, while for $n_z = 8$, $\tau_R = 54$ days, so that if an imbalance between the eddy heating and the radiative cooling from Q_{Do} exists at some level, the wave number 8 model run needs $(T_{Do} - [T])$ to be twice as big as the wave number 4 run for the Newtonian term to supply the necessary heating.

The profile of [T](z) for the RCE solutions indicates why changes in the model's lapse rate result in relatively small changes in the tropopause height. As a first approximation, the tropopause height is the level between 13 and 18 km where the [T](z) profile for a given lapse rate intersects the RCE [T](z) curve. For the RCE solution, there is a local minimum in the temperature profile at 12 km and [T](z) increases relatively rapidly with height above the minimum, so that the tropopause height increases much less when the lapse rate decreases than if there had been no local minimum in the RCE [T](z) profile.

The interaction between the eddy flux and the temperature structure depends more strongly upon the variation of temperature with height than upon [T] itself, since the computation of the model's eddy flux depends much more upon $N^2(z)$ than [T](z). Thus, a more dynamically relevant comparison is between the atmosphere's and the model's Brunt-Vaisalla frequency profiles. Figure 4.4 shows these profiles, where the model results are the $N^2(z)$ for the three solutions in Figure 4.2. The 1.5 E_w and 2 E_w solutions are strong eddy solutions, while the 1 E_w solution is a borderline case between the two categories shown in Figure 4.1. For a large enough eddy amplitude, the model's N^2 varies with height like the observed N^2. From a local maximum near the surface, N^2 decreases with height to a minimum at about 7 km and then increases with height up to about 15 km, where it becomes relatively constant. For later reference, note that the maximum near the ground becomes stronger with increasing eddy amplitude. The variation of the solutions between eddy amplitudes suggests that with some tuning, the model could reproduce the observed $N^2(z)$ almost exactly below 5 km. Above 5 km, there is little variation in the N^2 profiles with eddy

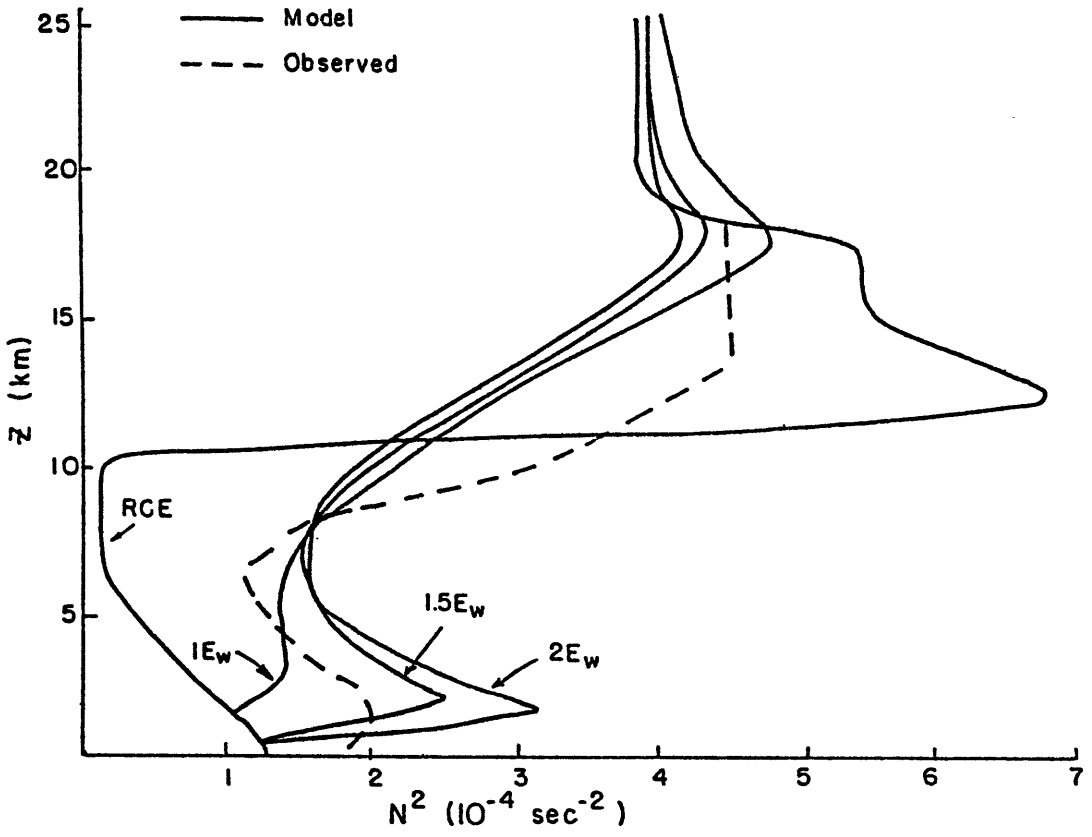


Fig. 4.4 - $N^2(z)$ for the temperature profiles in Figure 4.2. Again, the labels on the curves refer to the size of the specified EKE used to compute model solutions.

amplitude. The model's Brunt-Vaisalla frequency tends to be smaller than the observed N^2 above 5 km, but not greatly so. Since the model has only vertical heat fluxes, the similarity of the model's solutions with observations lends support to Hantel's (1976) conclusion that the primary balance in the time and zonal mean thermodynamic equation is among vertical heat fluxes.

A comparison of the RCE $N^2(z)$ profile in Figure 4.4 with the other model profiles shows that moist convection plays only a relatively small role in determining the structure directly. The depth of convective adjustment for each solution in Fig. 4.4 can be discerned from the depth of the layer extending from the surface where $N^2(z)$ has a nearly linear dependence on height z. This $N^2(z)$ height variation results from the adjustment of [T](z) to a moist adiabat. The convective flux goes no higher than 5 km in the RCE solution, but it is confined to even lower levels for the other model solutions, most especially for the strong eddy solutions. Although the convective adjustment is confined to a shallow layer in the RDE solutions, the convective adjustment's association with a fixed surface temperature does have important consequences, which discussion in the next chapter elucidates.

If the specified EKE is 0.5 E_w or less, each wave number produces a weak eddy solution. As the EKE is increased, each wave number eventually produces a strong eddy solution. The value of the EKE where the transition occurs varies with wavelength: the shorter the wavelength, the smaller the EKE necessary for a strong eddy solution. For $n_z = 6$, a 1 E_w amplitude is sufficient, while for $n_z = 3$, the 1.5 E_w amplitude is still too small for the wave to produce a strong eddy solution. The wave number dependence for the minimum EKE necessary

to produce a strong eddy solution appears to be the result of the variation of eddy flux depth with wave number. Shorter wavelengths tend to have a shallower eddy flux. For a given flux amplitude then, a shorter wave will tend to have stronger heating a kilometer or so above the flux maximum than a longer wave will have, since the shorter wave's flux will decrease more rapidly with height above the flux maximum than a longer wave's will. The model's eddy flux heating below 5 km apparently must be stronger than some threshold value for the specified wave to produce a strong eddy solution. Shallower waves will produce the necessary heating for a smaller flux amplitude than that required by deep waves to exceed the threshold. The 1.5 E_w $n_z = 3$ solution is an extreme example of how eddy flux heating is still important in the upper troposphere of weak eddy solutions. Despite this solution's classification based upon its $N^2(z)$ profile, this solution is actually warmer above 10 km than the $n_z = 4$ solution using the same specified EKE (Figure 4.3).

Vertical balance model runs using an ensemble of waves give only weak eddy solutions for the range of EKE values used to produce the single mode solutions in Figure 4.4. Figure 4.5 gives a representative example, showing $N^2(z)$ for a wave ensemble run where EKE = $1.5E_w$, comparing it with the observed profile. Being a weak eddy solution, the wave ensemble solution in Figure 4.5 has Brunt-Vaisalla frequencies that are too small compared to the observed Brunt-Vaisalla frequencies, but the solution's N^2 values above 7 km match the observed N^2 well, better than the most relevant mode solutions in Figure 4.4. This close match occurs for a variety of parameter choices in the winter wave ensemble solutions. Comparison of the $n_z = 3$ and $n_z = 4$ solutions in Figure

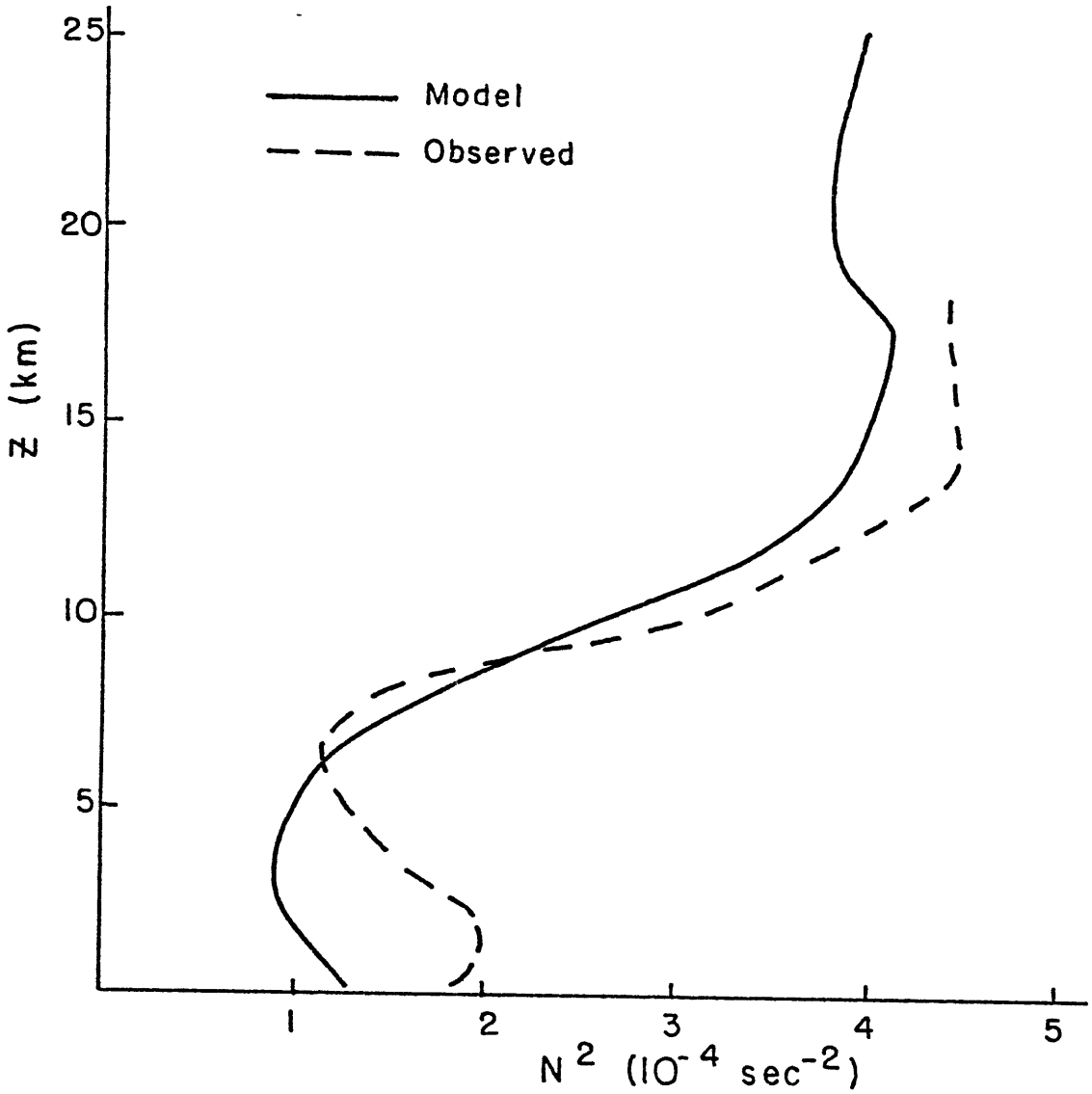


Fig. 4.5 - $N^2(z)$ for the winter conditions wave ensemble solution using a 1.5 E_w eddy kinetic energy.

4.3 suggests that heat fluxes from modes longer than the most unstable mode are necessary to give $N^2(z)$ values as strong as the observed values between 8 and 15 km. For the $n_z = 3$ solution, the Brunt-Vaisalla frequencies are actually stronger than observed between 8 and 15 km. The wave ensemble model runs have enough of the upward flux carried by deep waves to produce $N^2(z)$ profiles matching the observed profile.

Even though N^2 changes by 50% through the troposphere for each profile in Figure 4.4, each [T](z) profile in Figure 4.2 has a nearly linear dependence on height z. The model's combination of processes, with the eddies playing a prominent role, prevents the temperature profile from varying with height in a more complicated manner than a roughly linear decrease with height in the troposphere. An extreme example is shown in Figure 4.6, which compares [T](z) solutions for model runs using $n_z = 4$ and either a 1.5 E_w or 6 E_w amplitude. For the larger amplitude solution, there is a strong inversion near the ground, but between 4 and 15 km, the lapse rate is nearly constant. Despite the large increase in eddy amplitude and the accompanying warming of the atmosphere, the 6 E_w solution's lapse rate in the middle troposphere is not very different from the 1.5 E_w solution's. Between 5 and 10 km, the former has a lapse rate of 5.8 K/km, while the latter's is 5.2 K/km, a difference of about 12%. The relative constancy of the lapse rate here compared to the lapse rate changes in Figure 4.2 results from the influence of baroclinic adjustment on the equilibrium temperature profile in the strong eddy solutions, an effect discussed in detail in the next chapter. The tropopause height changes by about the same amount as the lapse rate, increasing by 14% when the EKE increases from 1.5 E_w to 6 E_w. The constancy of the lapse rate in the upper

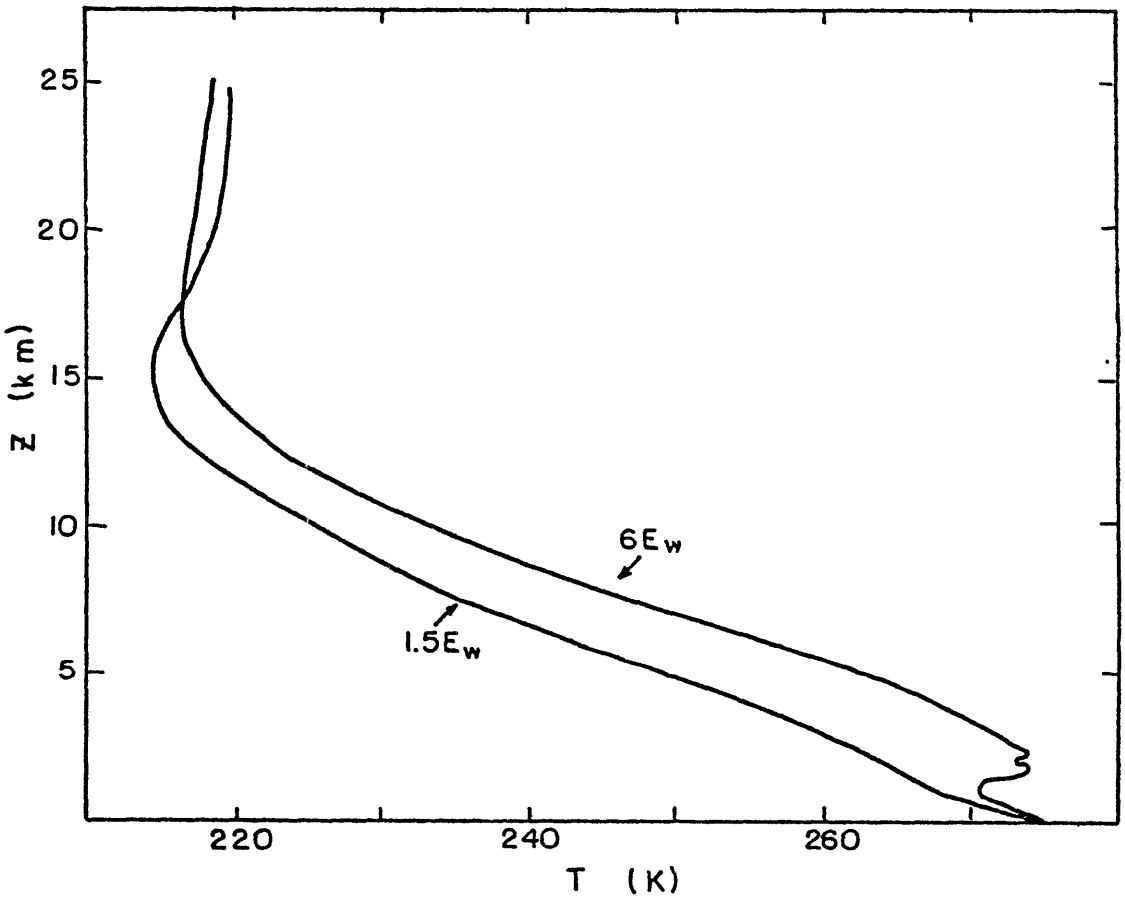


Fig. 4.6 - [T](z) for two single mode solutions, using the specified EKE indicated on the curve. Each solution uses $n_z = 4$.

troposphere indicates that relatively strong eddies do not alter the lapse rate so that the depth of their fluxes is about the same as a nearly constant tropopause height determined by radiation. As noted earlier, Held (1982) conjectures that the eddies do alter the lapse rate relative to a nearly constant tropopause height. The results presented here suggest that his conjecture applies only when the eddy fluxes are not strong enough to produce a temperature inversion near the surface.

One might assume that a nearly linear decrease of temperature with height in the troposphere implies a roughly constant $N^2(z)$ there. In reality, the observed $N^2(z)$ varies considerably in the troposphere. The discussion in Chapter II shows that this variation with height may indicate how baroclinically unstable atmospheric eddies act to reduce the instability of the zonal mean flow. Thus, the analysis of $[T](z)$ may not reveal important aspects of wave-mean flow interaction as fully, if at all, as an analysis of $N^2(z)$.

An important feature of the observed $N^2(z)$ profile is that it shows N^2 decreasing with height in the lower troposphere. The type of baroclinic adjustment analyzed in Chapter II suggests that the layer where $N^2(z)$ decreases with height occurs because eddy heat fluxes alter $N^2(z)$ so that $[Q]_y$ becomes relatively small there. Figure 4.7 shows the profiles of $[Q]_y(z)$ corresponding to the observed and modeled $N^2(z)$ appearing in Figure 4.4, along with the steering level in the model solutions. The calculation of the observed profile uses Oort and Rasmusson's (1971) temperature statistics and the thermal wind equation. H_ρ = 9 km for all calculations. Figure 4.7 also shows the constant value $[\tilde{Q}]_y$ that results if we compute $[Q]_y$ using the vertical mean N^2,

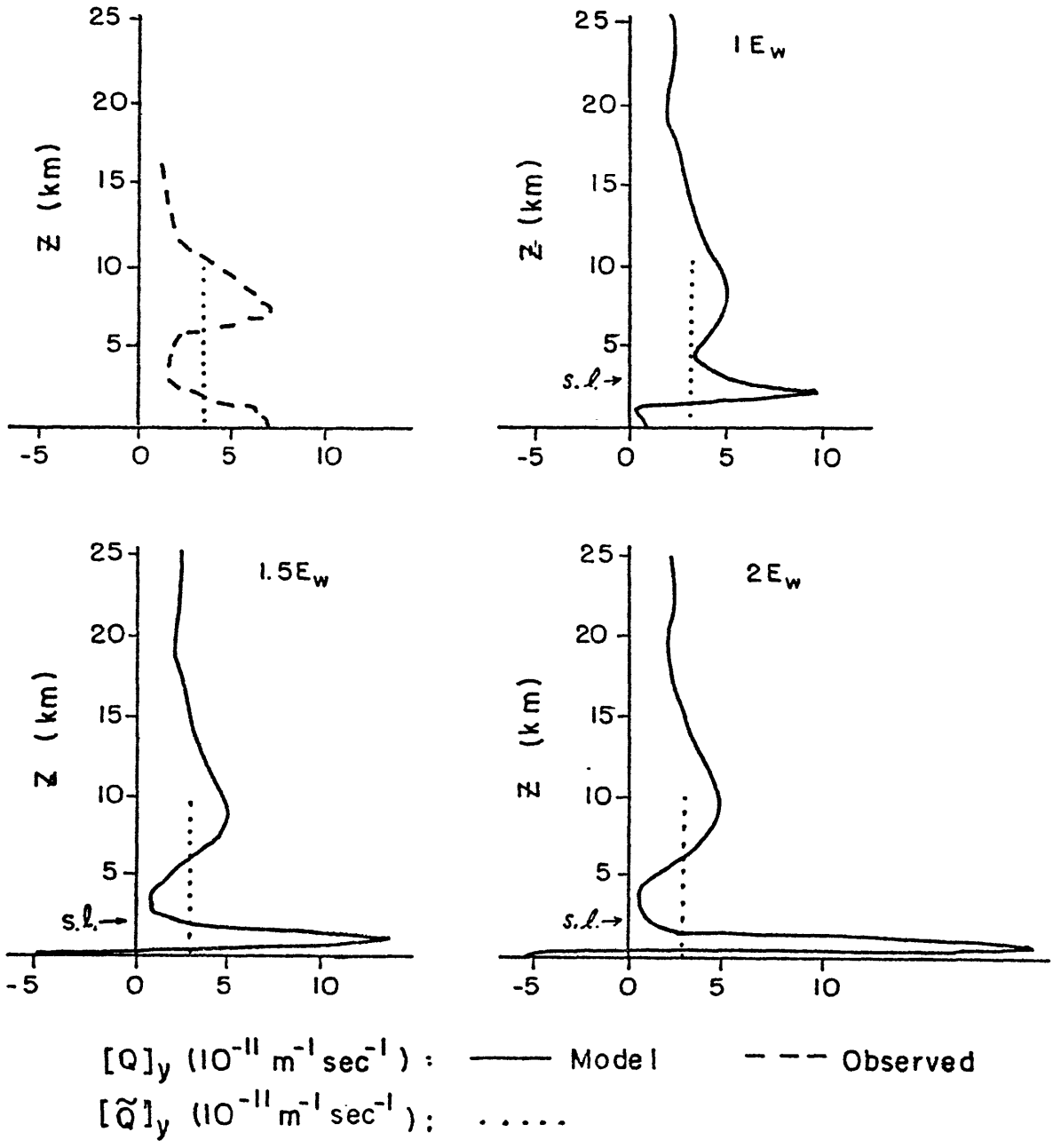


Fig. 4.7 - $[Q]_y(z)$ corresponding to the $N^2(z)$ profiles in Figure 4.2. The label for each model solution curve refers to the EKE used to compute the solution. Also shown are $[\tilde{Q}]_y$ for each profile and the steering level s.l. for each model solution.

$$\tilde{N}^2 = g \frac{([\theta](z_t) - [\theta](0))}{(z_t \cdot [\theta](z_t/2))} \quad , \tag{4.1.1}$$

where z_t is the tropopause height. Thus,

$$[\tilde{Q}]_y = \beta + \frac{f^2[U]_z}{\tilde{N}^2 H_\rho} \quad . \tag{4.1.2}$$

The general features of the observed $[Q]_y(z)$ profile and the single mode computation profiles are the same. There are two maxima, one near the ground and another at about 8 km. The maxima result from N^2 increasing with height. For the solutions, there is a layer of about 4 km depth between the maxima where $[Q]_y$ is less than $[\tilde{Q}]_y$. This region appears persistently for a variety of model parameter choices. The only requirement is that the particular set of input parameters produce a strong eddy solution. The next chapter discusses the appearance of the minimum in the $[Q]_y$ profile in more detail.

The discussion below of the vertical balance model's fluxes compares them with fluxes computed by four different methods. Hantel (1976) computes the total vertical flux by large-scale eddies and convection as a residual in a box model's heat balance equation, using observed and computed bluxes. He also provides the zonally-averaged surface fluxes of sensible and latent heats computed from Budyko's (1963) atlas. All fluxes from Hantel presented in this section are for the winter season, an average over December, January, and February. Tomatsu (1979), Chen et al. (1981) and Chen (1982) compute the net vertical eddy sensible heat flux using twice-daily NMC observations and the ω-equation. Schubert and Herman (1981) obtain the net vertical eddy sensible heat flux from a GCM assimilating observational data. The fluxes from these last four calculations are shown in Figure 1.4, along

with the data periods covered by each calculation. Finally, data averaged over five Januaries in a run of the Goddard Institute for Space Studies (GISS) Model II climate model (Hansen et al., 1983) provides all the fluxes above plus the convective heat flux and the eddy latent heat flux. An appealing feature of the GISS data is that all of the fluxes used in the comparisons here are available from one self-consistent computation. The flux comparisons thus include fluxes computed from a variety of sources, ranging from observations to numerical models. Unless noted otherwise, all fluxes from these sources are for 45°N, except for Hantel's atmospheric fluxes, which are from his mid-latitude box spanning 30°N - 49°N, and the GISS atmospheric fluxes, which are for 43°N. All vertical balance model fluxes in these comparisons are from the 1.5 E_w n_z = 4 solution.

Table 4.2 compares the surface heat flux for the 1.5 E_w n_z = 4 solution with the net surface heat flux in the GISS model and the net surface heat flux presented by Hantel derived from Budyko's atlas. The Budyko and the GISS values near 45°N are considerable smaller than the model's. However, the table also shows that the surface heat flux varies rapidly with latitude near 45°N, so that the difference may not be as large as implied by simply comparing fluxes at 45°N. The strong dependence of the surface heat flux upon latitude suggests that errors in measurement or differences in parameterization could greatly alter the size of computed flux for any of the three surface heat flux computations shown in the table. Climatological surface heat fluxes are not well-measured. For example, a comparison by Baumgartner and Reichel (1975) of different measurements of the surface latent heat flux shows differences ranging up to 100% at various points in the mid-latitudes.

Table 4.2 - Surface heat flux from Hantel, using on Budyko's data, from the GISS climate model, and from the vertical balance model's (VBM's) 1.5 E_w n_z = 4 solution. All fluxes are in W/m^2.

	Budyko	GISS	VBM	VBM (adjusted)
35°N	127	138		
45°N	76	82	134	123
55°N	44	60		

Based on the comparisons offered by Baumgartner and Reichel, the error in Budyko's mid-latitude surface heat fluxes is probably at least 25%. Lowering the specified EKE to obtain a closer match between the observed and the modeled $N^2(z)$ profiles in the lower atmosphere (Figure 4.4) would give a small reduction in the strength of the vertical balance model's surface heat flux and would thus lessen the difference between the strength of this flux and the strengths of the Budyko and the GISS fluxes. The 1 E_w most relevant mode solution, for example, has a surface heat flux of 119 W/m^2. Thus, although the Budyko and the GISS surface heat fluxes are much closer to each other than to the model's flux, the size of the model's flux is not inconsistent with the Budyko and the GISS fluxes.

Some adjustment in the model's surface heat flux is also possible which improves the comparison in Table 4.2. Figure 3.1 shows significant heating by horizontal flux convergences near the surface at 45°N. The model's convection parameterization implicitly includes this heating, but considers the heating to be part of the convective flux divergence. If the heating near the surface in Figure 3.1 is subtracted from the convective flux divergence, then the surface flux into the atmosphere, assumed by the model to be equal to the convective flux at

the surface, is smaller. Table 4.2 shows the adjusted heat flux for the model's solution.

Table 4.3 compares the vertical balance model's net heat flux by eddies and convection at 750 mb and 500 mb with the corresponding fluxes computed by Hantel and by the GISS climate model. There is a substantial difference between the GISS and the Hantel fluxes, but the vertical balance model's total heat flux is between the fluxes from the two at both levels. Thus, there is a consistency between the model's net flux and that from other sources, although there is a wide range of intensities at both levels in Table 4.3.

Figure 4.8 shows the eddy fluxes for the 1.5 E_w solution using wave number 4. For proper comparison with the fluxes from other sources, the fluxes plotted in Figure 4.8 are the sensible heat flux $(\frac{p}{p_0})^{\kappa}\{\rho C_p[w^*\theta^*]\}$, the latent heat flux $\Lambda(\frac{p}{p_0})^{\kappa}\{\rho C_p[w^*\theta^*]\}$, and their sum. The factor $(\frac{p}{p_0})^{\kappa}$ is necessary to convert from a flux of potential temperature to a flux of temperature. The sensible heat flux above is actually the vertical flux of sensible heat and potential energy. Oort and Rasmusson's (1971) data show that for standing eddies the vertical flux of sensible heat is much larger than the vertical flux of potential energy. The same relationship probably occurs for transient eddies, too, so that the first quantity is nearly the same as the vertical eddy sensible heat flux.

The latent heat flux in Figure 4.8 is much smaller than the sensible heat flux because the winter temperatures near the ground are relatively cool. The peaks of all three eddy fluxes occur near the surface, at 1 km. There is also a region of weak negative flux in the

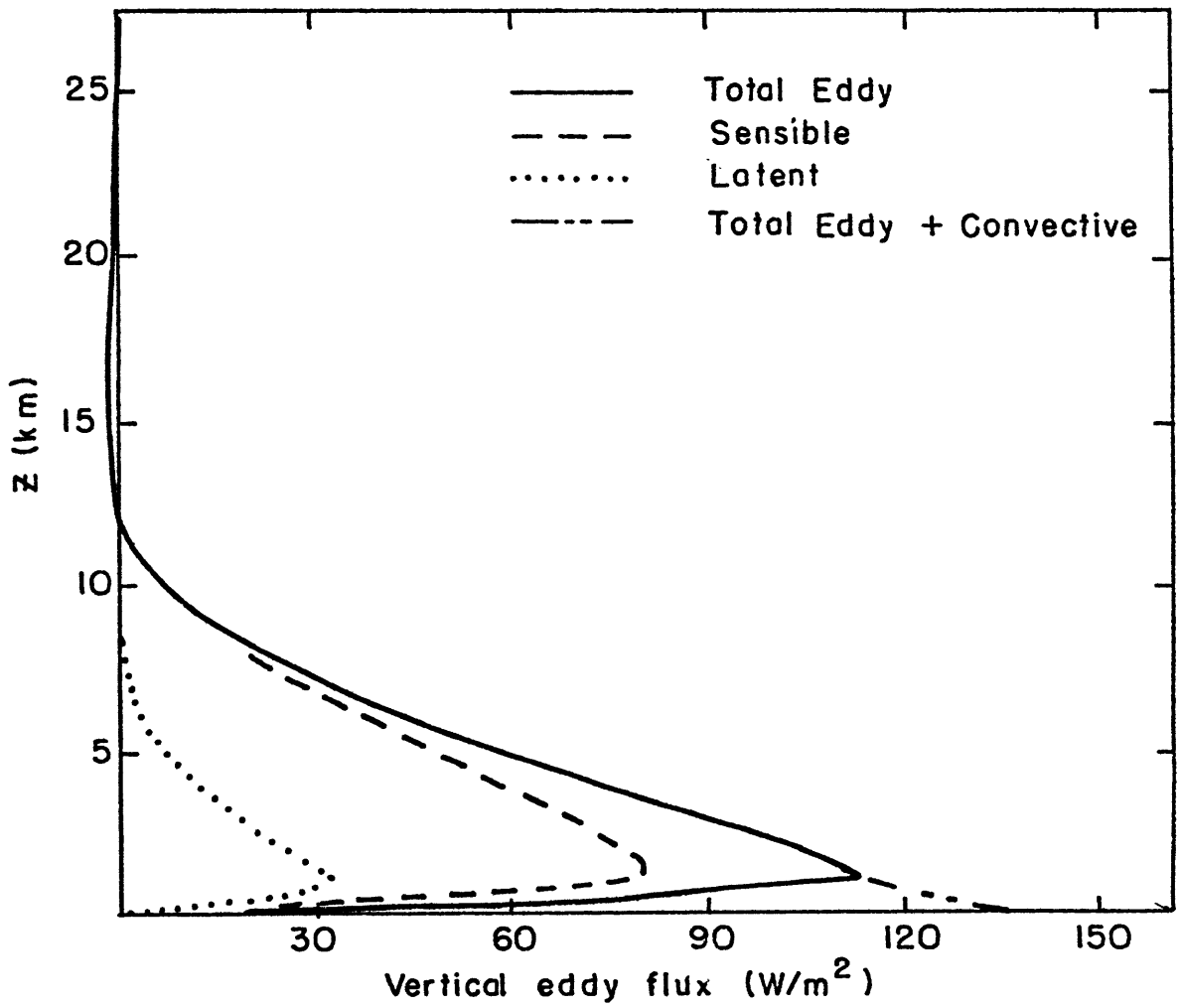


Fig. 4.8 - Vertical eddy fluxes of sensible heat, latent heat, and their sum and the sum of the eddy and convective fluxes, all for the 1.5 E_w n_z = 4 solution.

Table 4.3 - The net vertical heat flux (W/m^2) by eddies and convection, from computations by Hantel, the GISS climate model, and the vertical balance model (VBM).

	Hantel	GISS	VBM
500 mb	72	30	50
750 mb	103	68	97

model's upper levels. A similar height variation is discernible in Figure 1.4 for the eddy sensible heat fluxes computed by Chen et al. (1981), Schubert and Herman (1981), and Chen (1982). These analyses all show a peak vertical flux well below 500 mb and a weak negative flux above 200 mb. The negative flux occurs in the vicinity of the observed and modeled tropopauses, indicating perhaps that the increase in static stability at the tropopause causes a downward eddy flux of heat there. However, the Charney model has constant static stability and $[w^*\theta^*]$ still can be negative a scale height or so above the surface (e.g. Branscome, 1983). The negative flux explains why the RDE [T] may be cooler than the RCE [T] between 12 and 18 km (Figure 4.3), since the eddy flux cools the atmosphere in a layer above the flux minimum. For the $n_z = 3$ solution, the eddy flux never becomes negative. Thus, the $n_z = 3$ solution is warmer in the upper troposphere than the $n_z = 4$ solution not only because its flux is deeper and but also because its flux is never cooling the atmosphere anywhere above the flux maximum.

In the computations of Schubert and Herman, the peak flux is at 835 mb, roughly 1.5 km above the surface. The computations by Tomatsu, Chen et al., and Chen give a higher level for the flux maximum. However, the height variation of all these fluxes in comparison to the

vertical resolution of the data used to calculate them raises some question concerning the influence of the resolution upon the results appearing in Figure 1.4, as discussed in Chapter I. In all the more recent cases except Tomatsu (1979), the flux peaks at the second level above the ground, indicating that the resolution may not be fine enough for the computation to resolve well the region of the actual peak. Tomatsu's flux peaks at a higher level. Since he and Chen (1982) both use the ω-equation to compute vertical velocities, although with different data sets, Tomatsu's peak at a higher level may represent an undue influence of his lower boundary conditions. The fact that the vertical balance model's total flux in Figure 4.8 peaks at the second grid level above the ground implies that the model's resolution may also effect the behavior of the vertical eddy flux. The resolution study in Appendix B4, however, indicates that the model's resolution for single mode runs is actually finer than necessary.

The relatively low eddy flux maximum does suggest that the flux peaks as close to the surface as it can when allowed to interact with the zonal mean temperature structure. The adjustment hypothesis presented in Chapter II requires the flow to reduce the meridional gradient of potential vorticity $[Q]_y$ to zero in some adjustment layer extending upward from the ground. The derivation in Chapter II, section 3 suggests that the vertical eddy flux heating can reduce the potential vorticity gradient in some layer above the flux maximum. Thus, we might expect the vertical flux to peak at a relatively low level if it is going to reduce $[Q]_y$ near the surface. The low peak level in the model and, as well, in Schubert and Herman's results is consistent with this expectation.

Table 4.4 - Vertical eddy heat fluxes computed by Tomatsu (T), Chen et al. (C+), Chen (C), Schubert and Herman (SH), the GISS model, and the vertical balance model (VBM).

	T	C+	C	SH	GISS	VBM
500 mb:						
sensible	19	17	17	13	15	45
latent					8	5
total					23	50
750 mb:						
sensible	16	19	16	20	20	72
latent					16	25
total					36	97

In the atmosphere, boundary layer processes may prevent the flux from peaking as low as in the model. The model's convection parameterization provides some representation of small-scale boundary layer processes, primarily because the surface temperature is fixed. However, convection in the model is only a passive response to the eddy flux, while in the atmosphere, boundary layer processes play a more active role in determining the temperature structure near the ground.

Table 4.4 compares magnitudes of the large scale eddy fluxes at 750 mb and 500 mb, showing the total eddy flux as well as the individual fluxes of sensible and latent heats. As is the case with the vertical balance model, the GISS model eddy sensible heat flux includes the presumably small eddy flux of potential energy. Schubert and Herman's flux is for the transient eddies alone, but the discussion in Chapter I indicates that the vertical standing eddy heat flux is relatively unimportant. Despite differences in methods and models, there is agreement between the results appearing in the first five columns of the

table. Differences in these columns may be as much due to differences between data sets as due to differences between methods and models used. The vertical balance model's sensible heat fluxes are considerably larger than the sensible heat fluxes from the other sources, showing a significant discrepancy between the vertical balance model's flux and the flux given by all other sources. The vertical balance model's latent heat flux agrees fairly well with the GISS latent heat flux, but the agreement may be deceptive, for the vertical balance model's latent heat flux is proportional to the sensible heat flux. If the sensible heat flux had been about the same size as the GISS model sensible heat flux, then the model's latent heat flux would have been much smaller.

The consistency between the model's total flux and the total flux from other sources in Table 4.3 indicates that the discrepancy in the flux magnitudes is due to the model's partitioning of the total flux among various types of dynamic heat transport. Standing eddy heat fluxes may account for some of the discrepancy, but only a small portion. The partitioning between sensible and latent heat fluxes also may be incorrect in the model. The results of Berggren and Nyberg (1967) and Oort and Rasmusson (1971) discussed in Chapter I suggest that the ratio of sensible to latent heat flux in the atmosphere at 45°N and 750 mb is 4:3. In the GISS model, the ratio of sensible to latent heat flux at this level is about the same, 5:4. For the 1.5 E_w n_z = 4 solution, the ratio at 750 mb is 3:1. This difference also can account for a small portion of the discrepancy between the strength of the vertical eddy sensible heat flux given by the vertical balance model and the strength of the same flux given by other sources in Table 4.3.

A third source of discrepancy is the model's partitioning between eddy and convective fluxes. In the 1.5 E_w wave number 4 solution, convection is confined to a layer close to the surface and there is no convective flux above 1 km: the net heat flux by the vertical balance model listed in Table 4.3 is just the net large scale eddy flux. The model's convective adjustment is simply a passive response to the zonal mean temperature profile produced by radiation and the eddies. For winter conditions, there is generally no convective flux in the model above the eddy flux peak, convection being confined to the region where the eddies are cooling the troposphere. In the atmosphere, the time and zonal mean convective heating most likely extends to much higher levels, since local conditions, not zonal mean conditions, initiate convection.

In the GISS model, the convective flux penetrates to 10 km at 43°N, with strengths of 32 W/m^2 at 750 mb and 7 W/m^2 at 500 mb. We can estimate the vertical distribution of the convective flux in the atmosphere by using the eddy sensible heat fluxes in Table 4.3 and the net heat flux calculated by Hantel. Suppose that the ratio of 4:3 for the sensible to latent flux is realistic at both 750 mb and 500 mb. Then at both 750 mb and 500 mb, the total eddy heat flux is ~ 30 W/m^2. Subtracting these fluxes from Hantel's values for the net flux by all motions then gives a convective flux of ~ 70 W/m^2 at 750 mb and of ~ 40 W/m^2 at 500 mb. These values for the convective flux are larger than those in the GISS model, a reflection of the differences between Hantel's and the GISS model's net fluxes in Table 4.2.

Combining the convective flux strengths above, we can estimate a mean convective flux to be ~ 50 W/m^2 at 750 mb and ~ 25 W/m^2 at 500 mb.

Subtracting these estimated convective fluxes from the vertical balance model's sum of eddy and convective fluxes then gives a repartitioned total eddy flux in the vertical balance model that we might expect if the model were to use a more realistic convection parameterization. The repartitioned fluxes are 47 W/m^2 at 750 mb and 25 W/m^2 at 500 mb. Both repartioned fluxes agree much better with the total eddy fluxes in the GISS model than the vertical balance model's original fluxes do. Thus a more realistic convective flux may lessen considerably the discrepancy between the vertical balance model's eddy heat flux and the heat flux given by other sources in Table 4.3. A substantial change in the way the model computes convective heating would be necessary to accomplish part of the repartitioning. Some change in the model's procedure for computing the latent heat flux would seem to be necessary, as well.

Model runs with an ensemble of waves display a need for flux repartitioning even more than single mode runs. Winter wave ensemble model runs give weak eddy solutions (e.g. Figure 4.5) unless the specified EKE is $\gtrsim 5\ E_w$. Among winter single mode solutions, the most relevant deep mode is also the most efficient mode: it gives the warmest troposphere for a given EKE. The wave ensemble includes the most unstable deep mode, but its effectiveness is reduced because the EKE is spread over a number of modes besides the most unstable mode. The other modes will have smaller growth rates than the most unstable deep mode, shallower depths, or both. A less unstable or less deep mode will tend to transport less heat upward; the net flux is less than if all wave energy is concentrated in a single mode. In addition, the partitioning of the heat flux among different waves favors the longer waves, which require greater energy to produce strong eddy solutions

than relatively short waves do. If convection assumes a greater portion of the upward energy flux, then the redistribution of EKE from one mode to many modes may have less of an effect on the character of the solution for a specified EKE than it does presently.

Although the sensible heat fluxes in Table 4.4 other than those of the vertical balance model show a consistency in their strengths, they may be too weak. Schubert and Herman note that their data insertion process can produce large perturbations in their GCM's vertical velocity field. Their sampling procedures, designed to prevent the perturbations from contaminating their statistics may have the effect of weakening vertical velocities more than necessary. Manipulation of raw data to produce the NMC data sets which Tomatsu (1979), Chen et al. (1981), and Chen (1982) use may also cause computed vertical heat fluxes to be smaller than they actually are in the atmosphere. In addition, for single wave runs, the vertical balance model has 10 levels between 500 mb and the surface, more than twice as many as any of the models or data sets used by the other sources in Table 4.3 have. Since the vertical balance model results indicate that the eddy heat flux is sharply peaked, the other sources may not resolve the flux maximum, which may cause them to underestimate the strength of the flux at all levels.

The heating rate for [T] produced by the model's flux in the 1.5 E_w n_z = 4 solution and its balance with radiation and convection appears in Figure 4.9. The effective heating due to the filter is too small to be resolved. Convection contributes only near the ground, but its contribution is strong. As a first approximation, in the layer of convection, the balance is between the eddy flux cooling and the convective flux heating. The eddy flux cooling rate is large compared

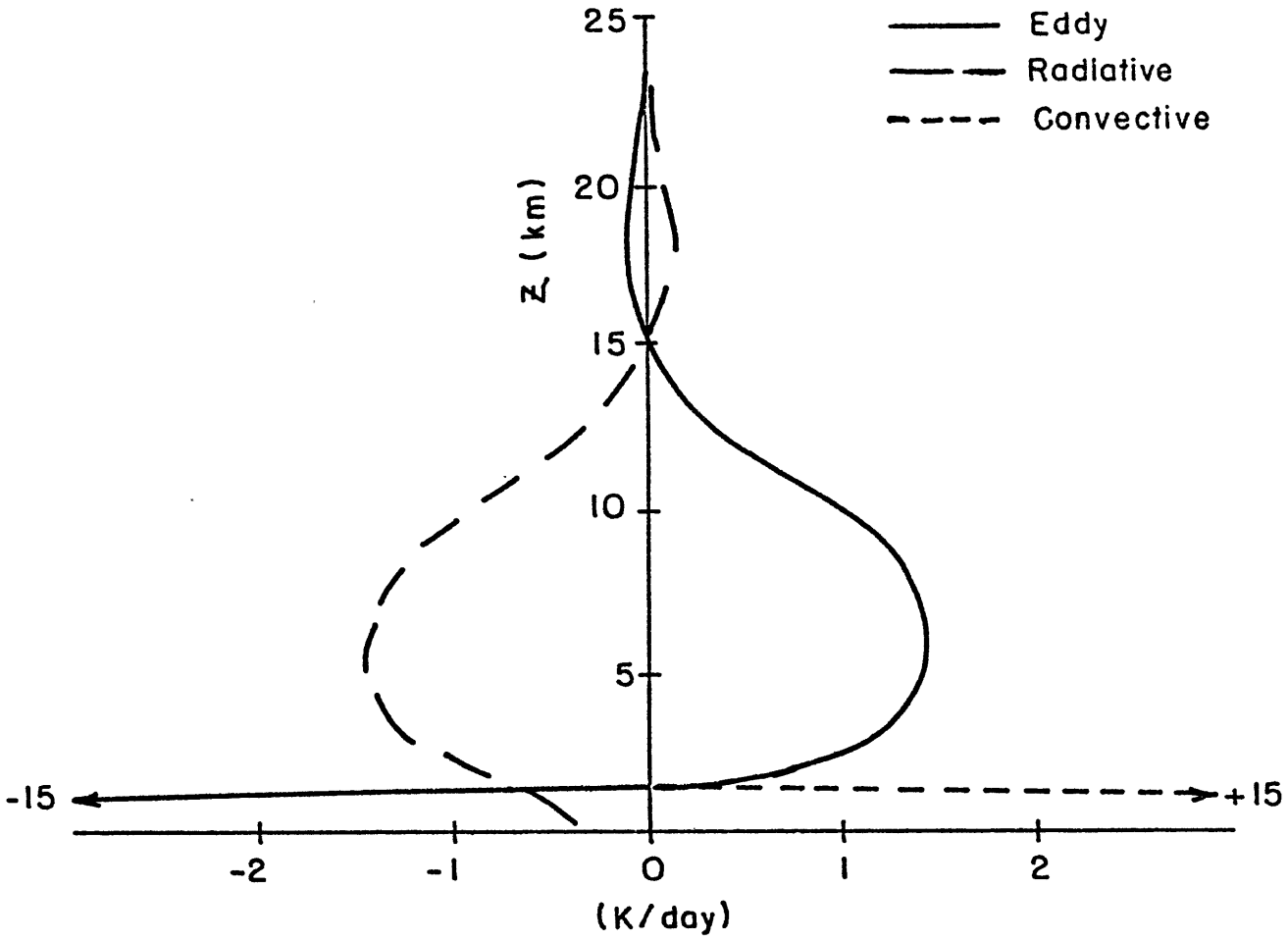


Fig. 4.9 Heating rates for the 1.5 E_w n_z = 4 solution.

to its heating rate at higher levels, yet the size of the surface heat flux, which occurs primarily as a response to the eddy flux cooling, is consistent with the observed surface flux. Radiation plays only a small direct role in the model's layer of convection. In the atmosphere, the radiative damping time near the surface may be less that half a day (Prinn, 1977), so that radiation could have a more direct influence on the levels near the surface than indicated by the model.

Above the convection layer, only radiative and eddy fluxes balance. Because this solution for [T](z) displays a good agreement with the observed [T](z), (T_{Do} - [T]) is small and the balance is essentially between Q_{Do} and the eddy heating. The model's achieving a balance shows that the eddy flux can adjust the temperature structure so that the eddy's heating matches the radiative cooling.

Although the primary focus of this work is not linear instability, some aspects of the linear instability computation for the 1.5 E_w n_z = 4 equilibrium are of interest since its computation involves a temperature structure similar to the atmosphere's. Figure 4.10 shows the amplitudes and phases for the eddy streamfunction, vertical velocity and temperature. The streamfunction amplitude displays two maxima, with the largest one being at the surface. The structure is similar to Branscome's (1980) approximate computation near the peak growth rate in the Charney stability problem, his Figure 2.10. There, the upper maximum occurs at about 6 km and the minimum in the lower troposphere is about 90% of the amplitude at the peaks. Here, the wave is deeper, with upper maximum at 9 km, and it exhibits greater variation with height. The minimum amplitude in the troposphere is about 70% of size of the maximum amplitude. The layer of rapid phase change is about the same

for both, 6 km, implying that the upper maximum would have little bearing on the vertical distribution of the horizontal eddy heat flux.

The vertical velocity peaks in the center of the grid, indicating a possible influence on the solutions of the choice of model depth. Results in Appendix B4 show that using a deeper grid gives negligible changes in the most unstable mode temperature distribution.

The eddy temperature amplitude displays considerable variation with height, but the phase changes relatively slowly, except for a major shift of about 120° near 10 km and another shift at the top. Tests with deeper grids show that the latter shift is an effect of the upper lid and has no importance since the flux is nearly zero there anyway. With only one major phase shift in the troposphere, the eddy temperature has a vertical wavelength of roughly 20 km. This is important, because the radiative damping time for such a wavelength, using the model's formula for τ_R, is about 30 days. This time is long compared to the e-folding e-folding time of the eddy, 3 days, so that radiative damping is not necessary in the linear instability computation.

The scaling analysis in Chapter II notes that a potentially important factor in the analysis is the relative phase coefficient, $C_{\psi_i\psi_j} = \frac{1}{2}\cos\phi_{ij}$, where ϕ_{ij} is the relative phase difference between two eddy quantities, Ψ_i and Ψ_j. Figure 4.10a provides a comparison of the relative phases of w^*, v^*, and θ^*. The phase of ψ^* in Figure 4.10a is shifted by $\pi/2$, so that it is the phase for v^*. The phase difference between w^* and θ^* is about the same as that between v^* and θ^* throughout most of the troposphere, so that $C_{w^*\theta^*} \approx C_{v^*\theta^*}$. Since $C_{\psi_i\psi_j}$ is a function of the cosine of the phase difference, both

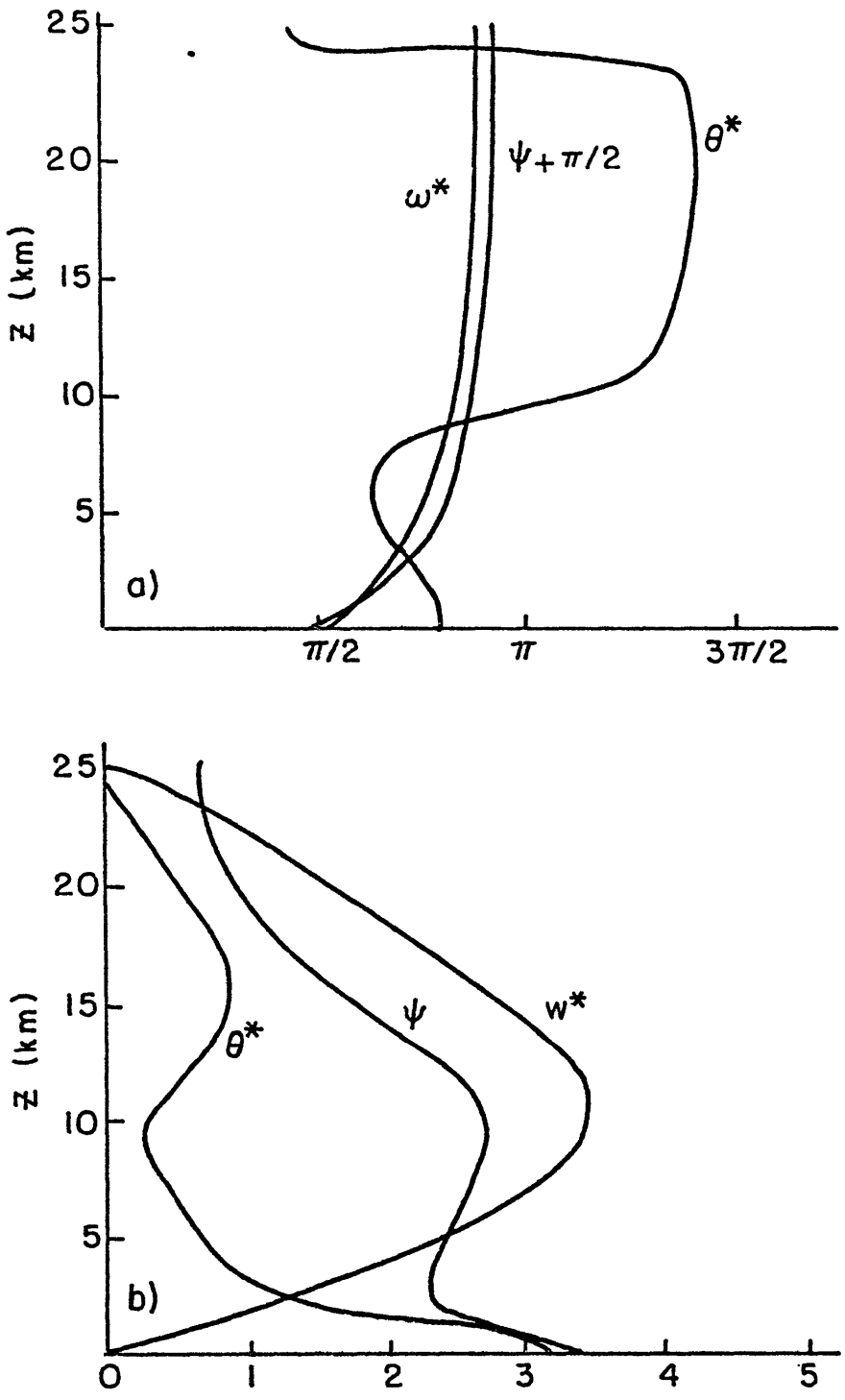


Fig. 4.10 - The a) phases and b) amplitudes of w^*, θ^*, and ψ for the 1.5 E_w n_z = 4 solution. Figure 4.10a shows the phase of ψ plus $\pi/2$ so that the curve is the phase of v^*. In Figure 4.10b, the units are: w^* - 10^{-2} m/sec, θ^* - 10 K, and ψ - 100 m.

$C_{v^*\theta^*}$ and $C_{w^*\theta^*}$ do not vary enough with height below 10 km for either to be a major factor in the scaling analysis, though there is a minimum in $C_{v^*\theta^*}$ at the surface, where $[v^*\theta^*]$ peaks. Note also that $[w^*\theta^*]$ becomes negative at 13 km because the phase of θ^* changes greatly between 10 and 13 km while the phase of w^* remains constant.

Figure 4.11a shows the growth rate spectrum for this solution, and Figure 4.11b shows the corresponding depths of the unstable modes, using the closure level, z_{cl}, defined in Chapter III as a measure of their depth. There is a minimum in the spectrum at wave number 2, a feature reminiscent of the growth rate minimum for the Charney problem, where a neutral point separates Charney modes from relatively deeper Green modes. Further inspection shows that the wave number 1 streamfunction has a maximum at the top lid and undergoes a phase change with height of about 180°. These features, especially the latter, are reminiscent of Green modes. Thus, the z_{cl} depths for $n_z = 1$ and $n_z = 2$ are probably not a good measure of these waves' actual depths. The growth rate curve on the short wavelength side of the minimum is skewed so that there is a sharp increase in growth rate as wave number increases from the neutral point to the wave number of maximum growth, again reminiscent of the variation of growth rate with wave number in the simpler Charney problem (Branscome, 1980). The closeness of the maximum growth rate wavenumber to the neutral point suggests that solutions for the most unstable mode are particularly sensitive to parameter changes which shift the neutral point.

Between $n_z = 6$ and $n_z = 20$, the growth rate increases steadily with wave number, so that the growth rate for $n_z = 20$ is as large as that for the maximum at $n_z = 4$. Over the same range of wave numbers,

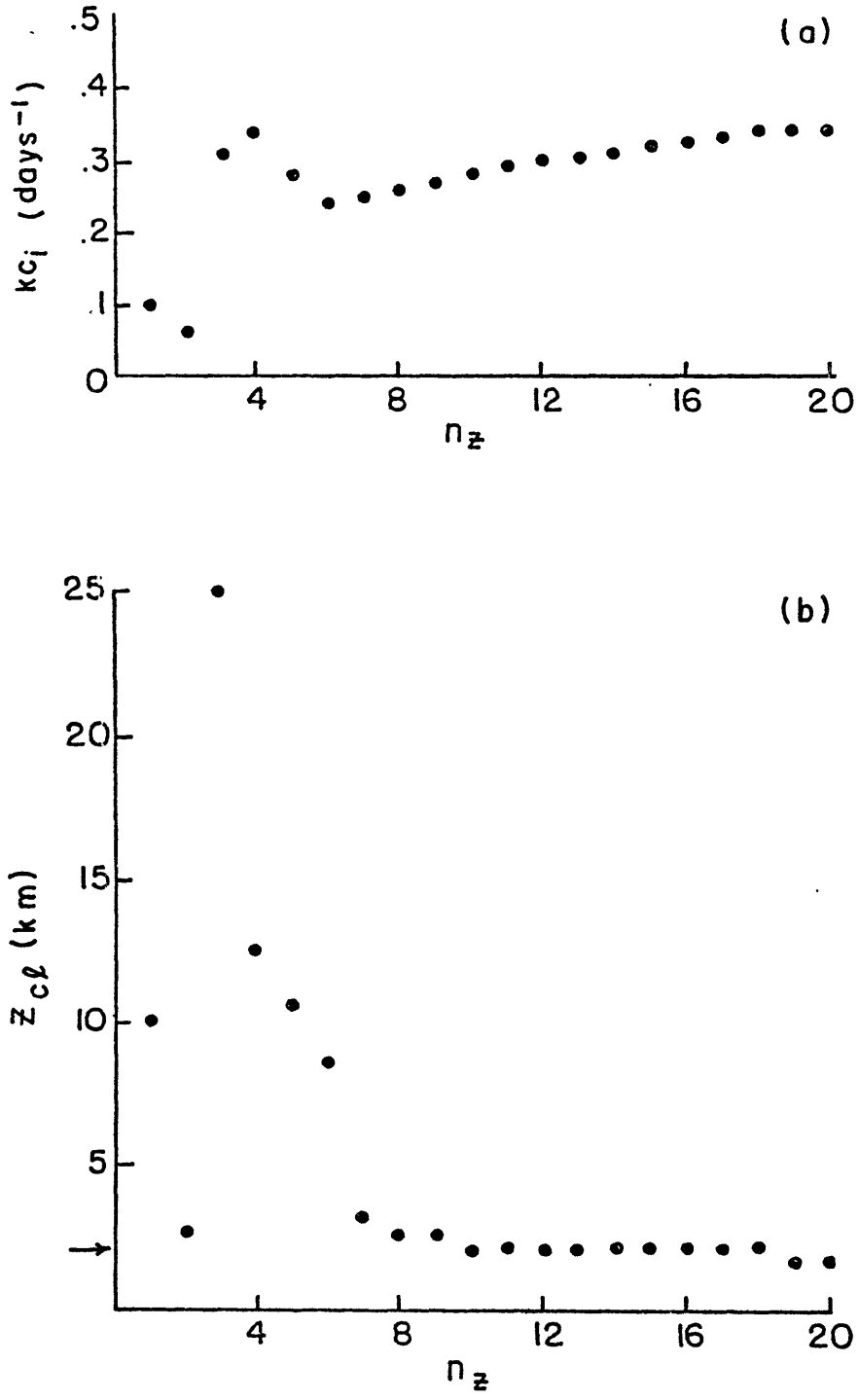


Fig. 4.11 - Spectra of a) growth rates and b) wave depths z_{cl} for baroclinically unstable waves, using the temperature profile from the 1.5 E_w n_z = 4 solution.

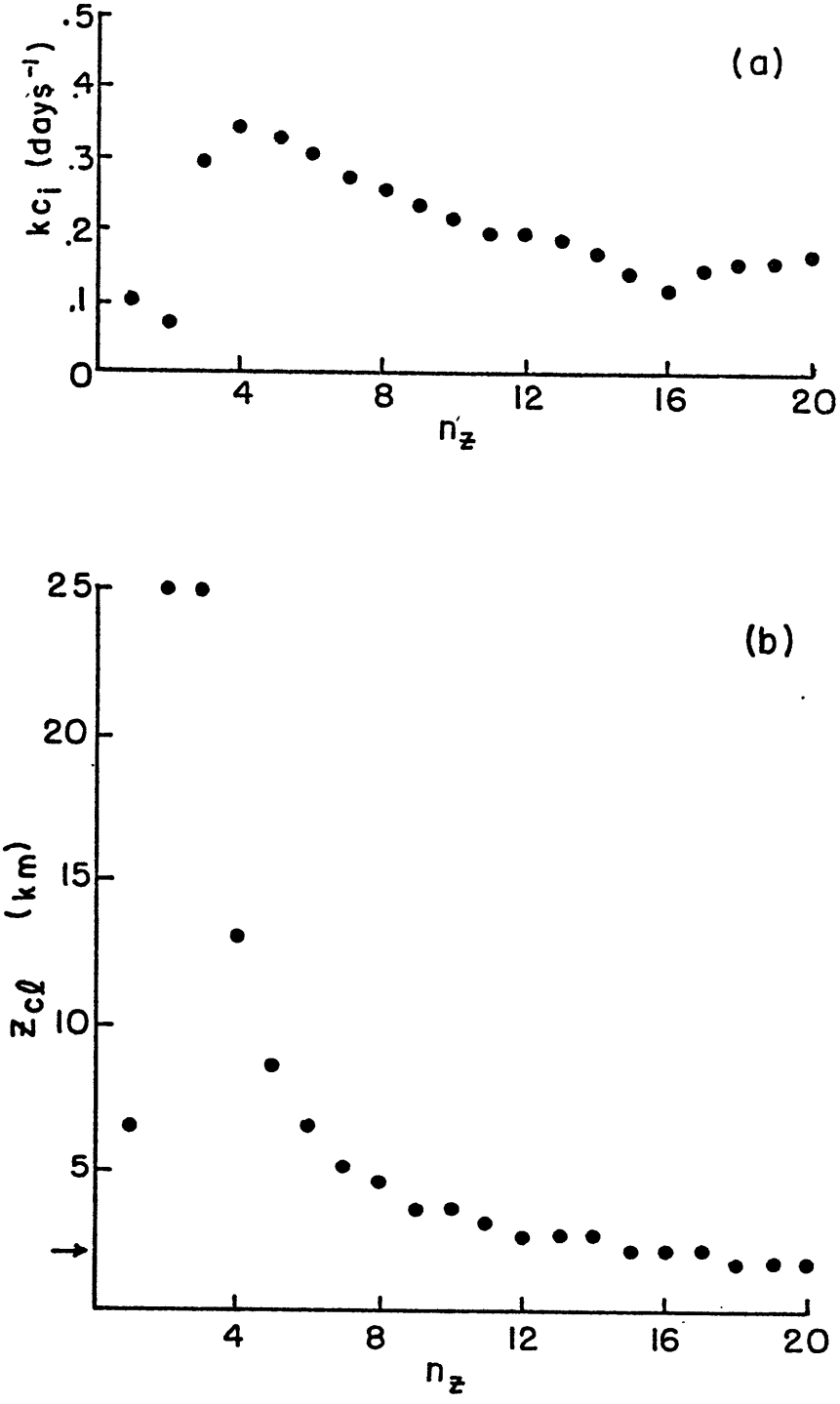


Fig. 4.12 - As in Figure 4.11, only using $N^2(z) = \tilde{N}^2$ from the 1.5 E_w $n_z = 4$ solution.

the wave depth decreases greatly with wave number, becoming less than 2 km for the shortest waves. The arrow in Figure 4.11b marks the local maximum in N^2 near the surface for the solution from which this wave depth spectrum is computed, the 1.5 E_w solution in Figure 4.4. Wave numbers 7 and larger are essentially confined to the layer of relatively small N^2 below 2 km.

The peak in growth rate for short wavelengths is similar to the short wavelength peak observed by Gall (1976a) in a linearized GCM and by Blumen (1979) in a model with two layers of different static stabilities. In Blumen's model, the long waves occupy both layers and their growth rates are a function of a weighted average of the static stabilities in each layer. The short waves are confined to the layer of lower static stability and their growth rates are a function of the static stability of that layer. In the present case, the short waves are confined to the layer of relatively small static stability near the surface. The sharp increase of N^2 in the vicinity of 2 km acts as a lid, causing the growth rates of the shallow modes to decrease with decreasing wave number, much like the decrease in growth rate as wave number becomes very small in Eady's (1947) model. Eventually, as wave number decreases, the waves become much deeper than 2 km, and their growth rates become larger. Figure 4.11a suggests that wave numbers beyond $n_z = 20$ may have growth rates even larger than any plotted in the figure. The model's computations do not include higher wave numbers because they become so shallow that the model may not adequately resolve them.

If the layer of relatively low N^2 near the surface is removed, the growth rates of the short waves change considerably. Figure 4.12 shows

the growth rate and wave depth spectra produced by the stability computations when all mean flow parameters are the same as for Figure 4.11, except that N^2 is constant with height, $N^2 = \tilde{N}^2$, the tropospheric mean defined in (4.1.1). For this particular case, the 1.5 E_w n_z = 4 solution, $\tilde{N}^2 = 2.0 \cdot 10^{-4}$ sec^{-2}. The biggest difference between Figures 4.11 and 4.12 is that the growth rates for the short waves are much smaller in the latter. The growth rates for the longer waves and the wave depths for all the waves are about the same in both figures. Being relatively shallow, the growth rates of the short waves are particularly sensitive to $N^2(z)$ near the ground, as noted previously by Staley and Gall (1977) and Blumen (1979). Here, the removal of a layer of relatively low static stability near the ground causes the growth rates of the short waves to decrease by about 50%.

In Figure 4.12a, the growth rate increases as wave number increases beyond $n_z = 16$. There does not seem to be any physical reason for there to be growth rate minimum at some large wave number. Most likely, the minimum is an effect of the waves' becoming relatively shallow compared to the model's 0.5 km resolution, further indication that stability computations for higher wave numbers may become inaccurate.

The flux parameterizations of Stone (1972) and Branscome (1980) have vertical structures based on linear instability computations in which the static stability is constant with height. In the atmosphere, static stability varies with height, suggesting a comparison of the vertical eddy heat fluxes computed by the model when N^2 is a function of height and when it is not. The comparison is of interest because Branscome (1980) has used his parameterizations to give the eddy heat

fluxes in a zonally symmetric version of the GISS climate model. Figure 4.13 shows the vertical eddy heat flux $\rho C_p[w^*\theta^*]$ given by the 1.5 E_w $n_z = 4$ solution and compares it with the corresponding flux computed by the model for wave number 4 when $N^2(z) = \tilde{N}^2$, the tropospheric mean value for this solution. The biggest difference between the two is that the $\tilde{N}^2$ computation gives a much larger peak flux. Both comparisons use a 1.5 E_w eddy amplitude and comparison of Figures 4.11 and 4.12 shows that in both cases, wave number 4 has a growth rate of 0.35 days. Thus, the discrepancy between the peak fluxes seems to be due to the manner in which $N^2(z)$ influences the vertical distribution of the flux. The comparison indicates that Branscome's parameterization of the vertical eddy heat flux may tend to produce too much heating between 2 and 10 km. Note also that the downward heat flux near 15 km is stronger when $N^2 = N^2(z)$.

2. Summer conditions solutions.

The summer vertical balance model runs differ from the winter model runs in that convection plays a more prominent role. The model can produce solutions corresponding to the winter strong eddy solutions if the eddy amplitude is large enough, but unless the specified EKE is fairly large ($\gtrsim 4\ E_s$), $[T](z)$ and $N^2(z)$ are not substantially different from summer solutions that are examined here. As with the winter conditions solutions, the two selection criteria for choosing the most relevant single mode tend to select the same or nearly the same wave number. In the summer runs, the two selection criteria may choose solutions produced by very different wave numbers if the eddy fluxes are

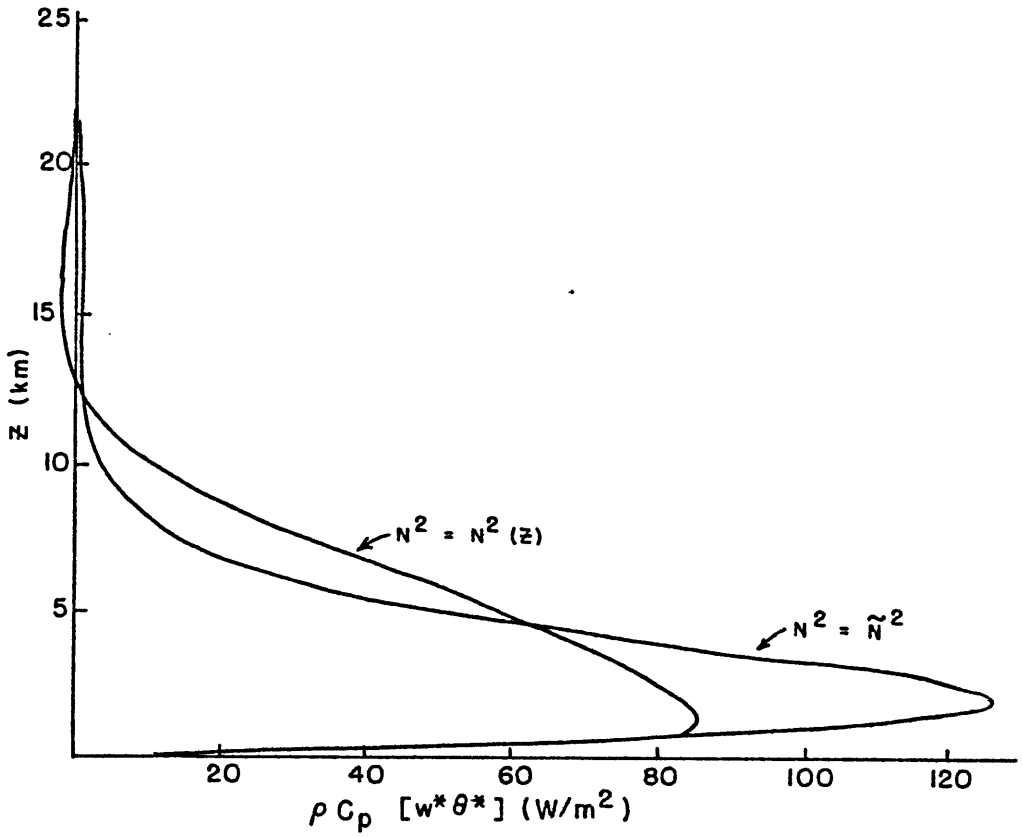


Fig. 4.13 - Comparison of $\rho C_p[w^*\theta^*]$ profiles computed by the model when $N^2 = N^2(z)$ and when $N^2 = \tilde{N}^2$. Both N^2 profiles are given by the 1.5 E_w $n_z = 4$ solution.

very weak, as occurs when the wind shear is smaller than the observed shear. In such cases, the eddy fluxes are so weak for all solutions that there is little difference between the solutions: they all are very similar to the RCE solution. Thus, the selection criteria in such cases do not matter.

The solutions presented here are of interest because they show greater interaction between the eddy flux and convection than occurs in the winter solutions. Although convection plays an important role in these solutions, they do not correspond to the winter weak eddy solutions for their eddy flux may still cause the appearance of a layer near the surface where the convective heating is zero and $[Q]_y \approx 0$. In contrast, the temperature structure near the surface of a weak eddy solution is determined completely by convection.

The summer runs shown here also differ from the winter runs in that neither the most unstable mode solution nor the most stabilizing mode solution yields the best reproduction of the observed temperature structure. Figure 4.14 compares the observed summer [T](z) at 45°N given by Oort and Rasmusson (1971) with that resulting from model runs in which the specified wave number is $n_z = 4$ or $n_z = 6$. The model parameters are for summer conditions as presented in Chapter III, and the eddy amplitude is $1.5E_s$ in each case. The figure also shows the RCE solution for summer conditions. Wave number 4 gives the most relevant single mode solution, but the three model solutions are indistinguishable below 10 km. When the model uses winter conditions, the most relevant single mode solution gives the warmest lower atmosphere temperature. Here, the lower atmosphere's [T](z) is nearly the same for all wave numbers. Thus, these summer solutions do not

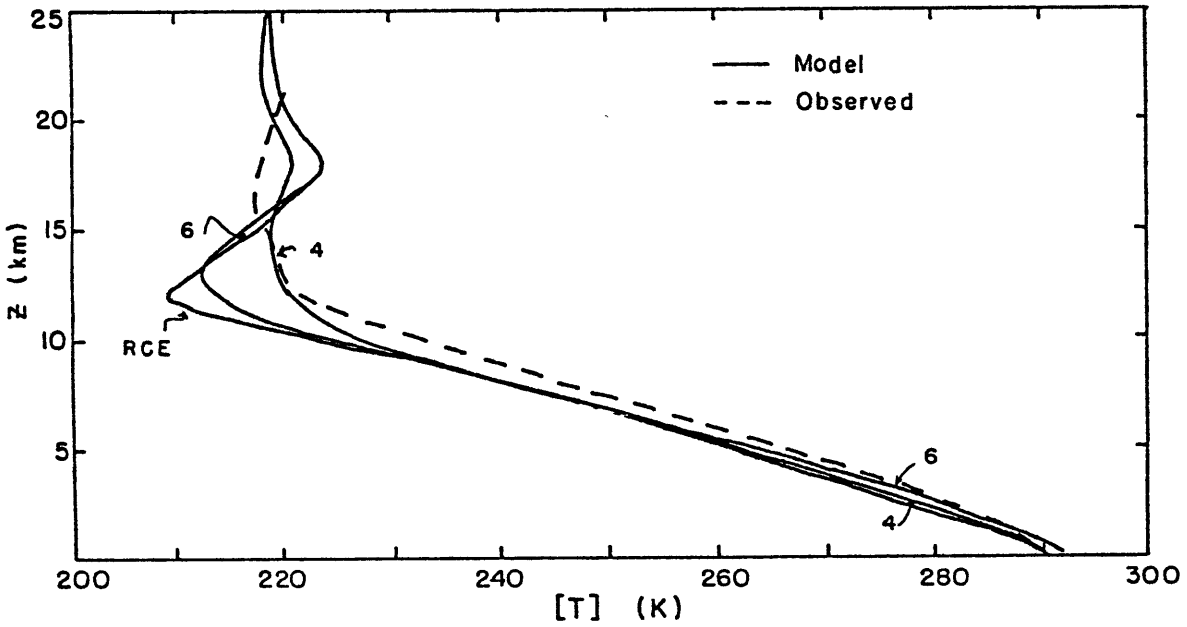


Fig. 4.14 - Summer [T](z) from observations at 45°N and from three solutions: 1.5 E_s n_z = 4, 1.5 E_s = 6, and RCE. Numbers on the curves refer to the zonal wave number used to produce the solution.

favor either selection criteria, in contrast to the winter solutions, where the most relevant mode appears to be a good choice. The temperature profile for each solution is about 3 K cooler than the oberved profile. Since convection determines [T](z) over most of the model atmosphere from 0 - 10 km, the slightly cooler than observed temperatures might be expected from Figure 3.5, which compares a moist adiabat nearly the same as that used by the model for convective adjustment with the observed temperature distribution in the vertical.

The RDE temperature profiles in Figure 4.14 are nearly the same as the RCE profile below 10 km, but convection does not determine [T](z) at all levels. Figure 4.15 compares the $N^2(z)$ profiles for the $n_z = 4$ and $n_z = 6$ solutions with the RCE and observed $N^2(z)$ profiles. For both the $n_z = 4$ and $n_z = 6$ solutions, most of the $N^2(z)$ profile below 5 km is not the same as the RCE profile. Discussion of the heating balance for the $n_z = 6$ solution will show that the eddy flux heating is especially important in the heating balance of this layer. The eddy heating causes the maximum in N^2 at 1.5 km to appear in the $n_z = 6$ solution and gives temperatures between 1 and 5 km that are slightly warmer than those given by the moist adiabat intersecting [T](0). Also, between 1 and 3 km, the $n_z = 6$ solution has N^2 greater than the RCE N^2 solution does.

The observed Brunt-Vaisalla frequency in the lowest 1.5 km is also greater than the moist adiabatic value. In the atmosphere's $N^2(z)$ profile, this would seem to be a boundary layer effect, except that the model's eddy flux also produces relatively large N^2 near the surface. The comparison suggests that the relatively large N^2 is at least partially an effect of baroclinically unstable eddies. The $n_z = 6$

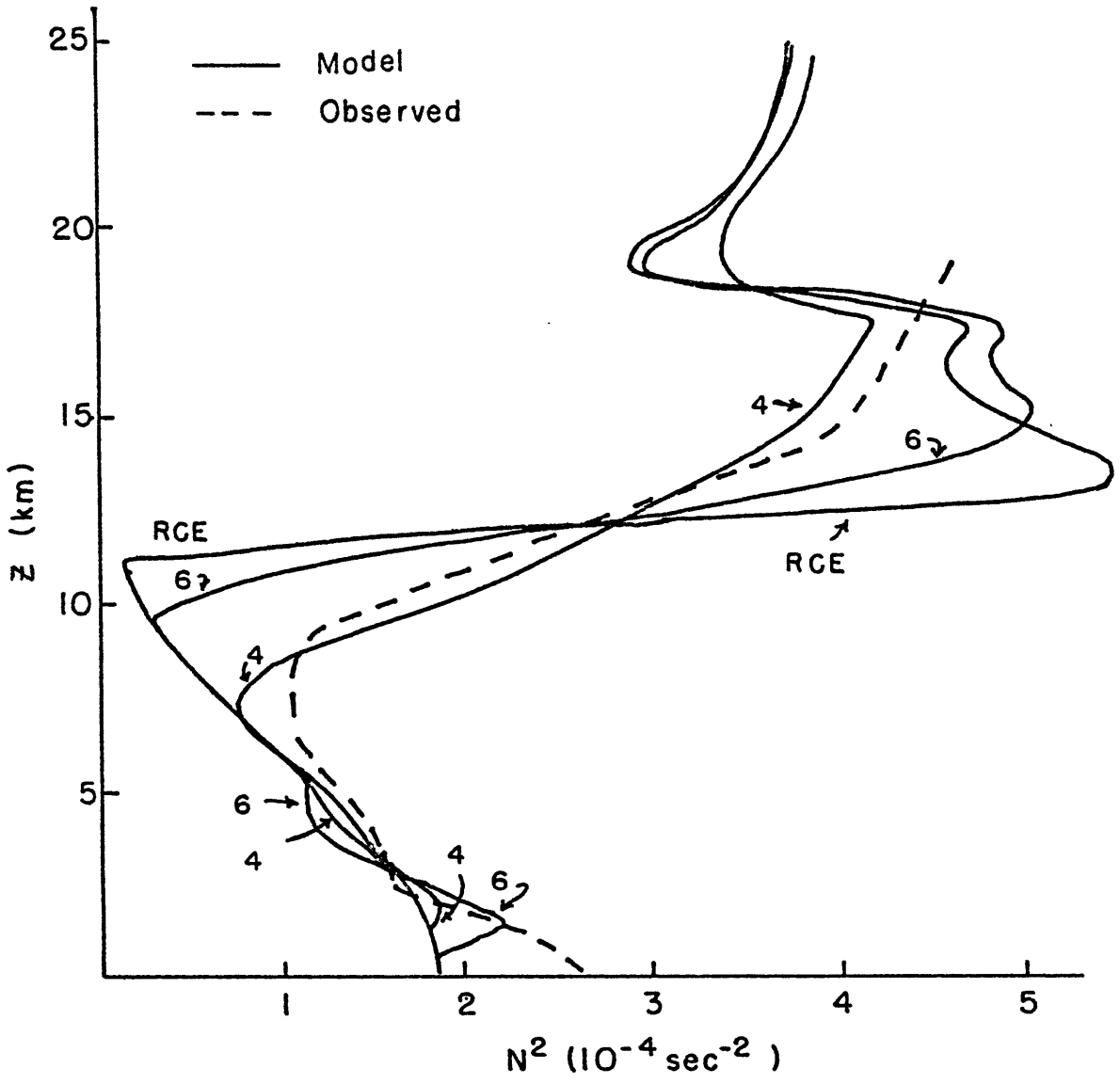


Fig. 4.15 - N^2 for the three temperature profiles in Figure 4.14.

solution gives a maximum in N^2 at a lower level than the $n_z = 4$ solution, indicating that relatively short, shallow unstable waves would be the ones helping to cause the N^2 maximum in the atmosphere. The discussion in Chapter II noted that the adjustment $N^2(z)$ profile in summer corresponded fairly well with the observed $N^2(z)$ profile in the lowest 1.5 km, though it seemed doubtful that a theory involving quasi-geostrophic eddies would be valid so close to the surface. The model results indicate that shallow eddies may indeed play an important role in determining the time and zonal mean temperature structure near the surface in the summer.

Figure 4.16 shows that the layer of relatively large N^2 corresponds to a layer where $[Q]_y$ is relatively small in magnitude. The figure shows $[Q]_y(z)$ and $[\tilde{Q}]_y$ (recall 4.1.2) for the $n_z = 4$ and $n_z = 6$ solutions and for the observed temperature distribution. The layer of relatively small magnitude $[Q]_y$ is at about the same height as it appears in the winter strong eddy solutions. The observed profile shows a similar layer of small $[Q]_y$ near the surface. Between 7 and 12 km, the model's $[Q]_y$ becomes very negative and then very positive in layers about 1 km deep, features not seen in the observed profile. The vertical resolution of Oort and Rasmusson's (1971) data and the fact that the observed profile is a zonal and seasonal mean makes it unlikely that extremely large values of $[Q]_y$ will appear in the $[Q]_y(z)$ profile computed from observations. However, the model's maximum in $[Q]_y$ for these solutions is at about the same height as the observed maximum. Also, in both the observations and the model solutions, the maximum in $[Q]_y$ is at a higher level in the summer than in the winter (cf. Figure 4.7).

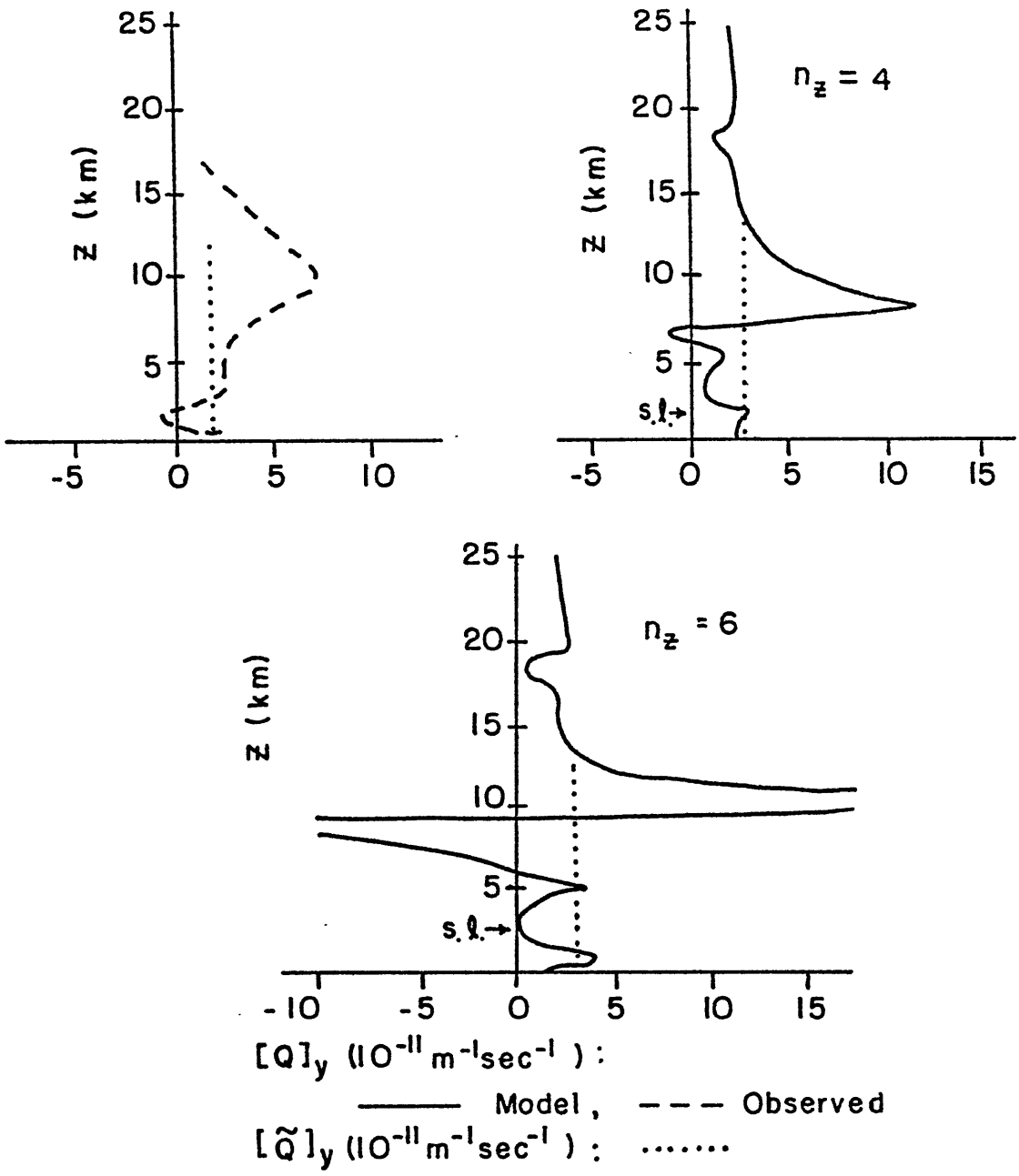


Fig. 4.16 - $[Q]_y(z)$ and $[\tilde{Q}]_y$ from observations and from the $n_z = 4$ and $n_z = 6$ solutions in Figure 4.14. Also shown is the steering level s.l. for each model solution.

Table 4.5 - Comparison of computations for summer surface heat fluxes (W/m^2) given by Hantel for Budyko's data and by the vertical balance model for 1.5 E_s solutions using $n_z = 4$ or $n_z = 6$.

	Budyko	$n_z = 4$	$n_z = 6$
35°N	86		
45°N	68	95	93
55°N	53		

There are fewer independent calculations available for the summer vertical heat fluxes compared to the number available for the winter fluxes. Again, Hantel's (1976) box model provides a measure of the net vertical heat flux by large scale eddies and convection between 30°N and 49°N at 750 mb and at 500 mb, and he also gives zonally-averaged surface heat fluxes derived from Budyko's (1963) climatological estimates. The box model and the Budyko data are both averaged over June, July, and August. In addition, Hantel also gives vertical profiles of the convective flux and the total vertical eddy flux at 43°N computed in a summer season run of the Geophysical Fluid Dynamics Laboratory (GFDL) climate model. Tomatsu (1979) calculates a vertical eddy sensible heat flux for summer in the same manner as he does for winter, using NMC ω-equation. His summer results are an average over June, July, and August, 1964. The next set of three tables compares their results with results from the vertical balance model's 1.5 E_s solutions using $n_z = 4$ or $n_z = 6$.

Table 4.5 shows the surface flux from Budyko's data at 35°N, 45°N, and 55°N and from the model solutions. The balance model's surface heat fluxes are substantially larger than Budyko's values. In contrast to winter, the heat flux in summer shows much less meridional variation, so

Table 4.6 - Comparison of computations for the sum of eddy and convective vertical heat fluxes (W/m^2) for summer.

	Hantel	GFDL	$n_z = 4$	$n_z = 6$
500 mb	66	35	37	35
750 mb	77	80	66	64

that the sensitivity of the calculations to latitude dependent factors can not be cited as a reason for the discrepancy, as they might perhaps be cited in the winter comparison. Some adjustment of the surface heat flux to remove an implicit meridional flux heating as was done for Table 4.2 is possible, but the results shown in Table 4.2 indicate that such an adjustment would eliminate only a portion of the discrepancy between the balance model and the Budyko value. Again, as noted in the previous section, Budyko's results may have errors of 25% or more.

Table 4.6 shows the net vertical heat flux by all atmospheric motions as computed by Hantel in his box model, by the GFDL model, and by the vertical balance model. The summer fluxes in Table 4.5 tend to be smaller than their winter counterparts in Table 4.2. There is a fairly good agreement among the computations, except for the 500 mb flux computed by Hantel's box model, which is much stronger than the other 500 mb fluxes. Hantel's stronger value may appear because the moist convective adjustment in the GFDL and the vertical balance models may not allow the convective flux to penetrate as deeply as it does in the atmosphere.

The strengths of the eddy fluxes alone appear in Table 4.7, with vertical profiles for the vertical balance model's fluxes appearing in Figure 4.17. As in the discussion of winter fluxes, the sensible heat

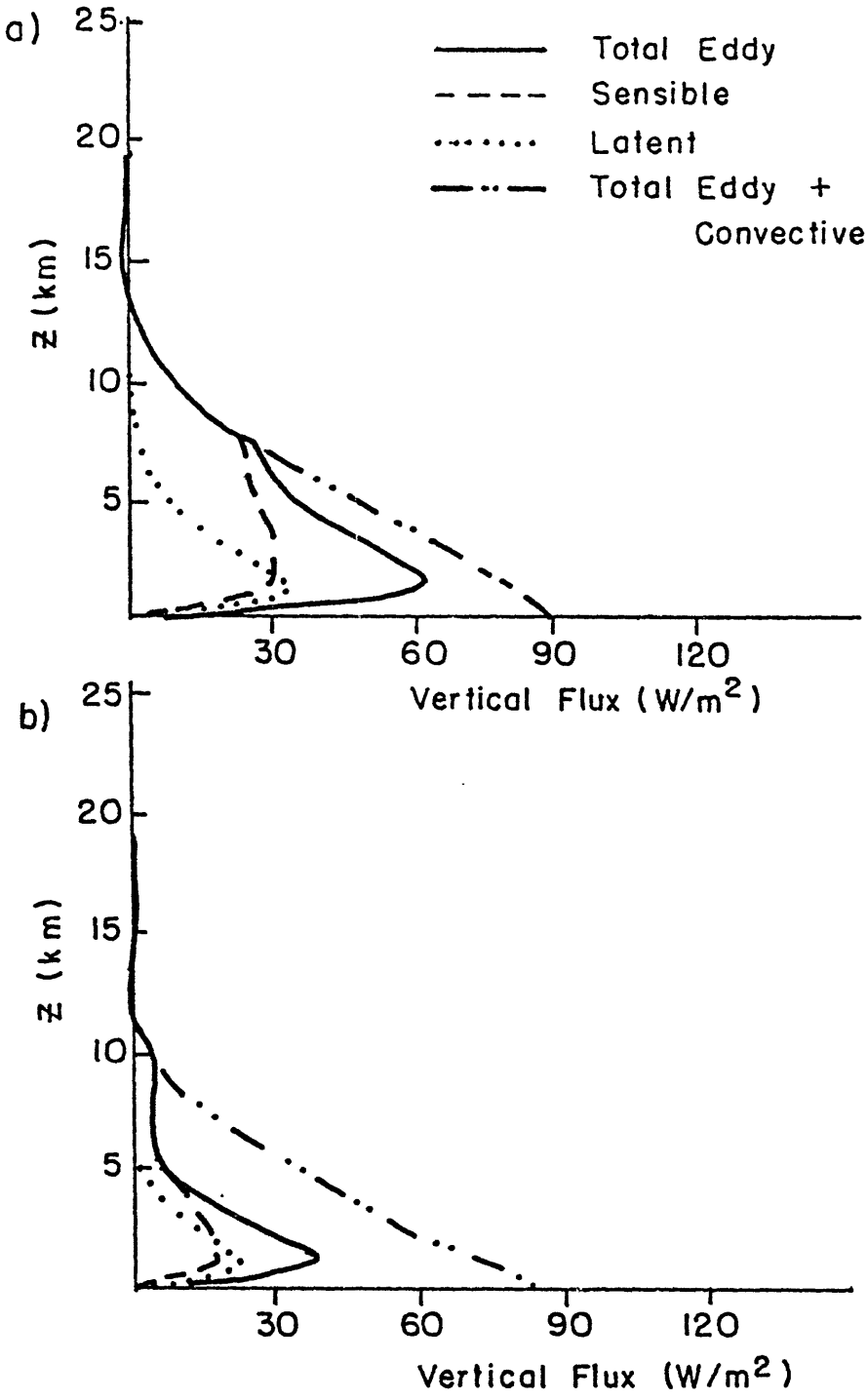


Fig. 4.17 - The eddy sensible heat flux, the eddy latent heat flux, the total eddy heat flux, and the total flux by all atmospheric motions in the model for a) the 1.5 E_s n_z = 4 solution and b) the 1.5 E_s n_z = 6 solution.

flux that appears in the table is $\left(\frac{p}{p_0}\right)^{\kappa}\{\rho C_p[w^*\theta^*]\}$, and the corresponding latent heat flux is $\Lambda\left(\frac{p}{p_0}\right)^{\kappa}\{\rho C_p[w^*\theta^*]\}$. Although the net fluxes for the two vertical balance model solutions are similar in strength, the total eddy flux for the $n_z = 6$ solution is much weaker than the total eddy flux for the $n_z = 4$ solution, and the convective flux is correspondingly stronger. The GFDL total eddy flux is between the two in strength, so that neither vertical balance model solution is favored by the comparison. The comparison suggests that a repartioning of the heat flux between convection and large scale eddy flux is not as necessary in the summer model runs as it is in the winter model runs. This result is consistent with there being a convective flux in summer solutions which penetrates through most of the troposphere and a convective flux in winter solutions which does not. The flux comparisons in Table 4.6, however, indicate that the vertical balance model's convective flux under summer conditions is still too weak at 500 mb.

The sensible heat fluxes calculated by Tomatsu tend to be weaker than the vertical balance model's fluxes, especially at 750 mb. The fluxes for the $n_z = 6$ solution compare more favorably with Tomatsu's fluxes than the fluxes for the $n_z = 4$ solution do, which might be another indication that waves shorter than the most relevant mode are more important in the summer simulation than the most relevant mode itself. However, the $n_z = 6$ solution's flux is still four times as large as large as Tomatsu's flux at 750 mb. The disagreement may indicate, as in the winter flux comparisons, that the model's parameterization of the latent heat flux produces too weak a flux. The disagreement may also indicate that the vertical resolution of Tomatsu's

Table 4.7 - Summer vertical eddy heat fluxes (W/m^2) from the GFDL model, from Tomatsu, and from 1.5 E_s vertical balance model solutions using $n_z = 4$ or $n_z = 6$.

	GFDL	Tomatsu	$n_z = 4$	$n_z = 6$
500 mb:				
sensible		4	28	6
latent			7	1
total	25		35	7
750 mb:				
sensible		4	31	17
latent			27	15
total	45		58	32

data set is not fine enough to resolve well the vertical eddy heat flux near the surface. As noted in the previous section, if the NMC data set used by Tomatsu does not resolve potentially important fluxes by shallow, short waves, then Tomatsu's calculation may underestimate the strength of the vertical eddy heat flux.

Comparing Figure 4.17a with Figure 4.8, the summer sensible heat flux is only about half as strong as the winter sensible heat flux. In contrast, the latent heat flux is about the same size in both figures, because the warmer summer temperatures strengthen the model's latent heat flux relative to the sensible heat flux. Thus, the peak sensible heat flux decreases by about 65%, but the peak total eddy flux decreases by 45%. In contrast to the relative constancy of the model's vertical latent heat flux from winter to summer, the vertically-averaged meridional latent heat flux is stronger in January than July (Figure 3.3). Mullan's (1979) comparison of the observed and parameterized fluxes indicates that the seasonal variation in the meridional flux can be understood in terms of an overall decrease in eddy fluxes from winter

to summer. As parameterized, the vertical latent heat flux can be as strong in summer as in winter, due to the warmer temperatures.

Figure 4.18a shows the balance of heating rates for the 1.5 E_s $n_z = 4$ solution. As with the winter balance (Figure 4.9), in the lowest 1.5 km, the balance is primarily between eddy flux cooling and convective heating. Above 1.5 km, the balance is between eddy flux heating and radiative cooling except in a layer where there is also convective heating as well. The eddy flux heating in this layer is substantially smaller than its strength immediately above and below the layer. In many summer runs with two layers of convective heating, the eddy flux heating becomes nearly zero in the upper layer and the balance is between convective heating and radiative cooling (e.g., Figure 4.18b).

The small eddy flux heating occurs because convection determines $[T](z)$ in any layer where its heating is nonzero in the model. Consideration of the relationship between the vertical eddy heat flux and the potential vorticity gradient derived in Chapter II, Section 3 shows how convection causes the eddy flux heating to become very small in this layer. Equation (2.3.4) and the discussion following it shows that for an unstable eddy, the heating by the vertical eddy sensible heat flux may be proportional to $[Q]_y$. Computations using approximate solutions to the Charney stability problem show that the proportionality may occur in a layer a few kilometers deep. Figure 4.19 shows the vertical profiles of the two terms on the left side of (2.3.4) in the $n_z = 4$ and $n_z = 6$ 1.5 E_s solution states. The $n_z = 6$ solution has a layer between 4 and 6 km where the vertical flux is much larger than the temperature variance term in (2.3.4), otherwise the temperature

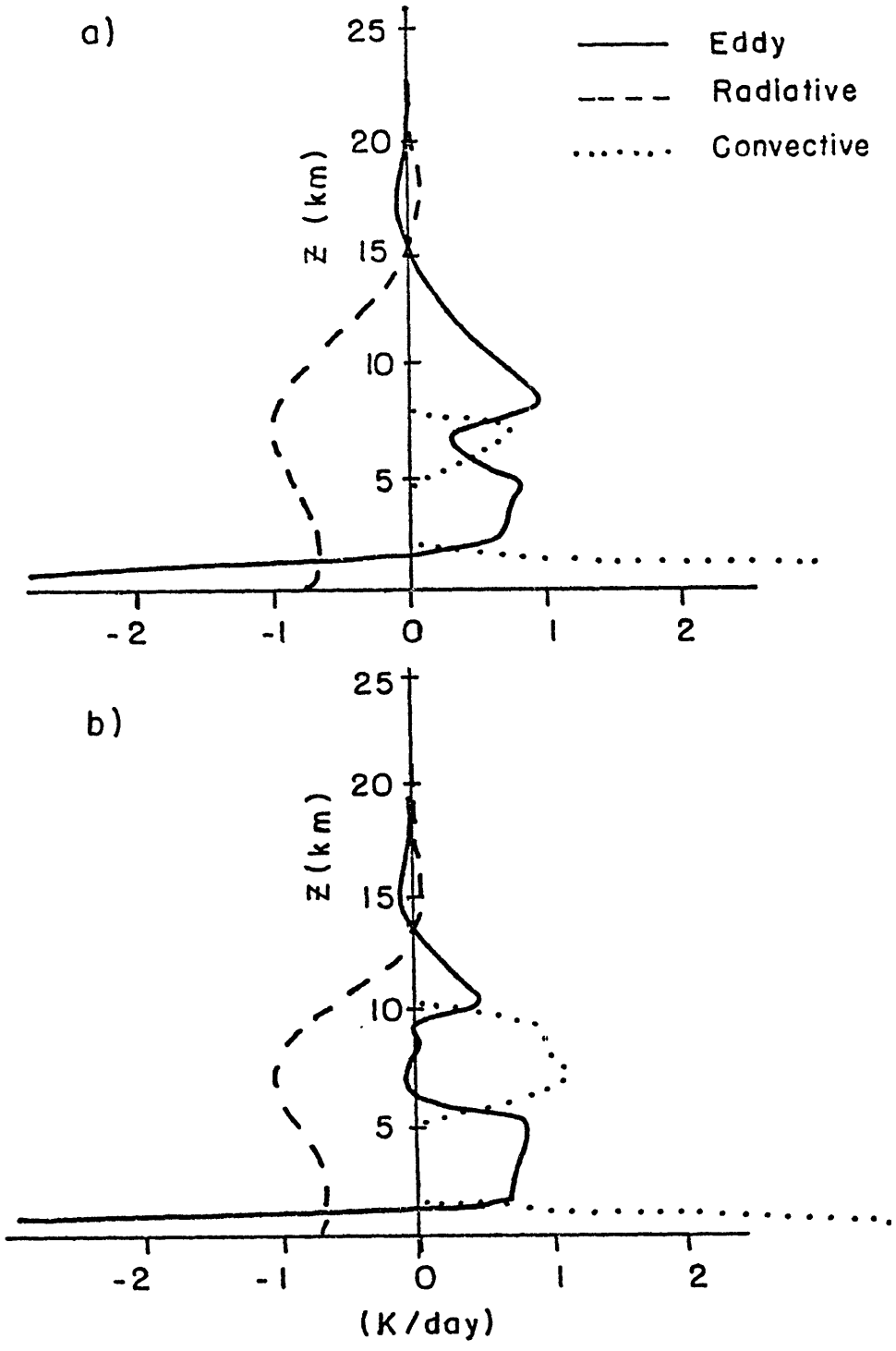


Fig. 4.18 - Heating rates for a) the 1.5 E_s n_z = 4 solution and b) the 1.5 E_s n_z = 6 solution.

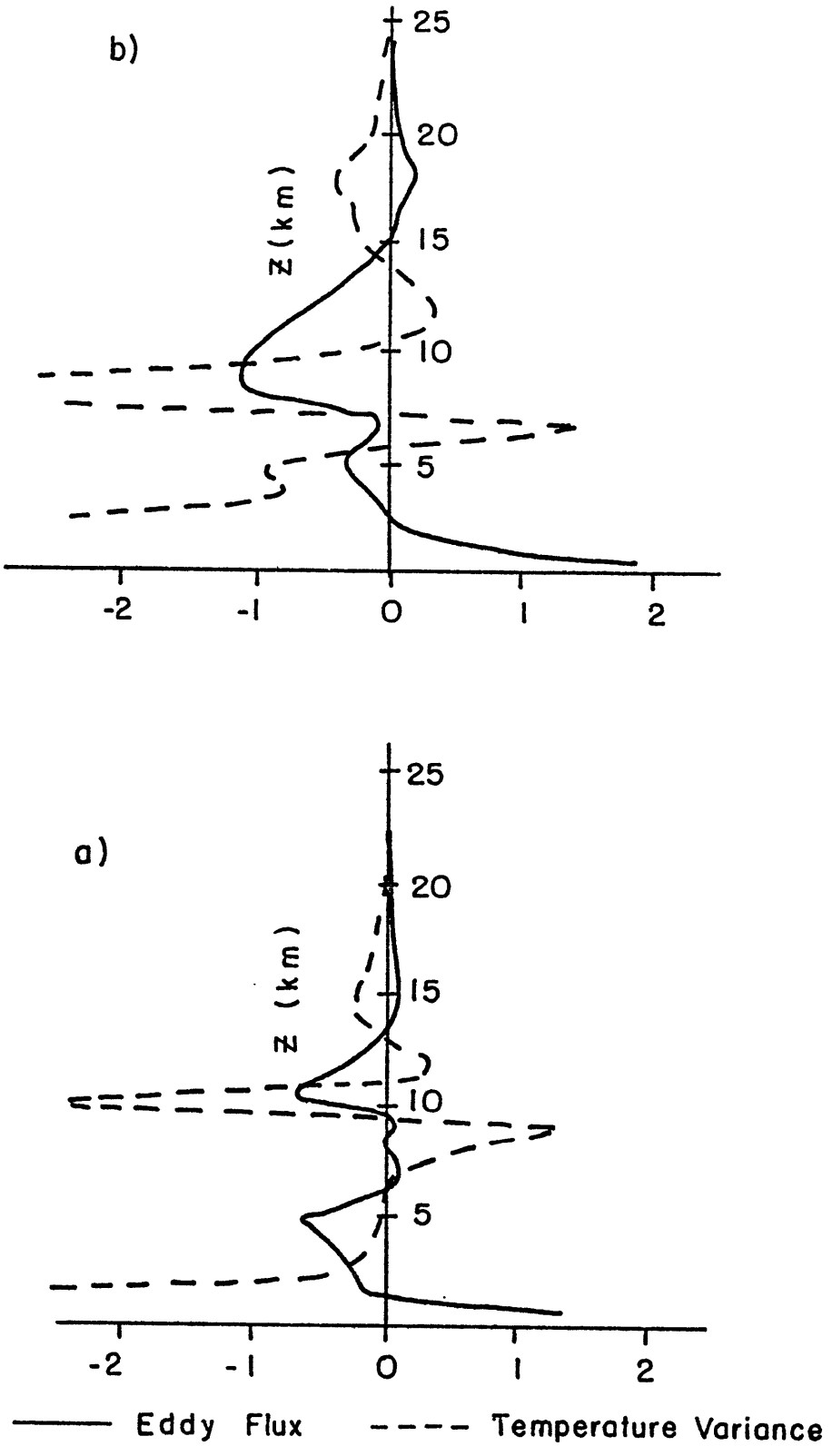


Fig. 4.19 - Vertical profiles of the two terms on the left side of (2.3.4) given by the 1.5 E_s solutions using a) $n_z = 4$ and b) $n_z = 6$.

variance term tends to be at least as large as the meridional eddy flux heating term. However, comparison of Figures 4.16, 4.17, and 4.19 shows that both terms on the left side of (2.3.4) tend to have the opposite sign of $[Q]_y$ between the vertical eddy flux maximum and minimum: both tend to be proportional to $-[Q]_y$. The heating of $[\theta]$ by the vertical eddy sensible heat flux, $-\frac{1}{\rho}\frac{\partial}{\partial z}\rho[w^*\theta^*]$, thus tends to have the same sign as $[Q]_y$.

The same correspondence between the vertical profiles of the eddy flux and the potential vorticity gradient exists in the wave ensemble solutions. The correspondence holds for most of the waves in the ensemble, so that it holds for the total eddy sensible heat flux, too.

The relationship between $-\frac{1}{\rho}\frac{\partial}{\partial z}\rho[w^*\theta^*]$ and $[Q]_y$ shows why, in the two summer solutions discussed here, the eddy heating is weak at the levels between 5 and 10 km where convection controls $[T](z)$. The moist adiabat used by the convective adjustment has $N^2(z)$ decrease so rapidly with height that $[Q]_y$ becomes negative in the upper convective heating layer. As a consequence, $\rho[w^*\theta^*]$ increases rather than decreases with height, and the total eddy flux heating is much less than above and below the convective layer. Conceivably, the sensible heat flux could increase so strongly that the eddy flux would be cooling the convectively heated layer at a rate as large as radiation. Such cooling has not appeared in any model solutions. Instead, whenever there is an upper layer of convective heating causing $[Q]_y$ to be very negative, the eddy flux becomes nearly constant with height and its heating is relatively small.

3. Sensitivity

By specifying certain quantities, such as zonal wind shear, the vertical balance model overlooks potentially important feedbacks between them and the vertical temperature structure. This section focuses on the sensitivity of the model to changes in these parameters. The analysis presented here illustrates the dependence of the model's solutions on the chosen specified parameters by observing changes in the solutions when certain parameters are increased and decreased by 50%. Particular attention focuses on the responses of the tropopause height, z_t, and the mean Brunt-Vaisalla frequency, $\tilde{N}^2$, two quantities measuring gross aspects of the tropospheric temperature structure. Discussion also includes the responses of the peak vertical heat flux, $\{\rho C_p(1+\Lambda)[w^*\theta^*]\}_{max}$, and the growth rate, kc_i, giving a measure of the eddy sensitivity to the parameter changes. To illustrate the possible influence of including $N^2(z)$ in the determination of eddy amplitude, the sensitivity calculations show results for both the closures presented in Chapter III.

The specified quantities which are of greatest interest are those which influence the vertical eddy flux directly. This section presents results for the sensitivity of the model to changes in the eddy amplitude and in the wind shear. The former affects the the magnitude of the flux directly. The latter affects the growth rate of the unstable mode, which in turn affects the magnitude of the eddy flux. The wind shear also affects the size of the eddy amplitude when the EKE $\approx$ ZAPE closure is used. Changes in water vapor amount can influence the magnitude of the eddy latent heat flux and, possibly, the magnitude of

the total eddy heat flux. Discussion in the second section of Chapter III notes that a negative feedback between the size of N^2 and the strength of the eddy flux may allow a compensation to occur between the strengths of the sensible and the latent heat fluxes, so that the total vertical eddy heat flux may remain nearly constant despite changes in the latent heat flux. Thus, this section also gives attention to the changes produced when the model neglects the latent heat flux.

Although the first section focuses on solutions whose specified EKE was 1.5 time the observed EKE, the standard value for the specified EKE in the sensitivity computations is 1 times the observed EKE. This EKE value gives solutions in a transition zone between the weak eddy solutions and strong eddy solutions (Table 4.1). The tests presented here all use wave number 4, which is often the most relevant single mode. Later discussion will show how using either the most unstable mode solution or the most stabilizing mode solution influences the results of the sensitivity tests.

Table 4.8 shows the percentage changes in the peak eddy heat flux $\max\{\rho C_p(1+\Lambda)[v^*\theta^*]\}$ and the growth rate kc_i for specified EKE solutions when either the EKE or $[U]_z$ changes by 50% from its base value. The base values for Table 4.8 are those for wintertime conditions, and they produce the standards for comparison shown in the table. For a particular zonal mean temperature structure, the strength of the vertical eddy heat flux is proportional to both the square of the eddy amplitude and the growth rate. The square of the eddy amplitude is proportional to the EKE and the growth rate is proportional to $[U]_z$, so that for a given vertical temperature structure, a 50% increase in either EKE or $[U]_z$ implies a 50% increase in the eddy heat flux. In

Table 4.8 - The percentage change of $\tilde{N}^2$, z_T, kc_i, and $\max\{\rho C_p(1+\Lambda)[w^*\theta^*]\}$ when $[U]_z$ or the specified EKE changes by ±50%. The standards for comparison are shown on the first line under the column headings.

Specified EKE closure:

	max. flux	kc_i	$\tilde{N}^2$	z_T
standards:	99 W m^{-2}	.42 $days^{-1}$	$1.85 \cdot 10^{-4}$ sec^{-2}	13.5 km
$0.5E_w$	-46	24	-22	-11
$1.5E_w$	19	-19	13	4
$0.5([U]_z)_w$	-100	-100	-76	-22
$1.5([U]_z)_w$	14	13	11	4

EKE ≈ ZAPE closure:

	max. flux	kc_i	$\tilde{N}^2$	z_T
standards:	70 W m^{-2}	.68 $days^{-1}$	$1.60 \cdot 10^{-4}$ sec^{-2}	12.5 km
$0.5([U]_z)_w$	-100	-100	-73	-16
$1.5([U]_z)_w$	67	1	24	16

the model, a stronger vertical heat flux causes N^2 to increase throughout most of the troposphere (e.g., Figure 4.4), which causes the eddy's growth rate and, consequently, the eddy's flux to decrease. This is a negative feedback, which appears in the Table 4.8 results for the specified EKE closure. In contrast to the changes that occur when either EKE or $[U]_z$ are increased, when either of the two are decreased by 50%, the resulting solution's peak flux decreases by about as much or more.

Figure 4.4 indicates why increasing either EKE or $[U]_z$ gives a negative feedback and why decreasing either of the two does not. The most relevant mode standard solution in Table 4.8 is a transitional

solution between the strong eddy solutions and the weak eddy solutions. When the strength of the flux is increased, by increasing either EKE of $[U]_z$, the model's solution becomes a strong eddy solution and the eddy flux plays an important role in determining the temperature structure over most of the troposphere. When the flux is decreased, the solution becomes a weak eddy solution and convection determines the temperature structure over the lower troposphere. Consequently, the eddy flux has less influence over the temperature structure in the latter case and the decrease in EKE or $[U]_z$ by 50% leads to a decrease in the peak flux by about the same percentage or more. In contrast, when the eddy flux increases, the eddy flux exerts control over most of the troposphere and the negative feedback is much stronger. The net change in the strength of the eddy flux is less than half the change that would occur for fixed vertical temperature structure.

The change in the growth rate under these variations displays a similar negative feedback, but with one difference. An increase in EKE leads to an increase in the peak flux and a decrease in kc_i, whereas an increase in $[U]_z$ leads to an increase in both the peak flux and kc_i. The EKE variations affect the eddy flux directly. Increasing the flux by increasing the EKE leads to a larger $\tilde{N}^2$ and, hence, smaller growth rate. The $[U]_z$ variations affect the growth rate more directly, for increasing $[U]_z$ produces a larger growth rate and, as a consequence, a stronger flux. The stronger flux causes $\tilde{N}^2$ to increase, so that the growth rate does not increase as much as $[U]_z$ does. Thus, the growth rate changes are of the same sign as the $[U]_z$ variations and the opposite sign of the EKE variations.

Consideration of $\tilde{N}^2$ and z_T indicates the manner in which the zonal mean temperature structure changes to produce the negative feedback. As noted earlier, the tropopause height changes relatively little compared to changes in the vertical mean lapse rate or, in Table 4.8, the mean Brunt-Vaisalla frequency, $\tilde{N}^2$, unless the eddy flux becomes so strong that an inversion appears near the surface. The effect of a change in the strength of the heat flux in Table 4.8 is to change the static stability with little change in the tropopause height.

Table 4.8 also shows the results of changing $[U]_z$ by ±50% for the ZAPE ≈ EKE closure assumption. In this case, for a fixed vertical temperature structure, the eddy amplitude is proportional to $([U]_z)^3$. Thus, increasing $[U]_z$ by 50% increases the flux by 240% for a fixed temperature structure. Under this closure assumption, we might expect a greater increase in the eddy flux when $[U]_z$ increases, an expectation confirmed by the results in Table 4.8. When $[U]_z$ increases by 50%, the peak flux for the most unstable mode increases by 67%. As with the specifed eddy amplitude results, $\tilde{N}^2$ tends to change more with changes in $[U]_z$ than z_T does. Note that the increase in $\tilde{N}^2$ as $[U]_z$ increases is large enough that the growth rate changes very little, the larger $\tilde{N}^2$ compensating the larger $[U]_z$ in the stability computation. Such compensation can occur for this closure but not for the specified EKE closure because this closure has the flux proportional to $(kc_i)\times([U]_z)^2$. The flux and $\tilde{N}^2$ can both increase without having kc_i increase. In contrast, for the specified EKE closure, the flux and $\tilde{N}^2$ increase with $[U]_z$ primarily because kc_i increases.

The sensitivity computation using the EKE ≈ ZAPE closure shows how the wave selection criterion can influence the model's sensitivity. If

instead of using a fixed wave number, we compute sensitivity under this closure using most unstable mode solutions, the flux changes considerably. The most unstable mode solution using the base parameter values is for $n_z = 7$ and has a peak eddy flux of 49 W m^{-2}. For $[U]_z = 1.5([U]_z)_w$, the most unstable mode solution is for $n_z = 3$ and it has a peak flux of 155 W/m^2, 216% larger than the standard most unstable mode solution; there is almost no negative feedback. The negative feedback occurs for an individual wave number, but the wave number of the unstable mode changes considerably, so that there is no apparent feedback. If we compute the sensitivity under this closure using instead the most stabilizing mode, the appropriate solutions to compare are the $n_z = 4$ solution for the base parameter values, giving a peak flux of 70 W/m^2, and the $n_z = 3$ solution for $[U]_z = 1.5([U]_z)_w$, giving a peak flux of 155 W/m^2. The increase is 121%, again a weaker negative feedback than occurs using $n_z = 4$ for all calculations.

Table 4.9 shows the results of computations like those in Table 4.8, except for summer conditions. In contrast to the winter solutions, the summer solutions show almost no negative feedback between changes in either the EKE or $[U]_z$ and changes in the peak flux. Also, $\tilde{N}^2$ is more sensitive to decreases of $[U]_z$ in the winter compared to the summer. Both of these differences between the sensitivities of summer and winter solutions occur because the convective adjustment controls [T](z) over most of the troposphere in the standard summer solution, while in the standard winter solution, the convective adjustment controls [T](z) only near the ground. Thus, unless the eddy fluxes increase considerably, [T](z) does not change greatly when either the EKE or $[U]_z$ changes, so that there is no negative feedback between the size of the EKE or $[U]_z$

Table 4.9 - Like Table 4.2, only for summer.

	max. flux	kc_i	$\tilde{N}^2$	z_T
Specified EKE closure:				
standards:	41 W m^{-2}	.25 $days^{-1}$	$1.45 \cdot 10^{-4}$ sec^{-2}	12.5 km
$0.5E_w$	-52	0	-14	-4
$1.5E_w$	57	17	8	8
$0.5([U]_z)_w$	-74	-89	-34	-8
$1.5([U]_z)_w$	70	67	21	12
EKE ≈ ZAPE closure:				
standards:	21 W m^{-2}	.25 $days^{-1}$	$1.25 \cdot 10^{-4}$ sec^{-2}	12.0 km
$0.5([U]_z)_w$	-100	-100	-20	0
$1.5([U]_z)_w$	197	66	34	13

and the strength of the peak flux. Also, much greater decreases in $\tilde{N}^2$ are possible in winter compared to summer because the convective adjustment controls temperature throughout all the troposphere in the summer conditions solutions.

The relative insensitivity of the winter conditions solutions to prescribed parameter changes is similar to the insensitivity noted by Stone (1972) in his radiative-dynamic model solutions. The insensitivity results in the vertical balance model because of a direct negative feedback between the vertical flux and N^2. In Stone's (1972) model, a further negative feedback occurs because his model allows both the vertical and horizontal temperature gradients to interact with the vertical and meridional heat fluxes. The form of the parameterizations is such that an indirect negative feedback occurs via the dependence of

the vertical flux on the meridional temperature gradient. Thus, we might expect even less sensitivity to occur in the actual atmosphere, where both the direct and indirect feedbacks operate.

For the model solutions presented in this thesis, the Newtonian damping term in the radiative cooling parameterization is typically much smaller than the specified term in the parameterization, Q_{Do}. Thus, the radiative cooling changes very little between different model solutions for the same season. Large changes in the radiative cooling can alter the vertical temperature structure, resulting in an alteration of the vertical eddy flux as well. Sensitivity tests show that a decrease of Q_{Do} by 50% produces changes between model solutions that are roughly the same size as those produced by an increase of EKE by 50%, the only difference being that the maximum flux decreases rather than increases when Q_{Do} decreases, since less heat needs to be transported upward to obtain a thermodynamic balance. Thus, a decrease in the model's specified radiative cooling has about the same effect on the vertical temperature structure as an increase in the eddy flux's amplitude. Similarly, an increase of Q_{Do} by 50% produces changes in model solutions that are roughly the same size as those produced by a 50% decrease in EKE.

The final sensitivity check shows how the model reacts to changes in the latent heat flux. Table 4.10 shows the results of setting the latent heat flux to zero in the model. The table shows the percentage changes of the eddy flux maximum, the growth rate, the mean Brunt-Vaisalla frequency, and the tropopause height for model runs the same as those used to compute the standard solutions in Tables 4.8 and 4.9, except that the model neglects the latent heat flux. The table

Table 4.10 - The percentage change of $\tilde{N}^2$, z_T, kc_i, and $\max\{\rho C_p(1+\Lambda)[w^*\theta^*]\}$ when the model neglects the vertical eddy latent heat flux. The standards for comparison are the corresponding model runs including the latent heat flux in Tables 4.8 and 4.9. Also shown is the percentage of the original maximum flux due to the latent heat flux, %LH.

	max. flux	kc_i	$\tilde{N}^2$	z_T	%LH
Winter:					
Specified EKE	-9	4	0	0	24
EKE ≈ ZAPE	-7	0	1	0	10
Summer:					
Specified EKE	-46	0	0	0	51
EKE ≈ ZAPE	-48	1	0	0	53

also shows what percentage of the eddy flux at the flux maximum is given by the latent heat flux in the original solutions.

In all cases, the temperature structure as measured by N^2 and z_T changes very little, if at all. Consequently, the growth rate kc_i changes little as well. In the winter specified EKE case, the temperature structure changes by a negligible amount because the sensible heat flux adjusts to account for flux maximum. When the latent heat flux is neglected, the maximum flux decreases, but only by 9% instead of 24%. The temperature structure undergoes some small changes because the growth rate increases by 4%, an increase in accord with the sensible heat flux becoming stronger. The compensation is not a simple replacement of one eddy flux with another, however, for when the latent heat flux is removed, the level of the maximum eddy flux shifts upward from 1.5 km to 2.5 km.

In the three other cases in Table 4.10, the percentage decrease in the flux maximum is the same size as the portion of the original flux that was given by the latent heat flux, indicating no compensation between eddy sensible and latent heat fluxes. The temperature structure remains unchanged because in the original solutions, the convective adjustment determines [T](z) throughout the layer where the latent heat flux is significantly large, greater than a few watts per meter squared. At the levels where the heating balance is between the eddy flux and radiation, the latent heat flux is negligible anyway. Thus, [T](z) changes very little when the latent heat flux is neglected in these cases, and the sensible heat flux remains the same. The radiative cooling also remains the same. Since this cooling implies that there is a certain net upward heat flux by eddies and convection combined to balance the loss of heat by radiation, the convective flux increases to account for the latent heat flux's absence. Note that the winter specified EKE case has kc_i change more than it does in any of these three cases. Some increase in growth rate is necessary for the eddy sensible heat flux to become stronger, but these three cases show very little change, if any.

CHAPTER V

MODEL RESULTS: BAROCLINIC ADJUSTMENT

The discussion in Chapter II shows that in the lower wintertime troposphere at 45°N the observed profile of $N^2(z)$ is similar to that resulting from a baroclinic adjustment which minimizes the baroclinic instability of the zonal mean flow by altering the vertical temperature structure while holding the meridional temperature gradient fixed. An adjustment which instead alters the meridional temperature gradient and holds N^2 fixed produces a profile for $\frac{\partial}{\partial y}[T](z)$ which does not agree well with obervations. The results of Chapter II suggest that baroclinically unstable eddies are able to minimize the instability of the time and zonal mean flow more by altering $N^2(z)$ than by altering $\frac{\partial}{\partial y}[T](z)$.

While the correspondence between the observed and adjusted $N^2(z)$ profiles is suggestive of baroclinic adjustment, such a correspondence does not demonstrate that the observed profile does occur because of a tendency by the eddies to minimize the zonal mean flow's instability. The first section of this chapter presents model results which show that the vertical eddy flux can produce a baroclinic adjutment by altering $N^2(z)$ as outlined in Chapter II. The second section reviews some of the model results presented in Chapter IV in terms of the baroclinic adjustment, showing why the strong eddy solutions category occurs and discussing the implications of the adjustment for model sensitivity. The model results suggest that the observed $N^2(z)$ profile occurs because eddies attempt to produce a

baroclinic adjustment involving $N^2(z)$ but other physical processes, most notably those controlling the temperature structure near the surface, prevent them from succeeding completely.

1. Stable Model Solutions

The model results in this section are all from a simplified version of the model, the E model, in which the only physical process is the interaction between the eddy flux and the vertical temperature structure: the E model has no radiation and no convection. E model runs evolve until the specified wave becomes stable. Unless stated otherwise, for E model runs, the initial [T](z) is the 1.5 E_w most relevant mode solution (Figures 4.2 and 4.4), the eddy has a 1.5 E_w amplitude, and all other input parameters have their winter values.

Figure 5.1 shows the evolution of the growth rate, kc_i, in E model runs using different specified wave numbers. In each run, the wave eventually becomes stable. When the $n_z = 3$ run becomes stable, all waves are stable. For all wave numbers greater than 6, the wave becomes stable in less than a day of model time.

Figure 5.2 compares the stable state produced by the $n_z = 3$ E model run with the E model's initial state. Because convective heating is absent, the eddy flux cooling causes the largest changes in the temperature structure to occur near the surface: T(0) decreases greatly, by 70 K, while $N^2(0)$ increases greatly. Furthermore, N^2 near the surface increases in a special way, nearly causing the potential vorticity gradient (Figure 5.2c) to vanish in the model's lower 5 km when the flow becomes stable. The adjustment to stability is in the

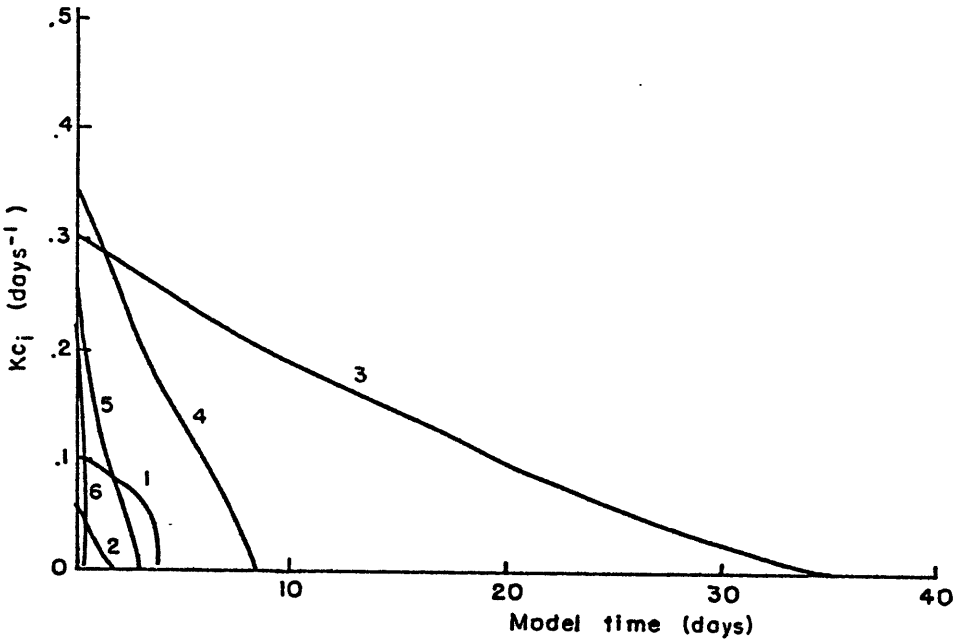


Fig. 5.1 - Growth rate kc_i as a function of model time for E model runs using various wave numbers, the number on each curve identifying the wave number used.

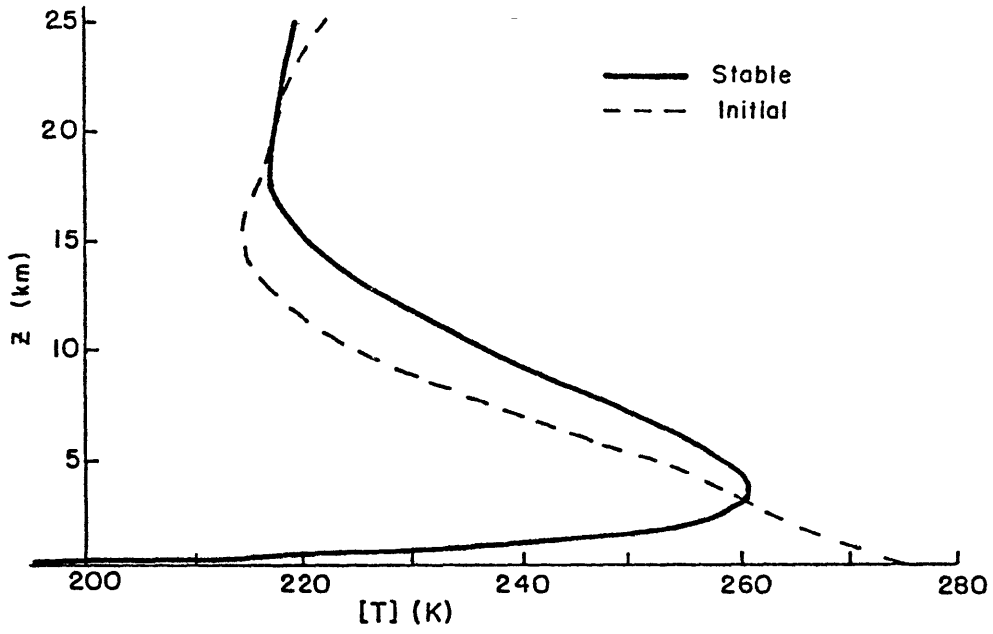


Fig. 5.2a - [T](z) for the initial state in the E model and for the stabilized state given by the $n_z = 3$ E model run.

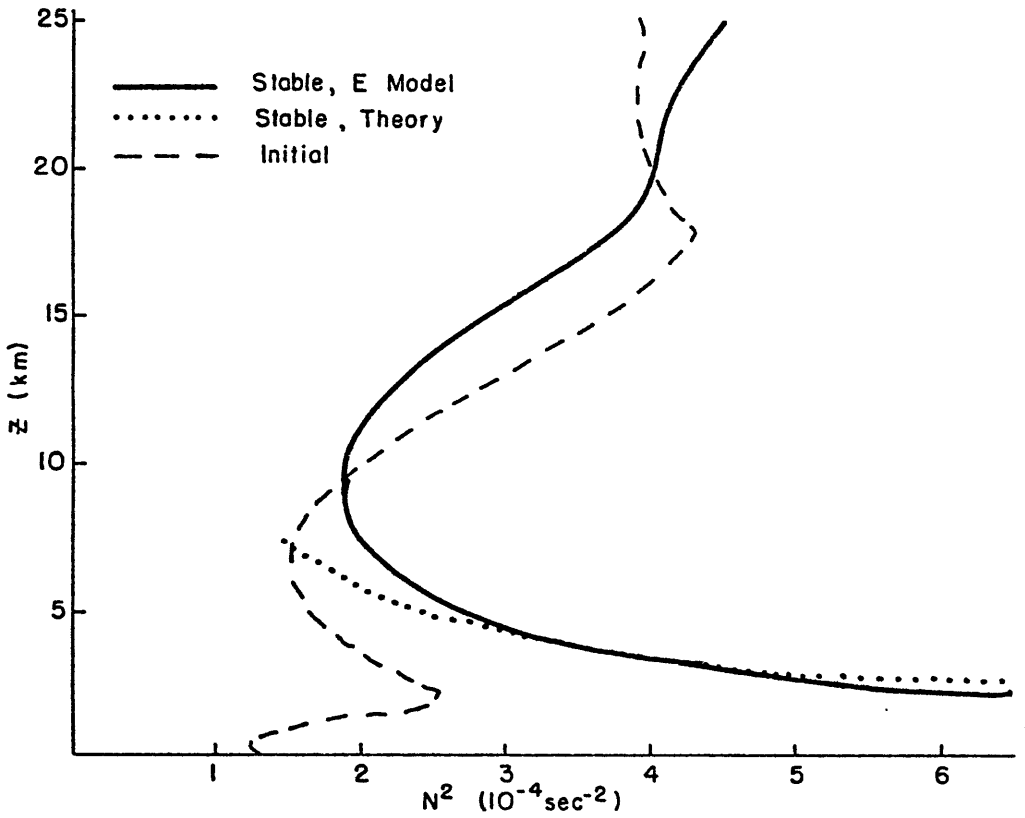


Fig. 5.2b - Like Figure 5.2a, but for $N^2(z)$. Also shown is $N^2(z)$ for a stabilize state according the adjustment theory in Chapter II.

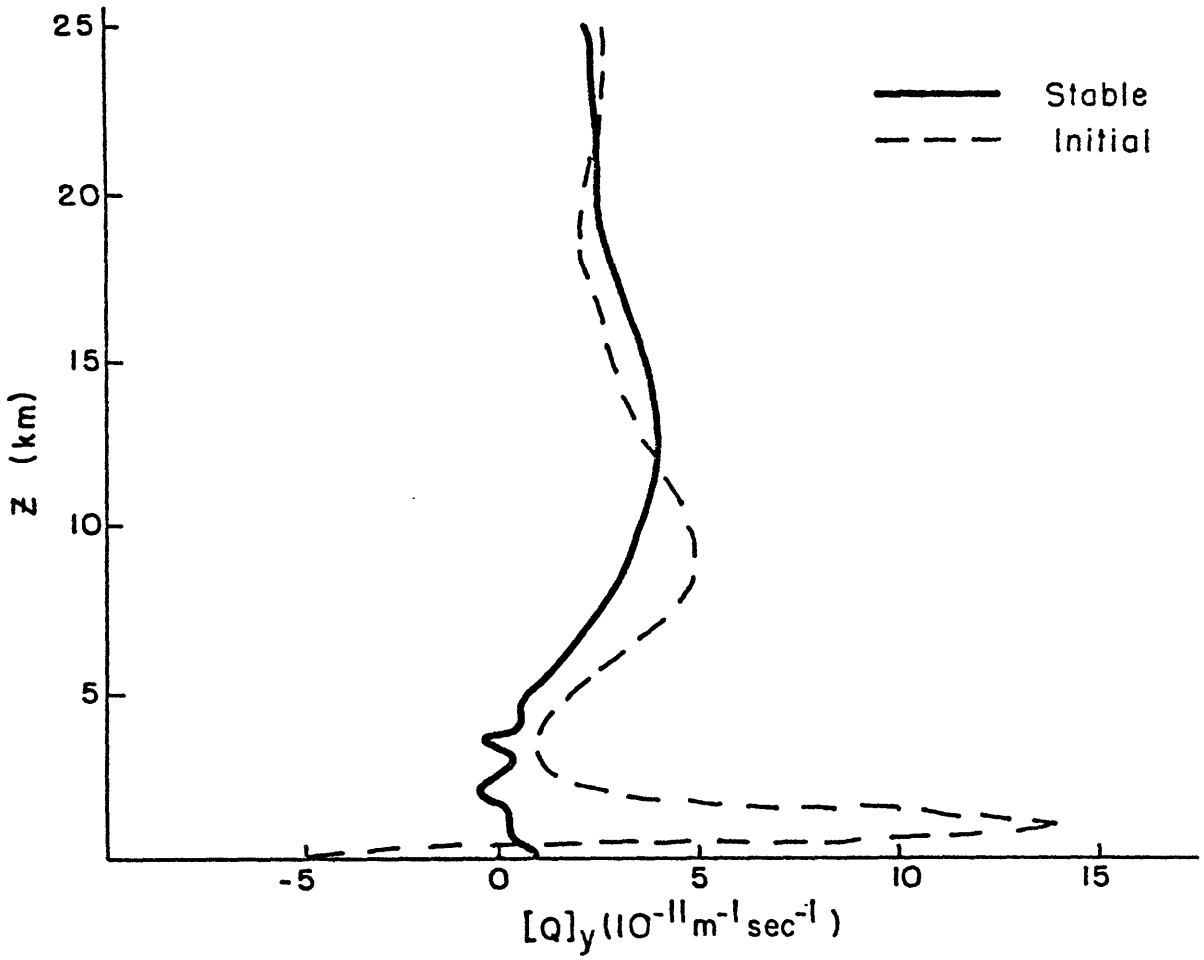


Fig. 5.2c - Like Figure 5.2a, but for $[Q]_y(z)$.

manner described in Chapter II: the potential vorticity gradient becomes relatively small over some adjstment depth extending up from the surface.

$[Q]_y$ changes relatively little above 5 km, the largest change occurring in the vicinity of 10 km. Discussion in section 2 of the previous chapter shows that the model's vertical eddy heat flux between the flux maximum and the flux minimum tends to act like a down-gradient potential vorticity flux and to be proportional to the size of the potential vorticity gradient. For wave number 3, the vertical eddy heat flux should behave this way between 3 km and 15 km. Thus, the initial state in Figure 5c indicates that the vertical eddy heat flux should act most strongly like a down-gradient meridional potential vorticity flux in the vicinity of 10 km. There is a correspondence between size of the effective down-gradient flux and the relatively large change in $[Q]_y$ that occurs at 10 km, but the greatest change in $[Q]_y$ occurs at 1 km. For the n_z = 3 E model run described here, the eddy flux is always cooling the atmosphere at 1 km. According to (2.3.4), the eddy flux should have a tendency to increase $[Q]_y$ near the surface, if anything. Thus, (2.3.4) appears to provide a useful diagnostic for understanding the $\rho[w^*\theta^*](z)$ profile between the flux maximum and minimum (Chapter IV, section 2), but it does not enable one to predict the time evolution of $[Q]_y(z)$.

From the discussion in Chapter II, the zonal mean state may be stable if $N^2(0) \to \infty$. The model cannot achieve such a condition, since N^2 tending to infinity would require a change in temperature between grid levels tending to infinity as well. However, an effective stability does occur: the flow's instability becomes so weak that the

model can not compute unstable phase speeds. In Chapter II, for $N^2(0) \to \infty$, the adjustment occurs over a layer $z_A = H_\rho \ln(\frac{1 + \gamma_0}{\gamma_0})$, where $\gamma_0 = \frac{\beta N_0^2 H_\rho}{f^2 [U]_z}$. If we use $N_0^2 = 1.5 \cdot 10^{-4}$ sec^{-2}, the local minimum in the initial state's $N^2(z)$ profile, then for the parameters of this run, $\gamma_0 = 0.86$ and $z_A = 7$ km. The predicted depth for stable flow agrees fairly well with the depth of $[Q]_y \approx 0$ in the model's effectively stable flow. Figure 5.2b also shows $N^2(z)$ for a completely stable flow: $N^2(0) \to \infty$, $[Q]_y = 0$ in the adjustment layer, using the parameter values of the E model run. As should be expected from Figure 5.2c, the effectively stable and completely stable curves compare well. The features shown in Figure 5.2 occur whenever the E model integrates to zonal mean flow stability starting from a variety of initial conditions. There is always a layer extending upward from the surface to about 5 km where $[Q]_y \approx 0$. Typically, the greatest changes in [T] and in N^2 between the initial and final states occur near the surface.

The vertical balance model has no interaction between eddy fluxes and the meridional temperature gradient. Since baroclinically unstable eddies do transport heat poleward, eddy fluxes in the atmosphere may tend to stabilize the flow more readily by adjusting the meridional temperature gradient. The meridional eddy heat flux does maintain the vertically-averaged meridional temperature gradient at a smaller value than it would be under radiative equilibrium, so that this flux causes the instability of the zonal mean flow to be less than it would be in radiative equilibrium. Yet, if we consider the changes in vertical profiles implied by an adjustment to stability, the discussion in Chapter II indicates that an adjustment of the $N^2(z)$ profile does occur in the atmosphere and that an adjustment of the $\frac{\partial}{\partial y}[T](z)$ profile does

not. Such a result may imply that atmospheric waves stabilize themselves more by altering $N^2(z)$ than by altering $\frac{\partial}{\partial y}[T](z)$. Gall's (1976b) wave-mean flow interaction study described in Chapter III shows eddy fluxes altering the zonal mean circulation toward stability mainly by adjusting $N^2(z)$ instead of $\frac{\partial}{\partial y}[T](z)$. Gall's model computes the time evolution of a flow consisting of a single wave and the zonal mean state. He removes all other physics from the model except friction, which appears primarily as a surface drag. Because his model is a GCM, its flow does not need to bequasi-geostrophic and, more important, the model can include temperature changes from both vertical and meridional eddy heat transports. For his wave-zonal mean flow interaction experiment using wave number 7, Gall shows the evolution of a form of the Richardson number,

$$Ri = \frac{[\alpha]}{[\theta]} \cdot \frac{\partial[\theta]}{\partial p} \Big/ \left(\frac{\partial[U]}{\partial p}\right)^2 ,$$

where $\alpha = 1/\rho$. The amount of zonal available potential energy and the degree of energy conversion by baroclinic instability both tend to vary as $(Ri)^{-1}$. As the flow evolves in the model, Ri increases greatly at the surface in mid-latidudes. Figure 5.3, taken from Figure 15 of Gall (1976b), shows that the increase is due primarily to an increase in his form of the static stability, $\frac{[\alpha]}{[\theta]} \cdot \frac{\partial[\theta]}{\partial p}$. His model's static stability evolves to a profile similar to the E model's static stability profile in Figure 5.2b, with the biggest changes during the model run occuring at the surface. In the vicinity of 700 mb, the change of $(\frac{\partial}{\partial p}[U])^2$ increases Ri by a factor of 2, but the Charney and Stern theorem shows that vertical and meridional temperature gradient changes at the surface can be more important since they affect the boundary

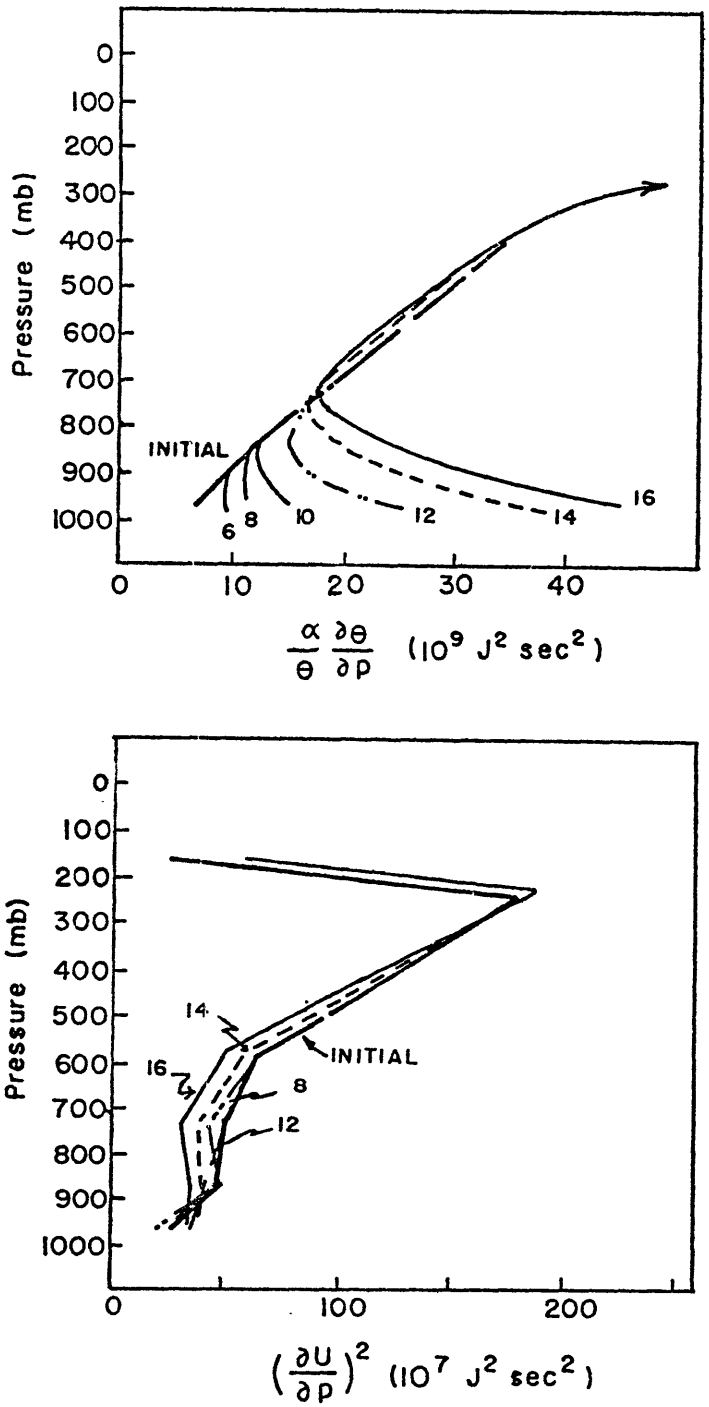


Fig. 5.3 - Gall's static stability and vertical wind shear squared as functions of pressure and time for his wave number 7 wave-mean flow interaction experiment. The data have been averaged between 35°N and 65°N. The numbers on the curves refer to the time in days from the beginning of the experiment.

term. In Gall's model, the $N^2(z)$ evolution increases Ri near the surface by a factor of 5 or better, while the wind shear evolution there has little effect on Ri.

Simmons and Hoskins (1978) also have performed wave-zonal mean flow interaction experiments in a GCM, but for inviscid flow. Their results differ from Gall's in that the meridional temperature gradient in their lowest level decreases substantially and even reverses in mid-latitudes. They note in passing that the static stability is "enhanced" in this region, as well. However, they do not present diagrams like Gall's showing the evolution of the vertical and the meridional temperature gradients; the relative changes of the two are not readily apparent.

Although the vertical balance model's eddy flux parameterizations are intended to represent the time mean flux, it is imteresting to note that the time evolution of the vertical flux in the E model is similar to that in Gall's wave-mean flow interaction study. Figure 5.4 shows the vertical flux at various times in the $n_z = 3$ E model run. As the flow evolves, the flux becomes less sharply peaked, as occurs in Gall's model (Figure 3.2). The E model flux peaks between 2.5 and 3.5 km. In Gall's model, the flux peaks at about the same level as in the E model during most of the evolution, with the flux maximum shifting to a higher level when the wave starts to decay in his model, at day 15. The linear instability parameterization, evolving with the temperature structure, appears to follow the nonlinear flux evolution of the GCM. An exact correspondence between the two fluxes should not be expected, of course, since the eddy's growth rate and the flux's amplitude in the GCM depend

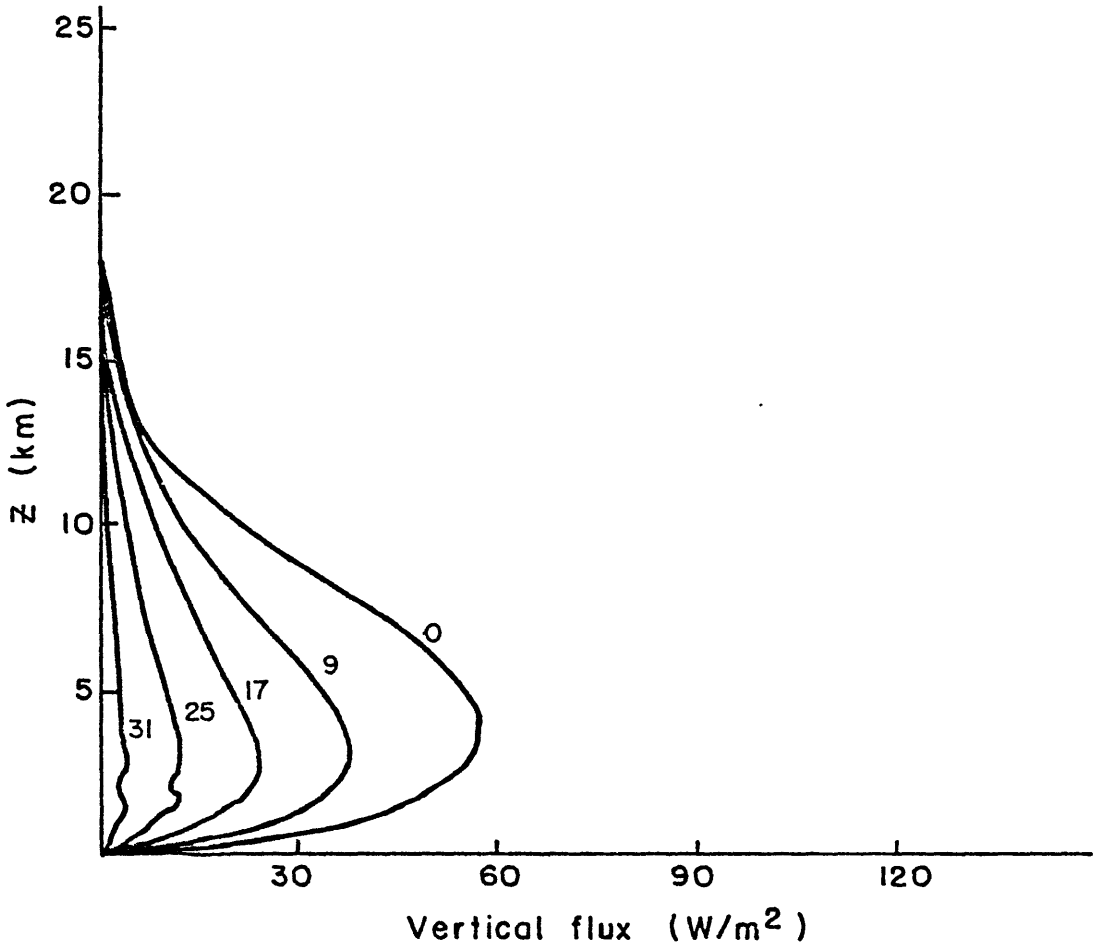


Fig. 5.4 - $[w^*\theta^*](z)$ as a function of time in the $n_z = 3$ E model run. The numbers on the curves refer to the time in days from the beginning of the run.

upon the recent history of the flow, while the eddy's growth rate and the flux's amplitude in the E model do not.

Simmons and Hoskins (1978) do not show the evolution of the vertical eddy heat flux in their wave-mean flow interaction study, but they do show the merdional cross section for the time-averaged vertical eddy heat flux from one of their experiments. Compared to the observed time-averaged vertical eddy heat flux (Figure 1.4), their averaged flux has a broader peak which occurs at a higher level. The vertical profile of their model's flux is similar to the E model's flux as the zonal mean flow approaches stability at days 17 and 25 in Figure 5.4. Their flux's vertical profile is also similar to the flux profile at day 16.5 in Gall's experiment (Figure 3.2), at which point the wave is decaying. Edmon et al. (1980) use the model of Simmons and Hoskins to compare time-averaged and linear instability fluxes. The contrast between the observed time-averaged flux and that in their model and the similarity betweeen their time-averaged flux and the vertical fluxes for zonal mean flows at or near stability are again indicative of the influence, discussed in Chapter III, that the strong eddy decay phase in the Simmons and Hoskins model has upon the time-averaged fluxes studied by Edmon et al. (1980).

Gall's model does not delineate between changes produced by the merdional flux heating and changes produced by the vertical flux heating. If the meridional heat flux decreases substantially with height, it can increase N^2 in the regions where it gives positive local heating and can cause $[Q]_y$ to decrease. The study of observed meridional eddy heat fluxes by Holopanien et al. (1982) discussed in Chapter II indicates that the meridional eddy heat fluxes do not tend to

decrease $[Q]_y$ in the lower atmosphere between 35°N and 55°N. Since Gall's GCM apparently has time mean eddy statistics similar to the observed (Gall, 1976a), we can perhaps conclude that in Gall's model the meridional eddy heat flux probably does not alter the static stability as strongly as the vertical eddy heat flux does.

In Figure 5.1, the short waves become stable very quickly. Figure 4.10 shows that in the initial state wave number 18 has a growth rate larger than wave number 3 has, but also that wave number 18 is much shallower than wave number 3. $[T](z)$ changes very little from its initial distribution when wave number 18 becomes stable, while $[T](z)$ changes by tens of degrees from the initial state when wave number 3 becomes stable. The quick stabilization with little alteration of the zonal mean temperature structure occurs because the short waves are much more sensitive to $N^2(z)$ near the surface than the longer waves are, as the comparison of Figures 4.10 and 4.11 in Chapter IV and the work by Staley and Gall (1977) indicate. Relatively small changes in temperature structure stabilize the shallow waves.

The relatively large growth rates and the relatively quick stabilization times of the short, shallow waves suggests that they may produce the short term fluctuations oberved by Stone et al. (1982). Their statistical model's show that the short term fluctuations can be characterized by baroclinically unstable waves with a growth rate ≈ 0.6 day^{-1} and by mean flow fluctuations with a damping time of ≈ 1.5 days. The short waves in the E model initially have growth rates of only 0.35 day^{-1}, but their growth rates are as large as any other wave's. Furthermore, since the short waves' growth rates are very sensitive to the temperature structure near the ground, small changes in the

temperature structure could likely give them growth rates as large or larger than the observed value. These waves then seem to be good candidates for the eddies producing the short term fluctuations observed by Stone et al. (1982).

2. Baroclinic Adjustment in the Full Model

The previous section shows that the interaction between the vertical eddy heat flux and the zonal mean flow can produce the N^2 adjustment described in Chapter II when the wave-mean flow interaction is the only physical processes in the model. The full model never produces a solution which is stable for all waves, indicating that radiation or convection or both constrain the flow to be unstable. Figure 5.5 gives a clue as to which of the two processes constrains the flow more strongly. This figure show the time variation of the growth rate in the $n_z = 3$ E model run, along with the time variation of the growth rate in two similar runs, one including radiation as well as the eddy flux, the E+R model, and one including convection as well as the eddy flux, the E+C model. The flow never stabilizes in either of the E+R or E+C models, but in the E+R model, the growth rate does decrease by a factor of two before becoming steady. In contrast, the growth rate remains essentially constant in the E+C model, indicating that some aspect of the convection process prevents the vertical eddy heat flux from stabilizing the flow.

For a strong eddy solution, such as the initial state for the three model runs in Figure 5.5, convection has a direct role in the solution's heat balance only in the lowest kilometer or two (e.g Figure

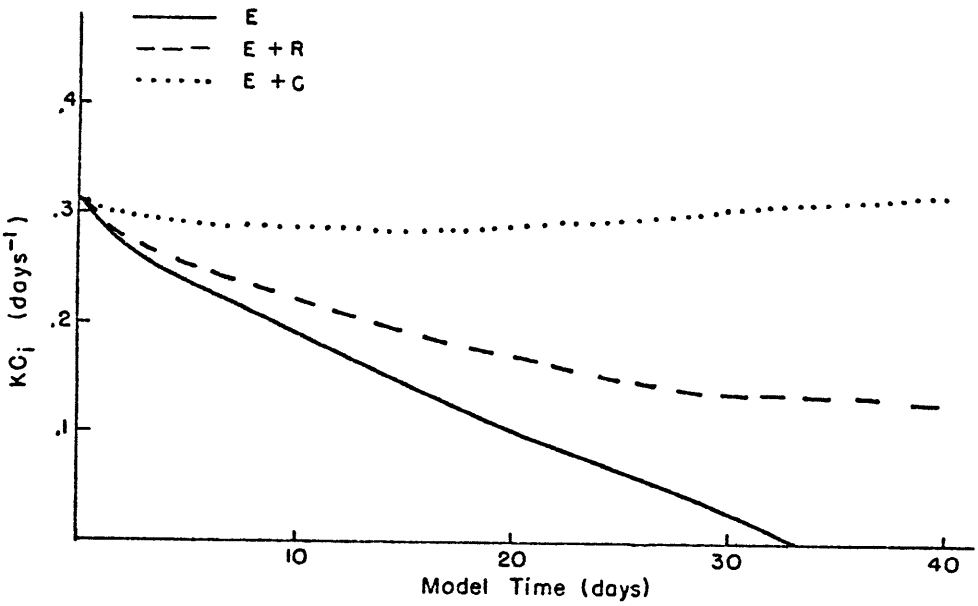


Fig. 5.5 - Growth rate kc_i as a function of time for the E, E+R, and E+C model runs, all using $n_z = 3$.

4.9). In the lowest kilometer, convection determines the temperature structure through the moist adjustment. The convective layer is relatively thin compared to the depth of deep unstable waves, and such a thin layer might seem incapable of having a strong influence on the flow's stability. Convection appears in the full model and in the E+C model because the ground temperature is fixed and because the model's convective adjustment in effect requires the air temperature at the surface to equal the ground temperature. In the model runs without convection, the E and E+R models, the air temperature at the surface may decrease by over 70 K (e.g. Figure 5.2a). Convection always occurs over at least the lowest 0.5 km in model runs that include it. Figure 5.6, for example, shows $N^2(z)$ in the $n_z = 3$ E+C model run after 40 days of evolution. In this run as in others which include convection, the convective adjustment causes N^2 near the surface to be only as large as a moist adiabat allows it to be, $\sim 10^{-4}$ sec^{-2}; $N^2(0)$ can not become large enough for the flow to be effectively stable. In the atmosphere, $[T](0)$ in mid-latitudes rarely, if ever, changes by 70 K over a 10 - 30 day period, the time for mean flow stabilization here and in Gall's (1976b) model. The results in Figure 5.5 suggest that processes controling temperature in the lowest kilometer of the atmosphere strongly constrain the flow from adjusting $N^2(z)$ to a baroclinically stable profile.

Figure 4.6 shows that vertical balance model solutions can have a layer of small $[Q]_y$ centered at about 3 km. This layer appears persistently for a variety of parameter choices. Figure 5.7 shows some other examples. The first two are model solutions for wave numbers 6 and 8, using a 1.5 E_w amplitude. The third example uses wave number

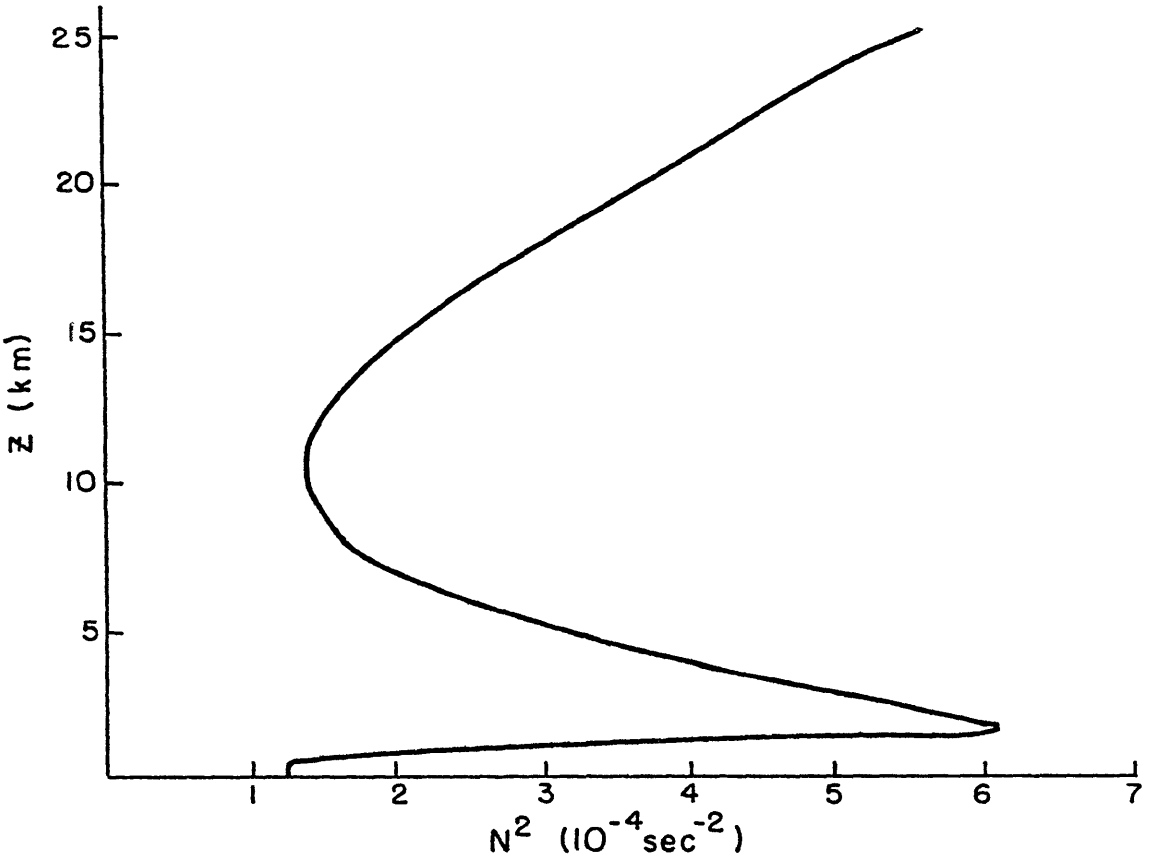


Fig. 5.6 - $N^2(z)$ after 40 days in the n_z = 3 E+C model run.

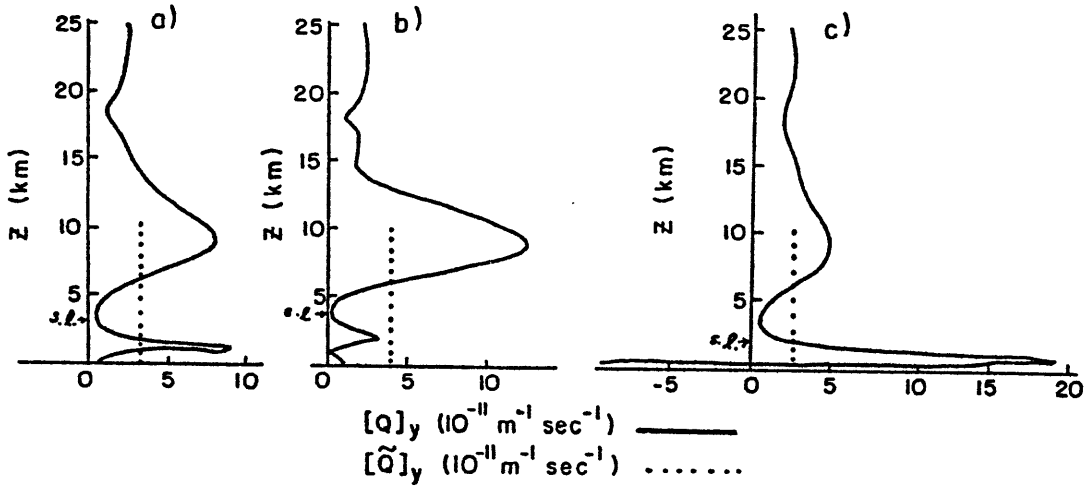


Fig. 5.7 - $[Q]_y(z)$ and $[\tilde{Q}]_y$ for three winter conditions solutions: a) 1.5 E_w n_z = 6, b) 1.5 E_w n_z = 8, and c) 1 E_w n_z = 4 with $Q_{Do}(z)$ at all levels equal to one half of Dopplick's cooling rates. Also shown is the steering level s.l. for each case.

4, with a 1 E_w amplitude and a specified radiative cooling, Q_{Do}, that is 50% smaller at all levels than the cooling computed by Dopplick (1979). For nearly all of the cases in Figures 4.6 and 5.4 $[Q]_y < [\tilde{Q}]_y$ in a layer 4 km deep centered at 3 km. The only requirement for the appearance of this layer in a winter conditions solution is that the solution must be a strong eddy solution. Figure 4.16 shows that the same layer can appear in summer conditions solutions even when the convective adjustment controls temperature in most of the troposphere.

In Figures 4.6 and 4.7, the steering level of the specified eddy tends to be in the region of the minimum. Lindzen et al. (1980) note that the down-gradient horizontal potential vorticity flux produced by a linearly unstable eddy tends to be centered about the steering level. This is the requisite down-gradient flux for growing disturbances described by Bretherton (1966). The vertical balance model has no interaction between horizontal fluxes and $[Q]_y$. However, the model results show that the vertical eddy heat flux tends to decrease $[Q]_y$ near the steering level, indicating that the vertical eddy heat flux also can minimize $[Q]_y$ in a layer centered about the steering level.

The close association of the steering level with the $[Q]_y$ minimum in the full model solutions is further indication that the relation between the vertical eddy heat flux and the meridional eddy potential vorticity flux derived in Chapter II serves as a useful diagnostic for understanding the variation of $\rho[w^*\theta^*]$ with height, but not as a useful guide for predicting changes in $[Q]_y$ produced by the vertical eddy heat flux.

The characteristics that define strong eddy solutions result from the vertical flux's attempt to stabilize the flow by adjusting $N^2(z)$.

Strong eddy solutions solutions all have a maximum in $N^2(z)$ near the surface, and $N^2(z)$ decreases with height above the maximum in such way that $[Q]_y$ is relatively small in the layer of decreasing N^2. The eddy heat flux in strong eddy solutions is generally much larger than it is in weak eddy solutions. The relatively strong eddy flux enables the eddy to play a dominant role in determining the lower atmosphere's vertical temperature structure. The E+C model run described above is an extreme case, for then there is no radiative cooling to counter the temperature changes caused by the eddy flux heating. Even with radiative cooling present, a strong eddy solution's eddy flux is strong enough to cause a tendency toward baroclinic stability to appear in the solution: there is a layer where $[Q]_y$ is small. Thus, all strong eddy solutions have similar $N^2(z)$ and $[Q]_y(z)$ profiles because the eddy flux attempts to adjust the temperature profile toward stability when the flux plays a significant role in determining the temperature structure. The weak eddy solutions have similar $N^2(z)$ because convection determines the temperature structure through the lower troposphere.

As the eddy flux becomes stronger, the N^2 maximum near 2 km in the strong eddy solutions becomes larger (Figure 4.4). The layer where $[Q]_y < [\tilde{Q}]_y$ changes relatively little, the major change being an increase in the $[Q]_y$ maximum corresponding to the increase in $\frac{\partial N^2}{\partial z}$ just above the layer of convection as the N^2 maximum increases. The difference between $N^2(z)$ in a strong eddy solution and the effectively stable $N^2(z)$ is greatest in the lowest 5 km (e.g. Figure 5.2b). Since the eddy flux tends to stabilize the zonal mean flow, as its strength increases, it tends to increase the size of $N^2(z)$ near the surface,

hence the largest changes in N^2 tend to occur in the lowest few kilometers of the troposphere as the eddy amplitude increases (e.g. Figure 4.4). As part of the adjustment toward stability, the eddy flux also tends to minimize $[Q]_y$ in the lower atmosphere. With constant $[U]_z$, small $[Q]_y$ implies a particular $N^2(z)$ profile. Thus, as the specified amplitude becomes larger, the $N^2(z)$ profile approaches the effectively stable profile. The effectively stable profile is an envelope limiting the increase of N^2 at all levels in the model's troposphere as the strength of the eddy flux increases. Since the greatest changes in N^2 occur below 5 km as the strength of the eddy flux changes, the mean lapse rate between 5 km and 10 km changes relatively little when the specified eddy EKE becomes large compared to the observed EKE, as noted in Chapter IV (Figure 4.6).

The limiting envelope of the stable $N^2(z)$ profile causes the negative feedback between the eddy flux and the temperature structure to become stronger as the eddy amplitude becomes larger. Figure 5.8 shows the variation with specified eddy amplitude of the eddy heat flux maximum, the eddy's growth rate kc_i, and the vertical mean Brunt-Vaisalla frequency squared $\tilde{N}^2$ (equation 4.1.1) in model solutions for $n_z = 4$ using winter conditions. As the EKE increases, the flux maximum increases, but more and more slowly. The growth rate decreases as the EKE increases, causing the peak eddy flux to increase at a progressively slower rate as the EKE increases. N^2 also increases as the EKE increases, and $\tilde{N}^2$ levels off even more quickly than the flux maximum does. The constraint imposed by the effectively stable $N^2(z)$ profile allows N^2 to increase greatly with increasing EKE only near the surface. Consequently, $\tilde{N}^2$ changes very little. Thus, doubling the EKE

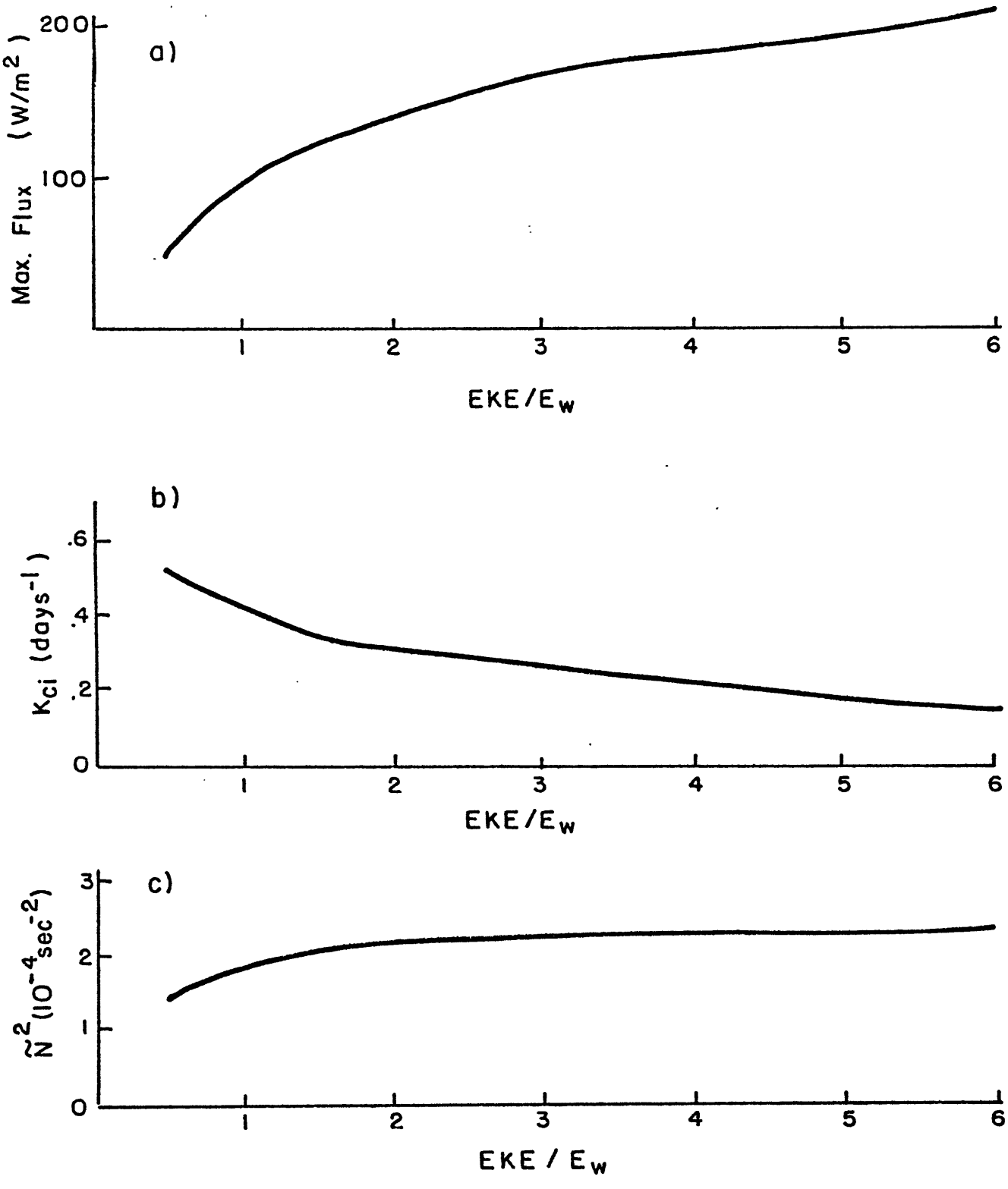


Fig. 5.8 - The variation with specified EKE of a) the maximum eddy flux, b) the growth rate $\tilde{kc}_i$, and c) the vertical mean Brunt-Vaisalla frequency squared $\tilde{N}^2$ in winter conditions solutions using $n_z = 4$.

from 1 E_w to 2 E_w causes the peak flux to increase by 35% and $\tilde{N}^2$ to increase by 16%, but doubling the EKE from 3 E_w to 6 E_w only causes the peak flux to increase by 20% and $\tilde{N}^2$ to increase by 4%.

The increase of N^2 near the ground does not in itself ensure that the flow will become more stable. The E+C model's $N^2(z)$ shown in Figure 5.6 also has large N^2 near the ground, but the peak deep mode growth rate at this point in the run has nearly the same value as it has in the initial state. Comparison of Figures 5.6 and 5.2b suggests that the growth rate does not change partly because $N^2(0)$ does not change, but also partly because N^2 between 8 km and 20 km is lower than it is in the initial state. The model's radiative heating causes N^2 to change relatively little between most relevant mode strong eddy solutions as the eddy amplitude increases (e.g., Figure 4.4). When the radiative heating is absent, N^2 can decrease enough in the middle levels of the model that the growth rate does not change much despite the large increase of N^2 just above the surface. Note, however, that in the E model, which has no convection as well as no radiation, N^2 may decrease in the middle levels of the model, but $N^2(0)$ increases so strongly that the decrease of N^2 in the middle levels is of little consequence.

The vertical balance model's requirement on all solutions is that the heating rates of radiation, convection, and the eddies all balance. The model does not stipulate that the eddies alter N^2 so that the $N^2(z)$ profile shows a tendency toward a baroclinically stable profile in the equilibrium state. For example, if the eddy flux heating is too strong compared to the radiative cooling, the model may cause the eddy heat flux to weaken by causing the vertical mean Brunt-Vaisalla frequency $\tilde{N}^2$ increase without necessarily causing $N^2(z)$ to shift toward an

effectively stable profile. Because the model computes a static equilibrium where the heating rates balance at each level, we might wonder how the model is able to obtain a balance between the heating rates and still have enough freedom to allow $N^2(z)$ to show a tendency toward a stable profile. A similar time mean $N^2(z)$ profile in the atmosphere is not as surprising, because one could envision the observed $N^2(z)$ profile resulting from a statistical equilibrium like the following. Heating by the eddies could adjust $N^2(z)$ to an effectively neutral profile, causing the eddy flux heating to diminish greatly or to disappear. Radiation could then cool the atmosphere so that the flow became unstable again, with the result that the eddy flux heating would cause $N^2(z)$ to approach an effectively stable profile again. The time mean profile could be similar to the effectively stable $N^2(z)$ because the eddies have relatively fast growth rates compared to radiative damping times; the repeated action of a succession of unstable waves could maintain $N^2(z)$ near the neutral profile. Boundary layer process could prevent $N^2(z)$ from being near the effectively stable profile in the lowest 1 - 2 km.

A more strict convergence criterion might show a statistical equilibrium to be occurring in the model, too, but the variations of heating rates and temperature with time would have to be very small. How does the model compute a solution balancing the heat fluxes which also has $N^2(z)$ varying with height through part of the troposphere like a baroclinically stable profile? The answer may lie in the relative sensitivities of the eddy heating and the radiative cooling to changes in the temperature structure.

The radiative cooling in the model is given mostly by the specified cooling, Q_{Do}, with a Newtonian damping providing a small modification to the specified cooling. The Newtonian damping term varies with temperature [T]. The eddy flux, on the other hand, is more a function of N^2 than [T], partly because the growth rate is a function of N^2. The eddy flux heating is thus more sensitive to changes in the temperature structure than the radiative cooling is, since the eddy flux heating is more dependent on higher order derivatives of [T](z) than the radiative cooling is. For a strong enough eddy amplitude, the model's eddy flux computed from, say, a constant $N^2(z)$ profile may produce a heating rate that is too large compared to the radiative cooling rate. The flux weakens as the growth rate decreases, so that changes in temperature structure which lower the growth rate can reduce the strengh of the eddy flux heating, bringing it into balance with the radiative cooling. Part of this change in temperature structure may simply be an increase in the vertical mean N^2, but part of the change is also a change in $N^2(z)$ such that $[Q]_y \approx 0$ in some layer near the surface. Because the eddy flux heating is more sensitive to these changes in the temperature structure than the radiative cooling is, the eddy can adjust the temperature structure so that its flux's heating matches the radiative cooling. Thus, in strong eddy solutions, the higher sensitivity enables the eddy heat flux to alter the temperature structure to produce a balance between the radiative cooling and eddy flux heating and, at the same time, alter the temperature structure such that $[Q]_y$ is relatively small in some layer. A radiative transfer computation may show the radiative cooling to be more sensitive to the details of the temperature structure than the radiative cooling in the

model is. If that is the case, then if the model were to use a radiative transfer computation for the radiative cooling, the model might not find a static balance as it does now, but a dynamic balance as discussed above might occur.

A motivation in Chapter II for considering an adjustment of $N^2(z)$ to make the flow baroclinically stable was the two-layer statistics presented by Stone (1978b) for the atmosphere. Does the adjustment in the E model or the tendency toward adjustment in the full model correspond to the two layer adjustment observed by Stone? We can answer this question by considering the values given by model solutions for a two-level mode stability parameter.

In a two-level model, the zonal mean flow is baroclinically stable unless the wind shear exceeds a critical shear. Thus, instability requires

$$\Delta U \equiv [U](z_1)-[U](z_2) > \Delta U_c \equiv \frac{\beta g}{f^2}\cdot\left(\frac{[\theta](z_1)-[\theta](z_2)}{[\theta](z_{mid})}\right)\cdot\left\{\frac{d_2\rho(z_2)}{\rho(z_{mid})}\right\} . \quad (5.2.1)$$

The level z_{mid} divides the flow into two layers of equal mass, where d_1 is the depth of the upper layer and d_2 is the depth of the lower layer. Similarly, the levels z_1 and z_2 are the mid-levels by mass of their respective layers. Other symbols in (5.2.1) have the same meaning as in Chapter II (cf. Table 2.1). When applying (5.2.1) to the vertical balance model, the top of the two-level model is the vertical balance model's tropopause, z_T.

If the density scale height is H_ρ, then the quantity in braces in (5.2.1) is H_ρ times an order 1 function of H_ρ and the tropopause height z_T. Thus, dividing (5.2.1) by (z_1-z_2), the flow is marginally stable if

$$[U]_z\left(\frac{1}{N_{00}^2}\right) \sim \frac{\beta H_\rho}{f^2} \quad , \tag{5.2.2}$$

where N_{00} is a Brunt-Vaisalla frequency that is constant with height. The adjustment described in Chapter II alters $N^2(z)$ over some adjustment depth z_A so that the flow is stable. The degree of baroclinic instability tends to vary with $1/N^2$. Computation of the mass-weighted mean value of $1/N^2$ averaged over the adjustment depth yields, for stable flow,

$$\left(\hat{\frac{1}{N^2}}\right) \equiv \frac{\int_0^{z_A} \rho/N^2 \, dz}{\int_0^{z_A} \rho \, dz} = \frac{\beta H_\rho}{[U]_z f^2}\left\{(1+\gamma_0)\ln\left(\frac{1+\gamma_0}{\gamma_0}\right) - 1\right\} \quad , \tag{5.2.3}$$

where γ_0 is a function of the unadjusted state (Table 2.1). The quantity in braces in (5.2.3) is an order 1 function of γ_0 for $10^{-2} \lesssim \gamma_0 \lesssim 1.5$, and a typical atmospheric value of γ_0 is 0.7. Thus, for a range of γ_0 values encompassing values characteristic of the atmosphere,

$$[U]_z\left(\hat{\frac{1}{N^2}}\right) \sim \frac{\beta H_\rho}{f^2} \quad . \tag{5.2.4}$$

The adjustment gives a relationship between $[U]_z$ and the vertical mean N^2 in the adjustment layer that is similar to the two-layer criterion for neutral stability.

We can evaluate the ability of the vertical eddy heat flux to produce model solutions near two-level baroclinic stability by considering the variation under parameter changes of the stability parameter

$$S \equiv \frac{\Delta U - \Delta U_c}{\Delta U_c} \quad ,$$

which measures the flow's two-level supercriticality in comparison to the critical shear, ΔU_c. The flow unstable in a two-level model sense, or supercritical, when S is positive. The flow is strongly supercritical if $(\Delta U - \Delta U_c) > \Delta U_c$, or $S > 1$, and it is near neutral stability if $\Delta U \approx \Delta U_c$, or $|S| \ll 1$. When the E model reaches stability in the $n_z = 3$ run, $S = -0.16$: $N^2(z)$ changes so that the actual wind shear is close to the critical wind shear, as might be expected from the discussion of (5.2.2) and (5.2.4).

Figure 5.9 shows how S varies with specified wind shear in full model solutions using winter conditions and the EKE ≈ ZAPE closure. Values of S for this particular closure are shown because this closure includes a dependence of the eddy amplitude on the strength of the wind shear, the closure presumably giving a more complete representation of the eddy-mean flow interaction than the specified EKE closure does. The figure shows S as a function of wind shear for most unstable mode solutions, for most stabilizing mode solutions, and for RCE solutions. $([U]_z)_w$ is the vertical balance model's standard winter zonal wind shear. Under both selection criteria, the solutions providing S for $[U]_z/([U]_z)_w < 1.25$ are weak eddy solutions, and those providing S for $[U]_z/([U]_z)_w > 1.25$ are strong eddy solutions, the solutions for $[U]_z/([U]_z)_w = 1.25$ being transitional cases between either category. For the weak eddy solutions, $S \geq 2$ and S is about the same as the RCE S. The difference between ΔU and ΔU_c is larger than ΔU_c itself; the flow is highly supercritical. For the strong eddy solutions, $S \sim 0.5$, much less than the RCE S for the same wind shears. The flow in strong eddy solutions is generally supercritical, but much less than for the weak eddy solutions. S also does not display as much dependence upon

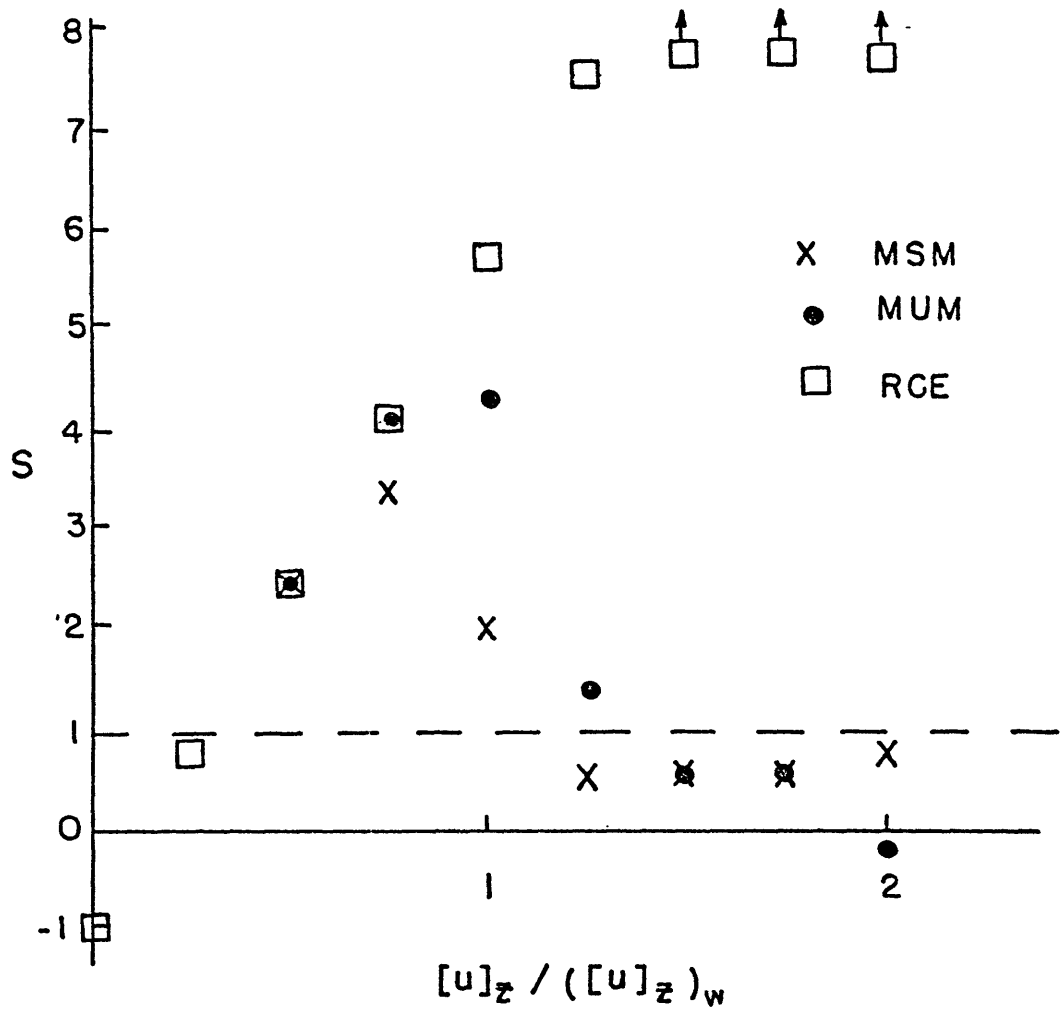


Fig. 5.9 - S as a function of $[U]_z$ for most stabilizing mode (MSM) solutions, most unstable mode (MUM) solutions, and RCE solutions.

$[U]_z$ in the strong eddy cases as it does in the weak eddy cases. As a first approximation in the strong eddy cases, $\Delta U \sim \Delta U_c$. When the eddies have relatively little influence on the $N^2(z)$ profile, the model solutions are strongly supercritical. When the eddies have a strong influence, the model solutions chosen by the selection criteria are relatively close to two-level model neutrality.

CHAPTER VI

SUMMARY AND SPECULATION

This thesis has presented a study of the interaction between vertical eddy heat fluxes and the temperature structure of the mid-latitude troposphere. The eddy fluxes result from baroclinic instability and tend to stabilize the zonal mean flow with respect to baroclinic instability. Much of the work presented here has been guided by the hypothesis that the tendency to stabilize the zonal mean flow should be visible in the time-averaged observed zonal mean flow, the baroclinic adjustment hypothesis.

Stone (1978b) has shown a corrrespondence between a two-layer model parameter for neutral baroclinic stability and two-layer statistics of the zonal mean atmosphere. Chapter II presents an investigation of zonal mean flow neutralization in a continuous atmosphere, using the Charney and Stern (1962) theorem. Lindzen et al. (1980) show how the zonal mean flow can be stabilized by adjusting the vertical profile of the zonal wind shear $[U]_z(z)$, while holding the Brunt-Vaisalla frequency N^2 constant. In Chapter II, consideration is given to an adjustment in which $N^2(z)$ is adjusted while $[U]_z$ is held constant, giving an adjusted profile $N_A^2(z)$. Both adjustments require $[U]_z/N^2 = 0$ at the surface, and both require the meridional gradient of quasi-geostrophic vorticity $[Q]_y$ to equal zero in an adjustment layer extending from the ground through an adjustment depth z_A. For the N^2 adjustment, the surface condition means that $N^2 \to \infty$ smoothly as $z \to 0$; a complete stabilization of the flow by this

adjustment is not realistic. Instead, it is hypothesized that an effective stabilization can occur: if $N^2(z)$ is similar to $N_A^2(z)$, then the flow may be only weakly unstable, so that friction in the atmosphere or grid resolution in a numerical model would prevent the instability from being realized. Thus, a similarity between $N_A^2(z)$ and $N^2(z)$ in the atmosphere or in a model could indicate a tendency of the eddy flux to stabilize the zonal mean flow.

The N^2 adjustment compares better with observations than the $[U]_z$ adjustment does. The N^2 adjustment shows a correspondence with the observed $N^2(z)$ in the lower atmosphere both in the height variation of $N^2(z)$ and in the depth over which the adjustment occurs. The comparison is hindered by the relatively low resolution of climatological statistics available.

Two important scales controlling features of the N^2 adjustment are the density scale height H_ρ and the scale h_β, where

$$h_\beta = \frac{\beta N^2(0)}{f^2 [U]_z} \quad .$$

These scales appear because the flow's dynamics are determined by the quasi-geostrophic potential vorticity equation. The adjustment depth z_A, the vertical decay scale for $N_A^2(z)$, and the adjustment's change of the zonal available potential energy (ZAPE) are all governed by these two scales. The N^2 adjustment does not need $[Q]_y = 0$ in the adjustment layer, only $[Q]_y = \beta_0$, where $\beta_0 \geq 0$. Further study shows that the adjustment depth is shallowest and the change in ZAPE is the least when β_0 equals zero as opposed to some positive constant. This result suggests that if β_0 were equal to a function of height, then

$\beta_0(z) \equiv 0$ would give the adjustment producing the least change of the zonal mean flow.

Chapter II also presents a scaling analysis of the zonally-averaged thermodynamic equation, using scales for eddy fluxes suggested by studies of linear baroclinic instability and by observations. The analysis shows that the heating produced by the vertical eddy heat flux can be as important as that produced by the meridional eddy heat flux. The vertical eddy heat flux term does not appear in the zonally-averaged quasi-geostrophic thermodynamic equation. The analysis shows how averaging operations may alter the relative sizes of terms in an equation so that terms considered unimportant before averaging can become important after averaging. The scales used still allow the momentum and thermodynamic equations for eddies to have the usual quasi-geostrophic form. As a consequence, the eddies still obey the quasi-geostrophic potential vorticity equation.

In order to investigate further the N^2 adjustment and its implications for the atmosphere, a model is developed in Chapter III for the atmospheric heating balance in the vertical direction. The basis of the model is Hantel's (1976) study indicating that, as a first approximation, the thermodynamic balance in the mid-latitude troposphere above the boundary layer is primarily between divergences of vertical heat fluxes. By highlighting the importance of the vertical eddy heat flux, the scaling analysis in Chapter II supports this approximation. The model developed in Chapter III computes vertical temperature structures in which the heating rates by vertical eddy heat fluxes, convection, and radiation all balance.

Since the primary intent of the vertical balance model is to study the interaction between the vertical eddy heat flux and the vertical temperature structure, the eddy flux has the most detailed parameterization. The eddy sensible heat flux parameterization consists of two parts: a vertical structure determination and an amplitude determination. A linear instability computation that includes the model's $N^2(z)$ profile provides the sensible heat flux's vertical structure. The time variation of the vertical heat flux profile in a GCM wave-mean flow interaction experiment performed by Gall (1976b) supports the use of a flux profile based on linear instability. Flux parameterizations whose vertical structures are based on linear stability computations have been used with success by Stone (1972), Mullan (1979), and Branscome (1980). Edmon et al. (1980) have raised objections to parameterizations of the time mean flux based on linear instability computations, but their objections appear to be model dependent and may not apply to the atmosphere. The eddy amplitude is determined by a closure assumption. One closure assumption used is Branscome's (1980), which states that the time mean eddy kinetic energy should equal the zonal available potential energy measured over the radius of deformation, or EKE $\approx$ ZAPE. Another closure assumption used simply specifies the EKE. Most of the examples discussed in Chapters IV and V use the specified EKE closure, but there is little difference between the properties of balance states produced by either. The model's eddy latent heat flux is proportional to the model's sensible heat flux and is obtained by a parameterization proposed by Leovy (1973) for Mars and applied to the earth by Mullan (1979).

Most model computations use a single specified wave to obtain the eddy flux, but the model also performs some computations using ensembles of waves. Guided by observational and theoretical studies, the model neglects direct interactions between different waves in the ensemble, computing each individual wave's flux by a separate zonal mean flow instability computation.

The model's convection is an adjustment to a saturation moist adiabatic temperature profile, the particular moist adiabat used being one having the same surface temperature as the model's temperature profile. This adjustment is suggested by a comparison of observed temperature profiles with moist adiabats. Whenever the model's temperature at some level is less than the moist adiabat's, the temperature is increased to match the moist adiabat's. The heating implied by this adjustment is interpreted as the divergence of an upward convective flux that originates as a flux of heat across the lower surface.

The model's radiative heating is given by Dopplick's (1979) computations for 45°N, to which a correction is added to account for the difference between the model's temperature profile and the temperature profile used by Dopplick in his computations. The correction is a Newtonian damping that uses the difference between the two temperature profiles and a damping time which depends on this difference to compute a heating rate.

Other quantities depend upon processes neglected in the vertical balance model. These quantities, such as zonal wind shear and surface temperature, are specified. Part of the work with the model seeks to determine the extent to which the model can produce balanced states

which are consistent with the specified parameters used. The specified parameters are based on observations or results from other models.

Chapter IV describes properties of the equilibrium states obtained by the vertical balance model and compares the states with observations and other models, the consistency check. Unless using a wave ensemble, the model computes an equilibrium state, or solution, using a single specified wave number. Thus, for a given set of input parameters, a number of different solutions are possible, depending on the wave number specified. Two different selection criteria are presented for choosing what is termed the most relevant single mode solution for the set of input parameters. One is the solution produced by the linearly most unstable mode; the other is the solution produced by the mode which stabilizes the zonal mean flow the most. Solutions chosen by either of these two criteria receive the most attention.

A model solution using winter conditions falls into one of two categories, termed strong eddy solutions and weak eddy solutions. For strong eddy solutions, the heating balance is predominantly between eddy flux heating and radiative cooling. These solutions have $N^2(z)$ decreasing with height through most of the lower troposphere in such a manner that there is a minimum in the $[Q]_y(z)$ profile centered around the specified wave's steering level. These two features appear because of the tendency for the wave to stabilize the zonal mean flow by the N^2 adjustment investigated in Chapter II. Long waves require a larger amplitude to produce a strong eddy solution than short waves do. Wave ensemble model runs that fall into the strong eddy solution category need even greater amplitudes. For weak eddy solutions, the convective adjustment is more important for determining the temperature structure

in the lower atmosphere. These solutions have $N^2(z)$ profiles that resemble $N^2(z)$ in the model's radiative-convective equilibrium (RCE), and their $N^2(z)$ profiles do not show a tendency toward mean flow stabilization by the N^2 adjustment. Weak eddy solutions tend to have weaker eddy fluxes than the strong eddy solutions have.

Another distinguishing feature of strong eddy versus weak eddy solutions is the degree of agreement between the two most relevant single mode selection criteria. For strong eddy solutions, the wave number producing the most unstable mode solution is always about the same as the wave number producing the most stabilized solution. In contrast, for weak eddy solutions, the two criteria often select solutions produced by very different wave numbers. Pedlosky (1981) presents results using weakly nonlinear baroclinic instability theory which indicates that the most unstable mode may only rarely be the mode that causes the greatest zonal mean flow stabilization. However, he does not determine the most unstable mode in his model's equilibrated states, only in the initial state. In principle, one can construct an initial state to have whatever wavelength desired be the most unstable mode, so that the most unstable mode for some specified initial state may not have much bearing on a study of wave-zonal mean flow interaction. Analysis of the vertical balance model's solutions compares growth rate spectra for equilibrium states produced by a wave-zonal mean flow interaction. The analysis suggests that, when the waves are allowed to interact with the zonal mean flow in a model with forcing and dissipation, the wave producing the most stabilized zonal mean flow will tend to have about the same wavelength as the most unstable mode in the equilibrium state. The selection of similar

wavelengths occurs most consistently when the eddies play a major role in the heating balance, as in the strong eddy solutions.

The most relevant single mode solution for winter conditions gives a vertical temperature structure that compares well with observations. Wave ensemble solutions suggest however that waves longer than the most relevant single mode are necessary to produce N^2 as large as observed in the upper troposphere. The longer waves tend to be deeper and, thus, can carry more heat to higher levels, resulting in larger N^2 there.

The model can also produce solutions for summer conditions which correspond to either strong eddy solutions or weak eddy soluions. However, there are solutions for summer conditions which do not fit into either category. For these solutions, convection determines $[T](z)$ over most of the lower troposphere, except in a layer between 3 km and 6 km, where the convective heating is zero and the eddy flux heating and the radiative cooling balance. In the layer between 3 km and 6 km, the eddy flux causes $N^2(z)$ and $[Q]_y(z)$ to show the features reminiscent of an N^2 adjustment. The model solutions most closely analyzed fall into this third category and their temperature structures compare well with the observed temperature structure. The comparison with observations indicates that waves shorter than the most relevant mode are important contributors to the heating balance determining the summertime vertical temperature structure.

The vertical balance model's most relevant mode solutions have $[T](z)$, $N^2(z)$, and $[Q]_y(z)$ like their observed profiles when the EKE is about the same size as its observed value; there is a consistency between the model results and the sizes of the observationally-based specified parameters. The consistency does not extend to all aspects of

the model, though. The model solutions give surface heat fluxes and combined fluxes by eddies and convection which agree fairly well with calculations of the corresponding fluxes in the atmosphere or in other models, but the model's partitioning of the combined flux between eddies and convection is not consistent with results from the other calculations: vertical balance model solutions tend to have the eddy flux too strong and the convective flux too weak. This discrepancy appears to be due to the model's convective adjustment being based on a zonal mean temperature profile. The zonally-averaged convective heating should be a function of local, not zonal mean, temperature profiles. The discrepancy is greater in winter conditions solutions than in summer conditions solutions, which is in accord with the observed summertime $[T](z)$ in mid-latitudes being similar to a moist adiabat below 10 km and the wintertime $[T](z)$ being rather different from a moist adiabat (e.g. Figure 3.6).

Held (1982) has hypothesized that mid-latitude eddies can adjust the lapse rate $\partial[T]/\partial z$ more readily than they can adjust the tropopause height, the tropopause height being determined by radiation. The model results suggest that this hypothesis is true only for a range of eddy flux strengths. As the flux becomes stronger, there is a tendency for a temperature inversion to appear near the surface. Up to the point where the inversion appears, the lapse rate tends to increase more rapidly with increasing eddy amplitude than the tropopause height does. As the eddy amplitude increases further after the inversion appears, the lapse rate continues to increase, but at a much slower rate, only about as fast as the tropopause height increases.

Chapter V gives an analysis of the vertical balance model solutions in terms of the N^2 adjustment. To understand more clearly the tendency of the vertical eddy flux to stabilize the flow, the chapter first presents the results of model runs where radiation and convection are neglected, leaving only the vertical eddy flux heating to alter $[T](z)$. These model runs evolve until the specified wave becomes stable. The state produced in this manner where all waves are stable is very similar to that produced by the N^2 adjustment: $N^2(z)$ decreases with height such that $[Q]_y \approx 0$ in a layer about as deep as predicted by the adjustment theory. The model's stable state is not strictly stable, for $N^2(0) \neq \infty$, but it is effectively stable, for the model's numerics find that no waves are unstable. Thus, the vertical eddy heat fluxes produce an effective stability in the model when heating by other processes is removed, the effectively stable state being very similar to the strictly stable state described in Chapter II.

Further model runs where either radiation or convection is reinstalled in the model show that convection acts as the greatest restraint against an eddy's tendency to stabilize the flow. The restraint appears to occur because the surface temperature is fixed in model runs where convection is included, allowing convection to determine $N^2(z)$ at the lowest model levels. As a consequence, $N^2(0)$ can not tend toward infinity as the flow evolves. The difference between the specified $[T](0)$ in a model run including convection and the $[T](0)$ in an effectively stable state is about 60 K. The atmosphere's $[T](0)$ rarely if ever changes by this amount in a few days, the time scale for baroclinic instability, suggesting that processes controlling surface temperature in the atmosphere prevent the N^2 adjustment from causing an

effective stability in the atmosphere. Radiation has less of an influence on the eddy's attempt to stabilize the the flow. In some cases, radiation appears to aid the eddy's stabilization of the flow by helping to maintain $N^2(z)$ in the upper troposphere at higher values than it might be if the eddy flux was to act alone on the temperature profile.

The strong eddy solutions presented in Chapter IV can be seen to result from an attempt by the eddy flux to stabilize the zonal mean flow. When the eddy flux plays an important role in the temperature balance, then the flux causes the features indicative of an attempt to stabilize the flow to appear: $N^2(z)$ decreases with height in such a manner that $[Q]_y$ is relatively small in part of the troposphere. The similarity of the temperature structures of certain strong eddy solutions with that of the atmosphere indicates that a similar adjustment occurs in the atmosphere.

Stone (1978b) has used two-layer statistics to suggest that a baroclinic adjustment occurs in the atmosphere. Two-layer stability has been investigated in vertical balance model solutions by using a two-layer model stability parameter that is positive when the flow is unstable. The parameter tends to be much larger in weak eddy solutions than in strong eddy solutions. In weak eddy solutions, the stability parameter has about the same value that it has in RCE solutions. In strong eddy solutions, the parameter is small enough to suggest that as a first approximation in these solutions, the critical wind shear for instability, a function of N^2, is equal to the actual wind shear, the relationship observed by Stone for the atmosphere.

Unstable waves transport heat upward and poleward, counteracting the tendency of radiation to increase the instability of the zonal mean flow. As a result, the vertically-averaged N^2 is larger than it would be in radiative equilibrium, and the vertically-averaged $\frac{\partial}{\partial y}[T]$ is smaller than it would be in radiative equilibrium: the instability of the mid-latitude flow is much less than it would be in radiative equilibrium. Yet for an unstable wave to become stable, changes in the vertical profiles of $N^2(z)$ and $\frac{\partial}{\partial y}[T](z)$ appear to be important, for these profile changes allow the flow to become effectively stable without requiring the zonal available potential energy to vanish. The appearance of features in the mid-latitude $N^2(z)$ and $[Q]_y(z)$ profiles indicative of zonal mean flow stabilization suggests that the N^2 adjustment is an important aspect of the wave-mean flow interaction in the atmosphere. The observed time-averaged profile of $N^2(z)$ could result because each wave stabilizes itself by adjusting $N^2(z)$ to an effectively stable profile, or it could result because a succession of waves tends to produce an effectively stable $N^2(z)$ profile, with individual waves stabilizing by some other means, perhaps by adjusting $[U]_z(z)$, so that no individual wave would produce an effectively stable $N^2(z)$ profile. The second case could occur, for example, if atmospheric radiation induced instability more by causing $[U]_z$ to increase than by causing N^2 to decrease. Then, N^2 would change relatively little during an eddy decay phase compared to the increase of $[U]_z$ during that period. Successive unstable waves could nudge $N^2(z)$ toward a stable profile. Although a growing unstable wave most likely alters both $N^2(z)$ and $[U]_z(z)$, we can wonder if changes in one or the other are more important for wave stabilization in the atmosphere. GCM

studies of baroclinic instability have not been conclusive. Gall's (1976b) results show an unstable wave stabilizing primarily by an alteration of $N^2(z)$, and Mudrick's (1982) study of wave evolution in numerical models indicates that changes in N^2 are at least an important part of the stabilization. Simmons and Hoskins's (1978) results however appear to favor stabilization primarily by the alteration of $[U]_z(z)$. Ghan's (1983) two-layer statistics for atmospheric fluctuations indicate that proportionately greater changes occur in $[U]_z$ than in N^2, but his two-layer statistics may not resolve important $N^2(z)$ changes in the lower atmosphere.

The vertical balance model cannot be used to determine whether the oberved $N^2(z)$ profile is a feature of atmospheric wave stabilization or whether the profile is only a feature of the cumulative influence of a succession of eddies. We can, however, consider the implications of either possibility. The implications are very important if unstable waves tend to stabilize by altering $N^2(z)$, for then models which fix $N^2(z)$ are missing an important part of atmospheric physics. Two-layer model studies of weakly nonlinear baroclinic instability are then especially deficient. Even the continuous atmosphere study by Pedlosky (1979) is then inadequate because his formulation of the problem does not include vertical eddy fluxes. As a result, the horizontally-averaged $N^2(z)$ can not change in his model as the unstable wave evolves. Two-level models which do allow N^2 to change are then inadequate because they only allow the vertical mean N^2 to change. A two-level model can not resolve any alteration of the $N^2(z)$ profile, which is an important part of the vertical flux interaction with the vertical temperature structure. Also, if waves stabilize primarily by

adjusting $N^2(z)$, then the meridional heat flux parameterization developed by Lindzen and Farrell (1980) is not valid, for atmospheric eddies then do not necessarily carry poleward the amount of heat needed to effect the $[U]_z$ adjustment, as Lindzen and Farrell hypothesize. This type of wave stabilization however would imply that an analysis of $N^2(z)$ might be useful in weather prediction, for it could indicate the likelihood of increasing eddy activity.

If unstable waves in the atmosphere stabilize primarily by altering $[U]_z(z)$, then the problems described above do not occur. In addition, the assumption of constant N^2 might be a reasonable approximation for use by models. A two-layer model, for example, could have its N^2 equal to the vertical mean of $N_A^2(z)$. However, if $N^2(z)$ adjustments are at least as important as $[U]_z(z)$ adjustments in a wave's stabilization, then the problems described above can be important.

The model results indicate that the tendency toward an N^2 adjustment is performed by waves with zonal wave number in the range $n_z = 3$ to $n_z = 8$. Discussion in Chapter IV shows that much shorter waves with wave numbers near $n_z = 18$ may have growth rates as large as the longer waves. In addition, discussion in Chapter V notes that these short waves, despite their relatively large growth rates, become stable very quickly when allowed to interact with the zonal mean temperature structure in the absence of convection and radiation. Further discussion suggests that such short waves may be the ones observed by Stone et al. (1982) to cause the relatively quick 1.5 day damping time for fluctuations of a two-layer model baroclinic stability parameter. We can perhaps think of the long waves, $n_z \approx 3 - 6$, and the short

waves, $n_z \sim 18$, as providing two different degrees of adjustment to the zonal mean flow. The long waves may cause a coarse tuning of the flow, producing the baroclinic adjustment of the time mean flow seen in the observed $N^2(z)$ profile and in Stone's (1978b) statistics. The short waves may participate in a fine tuning of the flow, growing relatively quickly to help damp out fluctuations in the flow which might otherwise increase its instability. Ghan (1983) has shown that the stability parameter fluctuations result primarily from fluctuations of $[U]_z$ rather than N^2. If his two-layer statistics are not missing potentially important $N^2(z)$ changes in the lower atmosphere, then his result is consistent with the observation in Chapter V that these short waves stabilize after causing only relatively small changes in the vertical temperature structure. However, if the short waves are important in causing the 1.5 day damping time in $[U]_z$ fluctuations to appear, then their merdional heat flux is not a direct cause, because Stone et al. remove the effect of the meridional eddy heat flux when they obtain this damping time. In their calculations, the meridional eddy heat flux has only a relatively weak direct influence on the fluctuation of the stability parameter, which may be consistent with the relatively shallow meridional heat flux produced by these waves.

In the scaling analysis presented in Chapter II, it was noted that for a wave number 6 eddy the meridional scale of the eddy's meridional heat flux might be too long to cause a zone of instability to shift back and forth across the mid-latitudes as unstable waves attempted to stabilize the zonal mean flow, a process that Held (1982) hypothesized might occur in the atmosphere. The short waves performing the fine tuning described above, however, might be able to behave in the manner

outlined by Held. The successive elimination of zones of instability described by Held would then correspond to the fine tuning. For example, a wave at 45°N with n_z = 18 has a zonal wavelength of 1600 km. This wavelength is about the size of a typical mid-latitude cyclone-anticyclone system. Successive cyclones, sweeping through the mid-latitudes and stabilizing the zonal mean flow, may then effect the fine tuning described above.

As noted in Chapter V, the adjustment $N^2(z)$ profile can constrain changes in the temperature structure that occur as the eddy flux strengthens or as the radiative cooling weakens. When the eddy flux becomes relatively strong, a temperature inversion may appear near the surface. Time and zonal mean temperature profiles at high latitudes show a temperature inversion near the surface, and the inversion may appear because of the influence baroclinically unstable eddies have on the vertical temperature structure. At 65°N in winter, for example, $N^2(z)$ is similar in shape to $N^2(z)$ at 45°N, only at 65°N, N^2 has much larger values near the ground, in accord with the temperature inversion observed there. The features of the vertical temperature structure at 65°N are similar to those of the temperature structures produced by the 6 E_w wave described in Chapter IV (Figure 4.6) and by the model run with no radiation described in Chapter V (Figure 5.6).

The changes in the vertical temperature structure produced by the eddy flux as its amplitude increases in Figures 4.4 and 4.6 may have climatic implications. The largest N^2 changes tend to occur near the surface, expecially as the eddy flux heating becomes stronger or the radiative cooling becomes weaker. If either the eddy flux heating or the radiative cooling should change, then the model results indicate

that temperature will change by about the same amount at all levels in the troposphere above 2 km, since the greatest changes in N^2 will occur near the surface.

The comparison of the N^2 adjustment's vertical temperature structure with the atmosphere's structure was hindered by the limited vertical resolution of the data compiled by Oort and Rasmusson (1971). If Oort and Rasmusson had compiled data at only the standard NMC levels, then the comparison would have been hindered even more, for there would have been even less resolution in the observed $N^2(z)$ and $[Q]_y(z)$ profiles. Because features of the $N^2(z)$ adjustment appear to be present in the time and zonal mean mid-latitude atmosphere, compilations of climatic data need to have higher vertical resolution, especially in the region between 2 km and 7 km. Perhaps in addition to data being archived at the standard NMC levels, data should also be archived at 400 mb, 600 mb, and 750 mb.

An even higher level of resolution may be necessary for calculating the vertical eddy heat flux. Computations of the vertical eddy heat flux by various researchers have very limited vertical resolution near the flux maximum. A resolution study described in Appendix B4 shows that the vertical balance model needs a vertical resolution of at least 1 km to adequately resolve the most influential waves, those in the range $n_z = 3 - 6$. Such a resolution is not achieved by the standard NMC levels, and some of the flux computations presented in Chapters I and IV use only data from those levels. In addition, a combination of model and observational results suggests that short, shallow waves may play a supplementary role to the longer, more influential waves, performing the fine tuning described above. The

vertical resolution of the NMC levels and of many GCM's could cause a severe underestimation of the strength of the vertical fluxes by the short, shallow waves. The resolution of the NMC levels and of many GCM's may have undue influence on the calculation of vertical fluxes by the longer waves, too.

Limited vertical resolution may influence models in another way, as well. Discussion in Chapter II noted that the jump in temperature at the top of a well-mixed planetary boundary layer could initiate baroclinic instability. Modeling of this feature in a GCM might enhance the eddy activity in a GCM. An association between the temperature jump and baroclinic instability would be another way that boundary layer physics could influence the flow in the rest of the troposphere.

Attempts to measure vertical eddy fluxes have had to use various indirect methods since vertical velocities in the atmosphere are difficult to measure directly. Recent advances in VHF Doppler radar (e.g. Larsen and Rottger, 1982) may allow direct measurements to be made. Some people have proposed that a network of such radars would be a useful addition to the current synoptic observing network (e.g. Balsley and Gage, 1982). The model results indicate that fairly long waves, $n_z \approx 3 - 6$, make the most important climatological contribution to the vertical heating balance, so that adequate horizontal resolution for the measurement of these fluxes should not be difficult to obtain. The vertical balance model results and the results of others indicate additional problems that might arise in measuring vertical eddy heat fluxes. The flux tends to peak fairly low in the atmosphere, perhaps too low for the VHF radar to measure the vertical velocity near the flux maximum well. Also, the peak vertical velocity may be at a different

level than that of the peak vertical flux (cf. Figures 4.8 and 4.10); the peak vertical flux may be in a layer where the vertical velocity is relatively small, making the flux measurement more difficult. Finally, the total vertical wind velocity at a given instant is a combination of velocities from many different scales of flow. Such a combination could obscure the climatologically relevant velocity field. Since the important waves vary on the synoptic time scale, while much of the unwanted portion of the velocity field may be due to motions, such as fast gravity waves, that have much shorter time scales, the unwanted velocities might be removed by filtering a time series of velocity measurements. Such problems may be more technical than fundamental in nature; a measurement of vertical eddy heat fluxes that is much less constrained by modeling assumptions than the measurements discussed in Chapters I and IV seems possible.

Appendix A - Solutions of (2.1.4) for negative $[U]_z$.

If $[U]_z$ is negative, (2.1.4) has a height independent solution which is stable with respect to dry convection,

$$N_A^2 = \frac{f^2(-[U]_z)}{\beta H_\rho} \quad . \tag{A1.1}$$

This solution is unacceptable if $r = N_0^2/N_A^2(0) \geq 1$, since the adjusted state then has more zonal available potential energy than the initial state, the ZAPE being proportional to $1/N^2$ (recall 3.2.3). Even if $r = 1$, the adjustment increases the ZAPE, since the adjustment decreases N^2 in the infinitesmal layer near the ground where initially $N^2 \to \infty$. If $r < 1$, the adjustment decreases the ZAPE, but for finite adjustment depths, the adjustment can not remove sources of instability in the vertical temperature structure. At the level z_A where the initial and adjusted temperatures match, $N^2(z)$ must decrease by jumping from N_A^2 to N_0^2. The jump produces another negative in the $[Q]_y(z)$; the $N^2(z)$ profile still causes the flow to be unstable.

Another possibility is to assume that, for $r < 1$, the entire atmosphere adjusts to the constant Brunt-Vaisalla frequency given above. In an unbounded atmosphere, this possibility is unacceptable because it would require an infinite adjustment time. Furthermore, since dynamic heat transports vanish at the boundaries or else tend to zero as $z \to \infty$, the thermal energy $\rho C_p T$ integrated over the model atmosphere must be conserved. In the present context, on an infinite β-plane where N^2 and $[U]$ have no y-dependence, conservation of $\rho C_p T$ means that

$$\int_0^\infty \rho C_p [T]_A \, dz = \int_0^\infty \rho C_p [T]_0 \, dz \quad . \qquad \text{(A1.2)}$$

(A1.2) may place a severe restriction on the adjustment, limiting the possibility that it can occur. For example, if pressure p obeys $p(z) = p_{00} e^{-z/H_p}$ before and after adjustment, then (A1.2) requires

$$\theta_A(0) \int_0^\infty \exp\{z(\frac{N_A^2}{g} + \frac{T}{H_p} - \frac{1}{H_\rho})\} \, dz$$

$$= \theta_0(0) \int_0^\infty \exp\{z(\frac{N_0^2}{g} + \frac{T}{H_p} - \frac{1}{H_\rho})\} \, dz \quad , \qquad \text{(A1.3)}$$

using $T = \theta(\frac{p_{00}}{p})^\kappa$, $N^2 = g\frac{d}{dz}\ln[\theta]$, and $T = \frac{d}{dz}\ln(\frac{N^2}{\rho})$. For N_A^2 given by (A1.1), (A1.3) then implies

$$\frac{f^2(-[U]_z)}{\beta H_\rho} = \frac{N_0^2}{g} + \frac{\Delta\theta}{\theta_0(0^+)-\Delta\theta} \{\frac{N_0^2}{g} + \frac{T}{H_p} - \frac{1}{H_\rho}\} \quad .$$

The adjustment through the entire depth of the fluid using constant N_A^2 can conserve thermal energy only if the original flow satisfies this relationship among its parameters.

The height dependent solution for negative $[U]_z$ is

$$N_A^2(z) = N_A^2(0) e^{-z/H_\rho} / \{1 - \gamma_-(1 - e^{-z/H_\rho})\} \quad , \qquad \text{(A1.4)}$$

where $\gamma_- = N_A^2(0)\beta H_\rho / f^2(-[U]_z)$. For $\gamma_- < 1$, the adjustment has the same properties that the positive $[U]_z$ adjustment has. For $\gamma_- \geq 1$, N_A^2 has a singularity at a height $z_c \equiv \ln\{(1 - r\gamma_-)/(r(1 - \gamma_-))\}$. Above z_c, N_A^2 in (A1.4) is negative; an acceptable solution must then have $z_A < z_c$. For N_0^2 a constant, there is no acceptable matching level, as illustrated schematically in Figure A.1. Where $N_A^2 = N_0^2$, $[\theta]_A$ can not equal $[\theta]_0$ since $[\theta]_0(0) > [\theta]_A(0)$ due to the jump $\Delta\theta$. $\Delta\theta$ must be positive in order for $[Q]_y$ to be negative near the surface in the initial state. Where $[\theta]_A = [\theta]_0$, then $N_A^2 > N_0^2$. As occurs with the

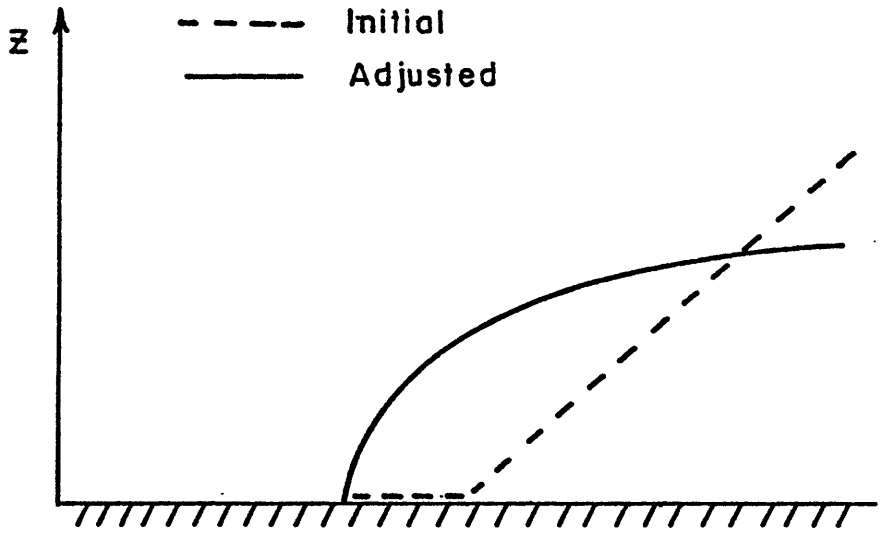


Fig. A.1 - Initial vertical profile of [θ] and the adjusted profile when $[U]_z < 0$.

height independent solution, a match there requires a sharp decrease in N^2 as height increases, giving negative $[Q]_y$, or another source of instability due to the vertical profile of N^2.

If $N_0^2 = N_0^2(z)$, then acceptable solutions for negative $[U]_z$ may be possible, depending upon the details of N_0^2's height dependence. Any acceptable solution must have $(ZAPE)_A < (ZAPE)_0$ and $N_A^2(z_A) \leq N_0^2(z_A)$.

Strict stabilization is not possible for any value of $[U]_z < 0$. As $N_A^2(0) \to \infty$ in (A1.4),

$$N_A^2(z) \to e^{-z/H_\rho} / \{ \frac{1}{N_A^2(0)} - \frac{\beta H_\rho}{f^2(-[U]_z)} (1 - e^{-z/H_\rho}) \} \quad .$$

The layer where N_A^2 is positive vanishes as $N_A^2(0)$ tends to infinity.

Appendix B - Numerical Considerations

B1. Finite Differencing.

The model requires derivatives of $[\theta](z)$, $N^2(z)$ and $[w^*\theta^*](z)$ in order to compute N^2, T, and the eddy heating. Away from the bottom and the top lids, the model uses centered finite differencing to approximate derivatives. For some function $\chi(z)$,

$$\frac{d}{dz}\chi\Big|_{z_j} \approx \frac{\chi_{j+1} - \chi_{j-1}}{2\Delta z} \quad ,$$

where z_j is the height of level j.

At the top and the bottom boundaries, the model uses a 3 point interpolation formula (parabolic approximation) to obtain derivatives. If x is the fractional distance between two grid levels, then

$$\frac{d}{dz}\chi(z+x\Delta z) \approx \frac{2x+1}{2\Delta z}\chi_{j+1} - \frac{2x}{\Delta z}\chi_j + \frac{2x-1}{2\Delta z}\chi_{j-1} \; . \qquad \text{(B1.1)}$$

At the top boundary, $z = z_T$ and $j = N$. Using $x = 1$, the derivative is

$$\frac{d}{dz}\chi(z_T) \approx \frac{3\chi_N - 4\chi_{N-1} + \chi_{N-2}}{2\Delta z} \; .$$

At the bottom, using $x = -1$ gives

$$\frac{d}{dz}\chi(0) \approx \frac{-\chi_3 + 2\chi_2 - 3\chi_1}{2\Delta z} \; .$$

Note that the centered differencing formula results if $x = 0$ in (B1.1); we may view all derivatives as 3 point approximations.

Small changes in the way the model computes derivatives can affect the appearance of the model's solution. In early model runs, the temperature derivative part of T(z) (e.g. 3.2.1) is approximated as

$$\frac{d}{dz}\ln(N^2) \approx \left(\frac{\partial^2\theta}{\partial z^2}\right)/\left(\frac{\partial\theta}{\partial z}\right)$$

$$\approx \frac{(\theta_{j+1} - 2\theta_j + \theta_{j-1})}{(\Delta z)^2/2} \Big/ \frac{(\theta_{j+1} - \theta_{j-1})}{\Delta z}$$

$$\approx \frac{\theta_{j+1} - 2\theta_j + \theta_{j-1}}{\theta_{j+1} - \theta_{j-1}} \left(\frac{2}{\Delta z}\right) \quad . \qquad \text{(Form 1)}$$

Figure B.1 shows a typical vertical profile for T_j in an early model integration. Above 8 km, T_j changes substantially from one level to the next, producing separate curves for the even j and the odd j levels. Later computations use

$$\frac{d}{dz}\ln(N^2) \approx \frac{N^2_{j+1} - N^2_{j-1}}{\Delta z} \Big/ N^2_j \quad . \qquad \text{(Form 2)}$$

For the same set of model parameters, Form 2 produces nearly the same temperature profile after 10,000 steps, only the separate curves for even j and odd j disappear, as Figure B.1 shows. By using temperatures over a greater range of levels, Form 2 produces a smoother T_j than Form 1 does. The $N^2(z_j)$ profiles are nearly identical in the two cases and as a result, the eddy's phase speeds are also: c(Form 1) = (20.7, 4.01), c(Form 2) = (21.1, 4.17). Thus, using Form 2 instead of Form 1 causes a model solution's T(z) to change slightly, but the general features of the solution otherwise remain the same.

Form 2 provides a numerical benefit: it is not as constrained by the grid spacing as Form 1. Consider a temperature profile which produces a large T_j: $\theta_{j-2} = \theta_{j-1} = \theta_j$, $\theta_{j+1} > \theta_j$, $\theta_{j+2} = \theta_{j+1} + \Delta\theta$. Then, Form 1 gives

$$T_j = \frac{2}{\Delta z} \quad ,$$

while Form 2 gives

$$T_j = \left\{1 + \frac{\Delta\theta}{\theta_{j+1} - \theta_j}\right\}\left(\frac{1}{\Delta z}\right) \quad .$$

Using Form 1, T_j can be no larger than $2/\Delta z$. Using Form 2, the size

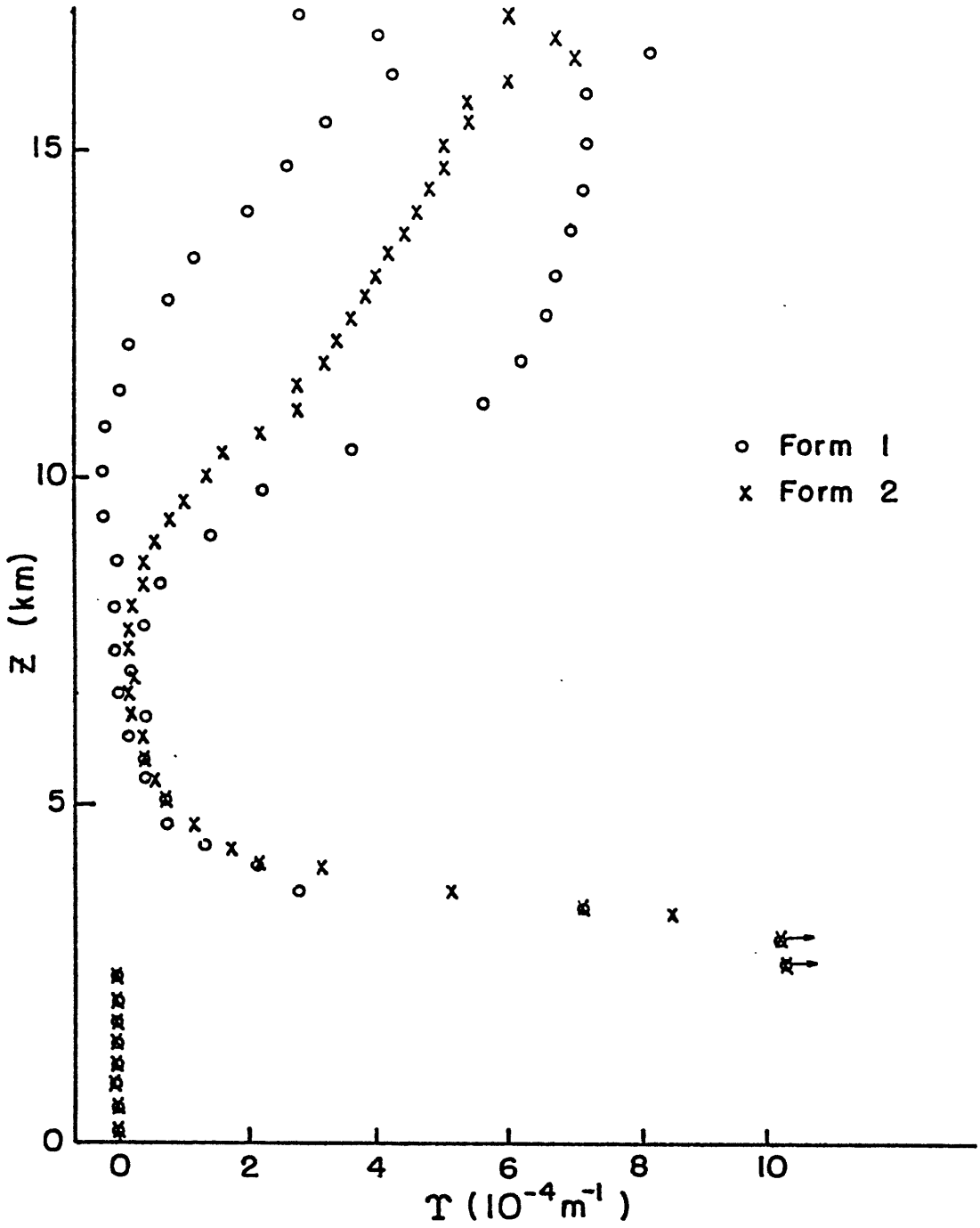


Fig. B.1 - T_j after 10,000 time steps from two model runs that are identical except that one calculates T using Form 1 and the other calculates T using Form 2.

of T_j is indefinite, because Form 2 uses a greater range of temperature levels. The model runs in Chapters IV and V have $\Delta z \leq$ 1 km. The maximum T_j using Form 1 is then $2 \cdot 10^{-3}$ m^{-1}. For most model runs, T_j is generally an order of magnitude smaller, though occasionally it does approach the Form 1 limit. By using temperatures over a wider layer, Form 2 insures that the grid spacing places no constraint upon the numerics of temperature structure computations.

B2. Eigenvalue Computations

a) Shooting Method

The shooting method interprets the eigenvalue problem posed by (3.2.1) plus the boundary conditions as an initial value problem (e.g. Dahlquist and Bjorck, 1974), integrating from one boundary to the other. Repeating the problem for reference here, the model must solve

$$\psi_{zz} = T\psi_z + \{\mu^2 - \frac{Q^*_y}{[U]-c}\}\psi \quad , \tag{B2.1}$$

where $Q^*_y = \beta_* + T[U]_z - [U]_{zz}$, subject to the boundary conditions,

$$\psi_z - \{\frac{[U]_z}{[U]-c}\}\psi = 0 \quad , z = 0, z_T \quad . \tag{B2.2}$$

(B2.1) is a second-order differential equation, so that two initial conditions are necessary in order to begin the forward marching. Since the problem is linear, we can choose some nonzero value for $\psi(0)$. By guessing a value for the eigenvalue c, we can then use (B2.2) to give $\psi_z(0)$.

The model uses a fourth-order Runge-Kutta scheme to integrate (B2.1) from $z = 0$ to $z = z_T$. Specifically, following Hildebrand (1956), when $(\psi)_j$ and $(\psi_z)_j$ are known, then

$$(\psi)_{j+1} = (\psi)_j + \Delta z(\psi_z)_j + \frac{\Delta z}{6}(r_1 + r_2 + r_3)$$

and

$$(\psi_z)_{j+1} = (\psi_z)_j + \frac{1}{6}(r_1 + 2r_2 + 2r_3 + r_4) \quad ,$$

where

$$r_1 = \Delta z\{T_j(\psi_z)_j + M_j\psi_j\} \ ,$$

$$r_2 = \Delta z\{\frac{1}{2}(T_j + T_{j+1})((\psi_z)_j + \frac{1}{2}r_1) + \frac{1}{2}(M_j + M_{j+1})(\psi_j + \frac{\Delta z}{2}(\psi_z)_j)\} \ ,$$

$$r_3 = \Delta z\{\frac{1}{2}(T_j + T_{j+1})((\psi_z)_j + \frac{1}{2}r_2) + \frac{1}{2}(M_j + M_{j+1})(\psi_j + \frac{\Delta z}{2}(\psi_z)_j + \frac{\Delta z}{4}r_1)\} \ ,$$

and

$$r_4 = \Delta z\{T_{j+1}((\psi_z)_j + r_3) + M_{j+1}(\psi_j + \Delta z(\psi_z)_j + \frac{\Delta z}{2}r_2)\} \ .$$

A convenient feature of this procedure is that it gives $\psi_z(z)$ as part of the computation without further finite differencing.

A given complex eigenvalue guess $c^{(i)}$ gives

$$\psi_z - \{\frac{[U]_z}{[U]-c}\}\psi = \varepsilon^{(i)}$$

at the upper boundary rather than zero (B2.2), so that $\varepsilon^{(i)}$ is an error associated with $c^{(i)}$. Having values of $c^{(i-1)}$ and $\varepsilon^{(i-1)}$ as well, Newton's method provides a means to obtain the next guess, or

$$c^{(i+1)} = c^{(i)} - \varepsilon^{(i)}\frac{c^{(i)} - c^{(i-1)}}{\varepsilon^{(i)} - \varepsilon^{(i-1)}} \quad ,$$

By iterating, the model computes successive approximations to the correct value. It assumes convergence when the modulus of the error after iteration i is less than a specified tolerance, $|\varepsilon^{(i)}| < \varepsilon_{max}$. Use of the shooting method in the model requires double precision to perform accurately, and an acceptable the error tolerance when the magnitude of ψ is determined by one of the model's closure assumptions

is $\varepsilon_{max} = 10^{-7}$. Under this tolerance, the method usually obtains convergence in 5-10 iterations.

When applying the shooting method during a model run, one of the initial guesses, $c^{(1)}$, is the eigenvalue for the previous time step. The second guess is simply a multiple of the first, $c^{(2)} = 1.1c^{(1)}$. The guesses $c^{(1)}$ and $c^{(2)}$ differ by only 10% because the zonal mean temperature structure typically changes by only a small amount from one time step to another. Therefore, $c^{(1)}$ and $c^{(2)}$ should both be good guesses to the convergent eigenvalue. For the first time step in a model run, no eigenvalue from a previous time step is available. Guided by eigenvalue computations for the Eady and Charney problems, the model assumes $c^{(1)} = [U](5km) + i \cdot [U](3km)$.

The model could use various predictor-corrector schemes in place of the fourth-order Runge-Kutta method. Predictor-corrector methods offer a possible advantage in accuracy in that they usually have an internal error control, but the use of a fixed grid spacing eliminates this advantage. More important, test computations comparing a fourth-order Adams-Bashforth (ABM) method (Acton, 1970) with the Runge-Kutta method indicate that the ABM method is more likely to amplify the oscillatory behavior which has motivated the use of a filter in the model (Appendix B5); the Runge-Kutta method produces a smoother time integration in the model than the ABM method does.

b) Matrix Method

Writing (B2.1) as

$$\left\{[U]\frac{D^2}{Dz^2} + Q^*_y\right\}\psi - c\,\frac{D^2}{Dz^2}\psi = 0 \quad , \qquad \text{(B2.3)}$$

where

$$\frac{D^2}{Dz^2} \equiv \frac{d^2}{dz^2} - T\frac{d}{dz} - \mu^2 \quad ,$$

renders a form suitable for matrix methods. In finite difference form, the differential operator above becomes

$$\frac{D^2\psi_j}{Dz^2} \approx \frac{\psi_{j+1} - 2\psi_j + \psi_{j-1}}{(\Delta z)^2} - T_j\frac{\psi_{j+1} - \psi_{j-1}}{2\Delta z} - \mu_j{}^2\psi_j$$

$$= \left\{\left(\frac{1}{\Delta z}\right)^2 - \frac{T_j}{2\Delta z}\right\}\psi_{j+1} + \left\{\frac{-2}{(\Delta z)^2} - \mu_j{}^2\right\}\psi + \left\{\left(\frac{1}{\Delta z}\right)^2 + \frac{T_j}{2\Delta z}\right\}\psi_{j-1}$$

$$= E_j\psi_{j+1} + F_j\psi_j + G_j\psi_{j-1} \quad . \tag{B2.4}$$

To apply the boundary conditions, first note that (B2.2) implies

$$([U]_1 - c)\psi_0 = ([U]_1 - c)\psi_2 - 2\Delta z([U]_z)_1\psi_1$$

and

$$([U]_N - c)\psi_{N+1} = ([U]_N - c)\psi_{N-1} + 2\Delta z([U]_z)_N\psi_N$$

Then,

$$\frac{D^2}{Dz^2}\psi_1 = E_1\psi_2 + F_1\psi_1 + G_1\psi_0$$

$$= \left\{F_1 - \frac{2\Delta z([U]_z)_1}{[U]_1 - c}\right\}\psi_1 + (E_1 + G_1)\psi_2 \quad , \tag{B2.5}$$

and

$$\frac{D^2}{Dz^2}\psi_N = \left\{F_N + \frac{2\Delta z([U]_z)_N}{[U]_N - c}\right\}\psi_N + (E_N + G_N)\psi_{N-1} \quad . \tag{B2.6}$$

In matrix form (B2.3) becomes, with the aid of (B2.4), (B2.5) and (B2.6),

$$\mathbf{A}\vec{\psi} - c\left(\mathbf{B}\vec{\psi}\right) = 0 \quad , \tag{B2.7}$$

where

$$\vec{\psi} = \begin{bmatrix} \psi_N \\ \cdot \\ \cdot \\ \cdot \\ \cdot \\ \psi_1 \end{bmatrix} ,$$

and **A** and **B** are the tridiagonal matrices

$$\mathbf{B} = \begin{bmatrix} F_N + \dfrac{2\Delta z([U]_z)_N}{} & E_N+G_N & 0 & & \\ E_{N-1} & F_{N-1} & G_{N-1} & & \\ 0 & E_{N-2} & F_{N-2} & & \\ & \cdot & \cdot & & \\ & \cdot & \cdot & & \\ & E_2 & F_2 & G_2 & \\ & 0 & E_1+G_1 & F_1 - \dfrac{2\Delta z([U]_z)_1}{[U]_1-c} & \end{bmatrix}$$

and $\mathbf{A} = \mathbf{B} + \mathbf{I} \begin{bmatrix} (Q_y^*)_N \\ \cdot \\ \cdot \\ \cdot \\ \cdot \\ (Q_y^*)_1 \end{bmatrix}$.

I is the identity matrix.

The method solves (B2.7) for the eigenvalue c by first computing the LU-decomposition of **B**, **B** = **LU**, where **L** is a lower triangular matrix

and **U** is an upper triangular matrix (e.g. Dahlquist and Bjorck, 1974). Then, applying $\mathbf{U}^{-1}\mathbf{L}^{-1}$ to both sides of (B2.7) gives

$$\{\mathbf{U}^{-1}\mathbf{L}^{-1}\mathbf{A}\}\psi - c\psi = 0 \quad .$$

The desired eigenvalues are eigenvalues of the matrix $\{\mathbf{U}^{-1}\mathbf{L}^{-1}\mathbf{A}\}$. The LU-decomposition procedure is more efficient and generally more accurate than computing $\mathbf{B}^{-1}$ and $\mathbf{B}^{-1}\mathbf{A}$. Having the matrix $\{\mathbf{U}^{-1}\mathbf{L}^{-1}\mathbf{A}\}$, the model then obtains the eigenvalues using the double precision version of the IMSL (International Mathematical & Statistical Libraries) subroutine EIGRF.

For model solutions, the matrix method almost always yields only one complex eigenvalue since $[Q]_y$ is generally of one sign through most of the model atmosphere. For these cases, the phase speeds given by the matrix and shooting methods usually agree to within 10% in both their real and their imaginary parts. Figure B.2 gives an example, comparing the phase speed spectrum computed by each method for the temperature structure in Figure B.3 produced by the 25 km grid. The greatest percentage difference occurs when the instability is weakest. In most cases, the agreement is actually far better than 10%, especially for solutions near the most unstable mode. For those wave numbers, the agreement between the two is typically on the order of 1%. Test computations with specified profiles indicates that the disagreement between the two methods for the size and location of the maximum vertical flux is generally the same size as the disagreement between the two methods for the size of c.

Occasionally, the matrix method produces two unstable modes, but one mode usually has a growth rate five times or more greater than the other, and the shooting method almost always obtains the larger growth

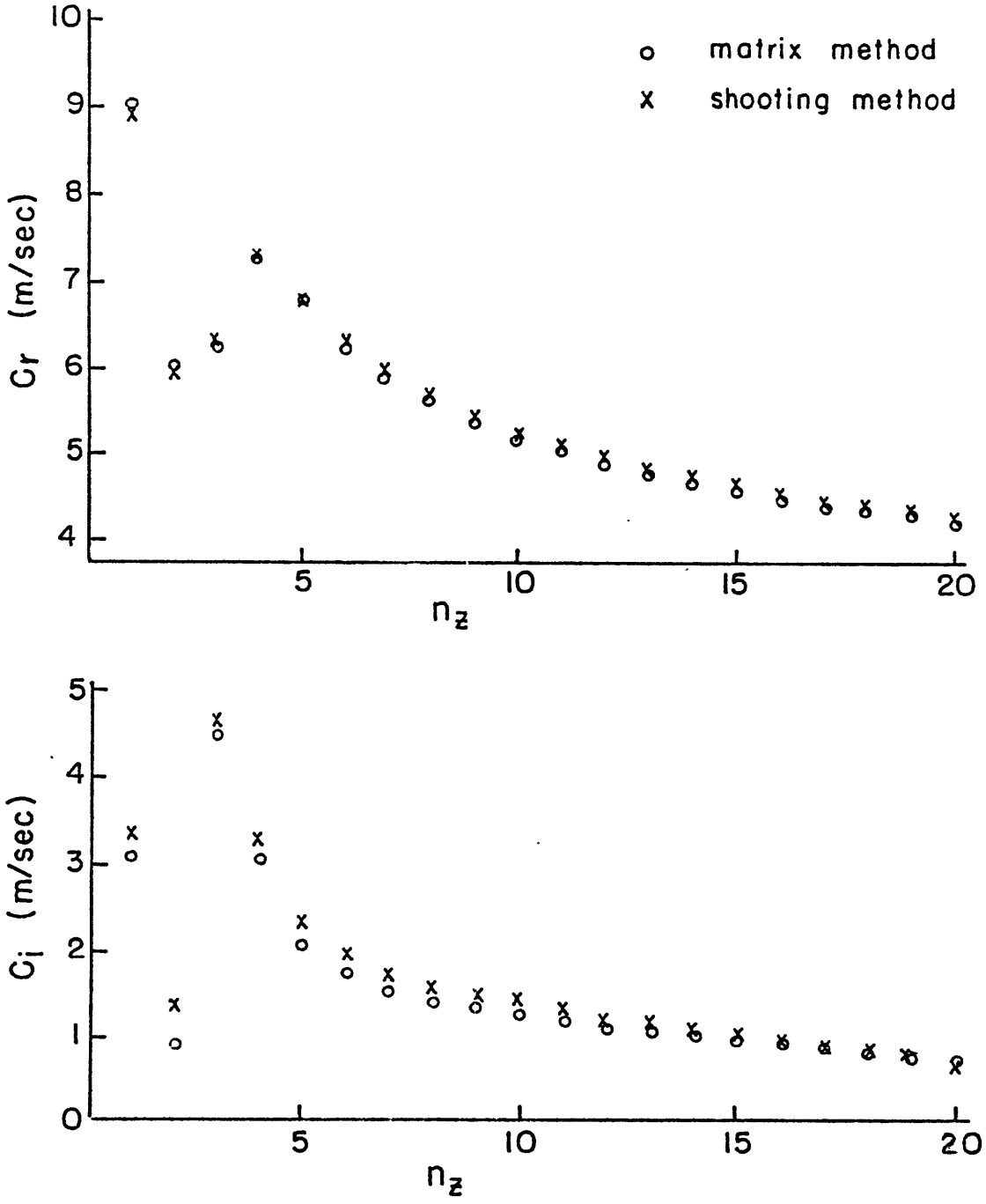


Fig. B.2 - A comparison of phase speed spectra computed by the matrix method and by the shooting method.

rate. Special cases do occur where a number of unstable modes exist which are not well-separated in size. Such cases, however, are rare.

B3. The Variable Time Step

The model's first attempts to integrate forward in time, using a simple forward stepping procedure, encountered difficulties before the model could obtain a convergent solution. A stepped structure would appear in the temperature profile, leading to large, grid-scale oscillations in $T = \frac{d}{dz}\ln(N^2) + \frac{1}{H_\rho}$. Accompanying this temperature structure was a similarly oscillating vertical flux. Closer inspection revealed that the vertical flux was attempting to smooth large values of T. However, at a given level, the flux's heating would cause the smoothing to overcorrect and again produce a large T, though of the opposite sign. The overcorrection tended to increase the absolute value of T, so that the oscillations of T with height would grow in time and, eventually, lead to machine overflow and underflow in the numerical computations. More sophisticated forward marching techniques could constrain the behavior so that the oscillations would not grow without bound, though they still would appear. The most successful technique retained the simple forward difference, but allowed the time step to vary in a manner that prevented the occurrence of the overcorrection.

The procedure to determine the time step attempts to find a time step Δt such that all the new values of T after marching forward are greater than some minimum value; the procedure restricts the appearance of very negative T values. Thus, at time step i, level j, the procedure attempts to find Δt such that

$$T_j^{i+1} \geq T_{min} \qquad \text{(B3.1)}$$

where T_{min} is the smallest T value considered acceptable. Using Form 2 from section B1, the value of T at a level j is

$$T_j = \frac{N^2_{j+1} - N^2_{j-1}}{N^2_j(2\Delta z)} \approx \frac{\theta_{j+2} - 2\theta_j + \theta_{j-2}}{\theta_{j+1} - \theta_{j-1}} \cdot \frac{1}{2\Delta z}$$

Denoting the sum of the radiative and eddy flux heatings at a level j, time step i by Q_j^i, the temperature at the same level after forward differencing is $\theta_j^{i+1} = \theta_j^i + \Delta t^i Q_j^i$ and the estimated new T value is

$$T_j^{i+1} = \frac{\theta_{j+2}^{i+1} - 2\theta_j^{i+1} + \theta_{j-2}^{i+1}}{(T_{j+1}^{i+1} - T_{j-1}^{i+1})(2\Delta z)}$$

$$= \frac{(\theta_{j+2}^i - 2\theta_j^i + \theta_{j-2}^i) + \Delta t^i(Q_{j+2}^i - 2Q_j^i + Q_{j-2}^i)}{2\Delta z\{(T_{j+1}^i - T_{j-1}^i) + \Delta t^i(Q_{j+1}^i - Q_{j-1}^i)\}}$$

$$= \frac{\Delta\theta^i T^i + \Delta t^i \Delta Q^i \hat{T}_j^i}{\Delta\theta^i + \Delta t^i \Delta Q^i} \quad , \qquad \text{(B3.2)}$$

where

$$\Delta\theta^i \equiv \theta_{j+1}^i - \theta_{j-1}^i \quad ,$$

$$\Delta Q^i \equiv Q_{j+1}^i - Q_{j-1}^i \quad ,$$

and

$$\hat{T}_j \equiv \frac{Q_{j+2}^i - 2Q_j^i + Q_{j-2}^i}{2\Delta z(Q_{j+1}^i - Q_{j-1}^i)} \quad .$$

The calcuation of T_j^{i+1} does not include heating due to convection. In the model runs, convection occurs as a response to the cooling by radiation and the eddy flux. Where it does occur, it generally adjusts the temperature to a profile in which T does not have

large values. For this reason, the procedure to determine Δt ignores the layer of convective heating in contact with the surface, which is often the only layer of convective heating (e.g. Figure 4.9). Also, the moist convective adjustment depends on Δt in a nonlinear manner, so that T_j^{i+1} would not be given by the relatively simple formula (B3.2). Ultimately, the requirement (B3.1) serves only as a guide and the procedure selects an appropriate Δt, not necessarily the best. Determining the best, if one exists, could be wasteful, consuming much computer time.

At each level, the model determines the value of Δt which gives $T_j^{i+1} = T_{min}$. Thus, using (B3.2) and dropping the superscripts for notational ease,

$$(\Delta t)_j = \frac{\Delta T_j (T_j - T_{min})}{\Delta Q_j (T_{min} - \hat{T}_j)} \quad .$$

Ideally, the model would march forward using the minimum value of Δt among the set $\{(\Delta t)_j\}$, since any Δt larger than the minimum would violate (B3.1) at one or more levels. In reality, the model rejects a number of the $(\Delta t)_j$ because they are negative. This can occur, for example, when ΔQ is negative. Since the vertical eddy flux usually does not transport much heat into the model's stratosphere, we can expect that the flux's heating will decrease with height in the model's upper levels, yielding $\Delta Q < 0$. $(\Delta t)_j$ at these levels may then be negative, too.

In addition, not all positive $(\Delta t)_j$ are acceptable. The smallest positive Δt may be so small that the fractional change in temperature at each level j, $\frac{\Delta t \cdot Q_j}{T_j}$, is smaller than the computer's round-off error.

This may occur if $T_j \approx T_{min}$. In practice, the model rejects not only these values of Δt, but also all positive $(\Delta t)_j$ smaller than 10 sec. For $\Delta t < 10$ sec, the fractional temperature changes may be larger than round-off error, but experiments with the model indicate that the model can reject these short time steps and still proceed smoothly.

Having obtained the smallest $(\Delta t)_j$ greater than 10 sec, $(\Delta t)_{min}$, the model choses the time step for marching forward to be $\Delta t = 0.25(\Delta t)_{min}$. This reduction in size has no useful purpose if there are a number of $(\Delta t)_j$ between 2.5 sec and 10^+ sec, since the model would obtain nearly the same Δt simply by lowering the cut-off to 2.5 sec and not reducing $(\Delta t)_{min}$ by 75%. The reduction does seem to be useful when $(\Delta t)_{min} \gg 10$ sec, for it allows T_j at the level providing $(\Delta t)_{min}$ to approach T_{min} without becoming equal to T_{min}. Then, in the subsequent time step, $(\Delta t)_j$ is not zero at that level and the procedure includes the Δt computation there in its next time step determination. Experiments with the model indicate that the approach to an equilibrium proceeds more rapidly when this reduction occurs.

Since the procedure rejects all $(\Delta t)_j$ less than 10 sec from further consideration, the model violates (B3.1) after stepping forward. This poses no problems because if T_j becomes very negative, the eddy heating generally tries to make it very positive. Once T_j is positive, the eddy heating and the variable time step can smooth T(z) so that T_j is not extremely large compared to T_{j+1} or T_{j-1}. The possiblity exists that when T_j becomes very positive, its associated time step $(\Delta t)_j$ is much less than 10 sec, so that after the next step, T_j is again very negative and an unbounded oscillation in time occurs. This possibility has not manifested itself in model runs. There is also a

special case discussed in Section B5 where the eddy flux does not attempt to eliminate a large T_j but amplifies it instead.

The model runs described in this thesis use $T_{min} = 0$, so that $T < 0$ can appear in model solutions but very negative T, say $T \ll -1$, does not, except possibly in regions of convection. Time steps in an integration may range from a few seconds to a few hours, with the size usually approching the latter as the model nears a convergent solution.

B4. Effects of Resolution and Grid Depth

The constraints of accuracy and of reasonably short execution time generally do not act on concert with each other in a numerical model. If round-off errors are small, then accuracy improves as the number of grid levels increases. The speed of the computation, however, decreases as the numbers of grid levels increases. Thus, some compromise between the two constraints is necessary. In addition, the overall depth of the grid is a matter of concern. The upper boundary condition of $w^* = 0$ at the top of the model is artificial and could have an undesired influence on the solutions. The results here indicate that the level of the upper boundary used by the model for most of its runs does not have a significant influence.

Table B.1 compares model runs using different grid resolutions. For all runs in Table B.1, the grid depth is 25 km, $\beta = 10^{-11}$ $m^{-1}sec^{-1}$, and $[U]_z = 2.0 \cdot 10^{-3}$ sec^{-1}. The eddy kinetic energy is $2.9 \cdot 10^6$ J/m^2 ($\approx 2\ E_w$) in all runs, so that the eddy flux should be strong enough to play a signficant role in these solutions (cf. Figures 4.1 and 4.4), and any influence of resolution upon the eddy flux and its heating for these parameters should be apparent. The radiative heating, $Q_{Do}(z)$, follows

the Dopplick's 1972 results. These runs do not use the Shapiro filter, since its effect would vary with resolution. Also, the wave number 3 computations use an older form of the moist convective adjustment, which requires that the equivalent potential temperature does not decrease with height anywhere. This type of adjustment depends upon the model's relative humidity profile. The convective adjustment scheme described in Chapter III does not. The differences between the two are negligible in this particular application for two reasons. The layer of convection extends only about 1 km from the surface for either adjustment. Also, the model's relative humidity is 80% near the surface, close enough to 100% that the relative humidity profile has little influence. Thus, the conclusions using Table B.1 should apply to nearly all other model runs.

The comparison of $\tilde{N}^2$ values (equation 4.1.1) indicates the sensitivity of the temperature structure produced by the model to grid resolution. The comparisons of c and the eddy flux show the sensitivity of the eddy computation to the resolution. Indirectly, they also indicate the sensitivity of the model's temperature structure to the resolution. There is relatively little change in all quantities once the grid resolution is about 1 km or smaller. The discrepancy between the 2.5 km resolution solutions and the others appears to be due mainly to changes in the latent heat flux as the resolution increases. The latent heat flux peaks close to the surface (e.g. Figure 4.8) and is nearly negligible at 5 km due to the combined decreases of temperature and relative humidity. Thus, a coarse resolution of 2.5 km does not resolve the peak latent heat flux adequately. Table B.1 suggests that a resolution of 1 km is acceptable, but for most single mode runs the model uses a more conservative value of 0.5 km. This provides a better

Table B.1 - The effects of grid resolution upon model solutions. The Brunt-Vaisailla frequency $\tilde{N}^2$ is in units of 10^{-4} sec^{-2}, the resolution and the level of the flux peak in km, the flux amplitudes in W/m^2, and phase speed in m/sec.

levels	res.	c	$\tilde{N}^2$	maximum vertical eddy heat flux					
				total		sensible		latent	
				amp.	level	amp.	level	amp.	level
Wave number 3									
11	2.5	(8.9,5.0)	1.7	66	2.5	56	5.0	10	2.5
21	1.2	(6.5,5.2)	2.1	84	1.2	66	2.5	22	1.2
31	0.8	(6.3,5.2)	2.1	85	1.7	66	1.7	22	0.8
41	0.6	(6.3,4.9)	2.1	89	1.2	66	1.2	24	1.2
51	0.5	(6.3,4.7)	2.1	91	1.0	66	1.5	26	1.0
61	0.4	(6.3,4.7)	2.1	90	1.3	66	1.3	25	1.3
Wave number 6									
11	2.5	(8.7,1.8)	1.0	56	2.5	47	2.5	9	2.5
21	1.2	(10.0,1.5)	1.2	63	1.7	49	1.7	17	0.8
31	0.8	(10.0,1.5)	1.2	64	1.5	49	1.5	17	1.0

resolution of features such as the $[Q]_y$ minimum (Figures 4.7, 4.16, and 5.7) and the peak in the vertical eddy heat flux, which is close to the surface (Figure 4.8). The wave ensemble runs integrate much more slowly, so that the model uses a 1 km resolution, yielding a much more acceptable integration rate. With the lower resolution, the wave ensemble runs generally require about 30 - 60 minutes of CPU time on an Amdahl 470 V/6 computer, a range of times which is still about 3 - 6 times longer than the time required by a typical single mode run.

The depth of the model's grid is especially important for eddies with long zonal wavelength ($n_z < 5$), since they tend to be deeper than the shorter waves. Figure B.3 compares $N^2(z)$, the eddy flux, and the eddy streamfunction amplitude produced by model runs using $n_z = 3$ that differ only in grid depth, which ranges from 15 to 34 km. The other model parameters are the same as those used in the resolution

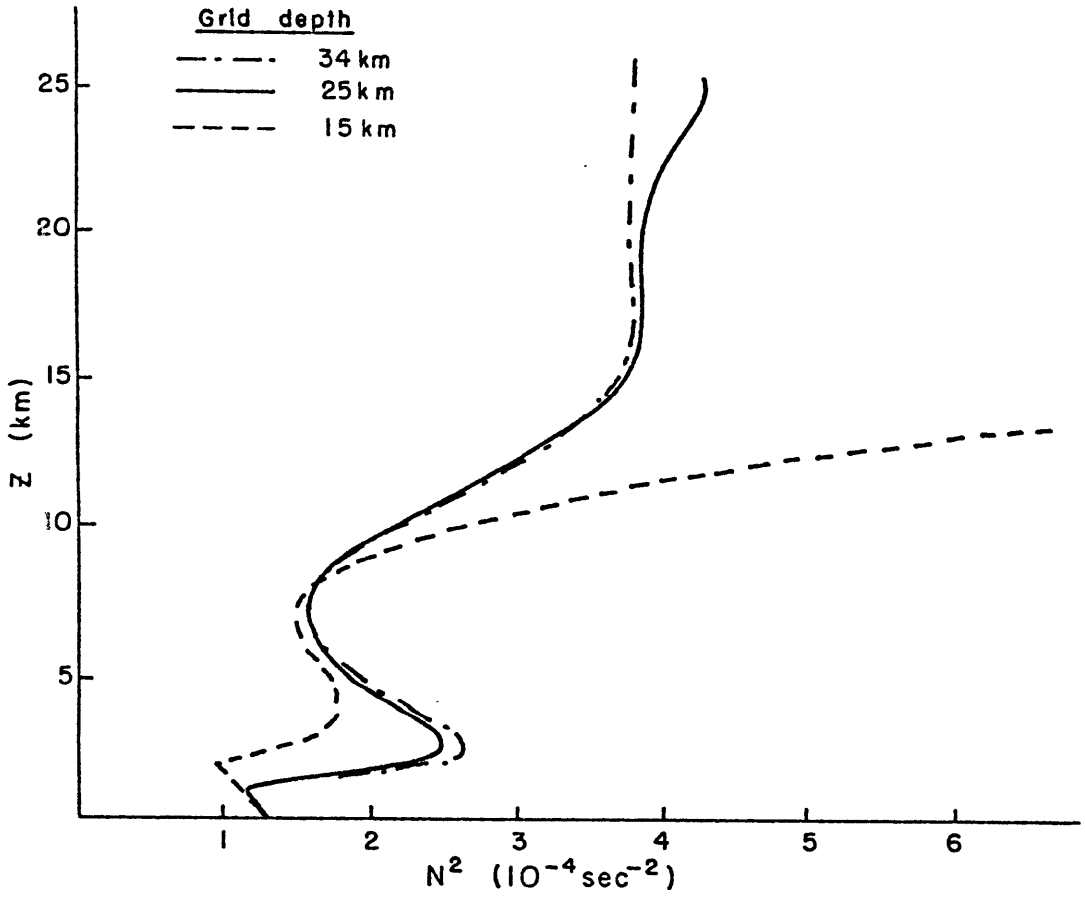


Fig. B.3a - $N^2(z)$ for three model runs that are alike except that each uses a different grid depth.

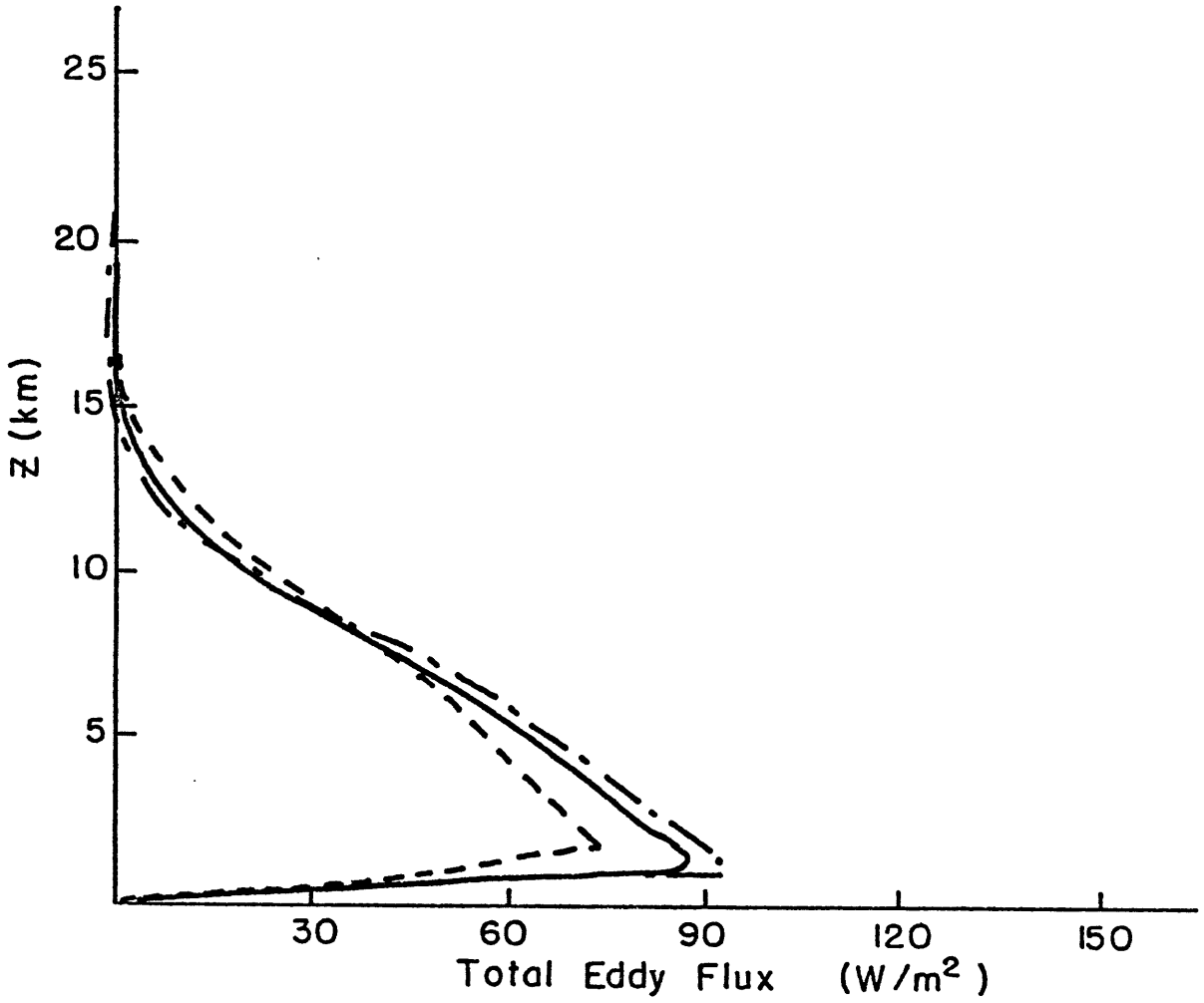


Fig. B.3b - Like Figure B.3a, except showing the total eddy flux $\rho(1 + \Lambda)[w^*\theta^*]$.

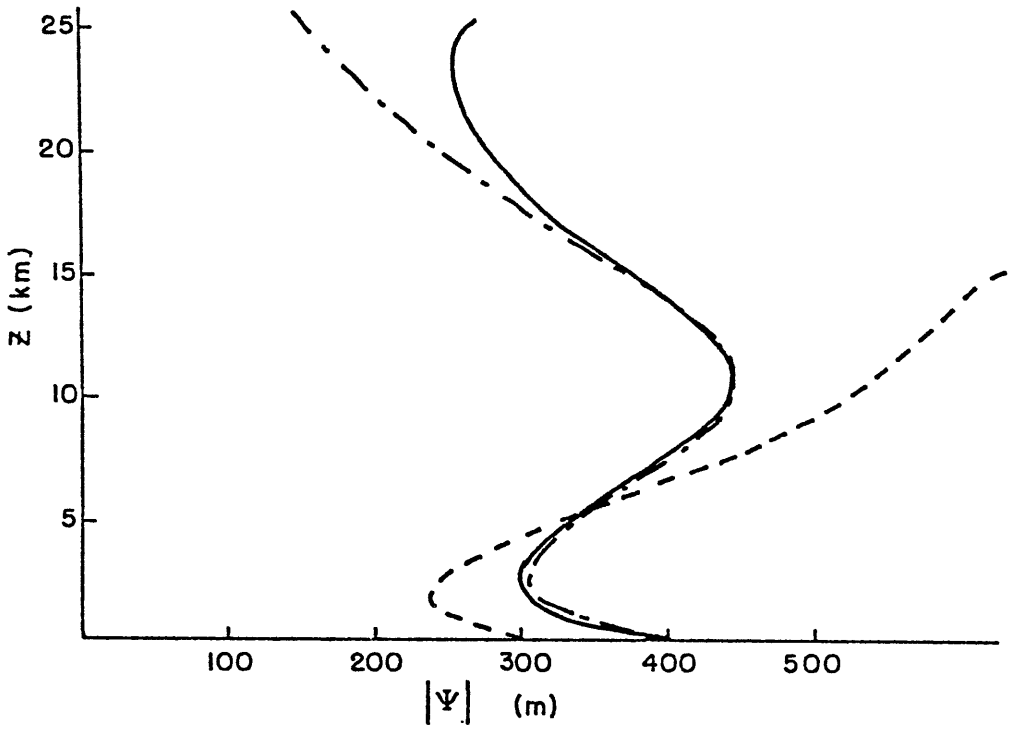


Fig. B.3c - Like Figure B.3a, except showing the eddy streamfunction amplitude $|\psi|$.

comparisons above. For the shallowest grid, the effect of the upper boundary is evident, especially in the profiles of $N^2(z)$ and $|\psi|(z)$. The upper boundary in this case has a strong influence on the model's solution in the troposphere. For the two deeper grids, there are some differences in the vicinity of 25 km. For example, the eddy streamfunction begins to increase with height in the 25 km grid run. This feature shifts upward with grid depth and appears near 34 km in the deeper model run. The 25 km grid $N^2(z)$ profile also shows a small influence of the upper lid. However, stability computations by Staley and Gall (1977) indicate that Charney-type modes are insensitive to features of the zonal mean flow appearing more than a scale height above the surface. Not surprisingly then, the phase speeds are nearly equal: c(35km) = (6.32, 4.66) m/sec, c(25km) = (6.29, 4.67) m/sec. In contrast, c(15km) = (5.50, 4.21) m/sec. As indicated by $N^2(z)$, there is little difference in the tropospheric temperature structures produced by the two deeper grids. Wave ensemble runs use a 34 km grid depth since very long waves such as wave number 1 appear to need a grid depth deeper than 25 km.

B5. Shapiro Filter

For some unfiltered model runs, the Brunt-Vaisailla frequency profile shows rapid oscillations with height in the stratosphere. Figure B.4 shows an example of this for an $n_z = 5$ model run, using the same parameters as the 25 km $n_z = 3$ run described in section B4. For these parameters, the $n_z = 5$ solution shows the oscillations most clearly compared to other possible wave numbers. The oscillations decrease rapidly in amplitude as the specified wave number increases or decreases

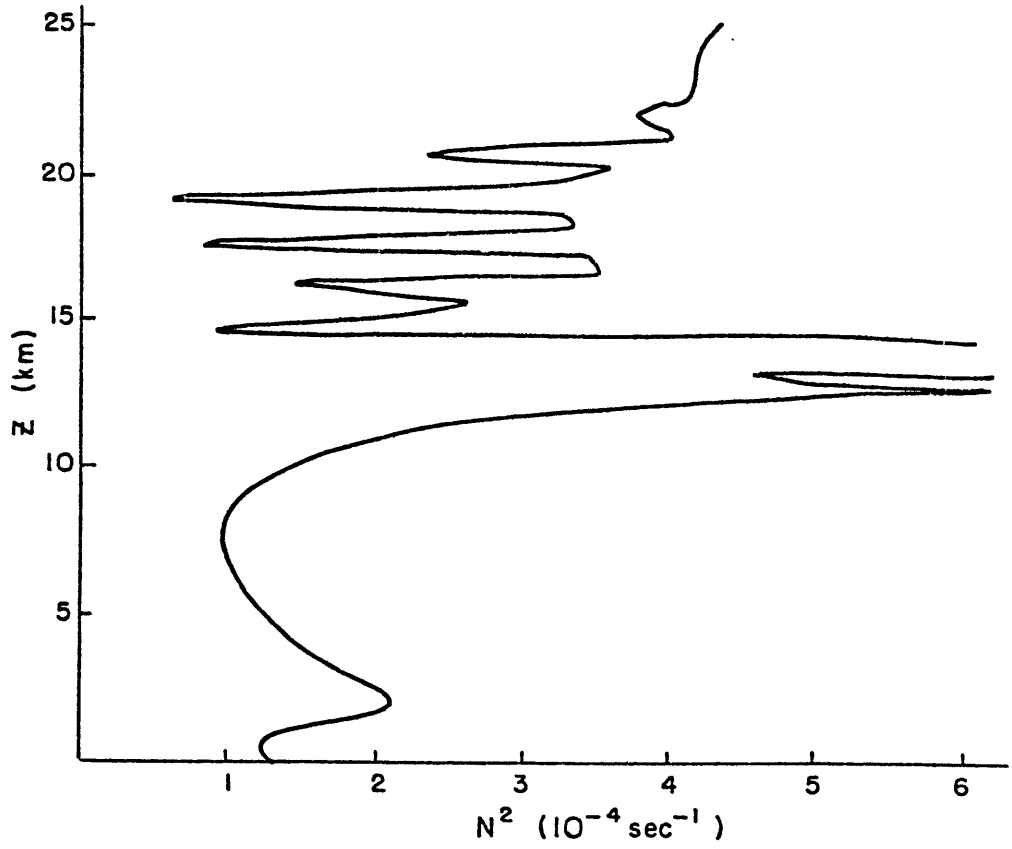


Fig. B.4 - $N^2(z)$ produced by an unfiltered model run.

away from $n_z = 5$, so that the $N^2(z)$ profiles produced by wave number 3 and wave number 7 have none.

Inspection reveals that, for the solution in Figure B.4, the eddy heating tends to reinforce the oscillations rather than eliminate them, which is opposite to the heating behavior motivating the use of a variable time step (section B3). Despite the oscillations, a model convergence does occur. Also, the oscillations do not appear to affect the integration rate. The time step at convergence is about the same size as in other model runs, on the order of an hour. However, if the oscillations are much larger, the time step may decrease by orders of magnitude.

Certain features appear to amplify the oscillations, so that they grow in an unbounded manner. For example, the amplitude of the oscillations is very sensitive to the stratospheric zonal wind shear. If $[U]_z$ for a unfiltered model run is nearly zero or else negative in the stratosphere, then the integration breaks down.

The reason for the appearance of the oscillation is not clear. Since the eddy flux results from the solution to an eigenvalue problem, analysis is difficult because the flux at a given level depends upon global, rather than just local, properties of the flow. The time sequences of T(z) and the eddy heating (Figure B.5) for the case leadng to Figure B.4 suggest that the oscillations are not caused directly by the eddy flux. Each of the quantities shown in Figure B.5 is sensitive to the appearance of small-scale oscillations in a model solution, the former using a second-derivative of the zonal mean temperature profile and the latter using second derivatives of the eddy streamfunction. The oscillations appear first in the temperature structure, suggesting that

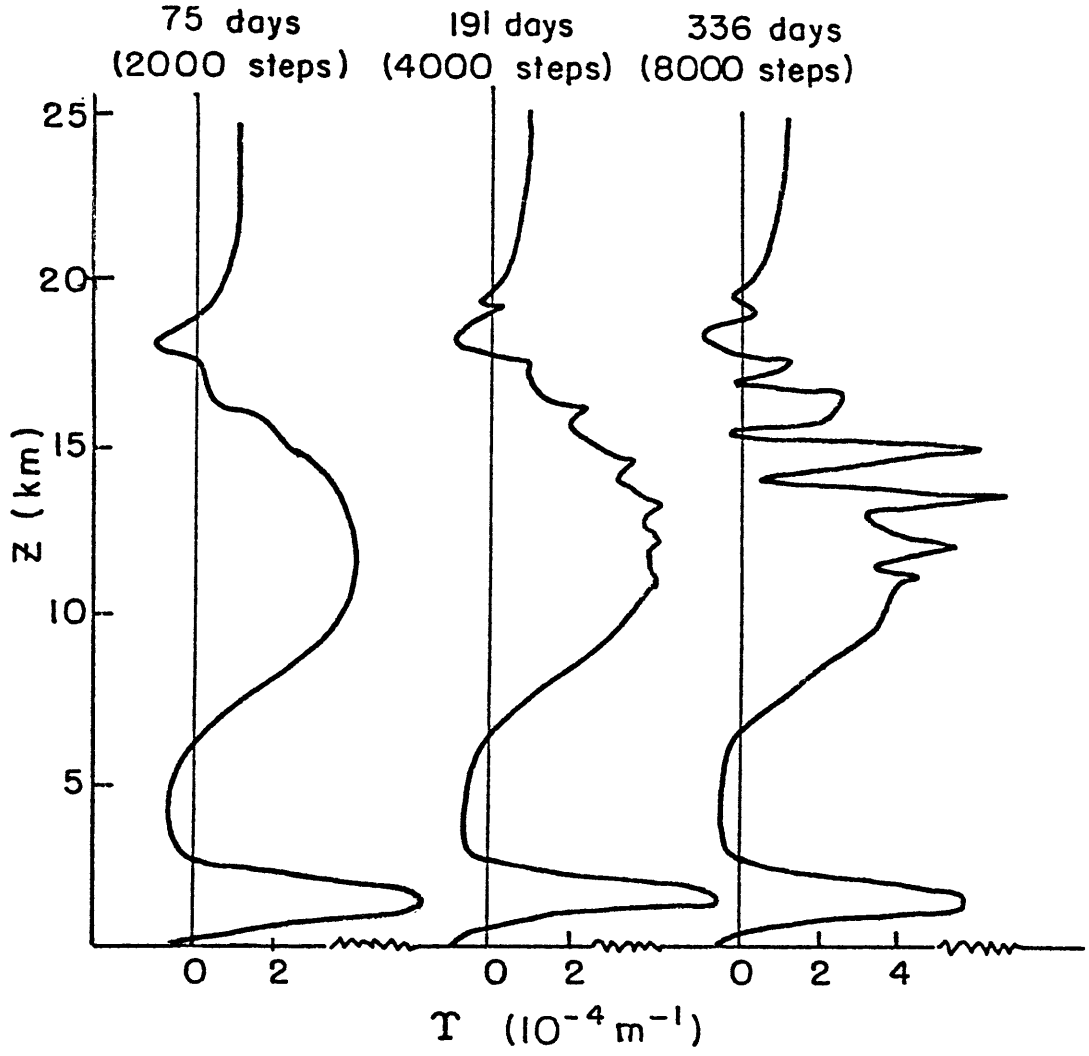


Fig. B.5a - T(z) for three different times in the integration leading to the solution in Figure B.4.

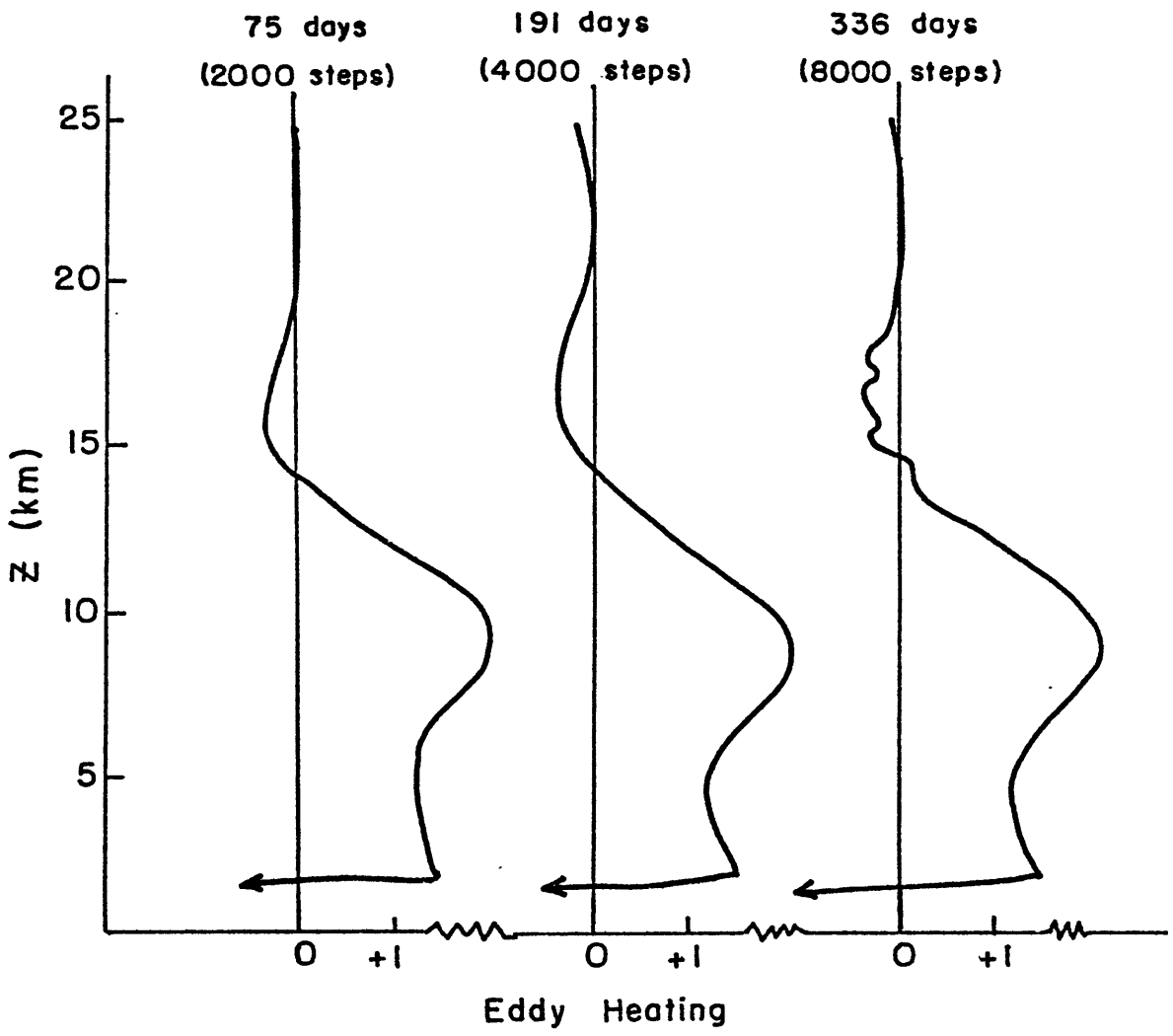


Fig. B.5b - Like Figure B.5a, only showing the eddy heating.

the cause is some process other than the eddy flux and that the eddy's behavior is simply a response which eventually acts to amplify the oscillations. The radiative equilibrium T(z) displays the same kink in its profile near 18 km that T(z) in the figure does, indicating that the model's radiative cooling initiates the small-scale oscillation. However, most model runs are unaffected by this feature in the T(z) profile and it is not apparent why a few parameter choices lead to its amplification.

The model's purpose is to simulate the stratosphere. While layered structures often appear in the stratosphere, the model's oscillations probably do not suggest a cause for their appearance. A possibility is that the oscillations represent some type of numerical noise, since their wavelength is close to the size of the model's grid spacing. The oscillations may appear for some physical reason, but if the model had contained a radiative transfer computation, radiative heating probably would have damped out the oscillations. While the filter is simply a numerical procedure for removing apparently unrealistic features from the model, the conditions for its use in the model are guided by the process of radiative temperature wave damping, as described in Chapter III.

Shapiro (1970) has studied in detail the effects on numerical calculations of smoothing and filtering operators. The model assumes that the filter's damping is similar to radiation, acting upon the temperature profile. The model uses the simplest of these filters, a three-point averaging operator. At a given level, the filtered temperature is thus

$$[\hat{T}]_j = \frac{1}{2}[T]_j + \frac{1}{4}\left([T]_{j+1} + [T]_{j-1}\right) \quad . \qquad \text{(B5.1)}$$

This filter is often called a first-order Shapiro filter. The filtering domain is not periodic, but bounded by grid points at the top, j=N, and bottom, j=1. At these two grid levels, the filter uses

$$[\hat{T}]_N = \frac{3}{4}[T]_N + \frac{1}{4}[T]_{N-1} \quad ,$$

and

$$[\hat{T}]_1 = \frac{3}{4}[T]_1 + \frac{1}{4}[T]_2 \quad ,$$

so that

$$\sum_{j=1}^{N} [\hat{T}]_j = \sum_{j=1}^{N} [T]_j \quad . \qquad \text{(B5.2)}$$

Boundary conditions may propagate inward and contaminate the interior temperature field, but as used by the model, the filter produces relatively little heating at any level, so that the contamination does not appear to occur.

The filter transforms one set of temperatures into another, or $\{[\hat{T}]_j\} = R_1(\{[T]_j\})$, where R_1 is the response function of the filter. R_1 varies with vertical wavelength λ, damping the shortest oscillations more strongly than the longer ones. For the particular choice of constants in (B5.1), $R_1 = \cos^2(\pi\Delta z/\lambda)$. The shortest wavelength resolved by the grid is $\lambda = 2\Delta z$, for which $R_1 = 0$, so that the set $\{[\hat{T}]_j\}$ contains no grid-scale oscillations. Figure B.6 depicts the dependence of R_1 on λ in the model, where $\Delta z = 0.5$ km. As vertical wavelength increases, the filter has less of an effect, a desirable property since the model's physics should give the temperature's height variation on the longer scales. The selective damping is similar to the damping produced by radiation in that it weakens as λ increases. Note also that $0 < R_1 < 1$. This filter does not amplify any wavelength, nor does it cause a phase change, which would occur for some λ if $R_1(\lambda) < 0$.

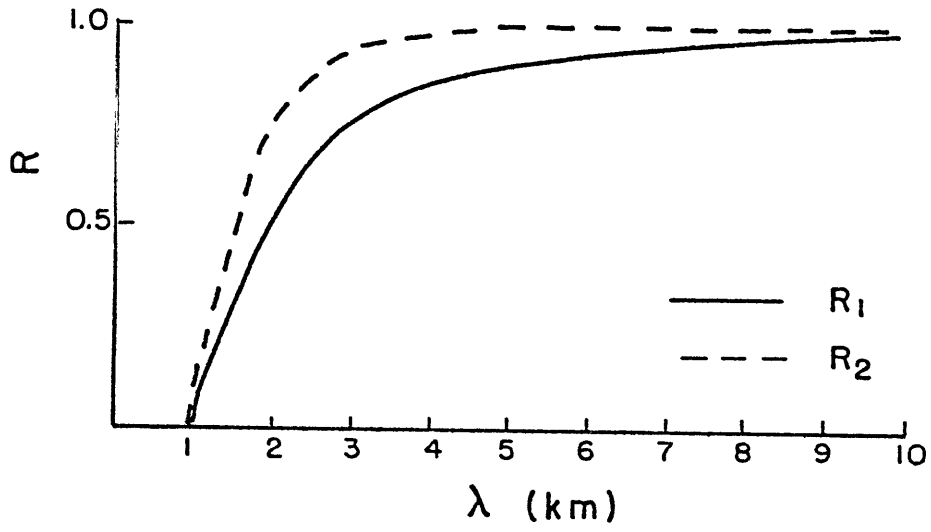


Fig. B.6 - The filter response functions $R_1(\lambda)$ and $R_2(\lambda)$.

Consideration of the same constraints, no damping and no phase change, leads to a second-order filter with response function $R_2(\lambda)$. For this filter,

$$[\hat{T}]_j = \frac{5}{8}[T] + \frac{1}{4}[T]_{j+1} + \frac{1}{4}[T]_{j-1} - \frac{1}{16}[T]_{j+2} - \frac{1}{16}[T]_{j-2} \quad ,$$

with boundary terms

$$[\hat{T}]_N = \frac{15}{16}[T]_N + \frac{1}{8}[T]_{N-1} - \frac{1}{16}[T]_{N-2} \quad ,$$

$$[\hat{T}]_{N-1} = \frac{1}{8}[T]_N + \frac{11}{16}[T]_{N-1} + \frac{1}{4}[T]_{N-2} - \frac{1}{16}[T]_{N-3} \quad ,$$

$$[\hat{T}]_2 = \frac{1}{8}[T]_1 + \frac{11}{16}[T]_2 + \frac{1}{4}[T]_3 - \frac{1}{16}[T]_4 \quad ,$$

and

$$[\hat{T}]_1 = \frac{15}{16}[T]_1 + \frac{1}{8}[T]_2 - \frac{1}{16}[T]_3 \quad .$$

The boundary terms for the R_2 filter also yield (B5.2). Their particular form results from assuming $[T]_0 = [T]_1 - \Delta T$ and $[T]_{-1} = [T]_1 - 2\Delta T$, where $\Delta T = [T]_2 - [T]_1$, and similarly at the top boundary. Figure B.6 displays $R_2(\lambda)$, also for a grid spacing of 0.5 km. Except at the shortest resolved wavelengths, the two filters have nearly the same smoothing effect on the temperature profile.

In practice, the difference between the two filters in terms of model solutions is usually negligible. Figure B.7 compares single wave model solutions for a 0.5 km grid spacing using either no filter, the R_1 filter, or the R_2 filter. The unfiltered solution is the one providing $N^2(z)$ in Figure B.4. The filtered solutions use the same set of model parameters as the unfiltered solution. The two filtered solutions are nearly indistinguishable from each other. In the troposphere, all three solutions are nearly identical, indicating that the filter does not interfere significantly with the physics of the model. As used by the

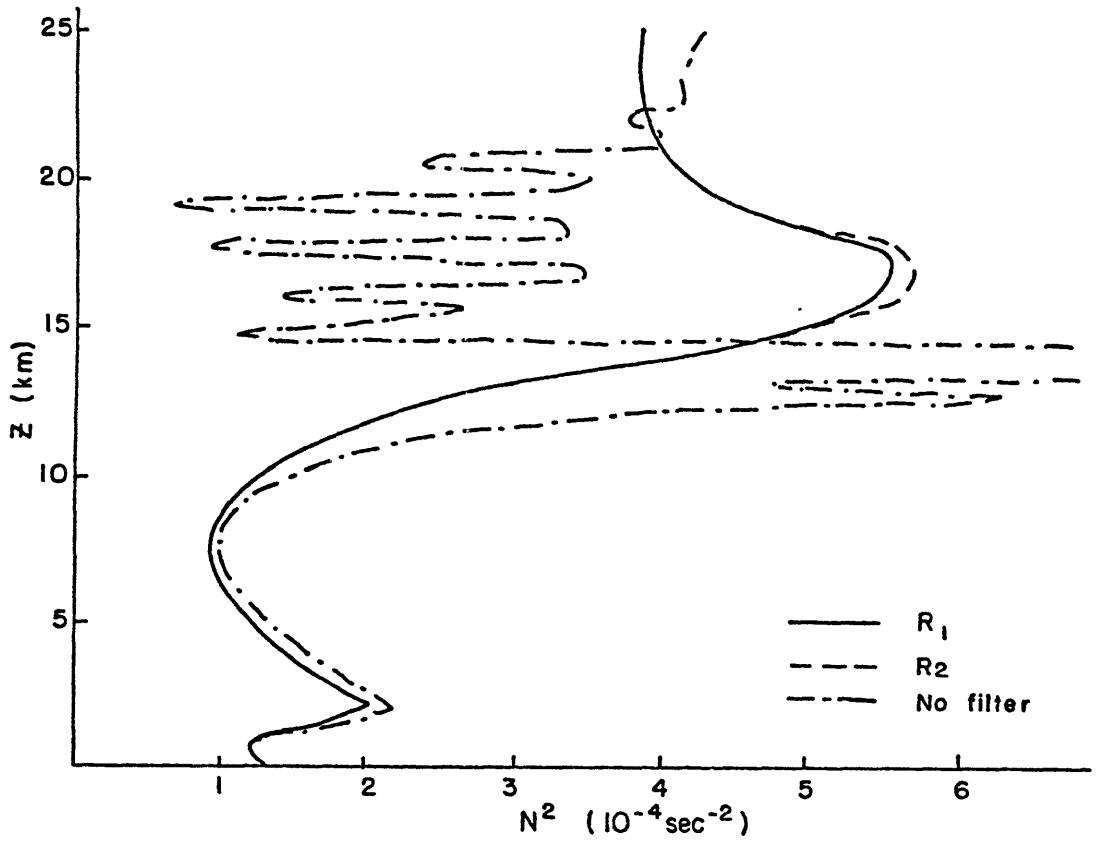


Fig. B.7 - $N^2(z)$ from three model solutions, one with no filter, one using the R_1 filter, and one using the R_2 filter. All model parameters are the same in the three solutions.

model, the heating at any level due to the filter is typically only a few 1/100's of a degree per day or less. The model uses the R_1 filter for all computations. When the model's grid spacing is 1 km instead of 0.5 km, the filter damps longer vertical wavelengths than it does under a 0.5 km grid spacing, but its effective heating still remains negligible in the model's solutions.

The filter appears to have little influence on the final balance, while removing features that are apparently unrealistic. The possiblity still exists that the filter has a significant impact on the final state the model obtains by limiting severely the range of solutions possible, even though it provides little heating in the solution the model does obtain. The impact would be significant if the model were to compute a different solution without the filter, a solution which the filter would eliminate by constraining the model behavior. The comparisons above indicate that this is not the case in the troposphere, at least when the unfiltered solution displays only relatively weak grid-scale oscillations. Also, the model has never given multiple solutions for the same set of input parameters, which also suggests that the filter does not have a significant impact in the troposphere when its heating rates are small.

Note that the radiation analogy described in Chapter III is only a rough guide. The filter does not account for differences in mass or optical thickness between layers. Also, the boundary conditions imply that there is no energy gain or loss out of the model's atmosphere due to the filter, whereas radiation could cause the atmosphere to lose into the ground nearly all of the thermal energy in short λ near the surface.

B6. The Influence of $[U]_z$ in the Stratosphere.

The model runs presented in Chapters IV and V all use $[U]_z$ equal to a positive constant. The mid-latitude stratosphere has negative $[U]_z$. The model also had negative $[U]_z$ in its stratosphere until the oscillations that eventually prompted the use of the filter appeared. Positive $[U]_z$ tended to suppress the oscillations, so that the model used $[U]_z$ positive everywhere.

Figure B.8 compares $N^2(z)$ from three model solutions that have different $[U]_z$ above 11 km. In these solutions,

$$[U]_z\left(\frac{m/sec}{km}\right) = U_{z0} - U_{z1}\cdot\tanh\big(0.2(z - 11)\big) \quad ,$$

where z is in kilometers. The three model solutions in the figure are for (U_{z0}, U_{z1}) combinations of a) (2.0, 0.0), b) (1.0, 1.0), c) (0.5, 1.5). All three combinations give $[U]_z \approx 2\ \frac{m/sec}{km}$ well below 11 km. The second combination gives $[U]_z \approx 0$ well above 11 km, and the third gives $[U]_z \approx -1\ \frac{m/sec}{km}$ well above 11 km. Each model run is unfiltered and uses $n_z = 4$, with the other model parameters being the same as for the 25 km grid $n_z = 3$ run described in section B4. The differences between N^2 profiles in the figure are small, indicating that the stratospheric $[U]_z$ has little influence on model solutions. This conclusion is also supported by a comparison of wave number 4 growth rates for these solutions, the growth rates in units of $days^{-1}$ being a) 0.23, b) 0.24, and c) 0.23.

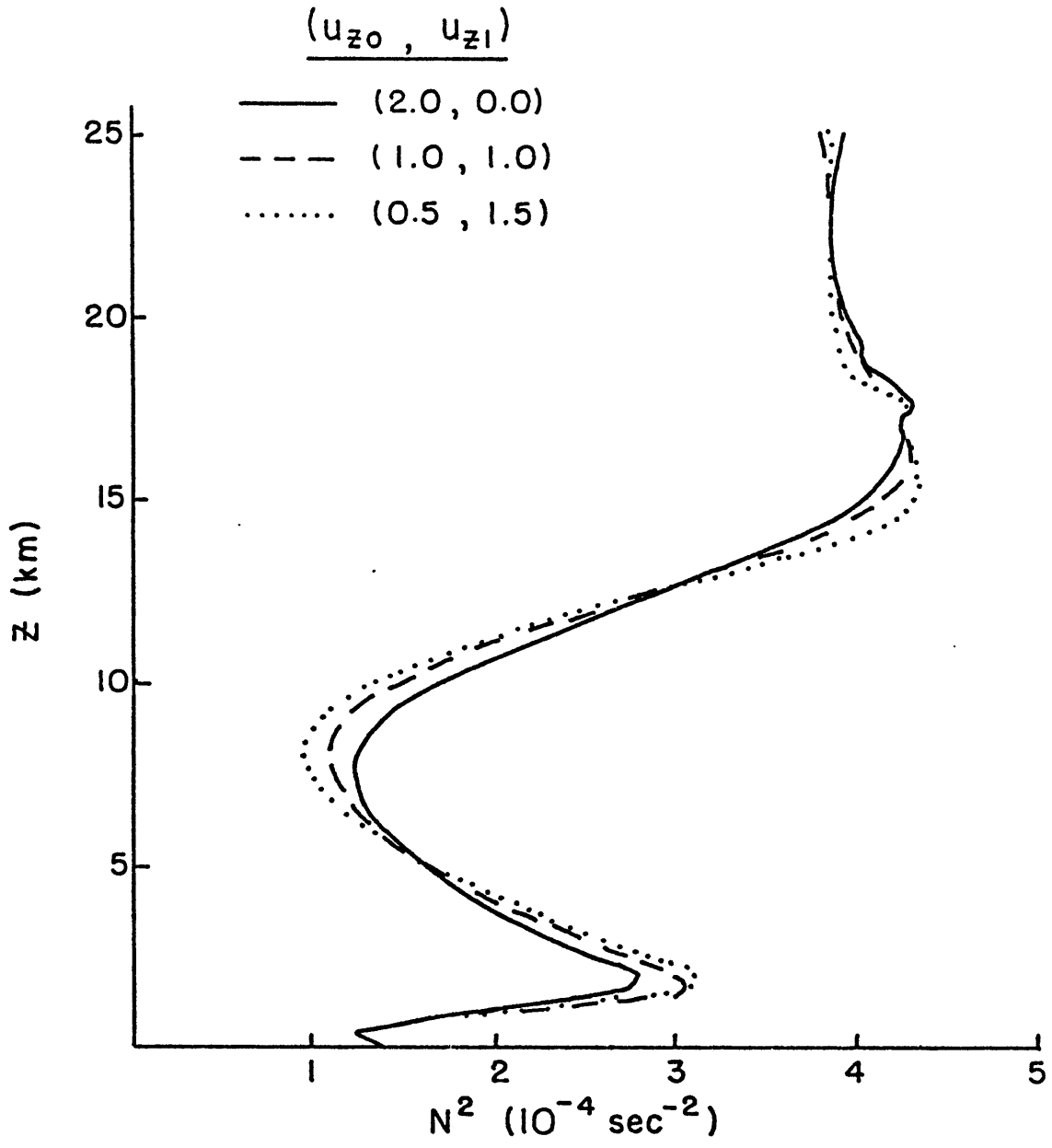


Fig. B.8 - $N^2(z)$ for three model solutions which differ in the [U](z) profiles used for their computations.

REFERENCES

Acton, F. S., 1970: Numerical Methods that Work. Harper & Row, 541 pp.

Balsley, B. B., and K. S. Gage, 1982: On the use of radars for operational wind profiling. Bull. Am. Meteorol. Soc., **63**, 1009-1018.

Baumgartner, A., and E. Reichel, 1975: The World Water Balance. Elsevier, 179 pp.

Bender, C. M., and S. A. Orzag, 1978: Advanced Mathematical Methods for Scientists and Engineers. McGraw-Hill, 593 pp.

Berggren, R., and A. Nyberg, 1967: Eddy vertical transport of latent and sensible heat. Tellus, **19**, 18-23.

Blackmon, M. L., J. M. Wallace, N.-C. Lau, and S. L. Mullen, 1977: An observational study of the Northern Hemisphere wintertime circulation. J. Atmos. Sci., 34, 1040-1053.

_____, and G. H. White, 1982: Zonal wavenumber characteristics of Northern Hemisphere transient eddies. J. Atmos. Sci., **39**, 1985-1998.

Blumen, W., 1979: On short-wave baroclinic instability. J. Atmos. Sci., **36**, 1925-1933.

Branscome, L. E., 1980: Scales and structures of baroclinic waves and their influence on climatic states. Ph. D. thesis, M. I. T., 201 pp.

_____, 1983: The Charney baroclinic stability problem: approximate solutions and modal structures. J. Atmos. Sci., **40**, 1393-1409.

Bretherton, F. P., 1966: Critical layer instability in baroclinic flows. Quart. J. Roy. Meteor. Soc., **92**, 325-334.

Budyko, M. I., 1963: Atlas teplovogo balansa zemnogo shara (Atlas of the heat balance of the Earth). Glavnaia Geofyz. Observ., Moscow, 69pp.

Charney, J. G., 1947: The dynamics of long waves in a baroclinic westerly current. J. Meteor., 4, 135-162.

_____, 1948: On the scale of atmospheric motions. Geophys. Pub., Vol. 17, No. 2, 17 pp.

_____, 1971: Geostrophic turbulence. J. Atmos. Sci., **28**, 1087-1095.

_____, 1973: Planetary fluid dynamics. Dynamic Meteorology, P. Morel, Ed., D. Reidel, 97-349.

_____, and M. E. Stern, 1962: On the stability of internal baroclinic jets in a rotating atmosphere. J. Atmos. Sci., 19, 159-172.

Chen, T.-C., 1982: A further study of spectral energetics in the winter atmosphere. Mon. Wea. Rev., 110, 947-961.

_____, A. R. Hansen, and J. J. Tribbia, 1981: A note on the release of available potential energy. J. Meteor. Soc. Japan, 59, 355-360.

Dahlquist, G., and A. Bjorck, 1974: Numerical Methods. Prentice-Hall, 573 pp.

Davies, D. W., 1979: The relative humidity of Mars' atmosphere. J. Geophys. Res., 84, 8335-8340.

Dickinson, R. E., 1973: Method of parameterization for infrared cooling between altitudes of 30 and 70 kilometers. J. Geophys. Res., 78, 4451-4457.

Dopplick, T. G., 1972: Radiative heating of the global atmosphere. J. Atmos. Sci., 29, 1278-1294.

_____, 1979: Radiative heating of the global atmosphere: Corrigendum. J. Atmos. Sci., 36, 1812-1817.

Drazin, P. G., 1972: Nonlinear baroclinic instability of a continuous zonal flow of viscous fluid. J. Fluid Mech., 55, 577-587.

Eady, E. T., 1949: Long waves and cyclone waves. Tellus, 1, 35-52.

Edmon, H. J., Jr., B. J. Hoskins, and M. E. McIntyre, 1980: Eliassen-Palm cross sections for the troposphere. J. Atmos. Sci., 37, 2600-2616.

Farrell, B. F., 1982: The initial growth of disturbances in a baroclinic flow. J. Atmos. Sci., 39, 1663-1686.

Fullmer, J. W. A., 1982a: Calculations of the quasi-geostrophic potential vorticity gradient from climatological data. J. Atmos. Sci., 39, 1873-1877.

_____, 1982b: The baroclinic instability of highly structured one-dimensional basic states. J. Atmos. Sci., 39, 2371-2387.

Gall, R. L., 1976a: A comparison of linear baroclinic instability theory with eddy statistics of a general circulation model. J. Atmos. Sci., 33, 349-373.

_____, 1976b: Structural changes of growing baroclinic waves. J. Atmos. Sci., 33, 374-390.

_____, 1976c: The effects of released latent heat in growing baroclinic waves. J. Atmos. Sci., 33, 1686-1701.

_____, 1977: Some non-quasigeostrophic effects in linear baroclinic waves. Mon. Wea. Rev., **105**, 1039-1051.

Ghan, S. J., 1983: Empirical models of the eddy heat flux and vertical shear on short time scales. J. Atmos. Sci., **40** (in press).

Gierasch, P., R. Goody, and P. Stone, 1970: The energy balance of planetary atmospheres. Geophys. Fluid Dyn., **1**, 1-18.

Green, J. S. A., 1960: A problem in baroclinic stability. Quart. J. Roy. Meteor. Soc., **86**, 237-251.

Hansen, J., G. Russell, D. Rind, P. Stone, A. Lacis, S. Lebedeff, R. Ruedy, and L. Travis, 1983: Efficient three-dimensional global models for climate studies: Models I and II. Mon. Wea. Rev., **111**, 609-662.

Hantel, M., 1976: On the vertical eddy transports in the northern atmosphere: 1. Vertical eddy heat transport for summer and winter. J. Geophys. Res., **81**, 1577-1588.

Hart, J. E., 1981: Wavenumber selection in nonlinear baroclinic instability. J. Atmos. Sci., **38**, 400-408.

Hasselmann, K., 1976: Stochastic climate models: Part I. Theory. Tellus, **28**, 473-485.

Held, I. M., 1978a: The vertical scale of an unstable baroclinic wave and its importance for eddy heat flux parameterizations. J. Atmos. Sci., **35**, 572-576.

_____, 1978b: The tropospheric lapse rate and climatic sensitivity: Experiments with a two-level atmospheric model. J. Atmos. Sci., **35**, 2083-2098.

_____, 1982: On the height of the tropopause and the static stability of the troposphere. J. Atmos. Sci., **39**, 412-417.

_____, and M. J. Suarez, 1978: A two-level primitive equation atmospheric model designed for climatic sensitivity experiments. J. Atmos. Sci., **35**, 206-229.

Hess, S. L., 1959: Introduction to Theoretical Meteorology. Holt-Dryden, 362 pp.

Hildebrand, F. B., 1956: Introduction to Numerical Analysis. McGraw-Hill, 511 pp.

Holopainen, E. O., L. Rontu, and N.-C. Lau, 1982: The effect of large-scale transient eddies on the time-mean flow in the atmosphere. J. Atmos. Sci., **39**, 1972-1984.

Jensen, C. E., 1961: Energy transformation and vertical flux processes over the northern hemisphere. J. Geophys. Res., **66**, 1145-1156.

Kasahara, A., and W. M. Washington, 1971: General circulation experiments with a six-layer NCAR model, including orography, cloudiness and surface temperature calculations. J. Atmos. Sci., **28**, 657-701.

Kida, H., 1977: A numerical investigation of the atmospheric general circulation and stratospheric-tropospheric mass exchange: II. Lagrangian motion of the atmosphere. J. Meteor. Soc. Japan, **55**, 71-88.

Killworth, P. D., 1980: Barotropic and baroclinic instability in rotating stratified fluids. Dyn. Atmos. Oceans, **4**, 143-184.

Kim, K., 1978: Instability of baroclinic Rossby waves; energetics in a two layer ocean. Deep-Sea Res., **25**, ,795-814.

Larsen, M. F., and J. Röttger, 1982: VHF and UHF Doppler radars as tools for synoptic research. Bull. Am. Meteorol. Soc., **63**, 996-1008.

Lau, N.-C., 1979: The structure and energetics of transient disturbances in the Northern Hemisphere wintertime circulation. J. Atmos. Sci., **36**, 982-995.

Leovy, C. B., 1973: Exchange of water vapor between the atmosphere and surface of Mars. Icarus, **18**, 120-125.

Lilly, D. K., 1968: Models of cloud-topped mixed layers under a strong inversion. Quart. J. Roy. Meteor. Soc., **94**, 292-309.

Lin, C. A., 1980: Eddy heat fluxes and stability of planetary waves: Part I. J. Atmos. Sci., **37**, 2353-2372.

Lindzen, R. S., and B. Farrell, 1980: The role of polar regions in global climate, and a new parameterization of global heat transport. Mon. Wea. Rev., **108**, 2064-2079.

_____, _____, and K.-K. Tung, 1980: The concept of wave overreflection and its application to baroclinic instability. J. Atmos. Sci., **37**, 44-63.

Lorenz, E. N., 1979: Forced and free variations of weather and climate. J. Atmos. Sci., **36**, 1367-1376.

Mak, M., 1982: On moist quasi-geostrophic baroclinic instability. J. Atmos. Sci., **39**, 2028-2037.

Manabe, S., and R. F. Strickler, 1964: Thermal equilibrium of the atmosphere with a convective adjustment. J. Atmos. Sci., **21**, 361-385.

_____, and R. T. Wetherald, 1967: Thermal equilibrium of the atmosphere with a given distribution of relative humidity. J. Atmos. Sci., **24**, 241-259.

_____, and T. B. Terpstra, 1974: The effects of mountains on the general circulation of the atmosphere as identified by numerical experiments. J. Atmos. Sci., 31, 3-42.

McIntosh, D. H., 1972: Meteorological Glossary. Chemical Publishing, 319 pp.

Melgarejo, O. W., and J. W. Deardorff, 1974: Stability functions for the boundary layer resistance laws based upon observed boundary layer heights. J. Atmos. Sci., 31, 1324-1333.

Mudrick, S. E., 1982: A study of the adequacy of quasi-geostrophic dynamics for modeling the effects of cyclone waves on the larger scale flow. J. Atmos. Sci., 39, 2414-2430.

Mullan, B., 1979: A mechanistic model for mid-latitude mean temperature structure. Ph. D. thesis, M. I. T., 248 pp.

Oerlemans, J., 1980: An observational study of the upward sensible heat flux by synoptic-scale transients. Tellus, 32, 6-14.

Oort, A. and E. Rasmusson, 1971: Atmospheric Circulation Statistics. NOAA Prof. Paper 5, 323 pp.

Panofsky, H. A., 1946: Methods of computing vertical motion in the atmosphere. J. Meteor., 3, 45-49.

Pedlosky, J., 1970: Finite-amplitude baroclinic waves. J. Atmos. Sci., 27, 15-30.

_____, 1971: Finite-amplitude baroclinic waves with small dissipation. J. Atmos. Sci., 28, 587-597.

_____, 1975: On secondary baroclinic instability and the meridional scale of motion in the ocean. J. Phys. Ocean., 5, 603-607.

_____, 1979a: Finite-amplitude baroclinic waves in a continuous model of the atmosphere. J. Atmos. Sci., 36, 1908-1924.

_____, 1979b: Geophysical Fluid Dynamics. Springer-Verlag, 624 pp.

_____, 1981: The nonlinear dynamics of baroclinic wave ensembles. J. Fluid Mech., 102, 169-209.

Peixoto, J. P. and A. Oort, 1974: The annual distribution of atmospheric energy on a planetary scale. J. Geophys. Res., 79, 2149-2159.

Prinn, R. G., 1977: On the radiative damping of atmospheric waves. J. Atmos. Sci., 34, 1386-1401.

Saltzman, B., 1970: Large-scale atmospheric energetics in the wavenumber domain. Rev. Geophys. Space Phys., 8, 289-302.

_____, 1978: A survey of statistical-dynamical models of the terrestrial climate. Advances in Geophysics, Vol. 20, Academic Press. 183-304.

_____, and A. Fleisher, 1961: Further statistics on the modes of release of available potential energy. J. Geophys. Res., 66, 2271-2273.

_____, and A. D. Vernekar, 1971: An equilibrium solution for the axially symmetric component of the earth's macroclimate. J. Geophys. Res., 76, 1498-1524.

_____, and C.-M. Tang, 1982: A review of some analytical studies of finite amplitude baroclinic waves, including a new algorithm for the saturation effects of static stability and baroclinicity variations. J. Meteor. Soc. Japan, 60, 1-15.

Sarachik, E. S., 1978: Tropical sea surface temperature: an interactive one-dimensional atmosphere-ocean model. Dyn. Atmos. Oceans, 2, 455-469.

Schubert, S. D., and G. F. Herman, 1981: Heat balance statistics derived from four-dimensional assimilations with a global circulation model. J. Atmos. Sci., 38, 1891-1905.

Shapiro, R., 1970: Smoothing, filtering and boundary effects. Rev. Geophys. Space Phys., 8, 359-387.

Simmons, A. J., and B. J. Hoskins, 1976: Baroclinic instability on the sphere: normal modes of the primitive and quasi-geostrophic equations. J. Atmos. Sci., 33, 1454-1477.

_____, and _____, 1978: The life cycles of some nonlinear baroclinic waves. J. Atmos. Sci., 35, 414-432.

_____, and _____, 1980: Barotropic influences on the growth and decay of nonlinear baroclinic waves. J. Atmos. Sci., 37, 1679-1684.

Staley, D. O., and R. L. Gall, 1977: On the wavelength of maximum baroclinic instability. J. Atmos. Sci., 34, 1679-1688.

Stephenson, J. A., 1977: The vertical temperature structure of the mid-latitude troposphere: a simple model. M. S. thesis, M. I. T., 78 pp.

Stone, P. H., 1972: A simplified radiative-dynamical model for the static stability of rotating atmospheres. J. Atmos. Sci., 29, 405-418.

_____, 1978a: Constraints on dynamical transports of energy on a spherical planet. Dyn. Atmos. Oc., 2, 123-139.

_____, 1978b: Baroclinic adjustment. J. Atmos. Sci., 35, 561-571.

_____, and J. H. Carlson, 1979: Atmospheric lapse rate regimes and their parameterization. J. Atmos. Sci., 36, 415-423.

_____, and D. A. Miller, 1980: Empirical relations between seasonal changes in meridional temperature gradients and meridional fluxes of heat. J. Atmos. Sci., 37, 1708-1721.

_____, S. J. Ghan, D. Spiegel, and S. Rambaldi, 1982: Short-term fluctuations in the eddy heat flux and baroclinic stability of the atmosphere. J. Atmos. Sci., 39, 1734-1746.

Tang, C.-M., and G. H. Fichtl, 1983: The role of latent heat release in baroclinic waves - without β effect. J. Atmos. Sci., 40, 53-72.

Telegadas, K., and J. London, 1954: A Physical Model of Northern Hemisphere Troposphere for Winter and Summer. Scientific Report No. 1, Contract AF19(122)-165, Research Div., College of Engineering, New York University, 55 pp.

Tenenbaum, J., 1976: Spectral and spatial energetics of the GISS model atmosphere. Mon. Wea. Rev., 104, 15-30.

Tomatsu, K., 1979: Spectral energetics of the troposphere and lower stratosphere. Advances in Geophysics, Vol. 21, Academic Press, 289-405.

Wetherald, R. T., and S. Manabe, 1975: The effects of changing the solar constant on the climate of a general circulation model. J. Atmos. Sci., 32, 2044-2059.

BIOGRAPHICAL NOTE

The author was born on April 21, 1954 in Northampton, Massachusetts, where he spent his childhood and attended local schools. He entered Yale University in September, 1972 as a National Merit Scholar and graduated from there in May, 1976, receiving a B.S. degree in astronomy and physics (magna cum laude). He was awarded a UCAR Graduate Fellowship (1977 - 1978) and he entered graduate school at M.I.T. in September, 1977.